

**CRASHWORTHINESS MODELLING OF THIN-WALLED
COMPOSITE STRUCTURES**

Konstantin Evgenievich Morozov

**Submitted in fulfillment of the academic requirements for the degree of Doctor of
Philosophy in the School of Mechanical Engineering**

All work for this thesis was completed at the former University of Natal

**Durban, South Africa
November 2003**

ABSTRACT

This thesis is concerned with the study of the crashworthiness of thin-walled composite structures. Composites are being used more and more in different fields of engineering, particularly, in aerospace and automotive industries because of their high strength-to-weight and stiffness-to-weight ratios, quality and cost advantages. More and more metal parts in cars for instance become or are already replaced by new advanced materials. Composite materials are included in these new advanced materials with the following advantages: weight reduction, corrosion resistance, aesthetics and style, isolation and the ability to integrate several parts into one single structural component. The introduction of new composite structural components (body panels, bumpers, crash absorbers, etc.) requires the development and implementation of new approaches to structural analysis and design. Crashworthiness is one of the foremost goals of aircraft and automotive design. It depends very much on the response of various components which absorb the energy of the crash. In order to design components for crashworthy structures, it is necessary to understand the effects of loading conditions, material behaviour, and structural response. Due to the complexity of the material structure (matrix reinforced with fibres) and specific mechanical properties the nature of transforming the collision kinetic energy into material deformation energy differs from that of conventional metal alloys. The energy absorption mechanics are different for the advanced composites and depend on the material structure (type of reinforcement) and structural design. The primary function of the energy absorption for the composites belongs to the progressive crushing of the materials themselves and structural components (beams, tubes, etc.) made of such materials. Since the mechanics of composite materials and structural components differs substantially from the conventional applications there is a need to develop an appropriate way of modelling and analysis relevant to this problem. Currently there are a large variety of design approaches, test results, and research investigations into the problem under consideration depending on the type of composite material and design geometry of the parts. It has been found that in general an application of fibre reinforced plastics (FRP) to vehicle compartments can satisfy the structural requirements of the passenger compartment including high strength and light weight. Implementation of new advanced composite materials provides the opportunity to develop designs of reliable structural composite parts in high volume for improved automotive fuel economy. Structural optimisation and crashworthiness of composite components should be incorporated into design calculations to control the mechanical performance.

The introduction which follows describes the aims of the present study of the crashworthiness modelling and simulation of the structural response of thin-walled composite components which are subjected to various loading conditions relevant to vehicle design. The research programme undertaken within the framework of this project includes development and validation of the modelling and simulation methodology applicable to the crashworthiness analysis of thin-walled composite structures. Development of computerised dynamic modelling of structural components offers the capability of investigating the design parameters without building the actual physical prototypes. In this approach, the dynamic behaviour of the structure is simulated for specified external inputs, and from the corresponding response data the designer is able to determine its dynamic response characteristics, and estimate the crashworthiness of the structure in vehicle engineering applications.

PREFACE

The author declares that this thesis is his own unaided work except where due acknowledgement is made to others. This thesis is being submitted for the Degree of Doctor of Philosophy to the University of Natal, Durban, and has not been submitted previously for any other degree or examination.

ACKNOWLEDGEMENTS

The author expresses his gratitude to his Supervisor, Professor V. E. Verijenko for his guidance and encouragement.

He would also like to thank:

National Research Foundation for the financial support

Administration staff and workshop technicians at the School of Mechanical Engineering for all their advice and assistance

His colleagues, postgraduate students, for all the encouragement, assistance and advice.

LIST OF FIGURES

Figure 2.1	Thin-walled structures	3
Figure 2.2	Plate buckling	4
Figure 2.3	Local and overall buckling interaction in a hollow box column	4
Figure 2.4	View of one-quarter of partially collapsed thin-walled rectangular column	5
Figure 2.5	Typical force-displacement curve for slow crush testing of an metal hexagonal box section	6
Figure 2.6	Moment-rotation curves for beams under bending	8
Figure 2.7	Modelling of a short fibre composite as a representative element volume with ellipsoid inhomogeneities representing microcracks	15
Figure 2.8	Representation of SMC by means of a multilayer composite consisting of unidirectional plies and designation of coordinate system.....	15
Figure 2.9	Damaging curve used for an SMC composite material	26
Figure 2.10	Isotropic damage function	27
Figure 2.11	Modified Jones' law	28
Figure 2.12	Elastic-plastic behaviour with kinematic and isotropic hardening	29
Figure 2.13	Assessment of damage variable d	33
Figure 2.14	Reduction in moduli	33
Figure 2.15	Experimentally obtained stress-strain curve	34
Figure 2.16	Interpolation of d	34
Figure 2.17	Phases of material degradation	35
Figure 2.18	Stress vs. Strain diagram for cycling test	40
Figure 3.1	Schematic tensile (a) and bending (b) set-up	48
Figure 3.2	Progressive deformation of SMC composite plate	50
Figure 3.3	Force-Displacement for PAM-CRASH simulation of SMC plate	50
Figure. 3.4	Force-Displacement for PAM-CRASH simulation of SMC plate	51
Figure 3.5	Distribution of displacements in X direction corresponding to the limit of elasticity	51
Figure 3.6	Distribution of σ_x corresponding to the limit of elasticity	52
Figure 3.7	Distribution of displacements in X direction corresponding to the maximum value of stress	52
Figure 3.8	Distribution of σ_x corresponding to the maximum value of stress	53

Figure 3.9	Distribution of displacements in X direction corresponding to the maximum value of stress	53
Figure 3.10	Distribution of σ_x corresponding to the maximum value of stress	54
Figure 3.11	Distribution of σ_x and Stress vs. Time curve for nodes 96, 89, 16	54
Figure 3.12	Progressive deformation of SMC composite plate under bending test at 33mm/s	56
Figure 3.13	Force-Displacement for PAM-CRASH simulation of SMC plate	56
Figure 3.14	Progressive deformation of SMC composite plate under bending test at 330mm/s	57
Figure 3.15	Force-Displacement for PAM-CRASH simulation of SMC plate	57
Figure 3.16	Maximum Bending Moment (M_x) distribution and Moment vs. Time curves	58
Figure 3.17	Plate deflection distribution corresponding to the maximum bending moment	58
Figure 3.18	Maximum Bending Moment (M_x) distribution and Moment vs. Time curves	59
Figure 3.19	Distribution of deflection corresponding to the maximum bending moment	59
Figure 3.20	Bending test simulation results (33mm/s)	60
Figure 3.21	Bending test simulation results (330mm/s).....	60
Figure 3.22	Progressive deformation of laminated plate under tensile test at 33mm/s	65
Figure 3.23	Force-Displacement curve for tensile simulation (PAM-CRASH, Bi-Phase Model)	66
Figure 3.24	Progressive deformation of laminated plate under tensile test at 330mm/s	66
Figure 3.25	Force-Displacement diagram for the tensile test simulation	67
Figure 3.26	Distribution of displacements in X direction corresponding to the maximum value of stress	67
Figure 3.27	Distribution of σ_x corresponding to the maximum value of stress	68
Figure 3.28	Distribution of σ_x corresponding to the moment of material failure	68
Figure 3.29	Distribution of displacements in X direction corresponding to the maximum value of stress	69
Figure 3.30	Distribution of σ_x corresponding to the maximum value of stress	69
Figure 3.31	Distribution of σ_x corresponding to the moment of material failure	70
Figure 3.32	Distribution of displacements in X direction corresponding to the maximum value of stress	70

Figure 3.33	Distribution of σ_x corresponding to the maximum value of stress	71
Figure 3.34	Distribution of σ_x corresponding to the moment of material failure	71
Figure 3.35	Distribution of displacements in X direction corresponding to the maximum value of stress	72
Figure 3.36	Distribution of σ_x corresponding to the maximum value of stress	72
Figure 3.37	Distribution of σ_x corresponding to the moment of material failure	73
Figure 3.38	Progressive deformation of laminated plate under bending test at 33mm/s	75
Figure 3.39	Force-Displacement curve for bending simulation	75
Figure 3.40	Progressive deformation of laminated plate under bending test at 330 mm/s	76
Figure 3.41	Force-Displacement for simulation of bending test	76
Figure 3.42	Progressive deformation of laminated plate under bending test at 33mm/s	77
Figure 3.43	Force-Displacement diagram for the bending test simulation	78
Figure 3.44	Progressive deformation of laminated plate under bending test at 330mm/s	78
Figure 3.45	Force-Displacement diagram for the bending test simulation	79
Figure 3.46	Distribution of deflection corresponding to the maximum bending moment	79
Figure 3.47	Maximum bending moment (M_x) distribution	80
Figure 3.48	Distribution of plate deflection corresponding to the maximum bending moment	80
Figure 3.49	Maximum bending moment (M_x) distribution	81
Figure 3.50	Distribution of plate deflection corresponding to the maximum bending moment	81
Figure 3.51	Maximum bending moment (M_x) distribution	82
Figure 3.52	Distribution of plate deflection corresponding to the maximum bending moment	82
Figure 3.53	Maximum bending moment (M_x) distribution	83
Figure 3.54	Laminated composite (Bi-Phase Model) bending simulation comparison (330 mm/s)	83

Figure 3.55	Laminated composite (Bi-Phase Model) bending simulation comparison (33 mm/s)	84
Figure 3.56	Laminated composite (Global Ply Model) bending simulation comparison (330 mm/s)	85
Figure 3.57	Laminated composite (Global Ply Model) bending simulation comparison (33 mm/s)	86
Figure 4.1	Electrical cartridge heaters	90
Figure 4.2	Specimen mould design including required fixtures	91
Figure 4.3	Schematic of the heated moulds showing thermocouple and element positions	92
Figure 4.4	Temperature controller (<i>ATC</i> , South Africa) and secondary temperature display	92
Figure 4.5	Temperature control system	93
Figure 4.6	Completed specimen mould (a) 'Male' section (b) 'Female' section	94
Figure 4.7	Hydraulic press used for specimen manufacture	94
Figure 4.8	Brackets used to fix mould to press	95
Figure 4.9	Alignment of mould using guide pins	95
Figure 4.10	Mould fitted and aligned	96
Figure 4.11	Installation of thermocouples and heating elements	96
Figure 4.12	Temperature controller and temperature display	97
Figure 4.13	The SMC material being cured under temperature and pressure	97
Figure 4.14	Moulded SMC plate	98
Figure 4.15	Cut samples ready for testing	98
Figure 4.16	Lloyds test setup	99
Figure 4.17	Stress-strain curves for SMC material	99
Figure 4.18	Lower tensile curve	100
Figure 4.19	Upper tensile curve	100
Figure 4.20	Middle tensile curve	101
Figure 4.21	Compressive curve	101
Figure 4.22	Destroyed compressive test samples	102
Figure 4.23	Schematic of three point bend test	103
Figure 4.24	Three point bend test (actual set-up)	103
Figure 4.25	lose up of failed sample (still mounted)	104
Figure 4.26	Close up of failed sample, showing fracture	104
Figure 4.27	Instron test rig ready for testing	104

Figure 4.28	MTS test rig with load cell	105
Figure 4.29	Force vs. Time experimental curve under loading with prescribed velocity of 2 mm/s	105
Figure 4.30	Experimental Force vs. Time curve for the bending loading with prescribed velocity of 100 mm/s	106
Figure 4.31	Meshed plate	106
Figure 4.32	Plate meshed with 128 plate elements (element size 5 x 5mm)	107
Figure 4.33	Plate meshed with 128 solid elements (element size 5 x 5 x 4mm)	107
Figure 4.34	Plate meshed with 1600 solid elements (element size 2 x 2 x 2mm)	107
Figure 4.35	Complete comparative results incorporating the tensile characterisation	108
Figure 4.36	Prototype geometry	109
Figure 4.37	Prototype mould 'male' section	110
Figure 4.38	Prototype mould 'female' section	110
Figure 4.39	Schematic of the prototype mould including mounting brackets, spacers, and guide pins	111
Figure 4.40	Prototype manufacturing process	112
Figure 4.41	Temperature controllers	112
Figure 4.42	Mould assembled on press	113
Figure 4.43	Raw SMC material being placed in mould	113
Figure 4.44	Closing the moulds	114
Figure 4.45	Prototype attached to male section after curing	114
Figure 4.46	Moulded prototype	114
Figure 4.47	The completed specimens and prototype	115
Figure 4.48	Prototype production run	115
Figure 4.49	Prototype test setup	116
Figure 4.50	Results for crash of prototype demonstrator	117
Figure 4.51	Destroyed prototype demonstrator	117
Figure 4.52	Meshed prototype	118
Figure 4.53	Force-Displacement curves for crushing of prototype (comparison of simulation and experiment)	119
Figure 4.54	Progressive prototype deformation	120
Figure 4.55	Progressive prototype deformation (Initial velocity 1 m/s)	122
Figure 4.56	Force-Time curve for simulation with initial velocity 1 m/s	122
Figure 4.57	Progressive prototype deformation (Initial velocity 5 m/s)	123
Figure 4.58	Force-Time curve for simulation with initial velocity 5 m/s	123

Figure 5.1	Cumulative distribution for failure stress of samples	129
Figure 5.2	Weibull Shape parameter identification	129
Figure 5.3	Probability of Failure vs. Stress	130
Figure 5.4	Progression of stress damage in tensile specimen	131
Figure 5.5	Applied Force vs. Displacement curve for illustrative example	132

LIST OF TABLES

Table 3.1.	Tensile test simulated results for SMC material. (33 mm/s prescribed velocity)	55
Table 3.2.	Tensile test simulated results for SMC material (330 mm/s prescribed velocity)	55
Table 3.3	Tensile test simulated results for Bi-Phase model of laminate material.(33 mm/s prescribed velocity)	73
Table 3.4	Tensile test simulated results for Global Ply model of laminated composite. (33mm/s prescribed velocity)	74
Table 3.5	Bending test simulated results for Bi-Phase laminate material. (330 mm/s prescribed velocity).....	84
Table 3.6	Bending test simulated results for Bi-Phase laminate material. (33 mm/s prescribed velocity)	84
Table 3.7	Bending test simulated results for Global Ply laminate material (330 mm/s prescribed velocity)	85
Table 3.8	Bending test simulated results for laminated plate (Global Ply Model) (33 mm/s prescribed velocity)	86
Table 4.1	Material characterisation parameters	102

CONTENTS

Abstract	ii
Preface	iii
Acknowledgements	iv
List of figures	v
List of tables	xi
Chapter 1 Introduction	1
Chapter 2 Thin-walled structural components in crashworthiness applications	3
2.1 Energy absorption capability and dynamic response of metal structures	3
2.1.1 Buckling of thin-walled structures. Axial collapse	3
2.1.2 Bending collapse	8
2.2 Crashworthiness modelling of composite structures	9
2.2.1 Crushing and damage modes and mechanisms in composites	10
2.2.1.1 Phenomenological crushing model	10
2.2.1.2 Failure model for laminates under in-plane shear and tension	11
2.2.1.3 Model incorporating transverse shear effects using an improved shear correction factor method	13
2.2.1.4 Damage model for composites reinforced with randomly oriented short fibres	14
2.2.1.5 Laminate model for damage processes in SMC	15
2.2.1.6 MLT damage model	17
2.2.2 Progressive failure models	18
2.2.2.1 Layerwise progressive failure model	18
2.2.2.2 Buckling analysis model	20
2.2.2.3 Effects of progressive fracture on buckling resistance	22
2.3 Crashworthiness modelling of composite structural components with complex shape and geometry	24

2.3.1	Modelling of short-fibre randomly reinforced composite materials	25
2.3.1.1	PAM-CRASH model for SMC composites	25
2.3.1.2	LS-DYNA model for SMC composites	29
2.3.2	Modelling of laminated continuously reinforced composites	30
2.3.2.1	Bi-Phase model (PAM-CRASH)	31
2.3.2.2	Global Ply model (PAM-CRASH)	38
2.3.2.3	Chang-Chang Composite Failure model (LS-DYNA)	43
2.3.2.4	Enhanced Composite Damage model (LS-DYNA)	45
Chapter 3	Numerical simulation. Comparative software and model analysis	48
3.1	SMC composites	49
3.1.1	Tensile test simulation	49
3.1.2	Bending test simulation	55
3.2	Laminates	61
3.2.1	Tensile test simulation	65
3.2.2	Bending test simulation	74
Chapter 4	Crashworthiness modelling of thin-walled components made from SMC composites	89
4.1	Material characterisation	89
4.1.1	Specimen manufacture	90
4.1.2	Specimen testing	98
4.2	Progressive failure of SMC plate under bending loading	103
4.3	Crashworthiness modelling and simulation of the thin-walled composite automotive component	108
4.3.1	Prototype manufacture	109
4.3.2	Prototype testing	116
4.3.3	Prototype simulation	117
Chapter 5	Progressive failure model development	125
5.1	Progressive failure criterion	125

5.1.1	Material constitution	125
5.1.2	Statistical damage law	127
5.2	Model application	128
Chapter 6	Conclusions	134
References	136

Chapter 1

INTRODUCTION

The structural crashworthiness represents one of the most important parts of the design process for different transportation systems. Crash resistance of the structure is characterised by the energy absorbing capability of crushing structural parts as well as the requirement to provide the necessary structural integrity to protect the vehicle occupants.

The basic principle of occupant crash protection has been used in the automotive field since the early 1950s (Barenyi, 1952). Nowadays, crash safety has become a well-established car design requirement. In aeronautics, the first structural design requirements for better crash protection were established for military helicopters and light fixed-wing aircraft in the form of the Aircraft Crash Survival Design Guide and the MIL-STD-1290A, 1998 (Kindervater and Georgi, 1993). Crashworthiness analysis is normally implemented at the design stage in order to control the ability of the structure to cope with the impact loads, i.e. to absorb the impact energy during the collapse, so that just a small amount of the energy is transferred to the vehicle occupant. The design goal in this case is to dissipate kinetic energy irreversibly rather than convert and accumulate it elastically. In particular, the effect of the energy restitution should be minimised.

There are two main approaches to the crashworthiness analysis: impact testing of the prototypes and numerical modelling and simulation. Physical full-scale impact testing of prototypes is expensive. For this reason the design engineer must be provided with an efficient design tool and methodology capable of analysing alternative design concepts in an economical and reliable way. Crash simulation technology is becoming widely adopted for the design and development of safe and efficient vehicles and involves both numerical modelling and experimental (material characterisation) studies.

The numerical tools for the crash simulation of metal and composite structures are, in particular, the finite element (FE) computer codes (e.g. PAM-CRASH, LS-DYNA, ABAQUS, etc.) including material model routines. In many cases the load-deflection characteristics of the single components can be superimposed to gain the overall crash response of a vehicle with sufficient accuracy. Thus component crash tests and simulations are powerful tools to provide the crash prediction of a structure.

While extensive crashworthiness simulation and modelling of metallic structures is by now well established and became a compulsory component of every day design practice, models for the numerical crashworthiness analysis of structural components made from composite materials are still emerging.

Composite materials are currently being used in a range of aerospace and automotive structures. These materials have considerable potential for absorbing kinetic energy during a crash. The composite energy absorption capability offers a combination of reduced structural weight and improved vehicle safety provided by higher or at least comparable with metal structures crash resistance. Controlled microfragmentation processes provide the capability to absorb kinetic energy during vehicle crashes. The material systems utilised in aerospace applications are higher-performance types such as epoxy resins reinforced with glass fibres and, increasingly, aramid and carbon fibres. In the automotive industry reinforced plastics must satisfy a complex set of design requirements including among others crash energy absorption management. At the same time, the decisive factors in automotive structures are the material costs compared with metal, and efficient fabrication procedures such as sheet moulding compound (SMC), high-speed resin transfer moulding (HSRTM), and thermoplastic stamping. For these reasons, the major reinforcement is

provided by glass fibres in combination with polyester resins and thermoplastic systems such as polyamides and polyethylene-terephthalate (PET).

Structural crash resistance is controlled by the material behaviour, the structural design, and geometrical parameters. Usually, composite materials reinforced with glass or carbon fibres exhibit a linear elastic response up to failure with little or no plasticity. In the case of composite materials, internal material failure is initiated on a micromechanical level and can be observed in many forms, such as breaking of the fibres, matrix microcracking, separation of fibres from the matrix (debonding or pull-out), and delamination. Progressive microfragmentation of composites generates relatively smooth deceleration-time functions in crashing vehicle components. Conventional metallic structures absorb impact and crash energy through plastic deformation and folding. Folding mechanisms, which could also occur with tough composite structures, usually produce undulated crush curves. This results in relatively low crush-force efficiencies.

Most of the studies to examine the energy absorbing characteristics of thin-walled composite structures have been directed towards the axial crush analysis of axially symmetric components such as tubes, beams, cylindrical shells, etc. However, impacted structures quite often fail in a bending mode. Review of existing approaches to the simulation of crushed composite thin-walled components can be found in (Mamalis et al., 1998).

The main objective of the present work is the development of the crashworthiness simulation approach and methodology applicable to the thin-walled composite structural components that have an arbitrary complex (mixed) shape and geometry. Dynamic structural analysis and crash simulation of such structures require the application of geometrically non-linear modelling. The problem is complicated with the fact that the structures are made from composite materials. Correspondingly, progressive failure analysis and crashworthiness predictions represent complex problems due to the variety of failure modes and fragmentation mechanisms. Material models that are normally used in the analysis include various types of material characteristics (physical parameters). These parameters should be determined experimentally. Depending on the adopted model the experimental characterisation of the material could be very complex and cumbersome. The proposed models and simulation techniques are to be experimentally verified and validated. The testing of the representative composite prototypes and comparison of the predicted numerical data on crushing behaviour with the experimental results should be undertaken.

According to the main goal, the scope of the present research programme includes geometrically non-linear dynamic structural analysis applicable to structures with complex (mixed) geometries, progressive damage modelling and experimental material characterisation. It is important, that the latter would be feasible for practical implementation since there are a lot of material models (especially based on micromechanical theories) that involve sets of physical material properties that could not be reliably determined from the tests.

The thesis consists of five chapters progressively presenting the work done in order to achieve the aforementioned goals and objectives. In particular, Chapter 2 deals with the existing approaches to the crashworthiness modelling of thin-walled metal and composite components. Chapter 3 considers numerical simulation and contains the comparative software and model analysis for SMC and laminated composite structures. Chapter 4 presents the experimental results of material characterisation, bending test validation analysis, and crashworthiness modelling and simulation of the composite prototype. Development of a new progressive failure material model for SMC composites is discussed in Chapter 5.

Chapter 2

THIN-WALLED STRUCTURAL COMPONENTS IN CRASHWORTHINESS APPLICATIONS

2.1 Energy absorption capability and dynamic response of metal structures

Thin-walled structural elements, such as plates and shells are important load carrying components in civil-, mechanical-, automotive-, aeronautical-, and marine engineering structures. Crashworthiness modelling and analysis of such structures includes considerations of progressive buckling, axial collapse and folding modes, and bending collapse.

This chapter describes existing models and mechanisms developed in this area. Such models could be classified as conventional ones. The review of conventional models will provide a better understanding of the possible ways and approaches to the analysis and modelling of composite structures.

2.1.1 Buckling of thin-walled structures. Axial collapse

Structural components made of material the thickness of which is much less than other structural dimensions are classified as thin-walled structures. Plate and shell assemblies, common hot- and cold- formed structural sections, tubes and cylinders, and many various automotive structures fall into this category.

Thin-walled sections such as those illustrated in Fig. 2.1 are increasingly supplanting traditional hot- rolled I-beams and channels. They are particularly prone to buckling and in general must be designed against several different types of buckling.

It is not difficult to visualize what may happen if a beam is made from such a cold-rolled channel section. One flange is in substantial compression and may therefore buckle locally at a low stress (i.e. much less than yield) thus reducing the load capacity of the beam as a whole. Buckling rather than strength considerations thus dictate the thin-walled beam's performance.

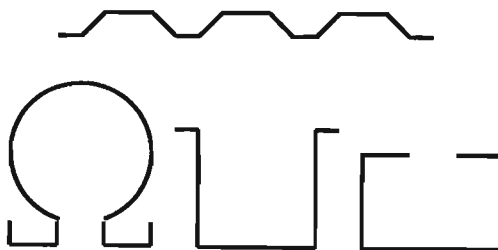


Fig. 2.1 Thin-walled structures.

Local buckling of an edge-supported thin plate (Fig. 2.2) does not necessarily lead to total collapse as in the case of columns, since plates can generally withstand loads greater than critical.

However the load-displacement curve, $P-\Delta l$ illustrates plates' greatly reduced stiffness after buckling, so plates cannot be used in the post-buckling region unless the behaviour in that region is predictable. It should be emphasised that the kink in the $P-\Delta l$ curve is not related to any elastic-plastic yield transition of the material. In fact, the systems being discussed are totally elastic. The kink is a reflection of overall geometry rather than material instability.

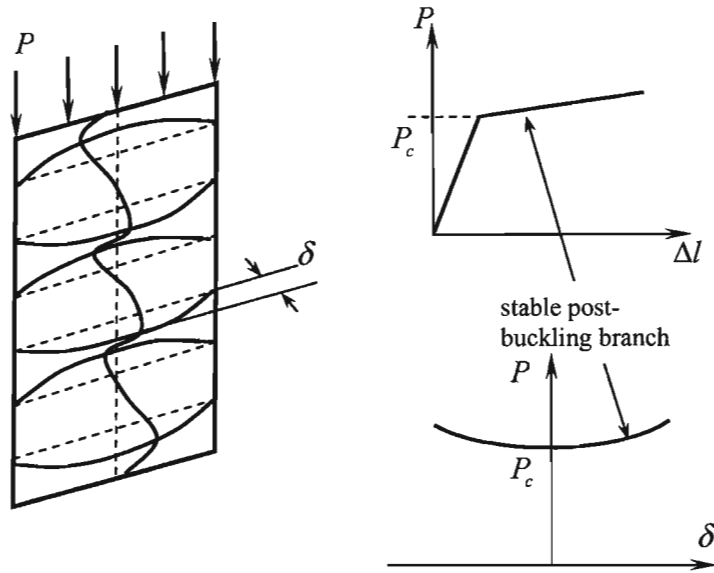


Fig. 2.2 Plate buckling.

The post-buckling behaviour of compressed cylindrical shells is quite different to that of plates. Since the displacements are uncontrolled in most practical systems, shells behave in a snap-buckling mode – i. e. as an increasing load reaches the bifurcation point, the cylinder must undergo an instantaneous increase in deflection in order to accommodate the increasing load. A subsequent decrease in load is accommodated by a corresponding decrease in buckling deflection.

It often happens that a thin-walled system is prone to buckling in various modes. These usually interact to reduce the load capacity of the system compared to that under the buckling modes individually. An example of mode interaction is the thin box section (Fig. 2.3), which develops local buckles at an early stage of loading.

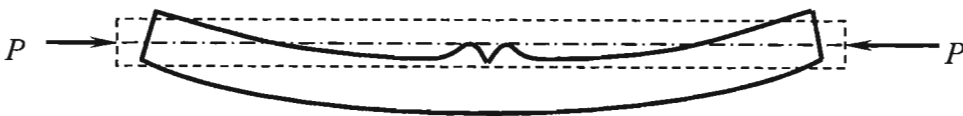


Fig. 2.3 Local and overall buckling interaction in a hollow box column.

These local buckles influence the behaviour of the column, and gross column buckle will occur at a load much less than Euler buckling load.

Non-linear buckling analysis and specifically developed models are normally used to investigate post-buckling behaviour of thin-walled systems. Combined models that take into account both the physical non-linearity of the material and geometrical non-linearity of structural components are developed to describe axial collapse of thin-walled structures.

A view of partially crashed metal rectangular column is shown in Fig.2.4 (Wierzbicki, 1983a). The fold line, which is of typically waved shape, forms a double curvature shell.

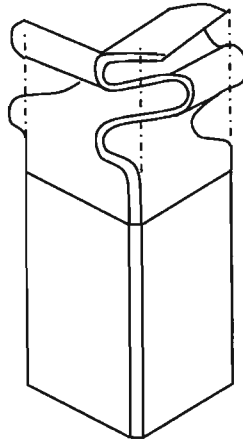


Fig. 2.4 View of one-quarter of partially collapsed thin-walled rectangular column.

The fold line is seen to stay in the plane inclined by 45° to the two planes of symmetry. This is an indication that the material is inextensible in the horizontal direction. The initially flat lateral surfaces of the column are transformed into a single curvature surface.

The plastic flow is not confined to a single wavelength but is spread over two consecutive folding modes. The crush behaviour of open-section structures is even more complicated since the local folding wave interacts with the global elastic or plastic mode of the plate buckling.

Many different folding modes with various degrees of simplicity have been suggested in the literature (Wierzbicki, 1983a, b). Some modes are purely inextensional and involve bending about stationary hinge lines which may be either straight or curved. Such modes can be activated only if sufficient freedom is left on all boundaries for deformation.

At the same time, they represent a minimum work path to reach the final, completely folded, state and thus provide a lower bound on the actual dissipated energy.

In some cases the extensions of the material and a continuous bending (Wierzbicki, 1983a) are taken into account. The bending changes the circumferential curvature. Detailed analysis of various crushing processes and modes can be found in (Wierzbicki, 1983a, b).

A good design of an axial impact member will demonstrate a controlled and progressive collapse, as well as achieving the required energy absorption. Fig. 2.5 shows the typical force-displacement curve for a slow crash test of aluminium hexagonal impact member (McGregor et al., 1993).

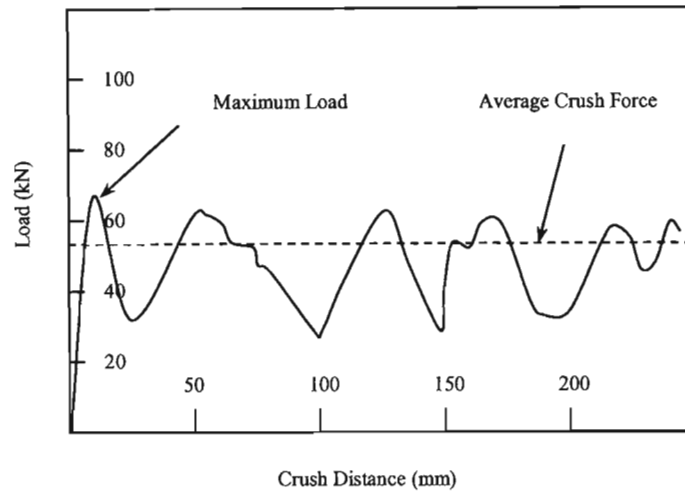


Fig. 2.5 Typical force-displacement curve for slow crush testing of a metal hexagonal box section.

The important design loads include the load to initiate collapse and the average crush force. In the design of vehicles for crashworthiness it is necessary to easily predict the energy absorption capability of the energy absorbing components. (It has been almost commonly adopted that the most efficient structures to that aim are tubular components with various cross-section shapes.) The circular thin-walled tubes have large values of the absorbed energy per volume unit, allowing very light and efficient deforming components (and are reasonably cheap being large-scale commercial products).

The axial crushing of circular sections can take place in either two modes: an axisymmetric mode (concertina mode) in which the material forms a series of successive axisymmetric lobes and a non-axisymmetric mode in which the material forms successive diamond shaped folds (diamond mode) (Horton et al., 1966). Sometimes, (Horton et al., 1966; Avalle et al, 1995), diamond lobes follow in a collapse begun in the axisymmetric modes.

The problem of the axial crushing of tubes has been thoroughly examined in the past for both types of collapse mode.

Two families of models based on concentrated plastic hinges and moving plastic hinges were developed in (Alexander, 1960, Avalle et al., 1995, Wierzbicki et al., 1992, Avalle and Belingardi, 1996, Wierzbicki et al., 1986, Belingardi and Avalle, 1995) for the axisymmetric mode.

In the literature there has not been the same effort on the analysis of the diamond mode of collapse as for the concertina mode. Only Pugsley and MacAulay (1960) developed a mechanical model based on fixed hinges. This work was followed by adjustments especially due to Wierzbicki et al. (1992).

The evaluation of the aptitude of a structure to dissipate energy during the crash can be performed using different non-dimensional parameters. The parameter, which briefly summarizes the geometry of a circular tube, is the thickness over the diameter ratio t/D . Another useful and widely used parameter is the *solidity ratio* SR which is defined as the ratio of the effective cross section of a tubular structure over the total area enclosed by the cross section.

For a circular tube the solidity ratio is:

$$SR = 4 (t/D)$$

The capability of a structural member to dissipate energy is evaluated by means of the mean stress σ_{mean} , ratio of the mean crushing force F_{mean} over the initial area of the cross section. For comparison between structural members made from different materials it is better to use the ratio of the mean stress σ_{mean} over the material yield stress σ_y . This non-dimensional parameter is generally named the *structural efficiency SE*:

$$SE = \sigma_{mean} / \sigma_y$$

The maximum force F_{max} value helps in evaluating the risk of severe damage to the occupant of a vehicle due to excessive deceleration during the impact. To better evaluate and compare the behaviour of different geometry and materials, the load uniformity *LU* parameter is used:

$$LU = F_{max} / F_{mean} = \sigma_{max} / \sigma_{mean}$$

The theoretical models previously cited give predictions of the structural efficiency in terms of the solidity ratio, and structural efficiency.

(The maximum force value depends on whether the collapse would occur in the elastic range or, whether plastic flow has already taken place.)

When the collapse occurs in the elastic range the classical theory (e. g. Timoshenko et al., 1963) predicts the following buckling load for a circular tube:

$$\frac{\sigma_{max}}{\sigma_y} = \frac{2}{\sqrt{3(1-\nu^2)}} \frac{t}{d} \frac{E}{\sigma_y}$$

However collapse occurs in the elastic range for only small values of the solidity ratio that are not of interest for automotive industry application (Wierzbicki, 1983).

If the initial collapse occurs in the plastic range the expression reported by Timoshenko et al. (1963) can be used:

$$\frac{\sigma_{max}}{\sigma_y} = \frac{2}{\sqrt{3(1-\nu^2)}} \frac{t}{D} \frac{E_t}{\sigma_y} = \frac{4}{3} \frac{E_t}{\sigma_y} \frac{t}{D}$$

in which Poisson's ratio for the plastic material has been set to 0.5.

To obtain a better fit of the experimental results Avasle et al., 1995 suggested the following relation for the plastic buckling:

$$\frac{\sigma_{max}}{\sigma_y} = \frac{4}{3} \frac{E_s}{\sigma_y} \frac{t}{D} = 1 + \frac{4}{3} \frac{E_t}{\sigma_y} \frac{t}{D}$$

It is important to stress the fact that the geometry plays the main role in determining the type of collapse. For thinner tubes, having values of solidity ratio less than 0.1 (diameter over the thickness ratios of more than 40) the main collapse mode is the diamond mode, whereas for thicker tubes the preferred collapse mode is the axisymmetric mode.

However in the range of values of the solidity ratio near to 0.1 (from 0.08 to 0.12) the two modes are possible. Actually the two modes often coexist and in these cases the collapse starts axisymmetrically and changes to the non-axisymmetric mode after one or more axisymmetric lobes. Theory and experiments show that the mean collapse load of the two modes is almost equal and therefore the two modes are indifferently alternative. However the axisymmetric mode is a less stable mode and therefore transition is likely to occur. From the design point of view, in this intermediate range of solidity ratios it is possible to use both approaches to predict the structural behaviour in terms of structural efficiency and load uniformity.

In both modes it is easy to see that both the structural efficiency, hence the mean absorbed energy, and the load uniformity improve when the solidity ratio increases, i. e. for thicker tubes.

With regard to the structural efficiency, which evaluates the capability of the component to absorb a great amount of energy, there are two different expressions corresponding to the two possible modes of collapse, the axisymmetric, concertina, and the non-axisymmetric, diamond. In the axisymmetric collapse the structural efficiency is proportional to the square root of the solidity ratio. In the diamond mode the structural efficiency is proportional to the solidity ratio to the power of $2/3$. The two formulae agree very well with the theory for what concerns the power exponent of the solidity ratio, but all the theories underestimate the constants in the formulae (Wierzbicki, 1983).

2.1.2 Bending collapse

Bending collapse of structural components is the other main deformation mode considered by designers. The three important aspects of performance for bending collapse are the maximum moment to initiate collapse, the energy absorbed and the mode of collapse.

Fig. 2.6 shows the typical moment-rotation curves for three beams demonstrating three different modes of collapse. The first curve shows the performance of a beam that fails by local buckling. This is typical of a beam with a high width-to-thickness ratio. Although the maximum moment and energy absorbed are low, the mode of collapse is stable and reliable.

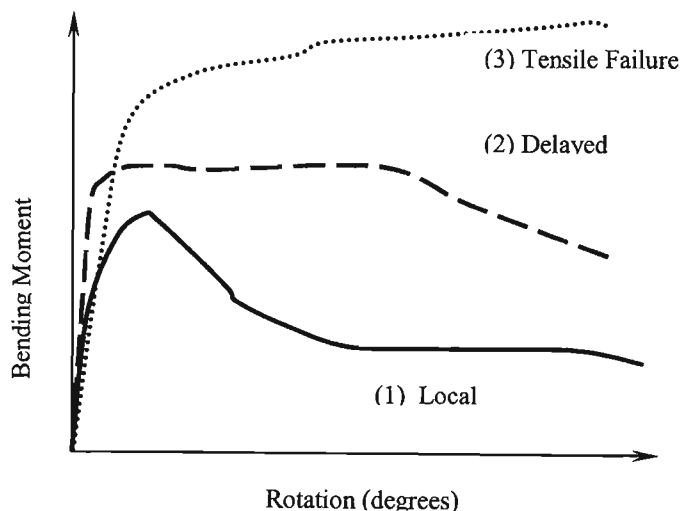


Fig. 2.6 Moment-rotation curves for beams under bending.

The second curve in Fig. 2.6 shows the response of a beam that fails by tensile tearing. In this failure, the beam deforms predominantly plastically until local tensile strains are exceeded, with subsequent failure of the beam. After failure, there is no residual load-carrying capacity. Although this failure mode gives the highest maximum moment and energy absorption, the abrupt

loss of bending strength and sensitivity to stress concentration makes this mode of failure undesirable.

The third curve in Fig. 2.6 shows the performance of a beam that fails by delayed buckling. Buckling of the section does not occur until well into the plastic range, with a subsequent high maximum moment and energy absorption. Beams designed for this type of failure give the most weight-efficient design.

The experimental results demonstrating the above modes of collapse for aluminium and steel sections were obtained by McGregor et al. (1993).

The deep plastic collapse of thin-walled structural members subjected to bending covers an important role in the vehicle crashworthiness design because a substantial fraction of the energy involved in a collision is dissipated by bending collapse of various members. Experience has demonstrated that the collapse mechanics of complex structures may often be studied by decomposition into its structural components. For this reason the collapse analysis of circular and square section tube has received a great deal of attention in the literature (Avalle et al., 1996)

Kecman (1983) made a comprehensive experimental study of the deep bending collapse of rectangular prismatic tubes. Beams were tested in a cantilever-bending mode from which the bending moment-rotation characteristic was calculated. Similar experiments for aluminium columns were reported by McGregor et al. (1993). Cimpoeru & Murray (1993) developed a complicated device to test thin-walled columns under pure bending conditions (four point bending) with large rotations.

A kinematic model involving stationary and moving plastic hinge lines, which allows theoretical prediction of the energy dissipated in the post-failure range by thin walled columns subjected to deep bending collapse, was proposed by Kecman (1989). Abramowicz (1983) developed a similar approach. This model was successively extended by Anceau (1994) to columns with different open cross-section (U -, H -, and W - sections).

Wierzbicki et al. (1994) studied the stress profiles in a square section thin-walled tube that buckles in bending, using the finite element method. In their article the authors also proposed a closed form solution for the moment-rotation characteristic in the plastic range.

The deep bending collapse of thin-walled columns observed in several experimental tests performed on aluminium and mild steel square/rectangular cross-section tubes proved to be very repeatable and are characterised by the formation of a plastic hinge, in which almost all the permanent deformation of the component takes place.

The length of the folding wave is approximately equal to the side dimension in square section columns and to the section width in rectangular section beams whose width is smaller than depth.

As can be seen the models considered above are predominantly based on plastic buckling. Various types of different folding modes were proposed to simulate plastic collapse of the thin-walled components. Kinematic models involving the stationary and moving plastic hinge lines provide a theoretical prediction of the energy dissipated in the post-failure range.

These technologies are not directly applicable to the analysis and modelling of similar components made from composite materials. However the discussion presented in this section gives a better understanding of the problem and provides basis for concept generation and selection of appropriate models for composite structural components.

2.2 Crashworthiness modelling of composite structures

Composite materials are increasingly being used in diverse applications such as the automotive and sports industries due to their many advantages over metallic counterparts. However

it is the nature of these advantages that also provides designers with challenging problems in accurately representing the materials. Unlike isotropic materials, anisotropic materials such as composites exhibit complicated mechanical behaviour that need to be accurately accounted for in constitutive models. This presents a problem in that composites essentially act very differently in different loading situations. Most composite models rely on modelling the material under certain assumptions so that computationally the problem is simplified. However any such assumptions also add to the inaccuracy of the solution, and must be considered carefully before being applied.

2.2.1 Crushing and damage modes and mechanisms in composites

2.2.1.1 Phenomenological crushing model

Most composites reinforced with brittle fibres crush in a combination of transverse shearing, lamina bending and local buckling, referred to as the brittle fracturing –crushing mode. Phenomena making up these modes include interlaminar, intralaminar and in-plane crack initiation and propagation, local fracturing of lamina bundles, and large deformations including large strains and large geometric rotations. Internal crushing and surface frictional effects are not included due to a limited amount of data for these effects.

A method of predicting the energy absorption capability of composite tubes, based on a phenomenological model of the crushing process exhibited by continuous fibre reinforced tubes, is presented by Farley & Jones (1992) and serves as the basis for an analytical model to predict crushing response.

A description of the crushing modes includes transverse shearing and lamina bending crushing modes and mechanisms. The first one is characterised by a wedge shaped cross section with one or multiple short interlaminar and longitudinal cracks, which form partial lamina bundles. In this case the crushing process is controlled by two mechanisms: interlaminar crack growth and lamina bundle fracture. The crack growth is controlled by the mechanical properties of the matrix and fibres, and fibre orientation. The lamina bundle fracture represents the principal energy absorption mechanism in the shear crushing mode. Tensile stress initiated by transverse bending force which creates a bending moment at the bundle base, causes fracture.

The lamina bending crushing mode is characterised by very long interlaminar, intralaminar, and parallel to fibre cracks. The lamina bundles do not fracture and the crushing process is controlled by two mechanisms: inter/intralaminar and parallel to fibre crack growth and friction. The lengths of cracks are at least one order of magnitude greater than in the transverse shearing mode. Bending against crushing surface and subsequent movement across the surface produces energy absorption through friction.

The combination of the above two modes is normally exhibited in the majority of crushing results for composite tubes under axial loading.

Additionally local buckling crushing mode and mechanisms similar to the buckling mode exhibited in ductile metals are to be considered. The mode consists of the formation of local buckles by means of plastic deformation of the material. Ductile fibre composites plastically deform at the buckle site along the compression side of the buckled fibres. The fibres can also split along the tension side, resulting in local delaminations between the plies. Brittle fibre composites exhibit this mode of crushing only when the interlaminar stresses are small relative to the strength of the matrix, and when the matrix has a higher failure strain than the fibres. So the ductile fibre composites exhibit yielding of both the fibres and matrix whereas brittle fibre composites crush in local buckling only if the matrix yields.

The model strain energy release rate is used as the indicator for interlaminar crack growth. Crack growth is modelled by disconnection of coincident nodes of adjacent finite elements along an interface, and calculating the strain energy associated with the resulting deformation.

The strain energy release rate is calculated as the difference in strain energy between the previous and present states, divided by the change in crack area, where the strain energies are calculated using geometric and material non-linear elastic analysis.

The geometric nonlinear response is modelled using a Newton-Raphson iterative scheme while an iterative process was also performed for material nonlinearity analysis. The material properties of the finite elements are calculated at point $i+1$ for each iteration and the material properties of the finite elements are updated in accordance with the strain state in each element. When the difference between the strains for successive iterations is zero, the analysis is assumed to be convergent.

2.2.1.2 Failure model for laminates under in-plane shear and tension

This model, developed by Shahid and Chang, (1993), predicts the failure response of fibre-reinforced matrix composite laminates under in-plane shear and tensile loading conditions. The model includes an analysis of matrix and fibre failures taking into account the effect of failure on the residual properties of the laminate. The model, as presented here, incorporates constitutive modelling, damage growth prediction and stress analysis.

The constitutive modelling is based on the assumption that the damaged composites may be analysed as a continuous elastic body with degraded material properties, and only deals with in-plane tension and shear failure modes viz. matrix cracking, fibre-matrix shear out and fibre breakage. The state of damage is characterised by the crack density (ϕ). An analytical model relating ply stiffness to crack density is used. The stiffness degradation of each ply is variable, depending upon ply orientation and thickness. The degree of degradation is a function of the accumulated cracks for each ply.

The three degradation models are combined to give an overall effective stiffness matrix, incorporating all three failure modes. In this case the ply constitutive relationships are:

$$|A^D|_m = \begin{pmatrix} A_{11}(\phi) & A_{12}(\phi) & 0 \\ A_{21}(\phi) & A_{22}(\phi) & 0 \\ 0 & 0 & A_{44}(\phi) \end{pmatrix}_m \begin{pmatrix} 1 & 0 & 0 \\ 0 & 1 & 0 \\ 0 & 0 & d_s \end{pmatrix}_m \begin{pmatrix} d_f & 0 & 0 \\ 0 & d_f & 0 \\ 0 & 0 & d_f \end{pmatrix}_m \quad (2.1)$$

where each separate matrix represents a specific failure mode: matrix cracking, fibre-matrix shearing and fibre breakage respectively, and

$$d_s = e^{-\left(\frac{\phi}{\phi_0}\right)^\eta} \quad (2.2)$$

and
$$d_f = e^{-\left(\frac{A_f}{\delta^2}\right)^\beta} \quad (2.3)$$

are shear damage and fibre breakage damage factors respectively. Here ϕ_0 is the saturation crack density of the m -th ply, η is the shape parameter dictating the rate of stiffness degradation due to shear out failure, A_f is the extent of the predicted fibre failure area, δ is the fibre interaction length for a unidirectional composite, and β is a parameter which controls the degradation rate

due to fibre failure. Parameters $A_{11}, A_{12}, A_{22}, A_{44}$ are the stiffness coefficients (Vasiliev & Morozov, 2001).

To consider the nonlinear shear stress-shear strain relationship in each ply the modified ply constitutive equations must be used as presented in (Shahid and Chang, 1992, 1993).

The damage growth criteria for each failure mode are as follows:

a. Matrix cracking

When ε_M is equal to or greater than l , as dictated by the values of the material properties and the following equation (2.4) below, matrix cracking will occur in the material

$$\left(\frac{\overline{\sigma}_{22}}{Y_t(\phi)} \right)^2 + \left(\frac{\overline{\sigma}_{12}}{S(\phi)} \right)^2 = \varepsilon_M^2 \quad (2.4)$$

where

$\overline{\sigma}_{22}$ and $\overline{\sigma}_{12}$ are the effective transverse tensile and shear stress and $Y_t(\phi)$ and $S(\phi)$ are the effective strengths of a ply in tension and shear respectively.

b. Fibre-matrix shear-out

Similarly to the above case, when the value of ε_S is greater than or equal to l , as calculated from equation (2.5) below, fibre-matrix shear out will occur in the material

$$\left(\frac{\overline{\sigma}_{11}}{X_t} \right)^2 + \left(\frac{\overline{\sigma}_{12}}{S(\phi)} \right)^2 = \varepsilon_S^2 \quad (2.5)$$

where

$\overline{\sigma}_{11}$ is the effective ply stress in the fibre direction and X_t is the longitudinal tensile strength of a unidirectional composite.

c. Fibre breakage

Again, failure by fibre breakage will occur when ε_F , as given by the following equation (2.6), is equal to or greater than l

$$\left(\frac{\overline{\sigma}_{11}}{X_t} \right) = \varepsilon_F \quad (2.6)$$

The stress analysis is performed using a nonlinear finite element method based on large deformation theory as presented in (Shahid, 1993). A computer code implementing this model, known as *PDCOMP*, was developed. This code provides the following information for a given laminate under in-plane tensile and shear loads: stiffness degradation, failure mode and state of damage, and the response of the laminate as a function of the applied loads.

As can be seen the model incorporates all the aspects required to perform failure analysis on a composite. However, the model is limited by the use of an abrupt degradation method (failed ply stiffnesses taken to be zero immediately after failure) rather than a more correct, gradual degradation model as used in other models. The model also, and more crucially, does not take into account the geometric nonlinearity of composites and in fact does not deal with the post failure structural geometry or analysis. Finally, the model is only implemented to account for uniaxial

tensile loading which is not consistent with the main goals of the current research, but use may be made of the principles presented when considering further models.

2.2.1.3 Model incorporating transverse shear effects using an improved shear correction factor method

This model, presented by Huang et al. (1993), makes use of Discrete Shear Triangle (DST) elements developed by Lardeur (1990), which include transverse shear effects in the stress analysis. The DST is a 2D, 3-node, 15-d.o.f. triangular element. Formulation of the element is based on a generalisation of the discrete Kirchoff's method as presented by Lardeur (1990).

In forming the stiffness matrix, the relation between shear force and shear strain, using shear correction factors as developed by Cheikh Saad Bouh (1992) has to be set up. The ply failure criteria include fibre failure, matrix cracking and delamination.

Failure by fibre breakage occurs when, in each instance, the stresses and strengths combine to satisfy the following relations

$$\begin{aligned} \left(\frac{\sigma_1}{X_T}\right)^2 + \left(\frac{\tau_{12}}{S_{12}}\right)^2 + \left(\frac{\tau_{13}}{S_{13}}\right)^2 &= 1, \text{ if } \sigma_1 > 0 \\ \left(\frac{\sigma_1}{X_C}\right)^2 &= 1, \text{ if } \sigma_1 < 0 \end{aligned} \quad (2.7)$$

where σ_1 is the stress acting in fibre direction, τ_{12} and τ_{13} shear stresses.

Failure by matrix cracking occurs when the following relations are satisfied:

$$\begin{aligned} \left(\frac{\sigma_2}{Y_T}\right)^2 + \left(\frac{\tau_{23}}{S_{23}}\right)^2 + \left(\frac{\tau_{12}}{S_{12}}\right)^2 + \left(\frac{\tau_{13}}{S_{13}}\right)^2 &= 1, \text{ if } \sigma_2 > 0 \\ \left[\left(\frac{Y_C}{2S_{23}}\right)^2 - 1\right] \frac{\sigma_2}{Y_C} + \left(\frac{\sigma_2}{2S_{23}}\right)^2 + \left(\frac{\tau_{23}}{S_{23}}\right)^2 + \left(\frac{\tau_{12}}{S_{12}}\right)^2 + \left(\frac{\tau_{13}}{S_{13}}\right)^2 &= 1, \text{ if } \sigma_2 < 0 \end{aligned} \quad (2.8)$$

where σ_2 is the transverse stress, $\tau_{12}, \tau_{13}, \tau_{23}$ are the shear stresses.

Delamination failure occurs when the following relation is satisfied:

$$\sqrt{(\tau_{13}^2 + \tau_{23}^2)} \geq S_I \quad (2.9)$$

Here, X_T is the longitudinal tensile strength, X_C is the longitudinal compressive strength, Y_T is the transverse tensile strength, Y_C is the transverse compressive strength, S_{12} is the shear strength in the 1-2 plane, S_{13} is the shear strength in the 1-3 plane, S_{23} is the shear strength in the 2-3 planes, and S_I is the interlaminar shear strength.

The stresses in the centre of the element are used for the failure check. Failure may occur in one mode only or in several combined modes. The stiffness of the ply is modified according to the failure mode. The ultimate failure strength is then obtained by iteration. A simplified post failure stiffness adjustment method is used, according to the failure modes. For example, if fibre failure takes place, the constitutive relation of the failed ply is changed to:

$$\begin{Bmatrix} \sigma_{11} \\ \sigma_{22} \\ \tau_{12} \\ \tau_{13} \\ \tau_{23} \end{Bmatrix} = \begin{Bmatrix} 0 & 0 & 0 & 0 & 0 \\ 0 & Q_{22} & 0 & 0 & 0 \\ 0 & 0 & 0 & 0 & 0 \\ 0 & 0 & 0 & 0 & 0 \\ 0 & 0 & 0 & 0 & C_{22} \end{Bmatrix} \begin{Bmatrix} \varepsilon_{11} \\ \varepsilon_{22} \\ \gamma_{12} \\ \gamma_{13} \\ \gamma_{23} \end{Bmatrix} \quad (2.10)$$

and if matrix cracking or delamination has occurred:

$$\begin{Bmatrix} \sigma_{11} \\ \sigma_{22} \\ \tau_{12} \\ \tau_{13} \\ \tau_{23} \end{Bmatrix} = \begin{Bmatrix} Q_{11} & 0 & 0 & 0 & 0 \\ 0 & 0 & 0 & 0 & 0 \\ 0 & 0 & 0 & 0 & 0 \\ 0 & 0 & 0 & C_{11} & 0 \\ 0 & 0 & 0 & 0 & 0 \end{Bmatrix} \begin{Bmatrix} \varepsilon_{11} \\ \varepsilon_{22} \\ \gamma_{12} \\ \gamma_{13} \\ \gamma_{23} \end{Bmatrix} \quad (2.11)$$

If both matrix and fibre failures have occurred, then the entire ply is removed from the laminate. Since the assignment of zero values to the stiffness coefficients C_{11} and C_{22} would cause problems (their inverses are used in the program), they are assigned very small non-zero values. When some of the plies have failed the constitutive relations are modified and element stiffness matrix is recalculated. After that another stress analysis is performed to find the new stress distribution.

It is noted that the adopted degradation method does not provide accurate enough reflection of the ply post-failure behaviour, and improvement here can certainly be made. In general, the model is considered to be viable to obtain results for the pre-failure stress distribution but a new method of material degradation should be implemented to obtain reasonable results for post-failure stress analysis.

2.2.1.4 Damage model for composites reinforced with randomly oriented short fibres

The following is a description of a micromechanical model by Meraghni & Benzeggagh (1995) which is based on the modified Mori-Tanaka model (Mori and Tanaka, 1973). The effects of damage processes on the behaviour of a randomly orientated discontinuous fibre composite (RODFC) are modelled.

Experimental identification of damage mechanisms using amplitude treatment of acoustic emission signals and microscopic observations is implemented in the model.

The model is formulated in two steps:

- initially only the mechanisms of failure related to the matrix degradation are introduced by means of an experimental parameter which represents the microcrack density,
- subsequently mechanisms associated with interfacial degradation other than those of the type above are introduced.

The model then allows for the identification of damage mechanisms as one of the above two types.

The microcracks are modelled as ellipsoid phases in the material with null rigidity (see Fig. 2.7 below). The model allows for the prediction of the stiffness reduction and simulation of tensile curves.

This model, as most short fibre composite models do, makes use of a representative element volume to model the material properties (see Figure 2.7 below)

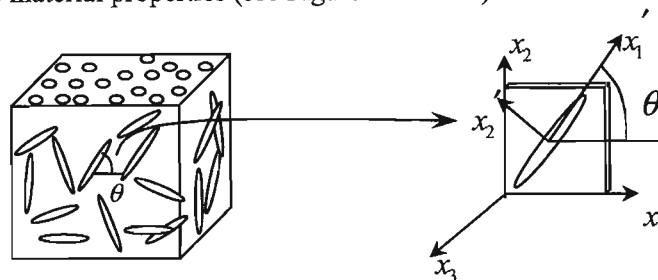


Fig. 2.7 Modelling of a short fibre composite as a representative element volume with ellipsoid inhomogeneities representing microcracks.

2.2.1.5 Laminate model for damage processes in SMC

In this model, presented by Hoffmann et al. (1995) SMC (Sheet Moulding Compound) composite is viewed as a laminate consisting of fibre bundles embedded in the resin/filler matrix where the individual layers are assumed void free and adhere firmly to one another. The stiffness of the bundles and the matrix is expected to be reduced by the development of cracks, which is viewed as a statistical process.

A combination of the quadratic criterion in stress space and the maximum strain criterion is used to predict failure in the fibres and matrix respectively. The model also includes residual stresses arising from high curing temperatures, anisotropic fibre orientation and varying content of filler particles in the matrix inside and outside of bundles.

This model also allows for the appreciation of the quantitative influence of different materials and processing parameters on SMC behaviour and in this way to optimise its composition.

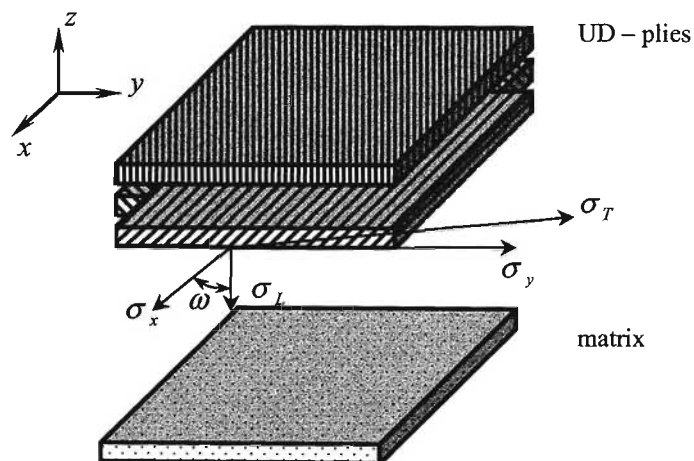


Fig. 2.8 Representation of SMC by means of a multilayer composite consisting of unidirectional plies and designation of coordinate system (σ_L, σ_T are longitudinal and transverse stresses, ω - angle of ply orientation).

The fundamental element of the SMC structure is modelled here (see Fig. 2.8) as the fibre bundle saturated by the matrix material (which is assumed isotropic with elastic properties), which represents a unidirectional (UD) composite. The thermo-elastic properties (TEP) of such layer may be calculated using formulae by Hashin (1979).

The TEP of the matrix may be calculated by combining the formulae of Kerner and Hashin as done in Kabelka & Ehrenstein (1992) and on the basis of the TEP's of the matrix and filler and of the filler fractions, the material properties can be calculated.

The fibre bundles saturated by the "internal" matrix are the effective reinforcing elements and can be viewed as macroscopic fibres with anisotropic properties embedded in the "external" matrix. These bundles are randomly distributed and are differently oriented.

By collecting all the bundles lying in the same direction into one ply, the stochastic structure is transformed in the multilayer composition, consisting of UD-plyes having identical TEP's. The total stiffness of the laminate is then determined by summing the individual layer stiffnesses.

The cracking mechanism development is based on the following elliptic failure criterion:

$$\frac{\sigma_T^2}{R_T^2} + \frac{\sigma_{LT}^2}{R_{LT}^2} = 1$$

where R_T and R_{LT} are tensile and shear strengths, deemed to be determined experimentally.

In multilayered composites, however the local fracture propagates through the layer and causes a stress concentration in the adjacent, unfractured laminae, which arrests its further propagation. The damaged ply cannot support any transverse tensile or shear load in the vicinity of the crack and its contribution to the total stiffness is in this way reduced but its stiffness in the fibre direction is unaffected. The stiffness reduction degradation function of the bundles is accepted in the form:

$$D_b(\sigma_T, \sigma_{LT}) = 1 - e^{-(0.707 \frac{\sigma}{R})^2}$$

A similar procedure is used to assess the crack creation in the matrix surrounding the bundles where in this case the maximum strain criterion is used. The ultimate elongation was found by experimentation to have the following form:

$$\varepsilon_{mu} = 1.5 \sqrt{\varepsilon_{ru}} (1 - 1.04 \sqrt{\phi_{pe}})$$

where ε_{ru} is the tensile elongation and ϕ_{pe} filler fraction.

So, the stiffness of each layer may be defined according to its level of stressing, and the total laminate stiffness is found as a sum of the stiffnesses of the degraded layers. The moduli of elasticity of SMC are calculated at stepwise increasing strain (ε_1) and the corresponding stress σ_1 is determined for each value of strain, assuming the SMC response to be linear. Thus, the σ - ε curve is obtained to describe the damage process in SMC.

It has been shown that the model is able to describe the SMC behaviour under tensile loading especially well at the beginning of loading, however when a higher level of crack density is reached, the damage process takes on a local character, which the model is not able to take into account. Also, substantial differences in the second half of the loading cycle can also be caused by the initial anisotropy of the investigated SMC samples. It should be noted that to prevent misrepresentation due to material anisotropy, measurements on specimens cut in two mutually

perpendicular directions are necessary. In addition, it should be noted that the results obtained are fairly artificial as the values of R_T and R_{LT} were chosen to best fit the experimental results.

This evaluation is feasible though, as it could mean that a database for these values could be built up, or initial testing could be done prior to modelling. The model will have to of course be modified to address the problems identified above.

2.2.1.6 MLT damage model

Most models assume that in the post-failure regime a lamina behaves in an ideally brittle manner with the dominant stiffness and stress components reduced to zero instantaneously. This is clearly unrealistic as it disregards the constraints that are imposed on the failed lamina by the adjacent laminate and undamaged elements in the neighbourhood of the damage site. The result of these constraints is that the stress release and stiffness reductions occur gradually rather than abruptly on a macroscopic level.

This may be integrated into numerical analyses through the use of homogenised models that incorporate strain softening. One example of such a model is the MLT model presented by Maltzenmiller, Lubliner & Taylor (1991).

This model was implemented in LS-DYNA3D by Williams & Vaziri (1995) and evaluated in comparison with a model by Chang & Chang (1987) (CC Model).

In the CC Model the lamina is assumed to be laminar up to failure and after failure a ply is assumed to lose its load carrying capacity in the dominant stress direction associated with the failure mode. The failure is assumed instantaneous and the elastic constants are reduced to zero in a predetermined number of time steps based on the dynamic stability of the model.

In the MLT model a unidirectional lamina is represented by a homogenised continuum irrespective of its damage state. Damage takes the form of disc like cracks parallel or normal to the fibre direction. Three damage parameters are introduced leading to the following plane stress compliance relationship:

$$\begin{Bmatrix} \varepsilon_{11} \\ \varepsilon_{22} \\ \gamma_{12} \end{Bmatrix} = \begin{bmatrix} \frac{1}{(1-\omega_{11})E_1} & \frac{-\nu_{12}}{E_1} & 0 \\ & \frac{1}{(1-\omega_{22})E_2} & 0 \\ \text{sym} & & \frac{1}{(1-\omega_{12})G_{12}} \end{bmatrix} \begin{Bmatrix} \sigma_{11} \\ \sigma_{22} \\ \tau_{12} \end{Bmatrix}$$

The prediction of failure is based on the concept of a threshold function, r . The elastic region is bounded by a series of surfaces, functions of σ_{ij} , ω_{ij} and r , associated with different lamina failure modes. This model uses Hashin's lamina failure criteria as presented in (Hashin, 1979). A general mathematical form of the damage variable is proposed and was implemented in DYNA-3D:

$$\omega = 1 - e^{-(\varepsilon/\varepsilon_f)^m}$$

where ε_f is the nominal failure strain and m is a constant.

The numerical simulation of the behaviour of the composite plate under impact loading was performed using the proposed model. Results were compared with CC model and experimentation. It was noted that the values of m represented two distinct responses namely a tough behaviour

($m=2$) and a brittle behaviour ($m=10$). The latter behaviour was very similar to the CC response up to the maximum stress level.

For the impact energy of $9.5J$ the predictions overlapped and illustrated the observed undamaged plate response. For the impact energy of $22J$ some deviations occurred about $0.4ms$ after impact (onset of failure): the $m=2$ model yielded results that simulate an elastic response with little or no damage, the CC model predicted very sharp oscillations indicative of the abrupt unloading assumption. The $m=10$ model seemed to yield a more realistic profile.

The results indicate that the MLT model has potential for application to progressive damage modelling of composite structures. Results show that the gradual degradation law applied in the MLT model are more indicative of the nature of failure in composite materials than the traditional degradation law as applied in the CC model. However, it must be noted that the MLT model is limited by the lack of a standard testing procedure to characterise the strain softening behaviour. One approach would be to calibrate the value of m through specific impact testing on a particular laminate and use this value in simulating the behaviour of the same laminates under different impact conditions.

2.2.2 Progressive failure models

Composite material failure is modelled using the concept of progressive failure due to the fact that composite materials may continue to bear loads even after initial failure. In such models the composite material properties are degraded according to the mode of failure that has been induced. The composite damage models devised on the basis of various types of failure modes were discussed in previous section. The delineation of these failure modes as well as the form of the degradation, coupled with the material constitutive equations define the nature of the model.

Thus variation in any of the parameters produces a new model that requires analysis in order to ascertain its applicability to a particular situation.

Following is a description of existing progressive failure models that may be applied to the crashworthiness analysis of thin-walled composite structural components. Included are models for both short fibre reinforced composites. Certain models are complete progressive failure models whereas others incorporate only specific aspects of the modelling, for example damage evolution.

In the selection of models discussed in this section the preferences were given to the models that would take into account both physical (material) and geometrical nonlinearities.

2.2.2.1 Layerwise progressive failure model

This model considered by Reddy & Reddy (1993) presents a non-linear finite element progressive failure algorithm using the Generalised Layerwise Plate Theory (GLWT) (Reddy, 1987). Here the material is modelled as a stable progressively fracturing solid. The geometric non-linearity taken into account in the Von-Karman sense and the effect of this geometric non-linearity on both the first ply and the ultimate failure loads is evaluated using generalized layerwise theory of laminates (GLWT) and first order shear deformation theory (FSDT), and the results compared and analysed.

The layerwise model incorporates the extensibility of the transverse normals as opposed to models based on the FSDT. Stiffness reduction is carried out at the reduced integration Gaussian points of the finite element mesh depending on failure mode.

The material used in this model has the following properties:

- loses stiffness due to stable progressive fracture or damage during loading,
- unloads in a linear elastic manner, and loses stiffness depending on the extent of progressive fracture or damage prior to unloading,
- the material may always be returned to a state of zero stress and strain by linear-elastic unloading.

Thus, for this material, the direct stiffness matrix and the tangent stiffness matrix are the same, and so the nonlinear iteration due to damage can be performed by the direct stiffness method.

For progressive failure analysis, the assumption is that the damaged material may be replaced with an equivalent material with degraded properties. The task is thus to determine in what manner these properties are to be degraded. In this model the degraded properties of the damaged material were assumed to be a constant multiple of the undamaged material properties. This constant, called the Stiffness Reduction Coefficient (SRC) must be determined experimentally. It is assumed that when the SRC is known for a given lamination sequence, the same value is applicable for any other lamination sequence as long as the material system is the same.

The procedure for stiffness reduction includes first of all the computation of contribution of each stress component towards the failure index of the failure criterion (Tsai-Wu criterion used here). As a result the component that contributes the maximum is identified. The failure mode is then identified for this component. It could be fibre breakage, transverse cracking or delamination.

According to the failure mode, material properties are degraded by multiplying by the SRC. For fibre breakage these would be $E_1, G_{12}, G_{13}, \nu_{13}, \nu_{12}$ and for transverse cracking $E_2, G_{23}, G_{12}, \nu_{21}, \nu_{23}$.

An appropriate logic is included in the computer code to ensure that restrictions on elastic constants are maintained.

The stresses are computed at the reduced integration Gauss points. However, since in the case of transverse loading the maximum normal stress always occurs at the top and bottom surfaces, the Gauss point stresses are extrapolated to the corner nodes of the finite element before applying the failure criterion, and the stiffness properties are reduced at the corner nodes. These stiffness properties are then interpolated (using linear Lagrange interpolation functions) to obtain the stiffness properties at the Gauss points, to obtain the direct and tangent stiffness matrices. Linear interpolation functions (as opposed to quadratic or higher order functions) are used to avoid the possibility of getting negative stiffness properties in between nodes when the stiffness property at the centre nodes is made equal to zero.

For the ultimate failure load analysis, the stiffness reduction is carried out only after the displacement has converged at a given load increment. It is noted that care must be taken in selecting the load increment for the nonlinear failure analysis: a large load step makes the specimen excessively stiff due to geometric nonlinearity while a small step size makes the specimen too compliant due to the effect of damage.

Application of the layerwise theory shows that damage due to the transverse normal stress is found to have a significant influence on the failure behaviour of composite laminates in bending and that these effects can not be discounted in analysis of composite materials under such loading.

2.2.2.2 Buckling analysis model

This model, presented by Hu (1993), incorporates a nonlinear material constitutive model which includes nonlinear in-plane shear formulation and failure criterion. A finite element buckling analysis for composite plates under uniaxial compressive loads is performed which shows that the nonlinear in-plane shear has a significant effect on the buckling of composite laminate plates. Comparison with models using linear material properties is made.

Each laminate is considered as an orthotropic layer in the plane stress condition. The incremental constitutive matrices for a composite lamina in the material coordinates are:

$$\Delta\{\sigma'_i\} = [Q'_1] \Delta\{\varepsilon'_i\} \text{ and } \Delta\{\tau'_i\} = [Q'_2] \Delta\{\gamma'_i\}$$

where

$$[Q'_1] = \begin{bmatrix} \frac{E_{11}}{1-\nu_{12}\nu_{21}} & \frac{\nu_{12}E_{22}}{1-\nu_{12}\nu_{21}} & 0 \\ \frac{\nu_{21}E_{11}}{1-\nu_{12}\nu_{21}} & \frac{E_{22}}{1-\nu_{12}\nu_{21}} & 0 \\ 0 & 0 & G_{12} \end{bmatrix} \text{ and } [Q'_2] = \begin{bmatrix} \alpha_1 G_{13} & 0 \\ 0 & \alpha_2 G_{23} \end{bmatrix}$$

and

$$\Delta\{\sigma'_i\} = \Delta\{\sigma_1, \sigma_2, \tau_{12}\}^T, \Delta\{\tau'_i\} = \Delta\{\tau_{13}, \tau_{23}\}^T, \Delta\{\varepsilon'_i\} = \Delta\{\varepsilon_1, \varepsilon_2, \gamma_{12}\}^T \text{ and } \Delta\{\gamma'_i\} = \Delta\{\gamma_{13}, \gamma_{23}\}^T.$$

α_1 and α_2 are shear correction terms (taken to be 0.83).

To model the nonlinear in-plane shear behaviour, the nonlinear stress-strain relations by Hahn & Tsai (1973) are used:

$$\begin{Bmatrix} \varepsilon_1 \\ \varepsilon_2 \\ \gamma_{12} \end{Bmatrix} = \begin{bmatrix} \frac{1}{E_{11}} & \frac{\nu_{21}}{E_{22}} & 0 \\ \frac{\nu_{12}}{E_{11}} & \frac{1}{E_{22}} & 0 \\ 0 & 0 & \frac{1}{G_{12}} \end{bmatrix} \begin{Bmatrix} \sigma_1 \\ \sigma_2 \\ \tau_{12} \end{Bmatrix} + S_{6666} \tau_{12}^2 \begin{Bmatrix} 0 \\ 0 \\ \tau_{12} \end{Bmatrix}$$

Thus only one constant (S_{6666}) is required to account for the in-plane shear nonlinearity and this value can be determined by a curve fit to various off-axis tension test data (Hahn and Tsai, 1973). Inverting and differentiating, the nonlinear incremental constitutive matrix for the lamina is obtained:

$$[Q_1] = \begin{bmatrix} \frac{E_{11}}{1-\nu_{12}\nu_{21}} & \frac{\nu_{12}E_{22}}{1-\nu_{12}\nu_{21}} & 0 \\ \frac{\nu_{21}E_{22}}{1-\nu_{12}\nu_{21}} & \frac{E_{22}}{1-\nu_{12}\nu_{21}} & 0 \\ 0 & 0 & \frac{1}{\frac{1}{G_{12}} + 3S_{6666}\tau_{12}^2} \end{bmatrix}$$

In the Tsai-Wu failure criterion, the stress interaction term F_{12} is set equal to zero, as suggested by Narayanaswami and Adelman (1977). Since Tsai-Wu criterion does not distinguish failure modes explicitly, the following rules have been used to determine whether failure occurs by matrix cracking or fibre breakage:

- (1) If ply failure occurs but the stress in the fibre direction is less than the uni-axial strength of the lamina in the fibre direction, the ply failure is assumed to be resin (matrix) induced. The laminate subsequently loses the ability to carry transverse and shear stresses and holds longitudinal stress only. The constitutive matrix then becomes:

$$[Q_1] = \begin{bmatrix} E_{11} & 0 & 0 \\ 0 & 0 & 0 \\ 0 & 0 & 0 \end{bmatrix}$$

- (2) If a ply fails with σ_1 exceeding the uniaxial strength of the lamina, fibre breakage is assumed to have occurred and total ply rupture is also assumed, thus:

$$[Q_1] = \begin{bmatrix} 0 & 0 & 0 \\ 0 & 0 & 0 \\ 0 & 0 & 0 \end{bmatrix}$$

Elements are eight node isoparametric shell elements with six degrees of freedom per node. The formulation allows for transverse shear deformation and may be used for thick or thin shells. Writing the constitutive equations for composite materials in the element coordinates (x,y,z) :

$$\Delta\{\sigma\} = [Q_1] \Delta\{\varepsilon\} \text{ and } \Delta\{\tau_i\} = [Q_2] \Delta\{\gamma_i\}$$

where

$$[Q_1] = [T_1]^T [Q_1'] [T_1] \text{ and } [Q_2] = [T_2]^T [Q_2'] [T_2]$$

$$[T_1] = \begin{bmatrix} \cos^2 \phi & \sin^2 \phi & \sin \phi \cos \phi \\ \sin^2 \phi & \cos^2 \phi & -\sin \phi \cos \phi \\ -2 \sin \phi \cos \phi & 2 \sin \phi \cos \phi & \cos^2 \phi - \sin^2 \phi \end{bmatrix} \text{ and } [T_2] = \begin{bmatrix} \cos \phi & \sin \phi \\ -\sin \phi & \cos \phi \end{bmatrix}$$

$\Delta\{\sigma\} = \Delta\{\sigma_x, \sigma_y, \tau_{xy}\}^T$, $\Delta\{\varepsilon\} = \Delta\{\varepsilon_x, \varepsilon_y, \gamma_{xy}\}^T$, $\Delta\{\tau_t\} = \Delta\{\tau_{xz}, \tau_{yz}\}^T$, $\Delta\{\gamma_t\} = \Delta\{\gamma_{xz}, \gamma_{yz}\}^T$ and ϕ is measured from the element x – axis counterclockwise to the material 1-axis.

Now, if $\Delta\{\varepsilon_{x_0}, \varepsilon_{y_0}, \gamma_{xy_0}\}^T$ are the incremental in-plane strains at the midsurface of the shell, and $\Delta\{\kappa_x, \kappa_y, \kappa_{xy}\}^T$ are the incremental curvatures, then the in-plane strains at a distance z from the midsurface are $\Delta\{\varepsilon\} = \Delta\{\varepsilon_0\} + z\Delta\{\kappa\}$. Subsequently the incremental stress resultants, $\Delta\{N\} = \Delta\{N_x, N_y, N_{xy}\}^T$, $\Delta\{M\} = \Delta\{M_x, M_y, M_{xy}\}^T$ and $\Delta\{V\} = \Delta\{V_x, V_y, V_{xy}\}^T$ are defined as:

$$\begin{Bmatrix} \Delta\{N\} \\ \Delta\{M\} \\ \Delta\{V\} \end{Bmatrix} = \int_{-h/2}^{h/2} \begin{Bmatrix} \Delta\{\sigma\} \\ z\Delta\{\sigma\} \\ \Delta\{\tau_t\} \end{Bmatrix} dz = \int_{-h/2}^{h/2} \begin{bmatrix} [Q_1] & z[Q_1] & [0] \\ [Q_1] & [Q_1] & [0] \\ [0]^T & [0]^T & [Q_2] \end{bmatrix} \begin{Bmatrix} \Delta\{\varepsilon_0\} \\ \Delta\{\kappa\} \\ \Delta\{\gamma_t\} \end{Bmatrix} dz$$

where h is the shell thickness and $[0]$ is a 3 by 2 matrix.

Finite element analysis was performed using ABAQUS. The nonlinear response of a system is modelled by an updated Lagrangian formulation using a non-linear incremental algorithm to construct the equilibrium solution path. To model bifurcation from the pre-buckling path to the post-buckling path, geometric imperfections are introduced by superimposing a small fraction (say 0.001 of the plate thickness) of the lowest eigenmode determined by a linearized buckling analysis to the original nodal coordinates of the plates.

As was found, the non-linear in-plane shear alone did not have much influence on the buckling behaviour of the $[90/0]_{2S}$ and the $[\pm\theta/90/0]_s$ laminates. The non-linear in plane shear together with the material failure had a substantial influence on the buckling and post-buckling response of the above two laminates. The effect on the reduction of ultimate strengths and post-buckling stiffness depended on the layup. The non-linear in-plane shear alone had a significant effect on the buckling response of the $[45/-45]_{2S}$ layup plate. Additionally, if the Tsai-Wu criterion were considered, the calculated ultimate strength of the plate was much lower than the linearized buckling load. The optimal fibre angle θ for $[\pm\theta/90/0]_s$ plates with the analysis using non-linear in-plane shear formulation was decidedly different from that obtained using the linearized buckling analysis.

The model presented, though primarily aimed at buckling analysis may be applied to general progressive failure. The simplified degradation present in previous models is once again used here and is once again noted to be not completely adequate. Some observations were made into the buckling analysis of composite materials as detailed above, which could be considered in the choice of a failure model. Comparative results against experimental data were not available.

2.2.2.3 Effects of progressive fracture on buckling resistance

This model as presented by Minnetyan & Chamis (1993) deals with the effects of local and regional damage on the load carrying capacity and structural behaviour of a composite cylindrical shell under external pressure.

The model includes the development of an integrated computer code (*CODSTRAN*) for the evaluation of composite structural degradation and buckling stability under external pressure. This code includes the simulation of damage initiation, growth, accumulation, and propagation to structural failure.

Under external pressure, composite shells display two types of global failure viz. elastic buckling and stress fracture. Under situations of low to moderate levels of external pressure, a design is usually satisfied with sufficiently large radius to thickness ratios such that buckling stability is the fundamental design constraint. However, in cases of very large external pressures, the shell thickness substantially increases and stress fracture is then the primary concern.

The *CODSTRAN* code is able to simulate damage initiation, damage growth, and fracture in composites under various loading and environmental conditions. Additional work into the code has enabled the investigation of:

- the effects of composite degradation on structural response and buckling stability
- composite damage induced by dynamic loading,
- composite structures global fracture toughness (Minnetyan, 1990),
- hygrothermal environment on durability,
- damage progression in composite shells subjected to internal pressure,
- an overall evaluation of the progressive fracture in polymer matrix composite structures (Chamis et al., 1996),
- the durability of stiffened composite shells under load combinations,
- design considerations for progressive fracture in composite shell structures (Minnetyan, 1992).

CODSTRAN consists of three modules:

- composite mechanics,
- finite element analysis,
- damage progression modelling.

The overall evaluation of composite structural durability is carried out in the damage progression module that keeps track of degradation of the entire structure. This module relies on *ICAN* (Integrated Composite Analyzer) developed by Murthy & Chamis (1986) for composite micromechanics, macromechanics and laminate analysis, and calls a finite element analysis module that uses anisotropic thick shell elements to model laminated composites and carry out stress and stability analyses.

The *ICAN* module is called before and after each finite element analysis. Prior to each analysis the *ICAN* module computes the composite properties from the fibre and matrix constituent characteristics and the composite layup. The finite element analysis module accepts the composite properties that *ICAN* computes at each node and then performs the analysis at each load increment. The computed generalized nodal force resultants and deformations are then supplied back to the *ICAN* module which then evaluates the nature and extent of local damage, if any, in the plies of the laminate. *ICAN* uses failure criteria based on the absolute value limits of the ply-stress components, a modified distortion-energy or combined stress failure criterion, and interply delamination.

The generalized stress-strain relationships for each node are then revised according to the results of the damage analysis after each finite element analysis. The model is automatically updated with the new properties, and the structure is then reanalysed for further deformation and damage. If at any increment there is no damage, the structure is considered to be in equilibrium and the load is incrementally increased.

The procedure is continued through the stages of damage progression until structural fracture, and the simulation is stopped when global structural failure is predicted by rapid damage propagation.

The following conclusions were drawn from the above investigations and from the use of *CODSTRAN* in general.

1. Computational simulation may be used to predict the influence of existing defects and accidental damage, as well as loading, on the safety and durability of composite structures.
2. The procedure used is flexible and applicable to all combinations of constituent materials, geometry, and loading conditions.
3. Fracture toughness parameters such as damage initiation load and structural fracture load are identifiable for any structure.
4. The *CODSTRAN* algorithm is similar to that which would be applied in any finite element analysis, and only provides an integrated interface to perform structural analyses. As such, no new modelling techniques are introduced, except that analyses is performed by a dedicated computer code as opposed to within a finite element program. The program will of course only provide details of the material degradation and failure and does not address the post-failure geometry of a specimen.

2.3 Crashworthiness modelling of composite structural components with complex shape and geometry

As can be seen (Sections 2.1 and 2.2) the majority of research results in the field under consideration were obtained for classical structural elements (rods, beams, tubes, plates, cylinders, etc.). The present work deals with the development of a crashworthiness simulation approach applicable to thin-walled composite structural components that have an arbitrary complex shape and geometry.

Dynamic structural analysis and crash simulation of such structures require the application of geometrically non-linear structural modelling and analysis. The problem is complicated by the fact that the structures to be analysed are made from composite materials. Progressive failure and damage modelling of composites represents a complex problem due to the variety of failure modes (see Section 2.2) specific for this kind of materials.

As could be seen, material models that are normally used in the analysis include various types of material characteristics (physical parameters). These parameters should be determined experimentally. Depending on the adopted model the experimental characterisation of the material could be a complex and cumbersome procedure. There are a lot of models (especially based on micromechanical theories) for which it is virtually impossible to obtain more or less reliable data concerning the physical (mechanical) characteristics.

As stated in the introduction, the main goal of this research is the development of the methodology of crash simulation involving geometrically non-linear structural analysis, applicable to structures with complex geometries, progressive damage modelling of composites, and material characterisation. It is important that the latter be feasible for practical implementation, which means that the set of material characteristics required for the model could be reliably determined using simple testing procedure.

The requirement of applicability of the dynamic crash technology to the arbitrary structural shapes and geometries dictates the choice of the simulation tool. Finite element analysis combined with an explicit or implicit dynamic simulation algorithm would provide the necessary flexibility with regard to the shape and geometry modelling and handling the non-linear dynamic structural response. Additionally, the appropriate progressive damage/failure composite material model should be implemented in the software.

The material model and software selection are discussed in this section. Two finite element crash simulation software packages (PAM-CRASH and LS-DYNA) including various material models were considered.

The LS-DYNA package is a general-purpose, explicit finite element program used to analyze the nonlinear dynamic response of three-dimensional inelastic structures. Its fully automated contact analysis capability and error-checking features have enabled users to solve successfully many complex crash and forming problems. Livermore Software Technology Corporation (LSTC) developed sophisticated tools for modelling and simulating the large deformation behaviour of structures. These tools include LS-DYNA for analysis, LS-INGRID for pre-processing, and LS-TAURUS for post-processing; which are interfaced with leading CAD, FEA, and FEM systems.

PAM-CRASH is application-specific industrial software used to perform realistic and predictive virtual crashworthiness simulations in the transportation industry. Since the first car crash simulation performed in 1983 with the VW Polo, PAM-CRASH has become a popular crash test simulation software. PAM-CRASH is specifically designed to simulate mechanical structural testing and meet in particular increasingly stringent regulatory crash tests.

The preference in the present software selection process is given to the material models for which the reasonable (from the practical point of view) material characterisation procedure could be developed and implemented.

2.3.1 Modelling of short-fibre randomly reinforced composite materials

2.3.1.1 PAM-CRASH model for SMC composites

Model description

The PAM-CRASH model used for SMC composite analysis is an Elastic-Plastic material model with isotropic damage behaviour (PAM-CRASH Material Type 105). The material is initially isotropic and includes both a plasticity analysis algorithm and a damage mechanics law based on experimentally obtained results. For our purposes only the damage law option was utilised to model SMC composite behaviour. Strain-rate effects may also be taken into account by virtue of a choice of strain-rate models.

The following parameters are required to define the material:

- Mass density, ρ
- Young's modulus, E
- Yield stress, σ_Y
- Damage behaviour parameters:

ε_i	the initial equivalent threshold strain for volume or shear damage
ε_1	the intermediate equivalent strain
ε_u	the ultimate equivalent strain
d_1	the damage value at strain ε_1

d_u the damage value at strain ε_u

In this model, damage is applied to the material stress tensor as follows:

$$\sigma = (1 - d(\varepsilon_p))\sigma_0 \quad (2.12)$$

where σ is the full stress tensor for the damaged material,

$d(\varepsilon_p)$ is the isotropic scalar damage function, a function of the strain, ε_p (accounting for plasticity effects if necessary),

σ_0 is the full stress tensor as calculated according to the elastic-plastic material law (with or without strain rate effects) for the undamaged material.

The damage curve is assumed piecewise linear between the strain points, $\varepsilon_i, \varepsilon_1, \varepsilon_u$, which are obtained off an experimental stress-strain curve for the material, as shown in Fig. 2.9. For SMC composite modelling, which includes no plasticity effects, the material is progressively degraded by the damage function only, and there is no reduction of the modulus of the material caused by plastic deformation.

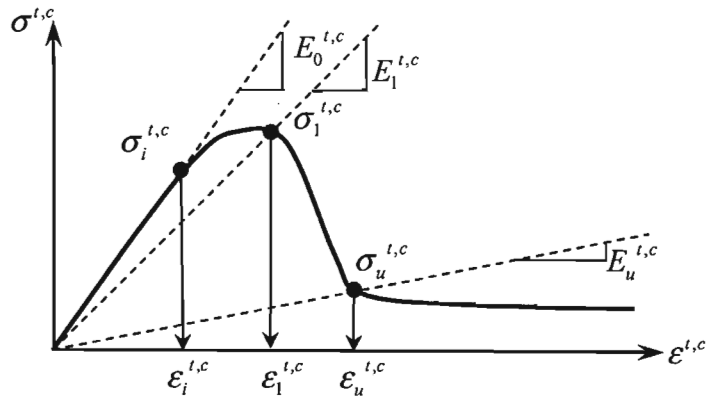


Fig. 2.9 Damaging curve used for an SMC composite material.

The isotropic scalar damage, function d is defined as follows:

$$d_1 = 1 - \frac{E_1}{E_0} \quad (2.13)$$

at ε_1 and

$$d_u = 1 - \frac{E_u}{E_1} \quad (2.14)$$

at ε_u .

Here E_0 is the initial elastic modulus and E_1, E_u are the secant moduli (see Fig. 2.9). Parameter d_u is the ultimate damage. Its value is usually taken less than 1 in order to assign a non-zero resistance for large strains. Between these defined points, d grows linearly from 0 to d_1 in the interval $\varepsilon_i \leq \varepsilon \leq \varepsilon_1$, and from d_1 to d_u in the interval $\varepsilon_1 \leq \varepsilon \leq \varepsilon_u$. Beyond the ultimate damage strain the damage function remains constant (see Fig. 2.10).

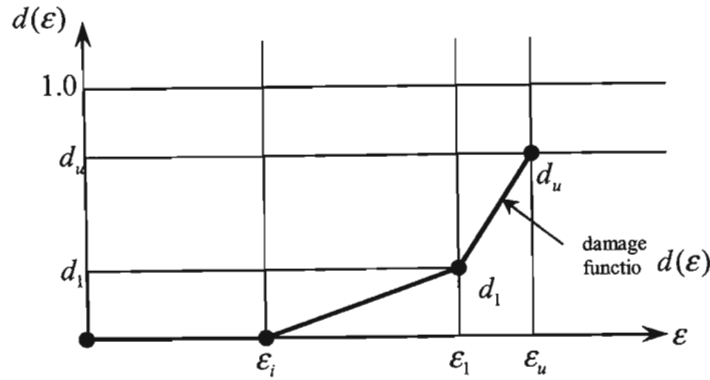


Fig. 2.10 Isotropic damage function.

Definition of the values of the three key strain points is done by analysis of experimental stress-strain curves on the material in question. These curves are obtained from uniaxial testing as explained below.

Material characterisation

Actual mechanical properties of the SMC material are determined experimentally by testing flat specimens. These properties of composites depend on the manufacturing process parameters. To obtain the adequate material characteristics that can be used for analysis of structural components, the specimens should be fabricated with the same processes that are used to manufacture the structural elements.

Tensile test yields the following properties of the SMC materials:

- Modulus of elasticity, E
- Poisson's ratio, ν

Shear modulus is calculated as

$$G = \frac{E}{2(1+\nu)}$$

Polymeric materials are characterised by pronounced viscoelastic properties resulting in time-dependent behaviour of polymeric composites that manifests itself in creep, stress relaxation, and dependence of the stress-strain diagram on the rate of loading. It should be noted that in composite materials, viscoelastic deformation of the polymeric matrix is restricted by fibres that usually are linear elastic and do not demonstrate time-dependent behaviour. For the processes under consideration the strain-rate effect on the material properties and behaviour could be taken into account using appropriate constitutive models.

Different laws can be used to model the strain rate effect (dependence of the stress-strain diagram on the rate of loading). Each law modifies the original strain-rate curve $\sigma_0(\epsilon)$ by multiplying it by a factor of amplification, which is a function of a number of parameters, depending on the complexity of the model:

- Cowper-Symonds law (PAM-CRASH Solver Notes, 2000):

$$\sigma(\varepsilon, \dot{\varepsilon}) = \sigma_0(\varepsilon) \left[1 + \left(\frac{\dot{\varepsilon}}{D} \right)^{1/p} \right] \quad (2.15)$$

Where $\sigma_0(\varepsilon)$ is the original stress-strain curve (without any strain-rate influence), $\dot{\varepsilon} = \frac{d\varepsilon}{dt}$ is the strain-rate, and D and p are two parameters used to fit the simulated curve to experimental results, i.e. to reflect the observed strain-rate dependency of the material.

- Johnson-Cook law (PAM-CRASH Solver notes, 2000):

$$\sigma(\varepsilon, \dot{\varepsilon}) = \sigma_0(\varepsilon) \left[1 + \frac{1}{p} \cdot \ln(\max(\dot{\varepsilon}/D, 1)) \right] \quad (2.16)$$

Where all the parameters have already been described for the Cowper-Symonds law.

- Modified Jones' law (PAM-CRASH Solver notes, 2000):

$$\sigma(\varepsilon, \dot{\varepsilon}) = \sigma_0(\varepsilon) \left\{ 1 + \left[\frac{(\varepsilon_u - \varepsilon_y) \dot{\varepsilon}}{D_u(\varepsilon - \varepsilon_y) + D_y(\varepsilon_u - \varepsilon)} \right]^{\frac{1}{A\varepsilon+B}} \right\} \quad (2.17)$$

Where $\sigma_0(\varepsilon)$ is the original stress-strain curve (without any strain-rate influence), and $\dot{\varepsilon} = \frac{d\varepsilon}{dt}$ is the strain-rate. D_u, D_y, A and B are four constants, which are used to fit the simulated curve with the experimental data. The stress-strain diagrams corresponding to this law are shown in Fig. 2.14.

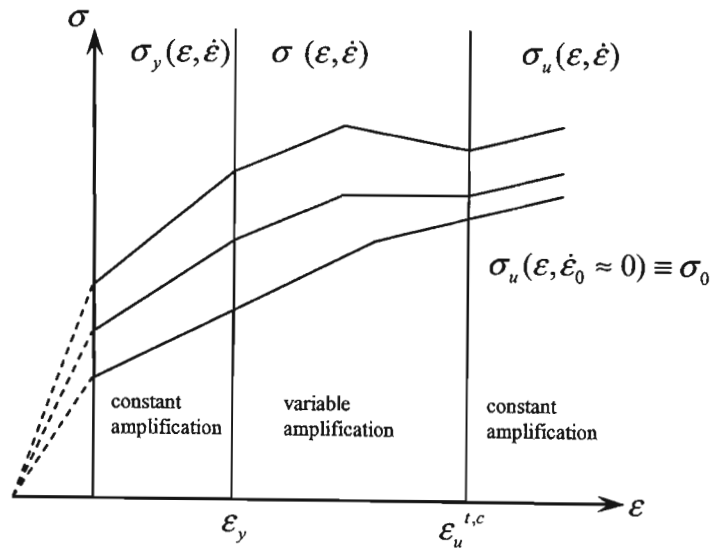


Fig. 2.11 Modified Jones' law.

Between ε_y and ε_u , the factor of amplification is equal to $\sigma(\varepsilon, \dot{\varepsilon})/\sigma_0(\varepsilon)$ due to the variable strain rate. This law can be considered as the Cowper-Symonds law, calibrated at strains ε_y and ε_u , corresponding respectively to σ_y and σ_u where σ_y extrapolates the function σ for strains lesser than ε_y and σ_u extrapolates it for strains greater than ε_u (PAM-CRASH Solver Notes, 2000). To avoid extrapolations, ε_y is usually set to 0 and ε_u is taken large enough to cover all strains encountered during the analysis.

2.3.1.2 LS-DYNA model for SMC composites

Model description

The Elastic Plastic with Kinematic Hardening material model (LS-DYNA Theory manual, 1998) could be used for the progressive damage simulation of SMC composites. This model is suitable for the modelling of isotropic and kinematic hardening plasticity with the option of including strain rate effects.

The following material properties are required for input into the LS-DYNA model:

- ρ , Mass density,
- E , Young's modulus,
- ν , Poisson's ratio,
- σ_y , Yield stress,
- E_t , Tangent modulus (see Fig. 2.12),
- β , Hardening parameter.

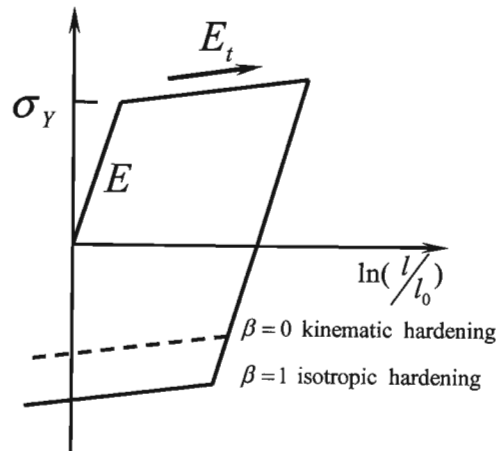


Fig. 2.12 Elastic-plastic behaviour with kinematic and isotropic hardening, where l_0 and l are undeformed and deformed lengths of uniaxial tension specimen, E_t is the slope of the bilinear stress-strain curve.

Isotropic, kinematic, or a combination of isotropic and kinematic hardening may be obtained by varying the hardening parameter β between 0 and 1. For β equal to 0 and 1 kinematic and isotropic hardening are obtained as shown in Fig. 2.12. Krieg and Key (1976) formulated this model and the implementation is based on their paper.

In isotropic hardening, the centre of the yield surface is fixed but the radius is a function of the plastic strain. In kinematic hardening, the radius of the yield surface is fixed but the centre translates in the direction of the plastic strain.

Material characterisation

The plastic-kinematic model is usually used for isotropic material, and the following parameters should be provided in this case. However, for SMC composite materials, some of these parameters (especially those defining the plasticity behaviour) are not used in the same way and must be reinterpreted within the framework of SMC composites modelling.

- ρ : mass density of the SMC material.
- E and ν : Young's modulus and Poisson's ratio found during tensile testing of a flat specimen made of the material to be modelled.
- σ_y, E_t, β : for isotropic materials, these parameters correspond respectively to the yield stress, tangent modulus and hardening parameter. Fig. 2.12 shows how to find these parameters in the isotropic case. Obviously, for SMC composites these characteristics need to be interpreted differently. To do this, we will need to perform some tensile and compression tests and plot the diagrams of Stress vs. $\ln(l/l_0)$. These diagrams yield the necessary parameters for SMC material.
- D, p : strain rate parameters for the Cowper-Symonds strain rate model. These parameters are used to best fit the simulated curves with the experimental data.

To model SMC composite behaviour with LS-DYNA, the flat specimens should be tested:

- 1 specimen should be tested under tension to find the Young's modulus and the Poisson's ratio.
- 1 specimen should be used to model SMC composite behaviour with isotropic plastic law.

2.3.2 Modelling of laminated continuously reinforced composites

Multilayered laminated composites are included in the analysis, chiefly as a secondary material to the SMC composite. In general automotive applications it is not usual to make use of laminated composites, as these are generally a much more expensive and lengthy option. Laminated composites are typically only used in high-end applications such as the aerospace industry or motorsport, where expense and time generally give way to functionality.

Laminates are usually modelled at the level of the unidirectional ply, and these plies, with assigned orientations, are stacked to form the entire laminate. The plies are assigned different stiffness and strength values in and transverse to the direction of fibres, and in shear, corresponding

to chiefly fibre properties in the direction of fibres, and matrix properties transverse to the fibres. The plies are then degraded according to separated failure criteria which distinguish fibre, matrix and shear failure (see Section 2.2.2). This approach is adopted in the Global Ply and Chang-Chang models that follow.

The Bi-Phase model which follows here immediately, however, models the fibres and matrix separately, and deduces the ply and then composite properties from the material properties of the two phases.

2.3.2.1 Bi-Phase model (PAM-CRASH)

Model description

The premise of this model is that the properties of a unidirectional ply may be obtained from superimposing the effects of an orthotropic material phase (matrix only) and of a one-dimensional material phase (fibres only). Each phase has its own material properties and damage is instituted as separate shear and volumetric effects.

Material parameters are input for the matrix and fibre materials separately, taken from certain testing procedures, and the parameters of the material are then deduced.

Damage is deduced from stress-strain curves for the material, and this damage may be separated into shear and volumetric influences.

The material constitution is based on the stress-strain relation

$$\sigma = C\varepsilon \quad (2.18)$$

where

$$C = C^{UD} = C^f + C^m$$

and C^{UD} is the stiffness matrix for the unidirectional ply, C^f for fibres, C^m for matrix

$$C^{UD} = \begin{bmatrix} \frac{E_{11}^{UD}}{N^{UD}} & \frac{E_{22}^{UD} \nu_{12}^{UD}}{N^{UD}} & 0 \\ \frac{E_{11}^{UD} \nu_{21}^{UD}}{N^{UD}} & \frac{E_{22}^{UD}}{N^{UD}} & 0 \\ 0 & 0 & G_{12}^{UD} \end{bmatrix} \quad (2.19)$$

$$C^f = \begin{bmatrix} E_{11}^f & 0 & 0 \\ 0 & 0 & 0 \\ 0 & 0 & 0 \end{bmatrix} \quad (2.20)$$

$$C^m = \begin{bmatrix} \frac{E_{11}^m}{N^m} & \frac{E_{22}^m v_{12}^m}{N^{UD}} & 0 \\ \frac{E_{11}^m v_{21}^m}{N^m} & \frac{E_{22}^m}{N^m} & 0 \\ 0 & 0 & G_{12}^m \end{bmatrix} \quad (2.21)$$

where $N^{m,UD} = 1 - v_{12}^{m,UD} v_{21}^{m,UD}$.

Fibre and composite properties may be measured, and thus the unknown matrix properties are given by $C^m = C^{UD} - C^f$ so that elastic constants in direction of fibres (11) and transverse direction (22) are:

$$E_{11} = E_{11}^m = E_{11}^{UD} - E_{11}^f$$

$$E_{22} = E_{22}^m = \frac{E_{22}^{UD}}{(1 + (v_{12}^{UD})^2) \left(\frac{E_{22}^{UD}}{E_{11}^{UD}} \left(\frac{E_{11}^f}{E_{11}^{UD} - E_{11}^f} \right) \right)}$$

$$v_{12} = v_{12}^m = \frac{v_{21}^{UD}}{\left(1 - \frac{E_{11}^f N^{UD}}{E_{11}^{UD}} \right)}$$

$$G_{12} = G_{12}^m = G_{12}^{UD}$$
(2.22)

where index m is for matrix, f is for fibre, UD is for the unidirectional material, and constants in normal direction are equal to the constants in transverse direction:

$$E_{33} = E_{22}, \quad G_{23} = G_{12}, \quad G_{13} = G_{12}, \quad v_{23} = v_{12}, \quad v_{13} = v_{12}$$

if not specifically known from other sources or tests.

The following properties may be measured from testing: $E_{11}^{UD}, E_{22}^{UD}, G_{12}^{UD}, v_{12}^{UD}, E_{true}^f$ (the true fibre modulus), α_f (the fibre volume fraction) and from these the following may be obtained thus:

$$v_{21}^{UD} = v_{12}^{UD} \frac{E_{22}^{UD}}{E_{11}^{UD}} \quad E_{11}^f = \alpha_f E_{true}^f$$

To take into account the progressive failure of the composite a damage function based on the strains in the material is introduced, such that

$$C(d) = C_o(1 - d) \quad (2.23)$$

where d is the damage function, in the interval $[0,1]$, $C(d)$ is the damaged stiffness matrix, and C_0 is the undamaged stiffness matrix.

Damage is initiated at ε_i determined by the chosen failure criterion, or by testing, linearly interpolated between first ε_i and ε_1 (determined again from the stress-strain diagram obtained experimentally) and then ε_1 and ε_u as shown in Fig. 2.13.

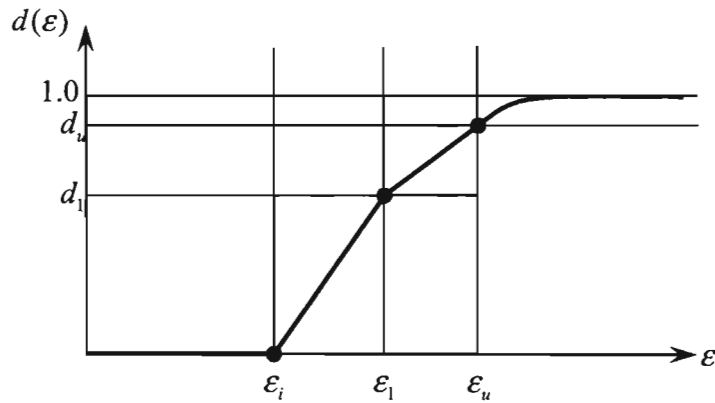


Fig. 2.13 Assessment of damage variable d .

The corresponding effect on the relevant modulus value is illustrated in Fig. 2.14, where

$$E(\varepsilon) = (1 - d(\varepsilon))E_0 \quad (2.24)$$

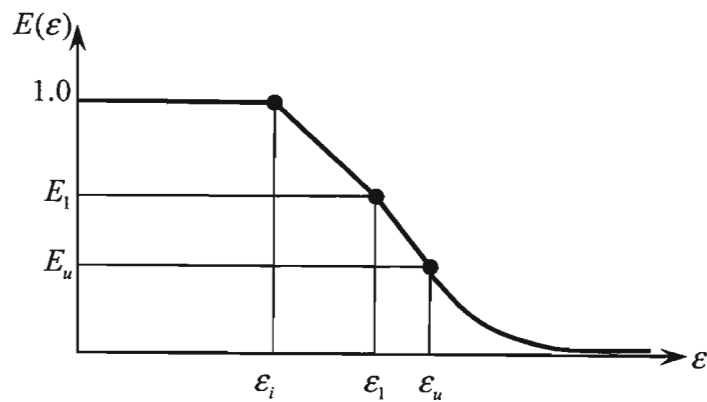


Fig. 2.14 Reduction in moduli.

The values for the above interpolations are obtained from tensile/compressive testing as shown in Fig. 2.15.

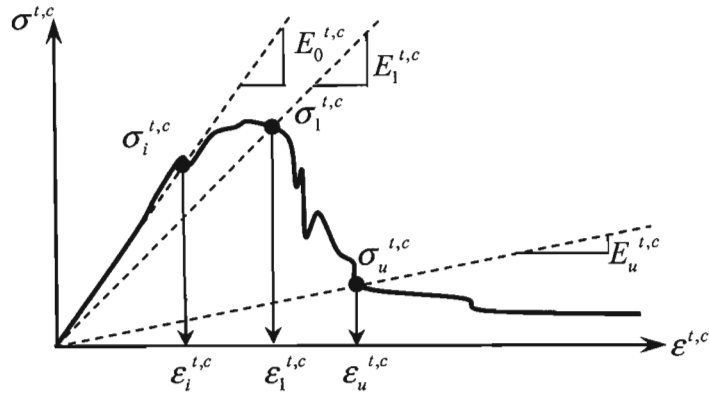


Fig 2.15 Experimentally obtained stress-strain curve.

The curve is then approximated using the key points of the elastic limit, the maximum stress point and the ultimate stress point as shown in Fig. 2.9.

The stress and strain ($\sigma_i, \sigma_1, \sigma_u, \epsilon_i, \epsilon_1, \epsilon_u$) values at the key points may be used to evaluate the effective elastic modulus at each of the points.

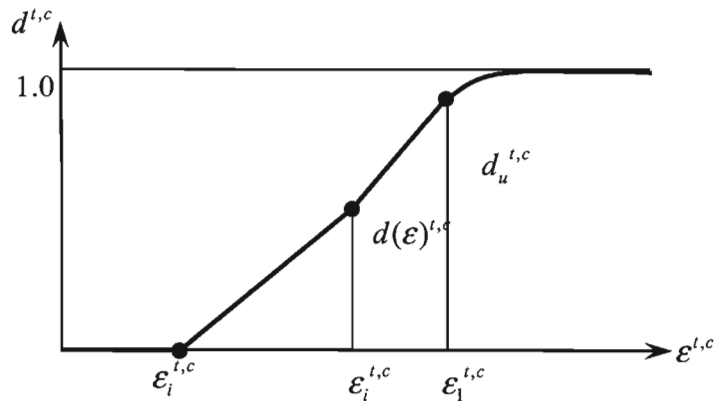


Fig. 2.16 Interpolation of d .

The damage function d is then obtained (see Fig. 2.16)

$$d_1^{t,c} = 1 - \frac{E_1^{t,c}}{E_0^{t,c}}, \quad d_u^{t,c} = 1 - \frac{E_u^{t,c}}{E_0^{t,c}} \quad (2.25)$$

where $E_0^{t,c}$ elastic modulus of undamaged material, $E_1^{t,c}$ elastic modulus of material after initial damage, and $E_u^{t,c}$ elastic modulus before ultimate damage.

The model takes into account the damage as the sum of the influence of volumetric d_v and shear d_s damage, in the fibre and matrix, such that

For the matrix:

$$d(\epsilon) = d_v(\epsilon_v) + d_s(\epsilon_s)$$

and for the fibre

$$d(\varepsilon) = d_v(\varepsilon_f)$$

The strains presented in the stress-strain diagrams above (see Fig. 2.13-2.16) are thus either equivalent volumetric strains ε_v or equivalent shear strains ε_s that are calculated as follows:

In the matrix

$$\begin{aligned} \varepsilon_v &= (1 - \nu_{12} - \nu_{13})\varepsilon_{11} \\ \varepsilon_s &= \left(\frac{\varepsilon_{11}}{\sqrt{3}} \right) \left(1 + \nu_{12} + \nu_{13} - \nu_{12}\nu_{13} + \nu_{12}^2 + \nu_{13}^2 \right)^{1/2} \end{aligned} \quad (2.26)$$

and in the fibre

$$\varepsilon_v^f = \varepsilon_{11} \quad (2.27)$$

The equivalent stresses may then be calculated as follows:

$$\sigma(\varepsilon) = E_0 \varepsilon \left(1 - \frac{d_1}{\varepsilon_1 - \varepsilon_i} (\varepsilon - \varepsilon_i) \right), \quad \varepsilon_i < \varepsilon < \varepsilon_1 \quad (2.28)$$

$$\sigma(\varepsilon) = E_0 \varepsilon \left(1 - d_1 \frac{d_u - d_1}{\varepsilon_u - \varepsilon_1} (\varepsilon - \varepsilon_1) \right), \quad \varepsilon_1 < \varepsilon < \varepsilon_u \quad (2.29)$$

$$\sigma_u = E_0 \varepsilon_u (1 - d_u) = \text{const}, \quad \varepsilon_u < \varepsilon < \infty \quad (2.30)$$

The corresponding stress-strain diagram is shown in Fig. 2.17.

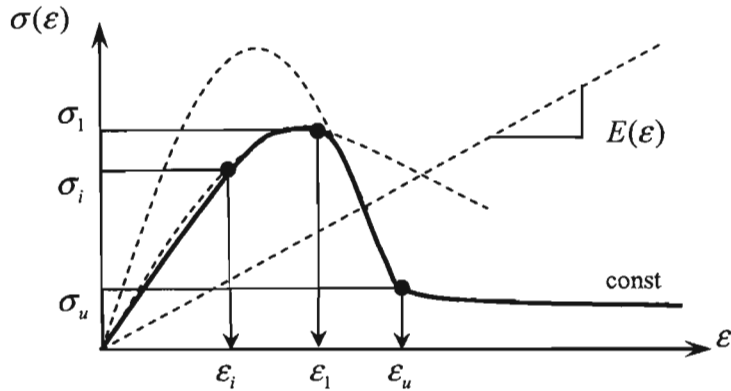


Fig. 2.17 Phases of material degradation.

In order to implement the model the following material properties are required for input:

- $E_{11}^{UD}, E_{22}^{UD}, G_{12}^{UD}, \nu_{12}^{UD}, E_{true}^f$ (the true fibre modulus), α_f (the fibre volume fraction)

The following must be deduced from the stress-strain diagram

- $(\sigma_i, \varepsilon_i)$, $(\sigma_1, \varepsilon_1)$, $(\sigma_u, \varepsilon_u)$
- evaluation of shear, volumetric and overall damage at any point to obtain moduli at each point.

Material characterisation

The set of parameters required for the implementation of the Bi-Phase model can be divided in several groups: unidirectional properties, matrix phase data, fibre phase data and damage behaviour of both phases. Some of these constants are obtained directly from testing while others could be calculated using material models. Corresponding testing methods and equations are presented below.

Unidirectional properties (whole material: fibres + matrix): these properties are indexed by the super script ^{UD}.

- E_{11}^{UD} , ν_{12}^{UD} : Young's modulus along the fibres and Poisson's ratio are determined from tension/compression test on unidirectional laminate loaded along the fibres
- E_{22}^{UD} : transverse Young's modulus determined from tension/compression test on unidirectional laminate loaded in transverse direction
- G_{12}^{UD} : shear modulus, could be obtained from a tension test on a $[\pm 45^\circ]_{2S}$ laminate using the following equation:

$$\frac{1}{G_{12}^{UD}} = \frac{4\varepsilon_{11}}{\sigma_{11}} - \frac{1}{E_{11}^{UD}} - \frac{1}{E_{22}^{UD}} + \frac{2\nu_{12}}{E_{11}^{UD}}$$

Fibre phase properties

The constants bound to this one-dimensional phase are inherent in the production of the material and thus, do not need any straight determination. These are E_{true}^f , the true fibre modulus and α_f , the fibre volume fraction. We can then compute the following parameter:

- $E_{11}^f = \alpha_f \times E_{true}^f$: Young's modulus describing the one-dimensional phase.

Matrix phase properties

All the matrix-related constants are deduced from the unidirectional properties of the material or of the fibre phase. Here are all the necessary equations (PAM-CRASH Solver notes, 2000):

$$\begin{aligned} E_{11}^m &= E_{11}^{UD} - E_{11}^f & \nu_{21}^m &= \frac{\nu_{21}^{UD}}{1 - E_{11}^f \frac{N^{UD}}{E_{11}^{UD}}} & E_{22}^m &= \frac{E_{22}^{UD}}{1 + (\nu_{12}^{UD})^2 \frac{E_{22}^{UD} \cdot E_{11}^{UD}}{E_{11}^f (E_{11}^{UD} - E_{11}^f)}} \\ \nu_{12}^m &= \nu_{12}^{UD} & G_{13}^m &= G_{23}^m = G_{12}^m & \nu_{13}^m &= \nu_{23}^m = \nu_{12}^m \\ G_{12}^m &= G_{12}^{UD} & & & & \\ E_{33}^m &= E_{22}^m & & & & \end{aligned}$$

Damage properties

The calculation of the complete damage law needs three points of the strain-stress diagram, corresponding to three strains $\varepsilon_i, \varepsilon_1$, and ε_u :

- $0 < \varepsilon < \varepsilon_i$: $d(\varepsilon) = 0$, ε_i is the initial equivalent threshold strain (volume or shear)
- $\varepsilon_i < \varepsilon < \varepsilon_1$: $d(\varepsilon)$ is linear, ε_1 is an intermediate equivalent strain corresponding to an intermediate damage d_1
- $\varepsilon_1 < \varepsilon < \varepsilon_u$: ε_u and d_u are respectively the ultimate equivalent strain and the ultimate damage

After the elastic phase, the damaging of the material can lead to a loss of stiffness of the fibres and/or of the matrix. Thus, these two phases have a new modulus that is calculated as: $E_d = E_0(1-d)$. For each phase, the damaging essentially comes from the hydrostatic pressure. However, shear strain damage for the matrix phase can be introduced and the "total" damage function is then: $d(\varepsilon) = d_v(\varepsilon_v) + d_s(\varepsilon_s)$ where $d_s = 0$ for the fibres. The equivalent volumetric strain and shear strain can be calculated from the strain tensor, for each phase, using the following formulae where j is an index from $\{i, 1, u\}$ (PAM-CRASH Solver notes, 2000):

Volumetric damage	$\varepsilon_v^f = \varepsilon_{11}$	$\varepsilon_v^m = tr(\varepsilon) = (1 - 2\nu_{12}^m)\varepsilon_{11}$
Shear damage	$\varepsilon_s^m = \sqrt{\frac{1}{2} tr\left(\varepsilon - \frac{1}{3}\varepsilon_v I\right)} = \frac{\varepsilon_{11}}{\sqrt{3}}(1 + \nu_{12}^m)$	$\varepsilon_s^f = 0$

Testing procedure summary

The material behaviour should be modelled both in tension and compression. This means that, for example, E_{11}^{UD} has to be estimated in tension and compression. The superscript t indicates a property of the material in tension and the superscript c for properties in compression case. The following tests should be performed in order to characterise the material.

- tensile test along the fibres: $\varepsilon_i^t, \varepsilon_1^t, \varepsilon_u^t$ (as shown in Fig. 2.9) $E_{11}^{UD,t}, \nu_{12}^{UD,t}$
- tensile test across the fibres: $E_{22}^{UD,t}$
- compression test along the fibres: $\varepsilon_i^c, \varepsilon_1^c, \varepsilon_u^c, E_{11}^{UD,c}, \nu_{12}^{UD,c}$
- compression test across the fibres: $E_{22}^{UD,c}$
- tensile test on a $[\pm 45^\circ]_{2S}$ laminate: $G_{12}^{UD,t}$. It is assumed that $G_{12}^{UD,c} \approx G_{12}^{UD,t}$ (Rozycki et al., 1998). Shear modulus could be found from the following equation: $\frac{1}{G_{12}^{UD,t}} = \frac{1}{G_{12}^{UD,c}} = \frac{4\varepsilon_{11}}{\sigma_{11}} - \frac{1}{E_{11}^{UD,t}} - \frac{1}{E_{22}^{UD,t}} + \frac{2\nu_{12}}{E_{11}^{UD,t}}$ where ε_{11} and σ_{11} are the strain and stress measured during the tension test.

- the fibre phase modulus in compression is found using the following equation: $E_{11}^{f,c} = \frac{E_{11}^{UD,c}}{E_{11}^{UD,t}} \times E_{11}^{f,t}$ (Rozycki et al., 1998).

Fig. 2.9 shows how to find the above Bi-Phase damage parameters. For the compression case, similar diagrams are used in the same way.

2.3.2.2 Global Ply model (PAM-CRASH)

Model description

As described earlier, the Global Ply model acts at the level of the unidirectional ply, with material parameters being defined for the ply in the respective directions. This modelling is achieved through homogenisation of the elementary layer. The properties may thus be defined by uniaxial testing of the unidirectional ply.

Damage is introduced in the form of matrix microcracking, fibre-matrix debonding and fibre failure. The damage parameters are introduced in the form of defined failure parameters which are obtained from a series of experimental testing.

A plasticity algorithm is also included in the software but was not considered relevant here. The constitutive relationship is given by

$$\begin{Bmatrix} \varepsilon_{11}^e \\ \varepsilon_{22}^e \\ 2\varepsilon_{12}^e \\ 2\varepsilon_{23}^e \\ 2\varepsilon_{13}^e \end{Bmatrix} = \begin{pmatrix} \frac{1}{E_1} & -\frac{\nu_{12}^0}{E_1} & 0 & 0 & 0 \\ -\frac{\nu_{12}^0}{E_1} & \frac{1}{E_2} & 0 & 0 & 0 \\ 0 & 0 & \frac{1}{G_{12}} & 0 & 0 \\ 0 & 0 & 0 & \frac{1}{G_{23}^0} & 0 \\ 0 & 0 & 0 & 0 & \frac{1}{G_{12}} \end{pmatrix} \begin{Bmatrix} \sigma_{11} \\ \sigma_{22} \\ \sigma_{12} \\ \sigma_{23} \\ \sigma_{13} \end{Bmatrix} \quad (2.31)$$

where

in the fibre direction (1)

$$\begin{aligned} E_1 &= E_1^t \text{ if } \varepsilon_{11} \geq 0 \text{ (tension)} \\ E_1^t &= E_1^{0t} (1 - d^t) \text{ if } \varepsilon_{11} \geq \varepsilon_i^t, \text{ else } E_1^t = E_1^{0t} \end{aligned}$$

E_1^t is the tensile Young's modulus in the fibre direction, E_1^{0t} is its initial (undamaged) value, and d^t is the tensile damage in the fibre direction.

$$E_1 = E_1^c \text{ if } \varepsilon_{11} < 0 \text{ (compression)}$$

$$E_1^c = E_1^{\gamma} (1 - d^{jc}) \text{ if } |\varepsilon_{11}| \geq \varepsilon_i^{jc}, \text{ else } E_1^c = E_1^{\gamma}$$

$$E_1^{\gamma} = \frac{E_1^{0c}}{1 - \gamma \cdot E_1^{0c} |\varepsilon_{11}|}$$

E_1^c is the compressive Young's modulus in fibre direction, E_1^γ is the non-linear compressive Young's modulus, E_1^{0c} is its initial (undamaged) value, γ is the non-linear compressive modulus factor, and d^{fc} is the compressive damage in the fibre direction.

In the transverse direction (2)

$$E_2 = E_2^0(1-d') \text{ if } \varepsilon_{22} \geq 0 \text{ (tension), else } E_2 = E_2^0$$

E_2^0 is the initial value of the transverse modulus E_2 , d' is the matrix transverse damage.

For shear,

$$G_{12} = G_{12}^0(1-d)$$

G_{12}^0 is the initial value of the ply shear modulus G_{12} , d is the matrix shear damage.

Shear and transverse damage in the matrix are defined respectively as follows:

$$\begin{aligned} \frac{\partial E_D}{\partial d} = Z_d &= \frac{1}{2} \frac{\sigma_{12}^2 + \sigma_{13}^2}{G_{12}^0(1-d)^2} \\ \frac{\partial E_D}{\partial d'} = Z_d' &= \frac{1}{2} \frac{\sigma_{22} + \sigma_{33}}{E_2^0(1-d')^2} \end{aligned} \quad (2.32)$$

Damage evolution over time is then defined as

$$Y(t) = \sqrt{Z_d(\tau) + bZ_d'(\tau)}_{\text{MAX for } \tau < t} \quad (2.33)$$

$$Y'(t) = \frac{1}{2} \sqrt{Z_d'(\tau)}_{\text{MAX for } \tau < t} \quad (2.34)$$

for shear and transverse damage respectively.

The fibre damage in tension, d^f , is modelled as for the Bi-Phase model above, defined from experimentation at three strain points, ε_i^f , ε_1^f and ε_u^f , and interpolated between these. d^f grows asymptotically to 1 after ε_u^f . Compressive fibre damage is modelled similarly, but grows to some other defined maximum d_u^{fc} .

The damage parameters are defined by experimentation as presented in the material characterisation section below.

Material characterisation

To characterise this model, the following set of material constants is needed: basic elastic constants (Young's and shear modulus, Poisson's ratio), matrix and fibre tensile damage-related constants, compressive fibre constants and plastic constants (if plastic behaviour needs to be taken into account). Some of these characteristics could be determined using cycling tests. The following notations are accepted for the parameters considered below. The value of some parameter (say

parameter A) measured in first cycle is denoted as A_0 . The same parameter determined at the cycle with number i has a subscript i (e.g. A_i).

Basic elastic constants

- E_1^{0i} , ν_{12}^0 : initial values of Young's modulus and Poisson's ratio for unidirectional material under tension in fibre direction.
- E_2^0 : initial value of Young's modulus across the fibre direction. Given by the initial slope of stress-strain diagram obtained from a cyclic test on a $[\pm 45^\circ]_{2S}$ laminate (see Fig. 2.18).
- G_{12}^0 and G_{23}^0 : initial values of shear moduli. Shear modulus G_{12}^0 is given by the slope of the stress-strain diagram during a cyclic test on $[\pm 45^\circ]_{2S}$ laminate.
- κ_{13} and κ_{23} : shear corrections factors defined by user.

Matrix and fibre tensile damage-related constants

- Y_0, Y_C : initial shear and critical shear limits. A cyclic simple tension test on a $[\pm 45^\circ]_{2S}$ laminate will give these values: Y_0 is the y -intercept and Y_C is the gradient of the graph of d_i vs. $Y(t_i)$ where:

$$d_i = 1 - \frac{G_{12,i}}{G_{12}^0}$$

and:

$$Y(t_i) = \sqrt{\frac{1}{2} G_{12}^0 (2\varepsilon_{12,i}^e)^2}$$

$\varepsilon_{12,i}^e$ is an elastic strain measured for each cycle as shown in Fig. 2.18.

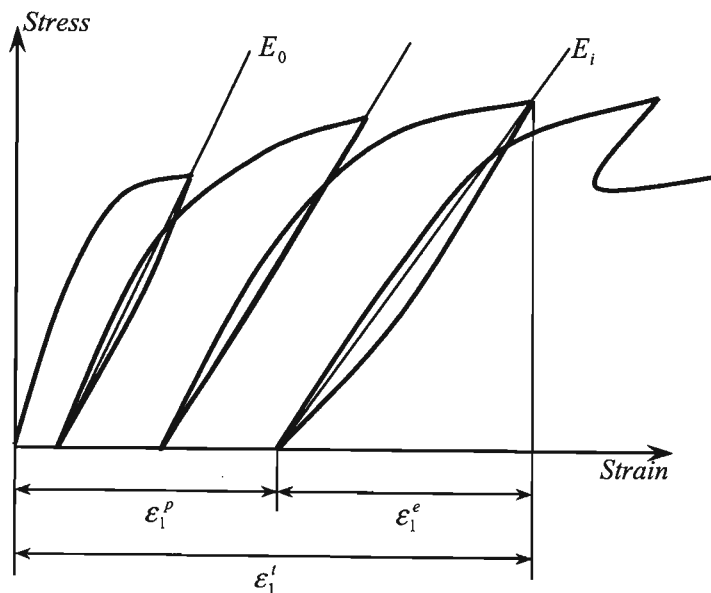


Fig. 2.18 Stress vs. Strain diagram for cycling test.

- d_{max} : maximum allowed value of the damage functions d and d' . It is a user defined parameter $0 < d_{max} \leq 1$. If $d_{max} = 1$ material is completely damaged.

Compressive fibre constants

- E_1^{0c} : compressive initial Young's modulus in the direction of fibres. This constant is given by the initial slope of a stress-strain diagram obtained from the compression test of a unidirectional material along the fibres.
- γ corrective factor for nonlinear fibre compressive behaviour. User-defined parameter to best fit the simulation results with experimental data in the case that some non-linearity takes place for the experimental stress-strain curve of the compression test along the fibres. Indeed, the longitudinal Young's modulus can decrease under compression, and the factor γ is introduced to take this into account. As a result, the effective non-linear undamaged fibre modulus in compression is given by:

$$E_1^\gamma = \frac{E_1^{0,c}}{1 + \gamma E_1^{0,c} |\epsilon_{11}|}$$

- ϵ_i^{fc} : initial longitudinal fibre compression damage threshold strain. This parameter is determined in the same way as for Bi-Phase model (see Fig. 2.18).
- ϵ_u^{fc} : ultimate longitudinal fibre tensile damage strain. This is ultimate strain value of the stress-strain diagram obtained from the compression test of a unidirectional material along the fibres, as shown in Fig. 2.18.
- d_u^{fc} : ultimate damage value in compression case. It is given by:

$$d_u^{fc} = 1 - \frac{E_u^{fc}}{E_0^{fc}} \quad (2.41)$$

- R_0 : initial yield stress. Obtained from the cyclic tension test on $[\pm 45^\circ]_{2S}$ laminate. As shown in Fig. 2.18, each loading/unloading cycle gives an "initial" yield stress $\sigma_{12,i}$ and a plastic strain $2\epsilon_{12,i}^p$ as follows:

$$\left. \begin{aligned} R_i &= \frac{\sigma_{12,i}}{1 - d_i} - R_0 \\ \epsilon_i^p &= \int \dot{\epsilon}_{12,i}^p (1 - d_i) \end{aligned} \right\} \Rightarrow R_i = \beta (\epsilon_i^p)^m$$

where β and m are defined as follows:

- β, m : hardening law multiplier and its exponent. During a cyclic tension test on a $[\pm 45^\circ]_{2S}$ laminate, $\ln(R_i)$ vs. $\ln(\varepsilon_i^p)$ curve is plotted: m is then given by the slope and β by the y -intercept value.
- $a^2 = A$: coupling factor between shear and transverse plastic strains. It can be found from the cyclic tension test on $[+45]_8$ laminate as follows :

$$A = \frac{(\varepsilon_{22,i}^p - \varepsilon_{22,i-1}^p) \cdot (1 - d'_i)^2}{(2\varepsilon_{12,i}^p - \varepsilon_{12,i-1}^p) \cdot (1 - d_i)^2} \quad (2.42)$$

The following experimental test series can be used to obtain the set of parameters required for computation.

- tension test of a unidirectional material along the fibres yields $E_1^{0t}, \nu_{12}^0, \varepsilon_i^{ft}, \varepsilon_u^{ft}$ and d_u^{ft} ,
- cyclic test on $[\pm 45^\circ]_{2S}$ yields $G_{12}^0, Y_C, Y_0, Y_R, R_0, \beta$ and m ,
- cyclic test on $[+45^\circ]_8$ yields A, E_2^0 ,
- cyclic test on $[\pm 67.5^\circ]_{2S}$ yields Y'_C, Y'_0, Y'_S and b ,
- compression test of a unidirectional material along the fibres yields $E_1^{0c}, \gamma, \varepsilon_i^{fc}, \varepsilon_u^{fc}$ and d_u^{fc} .

Five unidirectional laminated specimens are needed to perform these tests. Two specimens will be tested along the fibres (one in tension and one in compression). The three others will be subjected to the cyclic testing.

2.3.2.3 Chang-Chang Composite Failure model (LS-DYNA)

Model description

The constitutive material model taking into account the progressive failure of laminated composites was developed by Chang and Chang, (1987). This model represents a ply discount method based on the assumption of brittle failure. After failure, a ply is loosing its load capacity in the dominant stress direction associated with the failure mode. The failure is assumed to be instantaneous and the elastic constants are reduced to zero in a predetermined number of time steps. Three failure criteria are used in the model. The constitutive constants can vary through the shell thickness by using the user defined integration rule. The laminated shell theory can be activated to properly model the transverse shear deformation. Lamination theory is applied to correct for the assumption of a uniform constant shear strain through the thickness of the shell.

The following five material parameters are used in the failure criteria:

- S_1 , longitudinal tensile strength,
- S_2 , transverse tensile strength,
- S_{12} , shear strength,
- C_2 , transverse compressive strength,
- α , nonlinear shear stress parameter.

S_1, S_2, S_{12} , and C_2 are obtained from material strength measurements. α is defined by material shear stress-strain measurements. Constitutive equations, linking strains ε_1 , ε_2 , $\gamma_{12} = 2\varepsilon_{12}$ and stresses σ_1 , σ_2 , τ_{12} in the ply are:

$$\varepsilon_1 = \frac{1}{E_1}(\sigma_1 - \nu_1 \sigma_2) \quad (2.43)$$

$$\varepsilon_2 = \frac{1}{E_2}(\sigma_2 - \nu_2 \sigma_1) \quad (2.44)$$

$$2\varepsilon_{12} = \frac{1}{G_{12}}\tau_{12} + \alpha\tau_{12}^3 \quad (2.45)$$

where $E_1, E_2, G_{12}, \nu_1, \nu_2$ are elastic characteristics of a unidirectional ply. The third equation defines the nonlinear shear stress parameter α .

A fibre matrix shearing term augments each damage mode:

$$\bar{\tau} = \frac{\frac{\tau_{12}^2}{2G_{12}} + \frac{3}{4}\alpha\tau_{12}^4}{\frac{S_{12}^2}{2G_{12}} + \frac{3}{4}\alpha S_{12}^4} \quad (2.46)$$

which is the ratio of the shear stress to the shear strength.

The matrix cracking failure criteria is determined from:

$$F_{matrix} = \left(\frac{\sigma_2}{S_2} \right)^2 + \bar{\tau} \quad (2.47)$$

where failure is assumed whenever $F_{matrix} > 1$. If $F_{matrix} > 1$, then the material constants $E_2, G_{12}, \nu_1, \nu_2$ are set to zero.

The compression failure criteria is given as

$$F_{comp} = \left(\frac{\sigma_2}{2S_{12}} \right)^2 + \left[\left(\frac{C_2}{2S_{12}} \right)^2 - 1 \right] \frac{\sigma_2}{C_2} + \bar{\tau} \quad (2.48)$$

where failure is assumed whenever $F_{comp} > 1$. If $F_{comp} > 1$, then the material constants E_2, ν_1, ν_2 are set to zero.

The final failure mode is due to fibre breakage.

$$F_{fiber} = \left(\frac{\sigma_1}{S_1} \right)^2 + \bar{\tau} \quad (2.49)$$

Failure is assumed whenever $F_{fiber} > 1$. If $F_{fiber} > 1$, then the material constants $E_2, G_{12}, \nu_1, \nu_2$ are set to zero.

Material characterisation

Implementation of this model in LS-DYNA needs the introduction of the following elastic and strength parameters, characterizing the unidirectional material:

- ρ : mass density
- $E_a, E_b, E_c, \nu_{ba}, \nu_{ca}, \nu_{cb}$: Young's moduli in three directions and Poisson's ratios. (Tension tests in the three directions yield these parameters)
- G_{ab}, G_{bc}, G_{ca} : shear moduli in three planes (ab, bc, ca). Shear modulus G_{ab} could be obtained from a tension test on a $[\pm 45^\circ]_{2S}$ laminate using the following equation:

$$\frac{1}{G_{ab}} = \frac{4\varepsilon_{11}}{\sigma_{11}} - \frac{1}{E_a} - \frac{1}{E_b} + \frac{2\nu_{ab}}{E_a}$$

For transversely isotropic material: $E_c = E_b$, $\nu_{ca} = \nu_{ba}$, and $G_{ca} = G_{ab}$.

- K_{fail} : bulk modulus of failed material (for compressive failure).
- S_c : shear strength in ab plane. This parameter corresponds to the maximum shear stress occurred during a coupon test on a $[\pm 45^\circ]_{2S}$ laminates,
- X_T : longitudinal tensile strength. This is the ultimate stress, extracted from the stress-strain diagram of a tensile test along the fibres.
- Y_T : transverse tensile strength. This is the ultimate stress, extracted from the stress-strain diagram of a tensile test in the transverse direction.
- Y_C : transverse compressive strength. This is the ultimate stress, extracted from the stress-strain diagram of a compression test along the fibres.
- α : shear stress parameter for the nonlinear terms. Parameter α is defined as follows:

$$2\varepsilon_{12} = \frac{1}{G_{ab}}\tau_{12} + \alpha\tau_{12}^3$$

2.3.2.4 Enhanced Composite Damage model (LS-DYNA)

Model description

These are two material models (M1 and M2) which are enhanced versions of the previous composite material model. Orthotropic materials, e.g. unidirectional layers in composite shell structures can be defined. Optionally, various types of failure can be specified following either the criteria of Chang and Chang, (1987) (model M1) or Tsai and Wu (1981) (model M2). In addition special measures are taken for failure under compression (Matzenmiller and Schweizerhof, 1990). This model is only valid for thin shell elements. Lamination theory can be applied to this model in the same way as it was done for Chang-Chang model.

In plane ab the Chang-Chang criterion is given as follows:

For the tensile fibre mode,

$$\sigma_{aa} > 0 \quad \text{then} \quad e_f^2 = \left(\frac{\sigma_{aa}}{X_t} \right)^2 + \beta \left(\frac{\sigma_{ab}}{S_c} \right) - 1 \quad \left\{ \begin{array}{l} \geq 0 \text{ failed} \\ < 0 \text{ elastic} \end{array} \right. \quad (2.50)$$

$$E_a = E_b = G_{ab} = \nu_{ba} = \nu_{ab} = 0,$$

for the compressive fibre mode,

$$\sigma_{aa} < 0 \quad \text{then} \quad e_c^2 = \left(\frac{\sigma_{aa}}{X_c} \right)^2 - 1 \quad \left\{ \begin{array}{l} \geq 0 \text{ failed} \\ < 0 \text{ elastic} \end{array} \right. \quad (2.51)$$

$$E_a = \nu_{ba} = \nu_{ab} = 0,$$

for the tensile matrix mode,

$$\sigma_{bb} > 0 \quad \text{then} \quad e_m^2 = \left(\frac{\sigma_{bb}}{Y_t} \right)^2 + \beta \left(\frac{\sigma_{ab}}{S_c} \right) - 1 \quad \left\{ \begin{array}{l} \geq 0 \text{ failed} \\ < 0 \text{ elastic} \end{array} \right. \quad (2.52)$$

$$E_b = \nu_{ba} = 0 \longrightarrow G_{ab} = 0,$$

and for the compressive matrix mode,

$$\sigma_{bb} < 0 \quad \text{then} \quad e_d^2 = \left(\frac{\sigma_{bb}}{2S_c} \right)^2 + \left[\left(\frac{Y_c}{2S_c} \right)^2 - 1 \right] \frac{\sigma_{bb}}{Y_c} + \left(\frac{\sigma_{ab}}{S_c} \right)^2 - 1 \quad \left\{ \begin{array}{l} \geq 0 \text{ failed} \\ < 0 \text{ elastic} \end{array} \right. \quad (2.53)$$

$$E_b = \nu_{ba} = \nu_{ab} = 0 \longrightarrow G_{ab} = 0,$$

$$X_c = 2Y_c \quad \text{for 50\% fiber volume}$$

In the Tsai-Wu criteria the tensile and compressive fibre modes are treated as in the Chang-Chang criteria. The failure criterion for the tensile and compressive matrix mode is given as:

$$e_{md}^2 = \frac{\sigma_{bb}^2}{Y_c Y_t} + \left(\frac{\sigma_{ab}}{S_c} \right)^2 + \frac{(Y_c - Y_t) \sigma_{bb}}{Y_c Y_t} - 1 \quad \left\{ \begin{array}{l} \geq 0 \text{ failed} \\ < 0 \text{ elastic} \end{array} \right. \quad (2.54)$$

When failure has occurred in all the composite layers (through-thickness) the element is deleted. Elements, which share nodes with the deleted element, become “crashfront” elements and can have their strength reduced.

There are another two models available in LS-DYNA that can be used for modelling laminated composites: Composite Failure Option Model (CFOM) and Laminated Composite Fabric (LCF).

Both of them are very close in formulation to the previous models. CFOM has possibility to be used with solid elements. LCF may be used to model composite materials with unidirectional layers, complete laminates, and woven fabrics. This model is implemented for shell elements only.

Material characterisation

Implementation of this model in LS-DYNA needs the introduction of the following elastic and strength parameters, characterizing the unidirectional material:

- ρ : mass density.
- For in- plane characteristics E_a, E_b, G_{ab} , and ν_{ab} the corresponding test methods were discussed before.
- Transverse shear moduli G_{bc}, G_{ca} can be obtained by inducing pure shear in two symmetric specimens and calculating shear modulus as $G_{ac} = \frac{P}{2A\gamma}$, where A is the in-plane area of the specimen (Vasiliev and Morozov, 2001).
- *DFAILM*: maximum strain for matrix in tension or compression. It is the ultimate strain that can be obtained from stress-strain diagrams of matrix tensile or compression tests.
- *DFAILS*, S_C : maximum shear strain and shear strength respectively. This parameter corresponds to the maximum shear stress obtained during a coupon test on a $[\pm 45^\circ]_{2S}$ laminates.
- α : shear stress parameter for the nonlinear term. This parameter is defined from the following equation: $2\varepsilon_{12} = \frac{1}{G_{ab}}\tau_{12} + \alpha\tau_{12}^3$
- X_C, X_T : longitudinal compressive and tensile strength. These are the ultimate stresses, extracted from the stress-strain diagrams of a compression and a tensile tests along the fibres respectively.
- Y_C, Y_T : transverse compressive strength. These are the ultimate stresses, extracted from the stress-strain diagrams of a compression and tensile tests in the transverse direction respectively.

Chapter 3

NUMERICAL SIMULATION. COMPARATIVE SOFTWARE AND MODEL ANALYSIS

This part deals with the selection of both the material models to be used to define the two classes of composite materials to be analysed, namely an SMC type short fibre composite and a laminated composite, and the finite element crash simulation software package to be adopted as a simulation test.

The model selection has been undertaken in the following manner. Existing material models already present within both the software packages considered (PAM-CRASH and LS-DYNA see Section 2.3) were applied to a set of similar loading, initial and boundary conditions. The implementation and results of each of these simulations were then analysed and compared to explore any advantages and/or disadvantages that each may have over another. The actual processes of defining the required material parameters are considered of major significance, as well as the actual make-up of the model and the theory supporting it. The numerically obtained results are the final source of comparison.

The software selection is based on what is believed to be key elements for consideration. These include the selected material models as the obvious criteria, as well as ease of implementation, ease of use, and flexibility.

The two finite element analysis tools, PAM-CRASH and LS-DYNA, were evaluated using composite material models available within the software. It was attempted to maintain coherency in the two packages, by implementing similar geometric, loading, constraint and material conditions in each case. This, however, was not always possible, due to the differences between the packages with regards to choices available in load application, constraints and material definitions. In these instances either a “most similar” approach is used in each application, or if the two chosen approaches vary substantially, the results were related analytically using simplified approaches.

A series of both tensile and bending tests were simulated, at loading velocities of both 33mm/s and 330mm/s. Applied tests conditions are schematically shown on Fig. 3.1. For the tensile case, a plate of dimensions 150 x 100 x 5 mm was loaded by the application of a prescribed velocity, v at one end of the plate, while the other end was fixed in position. For the bending case, a prescribed constant velocity was applied to the centre of a plate of geometry identical to the tensile case, supported a third of the length from each end.

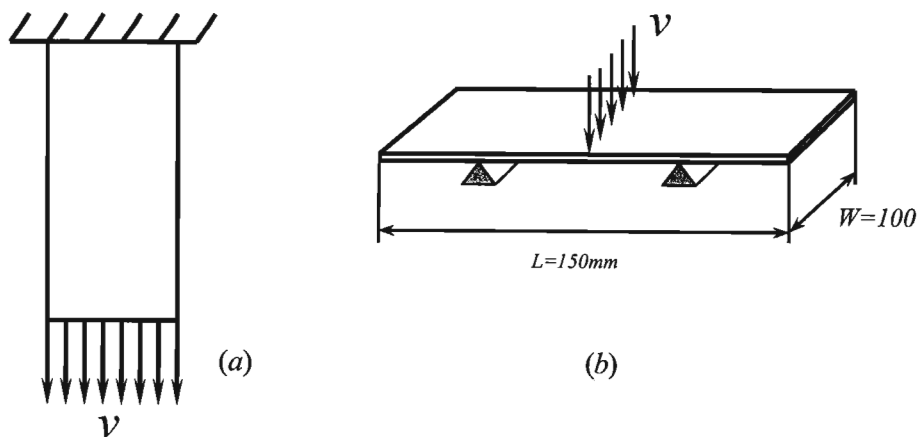


Fig. 3.1 Schematic tensile (a) and bending (b) set-up, v is the prescribed velocity.

3.1 SMC composites

The model, selected as representative of those currently available for SMC composite materials in the PAM-CRASH software, is an elastic-plastic material model incorporating isotropic progressive damage behaviour (see Section 2.3). The material is isotropic and is degraded using a damage mechanics law based on experimentally obtained results (plasticity is ignored for the purposes of SMC composite analysis). The undamaged material constitution is defined in terms of the material elastic modulus, mass density and ‘yield stress’ (interpreted for SMC composite analysis).

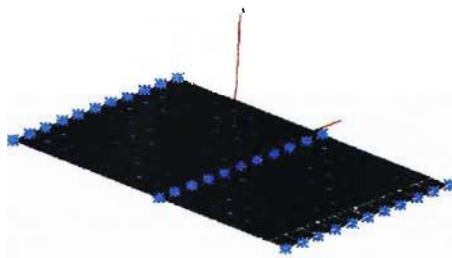
For simulation in LS-DYNA, due to the materials quasi-isotropic and non-linear behaviour under progressive crash, it was decided to employ an elastic-plastic material model incorporating kinematic hardening (as presented in Section 2.3). The material constitution is defined in terms of the material elastic modulus, mass density and ‘yield stress’ (interpreted for SMC composite analysis). These characteristics could be obtained from the experimental stress-strain curves plotted for tensile and compressive loading (see Section 2.3).

The plate under consideration is assumed to be made from the Glass-Epoxy SMC composite. Mechanical properties of the material are as follows: modulus of elasticity $E = 23.28$ GPa, Poisson’s ratio $\nu = 0.3$, density $\rho = 1.8$ g/sm³, ‘yield stress’ $\tilde{\sigma} = 465.6$ MPa, key strain points: $\varepsilon_i = 0.02$, $\varepsilon_1 = 0.06$, $\varepsilon_u = 0.09$, damage factors $d_l = 0.2$, $d_u = 0.9$.

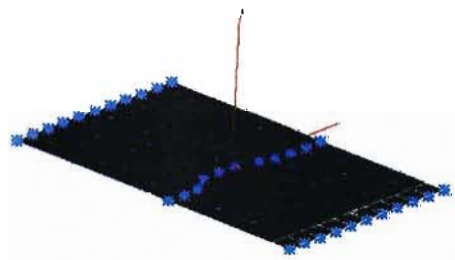
3.1.1 Tensile test simulation

Simulation results for the tensile testing, from each of the two software packages, were analysed and compared on the basis of the stress and strain, at the material elastic limit and at the maximum load carrying point.

Results obtained using PAM-CRASH are shown in the form of ‘‘Transmitted force in cross-section vs. Displacement in the direction of loading’’ graphs, as well as deformed meshes for certain cases (see Figs 3.2-3.4). The force and displacement values are taken at the point of application of the force, at the central node along the axis of loading.



a. $t = 0.00s$



b. $t = 0.72s$

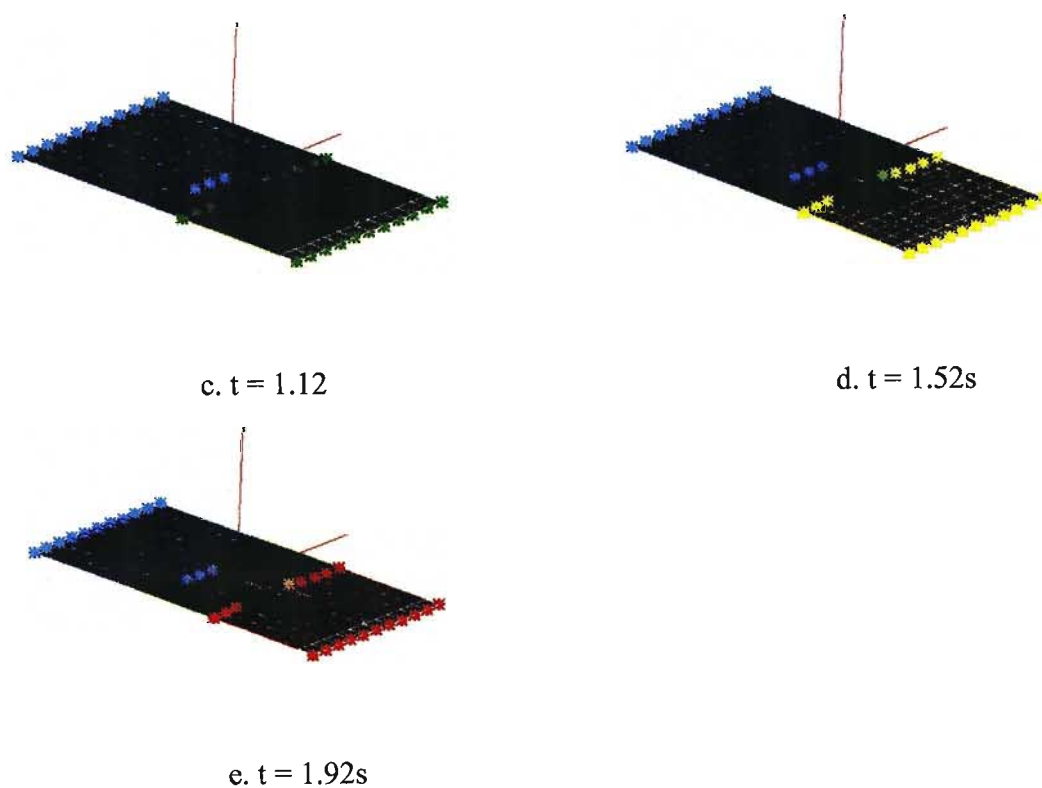


Fig. 3.2 Progressive deformation of SMC composite plate under tensile test at 33mm/s.

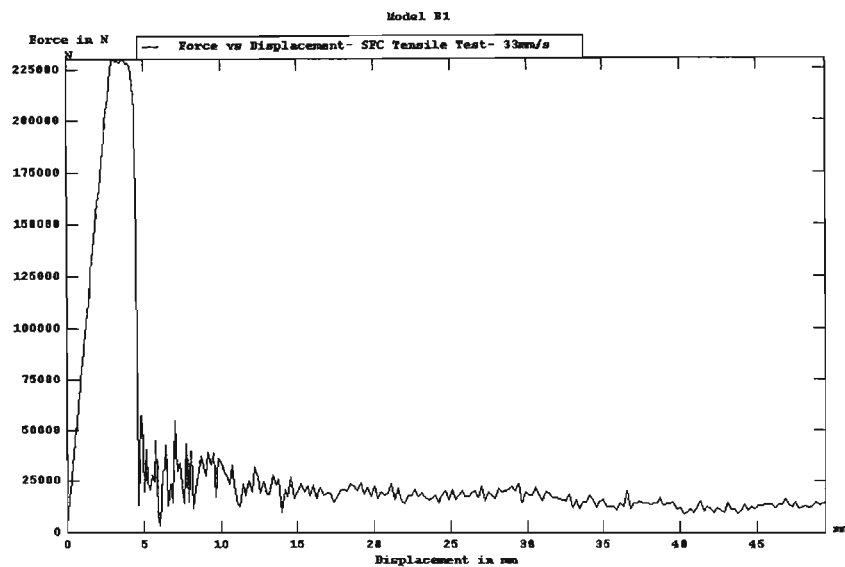


Fig. 3.3 Force-Displacement for PAM-CRASH simulation of SMC plate
using an applied constant velocity of 33mm/s

As shown in Fig. 3.3 the material is clearly elastic up to a load of 225 kN, and ultimate failure occurs at an elongation of 4.5 mm.

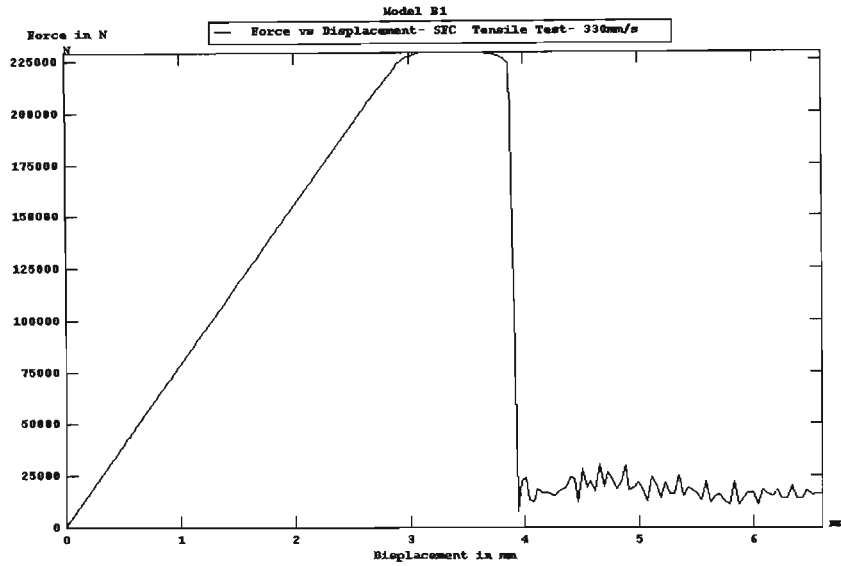


Fig. 3.4 Force-Displacement for PAM-CRASH simulation of SMC plate using an applied constant velocity of 330mm/s.

The plot presented in Fig. 3.4 fairly mirrors the previous one (Fig. 3.3), showing a similar trend as well as a similar maximum force point.

Note that in each case a residual force of $\approx 20\text{kN}$ remains, which is as a result of assigning an ultimate damage of less than 1 for the material (see Section 2.3 for an explanation of this parameter).

Simulation results obtained using LS-DYNA for the applied velocity of $v = 33 \text{ m/s}$ are shown in the form of stress and displacements distributions at the different moments of time (see Figs 3.5-3.8). The outputs were supplemented with Stress vs. Time and Displacement vs. Time curves plotted for selected nodes.

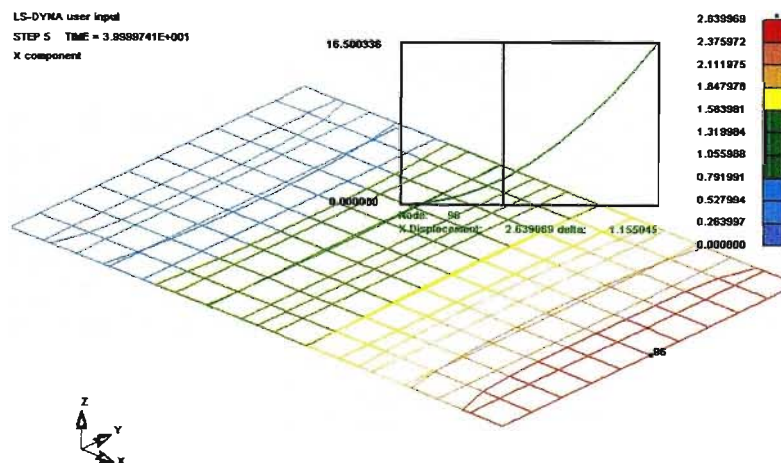


Fig. 3.5 Distribution of displacements in X direction corresponding to the limit of elasticity and Displacement vs. Time curve for node 96.

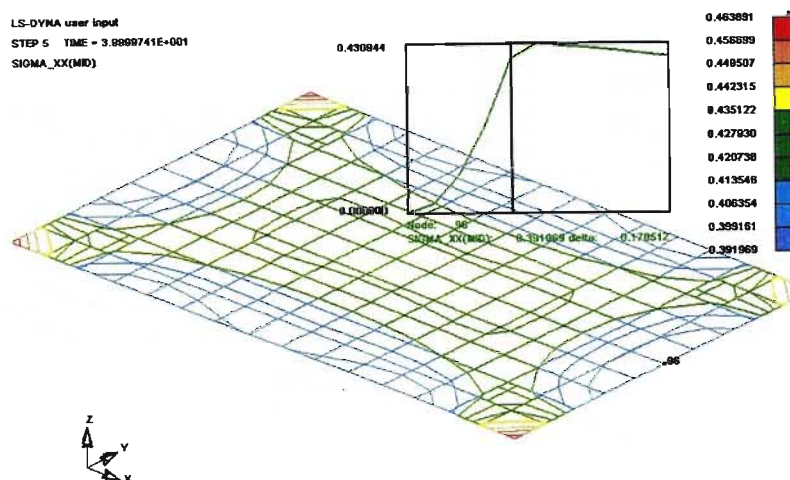


Fig. 3.6 Distribution of σ_x corresponding to the limit of elasticity and Stress vs. Time curve for node 96.

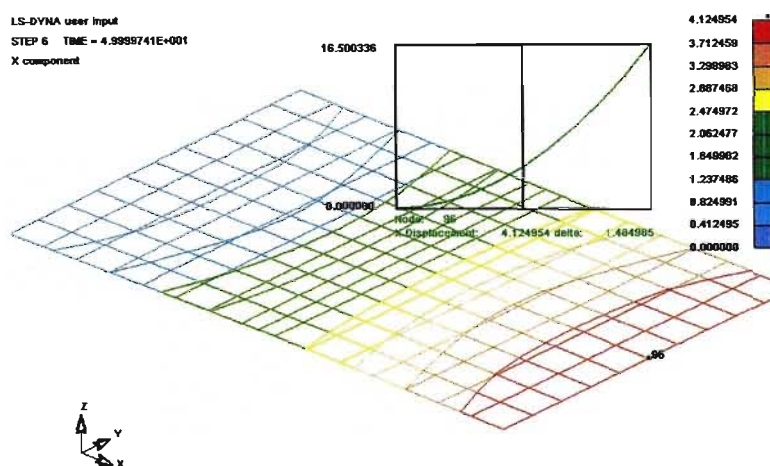


Fig. 3.7 Distribution of displacements in X direction corresponding to the maximum value of stress and Displacement vs. Time curve for node 96.

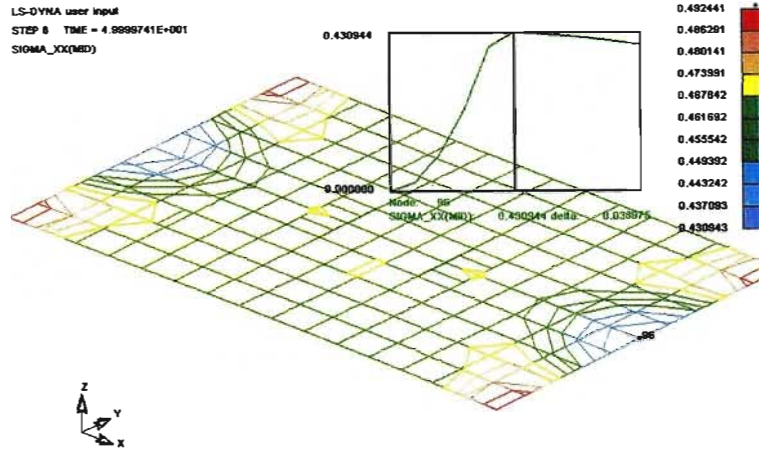


Fig. 3.8 Distribution of σ_x corresponding to the maximum value of stress and Stress vs. Time curve for node 96.

As shown in the plots presented above (see Fig. 3.5-3.6) the material follows an elastic law up to 0.039 sec. At this moment corresponding stress is $\sigma_x = 391$ MPa and displacement is 2.63 mm for node 96. Beyond this point the material behaviour is non-linear. A maximum stress of 430 MPa is shown in Fig. 3.8 (0.049 sec of simulation) and corresponding displacement is equal to 4.124 mm (see Fig. 3.7).

Displacement and stress distributions for a tensile test with applied velocity of 330 mm/s are shown in Figs 3.9-3.11.

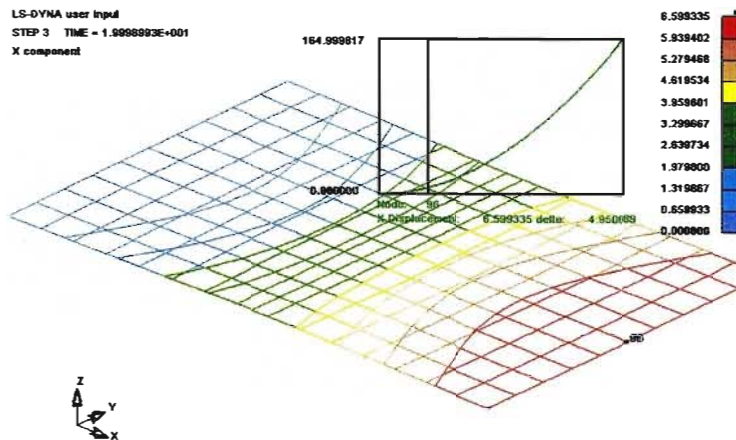


Fig. 3.9 Distribution of displacements in X direction corresponding to the maximum value of stress and Displacement vs. Time curve for node 96.

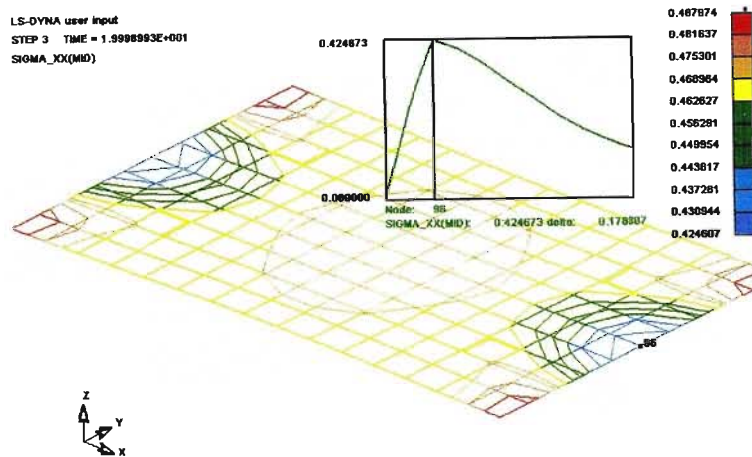


Fig. 3.10 Distribution of σ_x corresponding to the maximum value of stress and Stress vs. Time curve for node 96.

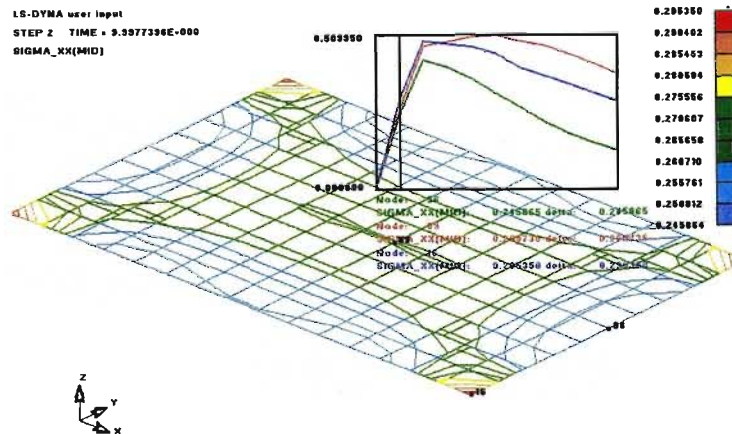


Fig. 3.11 Distribution of σ_x and Stress vs. Time curve for nodes 96, 89, 16.

In this case (applied velocity of 330 mm/s) the elasticity limit and maximum stress $\sigma_x = 424.6$ MPa are reached at 0.0199sec (see Fig. 3.10). As can be seen the corresponding displacement at this moment is equal to 3.34 mm (see Fig. 3.9). The stress distribution before the moment when the elastic limit is reached and Stress vs. Time curves for several nodes are shown in Fig. 3.11.

The two sets of results obtained in PAM-CRASH and LS-DYNA simulations are presented in different formats, due to the nature of the variables available for graphing in the two packages.

PAM-CRASH results for all cases are presented in the form of Force vs. Displacement plots, whereas Stress vs. Time were plotted in LS-DYNA. The compatible parameters have been calculated for each set of simulation outputs. The results are shown in Tables 3.1-3.2.

Table 3.1. Tensile test simulated results for SMC material (33 mm/s prescribed velocity).

Simulation results	Elastic limit (MPa)	Displacement at elastic limit (mm)	Maximum Stress (MPa)	Displacement at maximum stress (mm)
PAM-CRASH	457	3.20	460	4.00
LS-DYNA	391	2.63	430	4.12
% Deviation	14	18	7	3

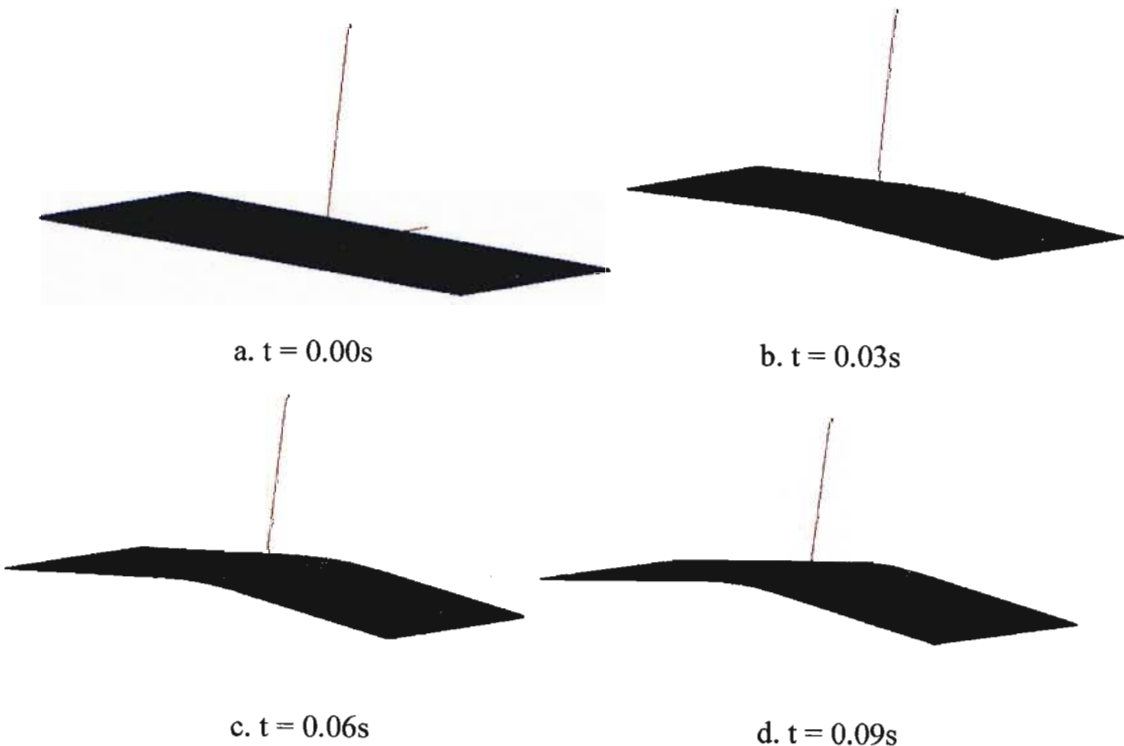
Table 3.2. Tensile test simulated results for SMC material (330 mm/s prescribed velocity).

Simulation results	Elastic limit (MPa)	Displacement at elastic limit (mm)	Maximum Stress (MPa)	Displacement at maximum stress (mm)
PAM-CRASH	442	2.85	456	3.50
LS-DYNA	424	3.34	424	3.34
% Deviation	4	17	7	5

The results show fairly good correlation, within 7% discrepancy for the maximum stress data point.

3.1.2 Bending test simulation

Results of bending test simulations using PAM-CRASH are shown in Figs 3.12-3.15



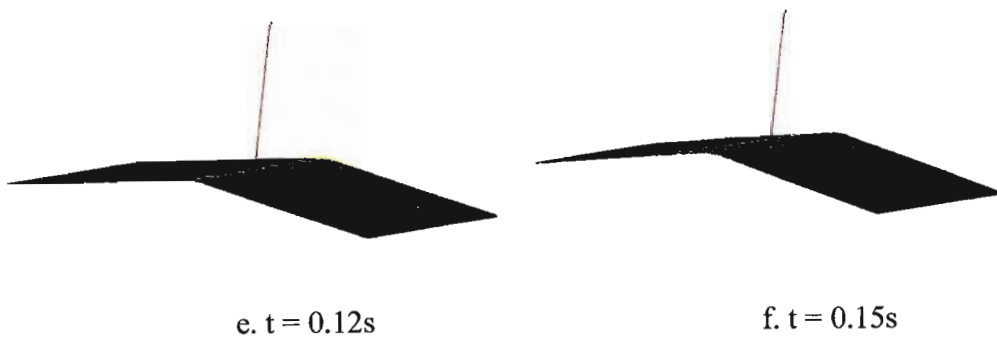


Fig. 3.12 Progressive deformation of SMC composite plate under bending test at 33mm/s (PAM-CRASH simulation).

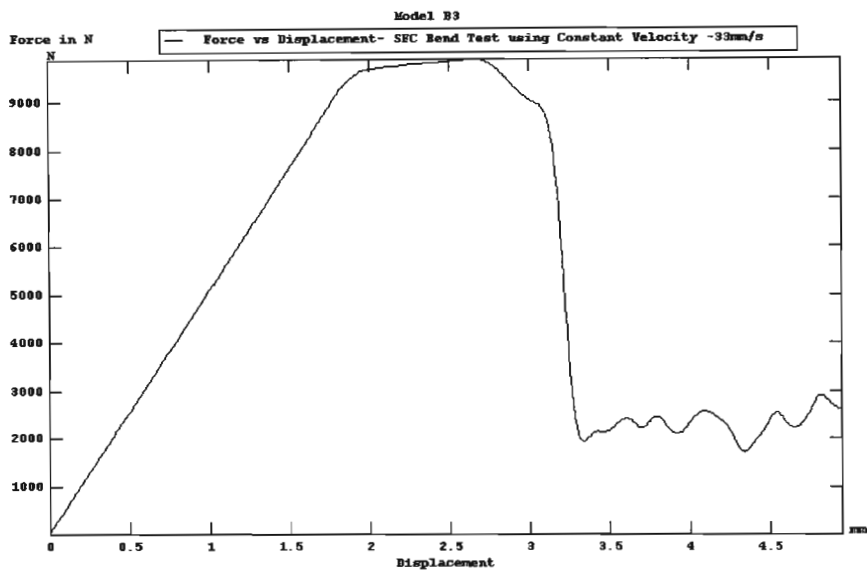
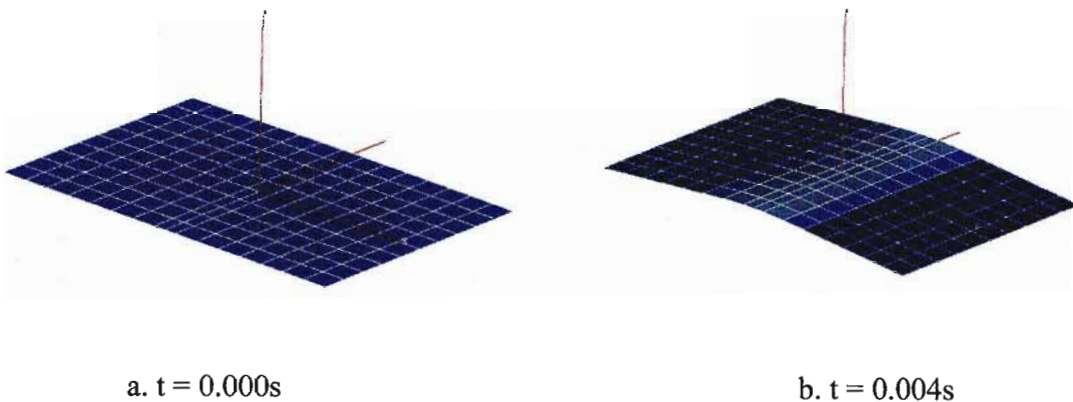


Fig. 3.13 Force-Displacement for PAM-CRASH simulation of SMC plate using a constant applied velocity of 33mm/s.

The plot presented in Fig. 3.13 shows the results for the 33mm/s bending test on SMC material. The maximum force is $\approx 10kN$ and corresponding deflection is $\approx 2.7mm$.



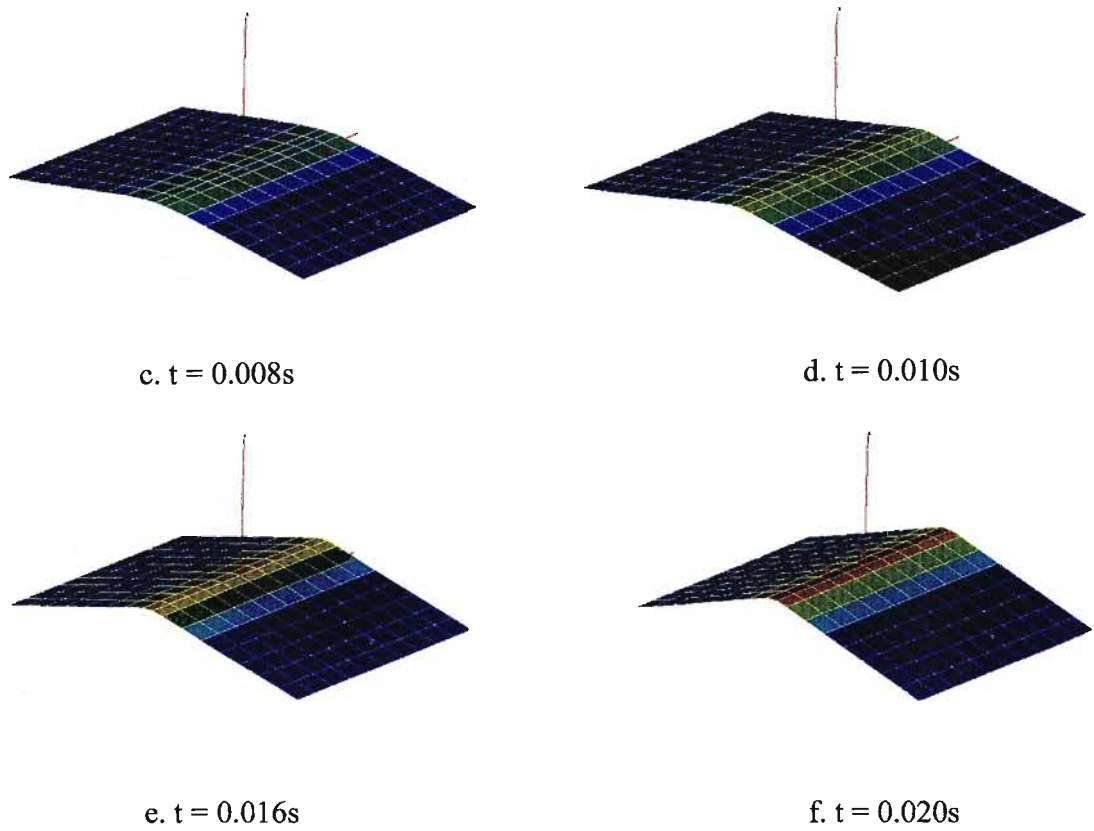


Fig. 3.14 Progressive deformation of SMC composite plate under bending test at 330mm/s (PAM-CRASH simulation)

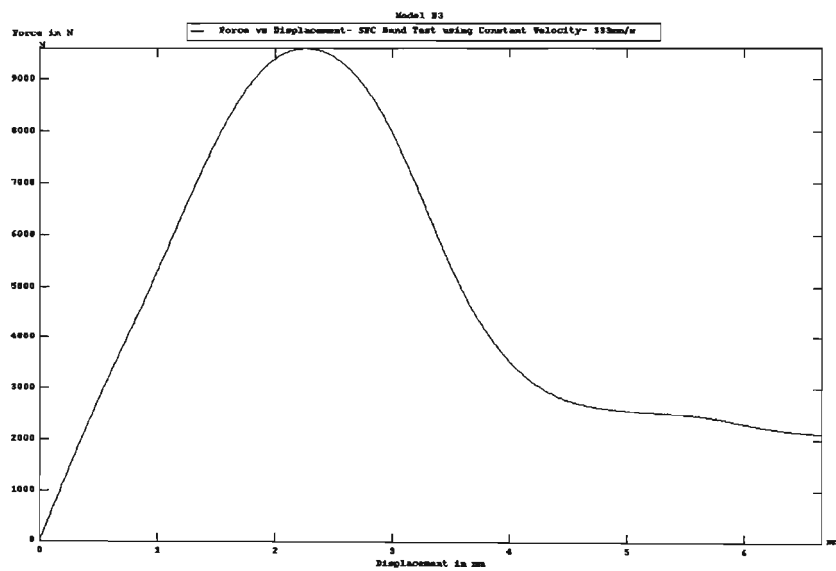


Fig. 3.15 Force-Displacement for PAM-CRASH simulation of SMC plate using a constant applied velocity of 330mm/s.

The plot presented in Fig. 3.15 shows the results for the 330mm/s bending test on the SMC material. The maximum force is $\approx 9.6\text{kN}$ and slightly lower than for previous test. The corresponding deflection is equal to $\approx 2.2\text{ mm}$.

The Displacement and Bending Moment vs. Time diagrams obtained from the LS-DYNA simulation are shown in Figs 3.16-3.19.

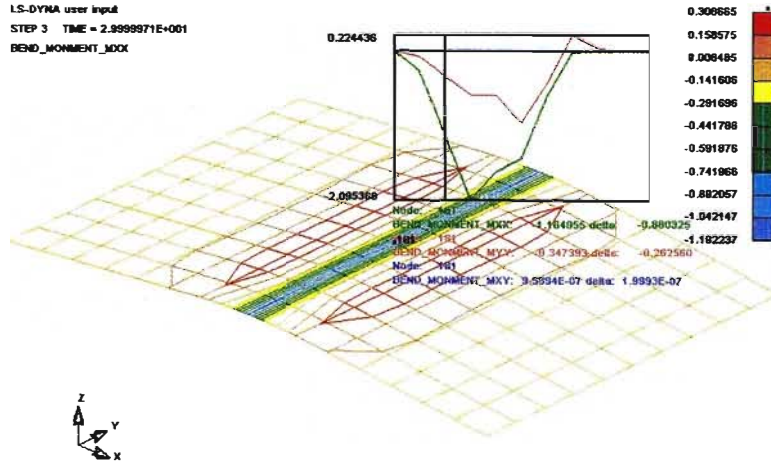


Fig. 3.16 Maximum Bending Moment (M_x) distribution and Moment vs. Time curves for node 181 (LS-DYNA simulation, applied velocity 33 mm/s).

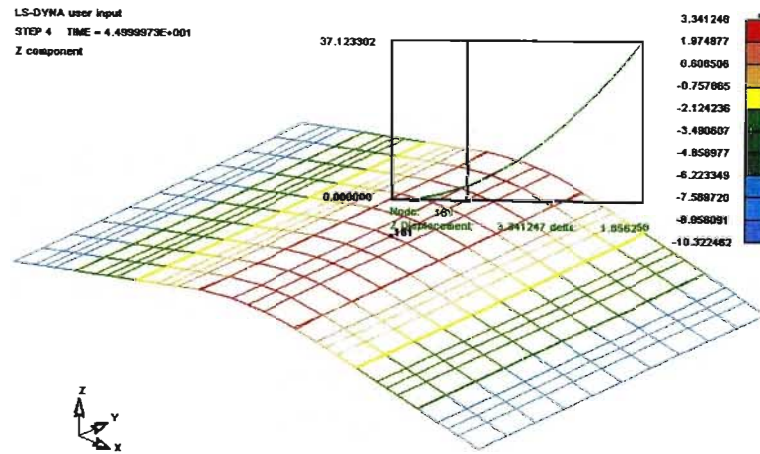


Fig. 3.17 Plate deflection distribution corresponding to the maximum bending moment and Displacement vs. Time curve for node 181 (LS-DYNA simulation, applied velocity 33 mm/s).

As shown, the maximum bending moment is equal to 2.095 kNmm and the corresponding displacement (deflection) is equal to 3.34 mm (see Fig. 3.16 and Fig. 3.17).

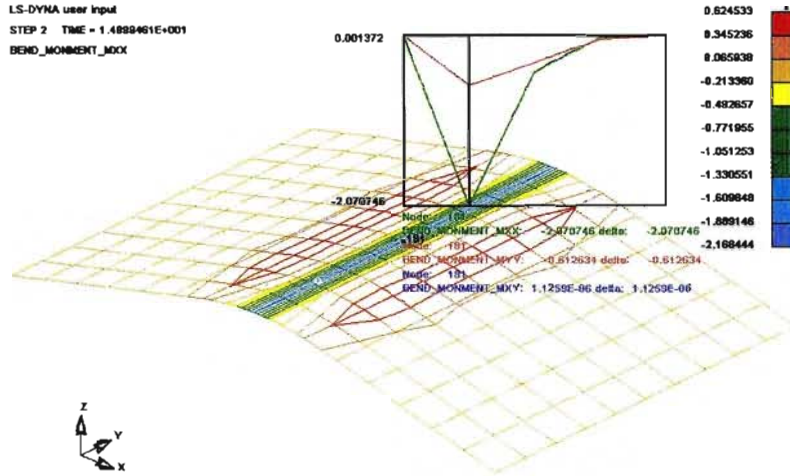


Fig. 3.18 Maximum Bending Moment (M_x) distribution and Moment vs. Time curves for node 181 (LS-DYNA simulation, applied velocity 330 mm/s).

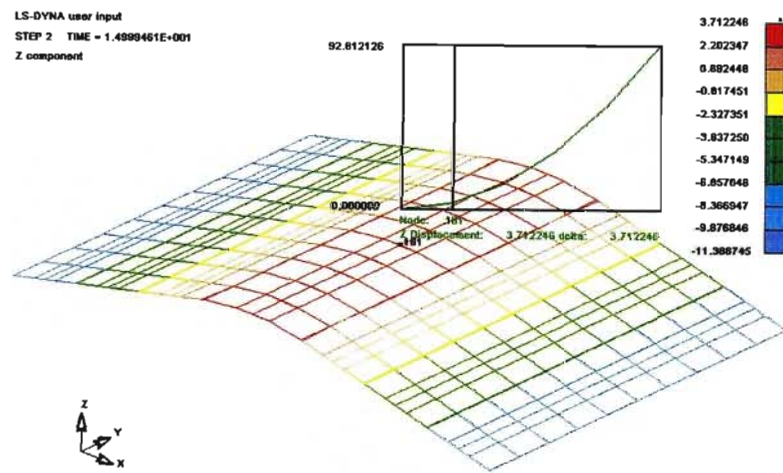


Fig. 3.19 Distribution of deflection corresponding to the maximum bending moment and Displacement vs. Time curve for node 181 (LS-DYNA simulation, applied velocity 330 mm/s).

As could be seen from the Moment vs. Time curve (Fig. 3.18) in this case the maximum bending moment of 2.07 kNmm is reached at 0.0149 s of simulation time and the corresponding displacement is equal to 3.71 mm (see Displacement vs. Time curve in Fig. 3.19).

Force displacement diagrams obtained from the bending test simulations with different velocities are shown in Figs 3.20-3.21. The bending test simulations showed a larger discrepancy, and it is in the comparison of the obtained force-displacement plots for the two models for this loading condition, that the effect of the incorporation of a progressive damage law is clearly seen.

SMC Composite Bending Test Simulation (33mm/s)

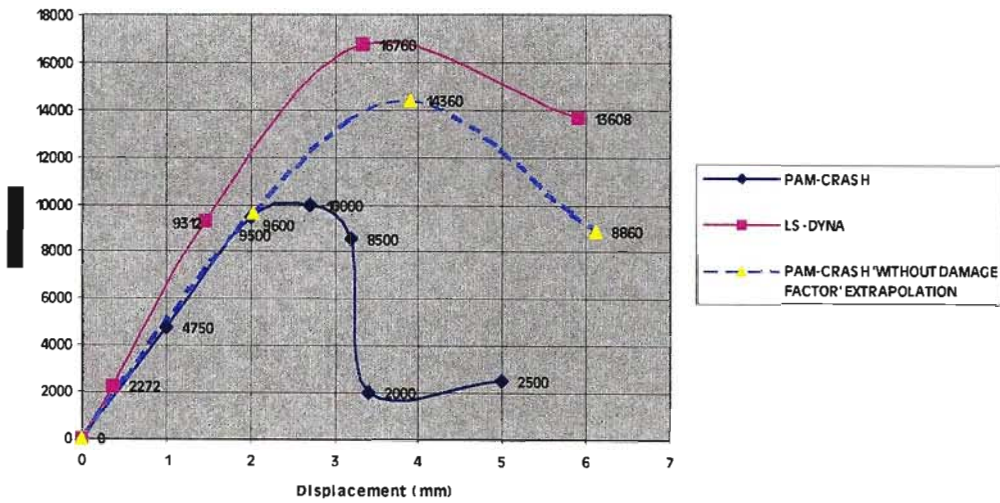


Fig. 3.20 Bending test simulation results (33mm/s).

SMC Composite Bending Test Simulation (330mm/s)

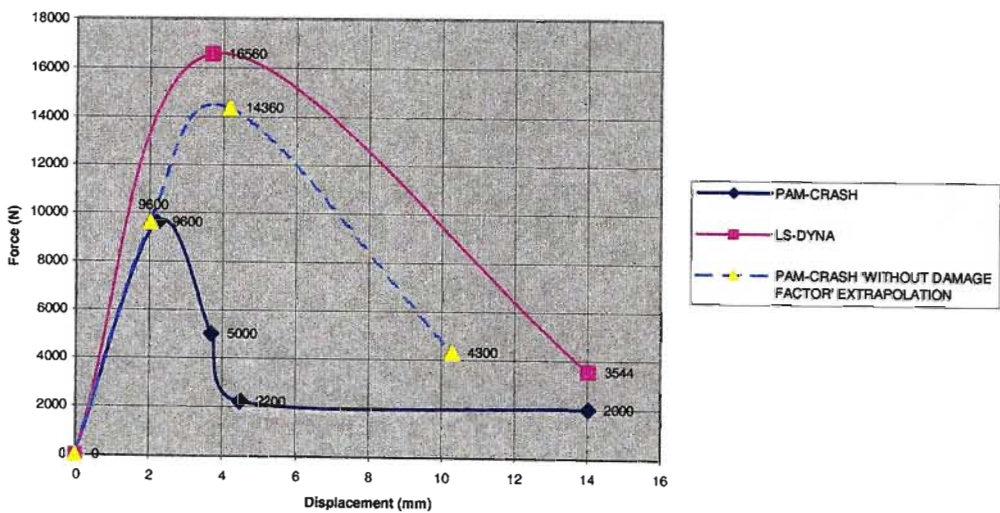


Fig. 3.21 Bending test simulation results (330mm/s).

The two sets of results show a large discrepancy at the maximum stress point, and so comparative curves are shown, estimated using a few points taken from the respective plots in PAM-CRASH and LS-DYNA (see Fig. 3.21). The trend of the two curves is similar, when it is noted that the LS-DYNA plot has to be approximated using fewer points due to restrictions placed on the time-step by long simulation times. A third plot (shown with dashed line) is included to emphasise the effect of the input damage variables on the output of the PAM-CRASH simulation. As explained in Section 2.3, the damage variable degrades the value of the modulus of the material, which serves to decrease the maximum bending moment, as now can clearly be seen. Without these damage variables, which were rather arbitrarily chosen for the SMC composite material, the two plots would follow very similar trends. The value of the maximum bending moment would be increased without the effect of damaging the material, and the degradation of the material would prove to be gradual, as in the LS-DYNA case.

As can be seen, the deviation is attributed to the effect of the damage law implemented in PAM-CRASH, which is not accounted for in LS-DYNA. LS-DYNA therefore over-predicts the material strength and does not take into account true composite behaviour. A third plot (shown with dashed line), roughly estimating the removal of the influence of the user-input damage law shows the good correlation of the two simulations if not for the additional damage law implemented in PAM-CRASH.

The difference between the modelling of the material is evident from the comparative plots. Whereas in PAM-CRASH damage law governs the material degradation, only plasticity effects govern the LS-DYNA model. This explains the gradual drop-off in the LS-DYNA material, as compared to the quick degradation in the PAM-CRASH case, corresponding to the points of intermediate material failure. A third plot is included above showing the curve corresponding to a PAM-CRASH simulation without implementation of the damage law. This shows the conformance of the results of the basic modelling in the two packages, and the effect of the incorporation of the damage law.

Numerical experimentation suggests that composite materials behave as depicted by the PAM-CRASH simulation, with definite progressive failure of the constituents evident, resulting in a truncated force-displacement curve. This truncation is controlled in the simulation by the input of experimentally obtained damage coefficients, which define the shape of the material stress-strain curve by reducing the material modulus. For practical implementation of these results, physical experimentation should be performed to characterise the SMC material fully, and for the results verification.

3.2 Laminates

The tensile and bending test simulations have been carried on for the laminated composite plate with the following structure: $[0^\circ / \pm 60^\circ / 0^\circ]$.

The PAM-CRASH simulation was performed using Bi-Phase and Composite Global Ply Models (see Section 2.3). The Chang-Chang model was selected for the LS-DYNA modelling and simulation (see Section 2.3).

The following material properties were used as required for input into the PAM-CRASH Bi-Phase model (see Section 2.3):

Density:	$2.1e^{-9} \text{ t/mm}^3$
Lay-up:	$[0^\circ/+60^\circ/-60^\circ/0^\circ]$
Ply thickness:	1.25mm

Matrix properties:

 $E_1=E_2=E_3:$ 2400 MPa $G_{12}=G_{23}=G_{13}:$ 60 MPa $\nu_{12}=\nu_{23}=\nu_{13}:$ 0.3

Tensile damage

 $\varepsilon_i:$ 0.0032 $\varepsilon_f:$ 0.0033 $d_f:$ 0.001 $\varepsilon_u:$ 0.0034 $d_u:$ 0.999

Compressive damage

 $\varepsilon_i:$ 0.0079 $\varepsilon_f:$ 0.0080 $d_f:$ 0.001 $\varepsilon_u:$ 0.0081 $d_u:$ 0.999

Shear damage

 $\varepsilon_i:$ 0.0080 $\varepsilon_f:$ 0.0433 $d_f:$ 0.585 $\varepsilon_u:$ 0.0434 $d_u:$ 0.999

Fibre properties:

Young's modulus: $60e^3$ MPa

Fibre volume ratio: 0.65

Tensile damage

 $\varepsilon_i:$ 0.0290 $\varepsilon_f:$ 0.0300 $d_f:$ 0.001 $\varepsilon_u:$ 0.0310 $d_u:$ 0.999

Compressive damage

 $\varepsilon_i:$ 0.0090 $\varepsilon_f:$ 0.0140 $d_f:$ 0.202 $\varepsilon_u:$ 0.0141 $d_u:$ 0.999

The characteristics of the Bi-Phase material were theoretically defined, based on a glass-epoxy type material, with properties mirrored in LS-DYNA's Chang-Chang Model for comparison.

In case of the plate simulation based on Global Ply Model the material (Glass-Epoxy Unidirectional Composite) has the following characteristics:

(as required for input into the PAM-CRASH Global Ply Model)

Mass density: 1620 kg/m³

Lay-up: [0°/+60°/-60°/0°]

Ply thickness: 1.25mm

Young's modulus in fibre direction: 22753 MPa

Young's modulus transverse to fibres: 1955 MPa

Shear modulus:	6487 MPa
Poisson's ratio:	0.23
Critical Shear Damage Limit:	1.924
Initial Shear Damage Limit:	0.189
Critical Transverse Damage Limit:	1.935
Initial Transverse Damage Limit:	0.375
Coupling Factor:	1.672
Brittle Transverse Damage Limit of Interface:	0.181
Elementary Shear Damage Fracture Limit:	0.618
Maximum Shear Damage:	0.999
Fibre Critical Fracture Limit Strain:	0.021

(For an explanation of these damage variables, refer to Section 2.3)

The above data was obtained from (Coutellier and Rozycki, 2000), rather than being obtained through original experimentation on the same chosen material analysed using the Bi-Phase model. As a result the Bi-Phase and Global Ply materials do not replica each other, which of course does not allow for direct comparison. Trend comparison and analytical analysis may however be carried out. The properties were however mirrored in LS-DYNA, which facilitated comparison between the Chang-Chang Model and the Global Ply Model.

The Chang-Chang Composite Failure model of LS-DYNA was used to simulate the behaviour of laminated plate. The analyses were performed for two different sets of material parameters, namely:

(1) Model material (to compare results with PAM-CRASH Bi-Phase Model simulation)

The properties of unidirectional material required for LS-DYNA analysis were taken as:

Mass density:	2.1e-9 t/mm ³
Lay-up:	[0° /± 60° / 0°]
Thickness of the ply:	1.25 mm per ply

Young's modulus in *a*-direction (E_1): 40e3 MPa

Young's modulus in *b*-direction (E_2): 7535 MPa

Young's modulus in *c*-direction (E_3): 7535 MPa

Poisson ratio, *ba* (ν_{21}): 0.3

Poisson ratio, *ca* (ν_{31}): 0.3

Poisson ratio, *cb* (ν_{32}): 0.3

Shear modulus, *ab* (G_{12}): 170 MPa

Shear modulus, bc (G_{23}):	170 MPa
Shear modulus, ca (G_{31}):	170 MPa
Shear strength, ab -plane:	45 MPa
Longitudinal tensile strength:	1750 MPa
Transverse tensile strength:	90 MPa
Transverse compressive strength:	40 MPa
Non-linear shear stress parameter (α):	$2.57e-5$

These characteristics could be obtained from stress-strain curves for the unidirectional composite material under tensile and compressive loading.

(2) Glass-Epoxy laminated composite (to compare results with PAM-CRASH Global Ply

Model simulation)

The properties of unidirectional material required for LS-DYNA analysis are:

Mass density:	$1.62e-9$ t/mm ³
Lay-up:	$[0^\circ / \pm 60^\circ / 0^\circ]$
Thickness of ply:	1.25 mm

Young's modulus in a -direction (E_1):	$22.75e3$ MPa
Young's modulus in b -direction (E_2):	1955 MPa
Young's modulus in c -direction (E_3):	1955 MPa

Poisson ratio, ba (ν_{21}):	0.23
Poisson ratio, ca (ν_{31}):	0.23
Poisson ratio, cb (ν_{32}):	0.23

Shear modulus, ab (G_{12}):	6487 MPa
Shear modulus, bc (G_{23}):	6487 MPa
Shear modulus, ca (G_{31}):	6487 MPa

Shear strength, ab -plane:	80 MPa
Longitudinal tensile strength:	1478.9 MPa
Transverse tensile strength:	50 MPa
Transverse compressive strength (α):	20 MPa

These characteristics could be obtained from experimental stress-strain curves for the unidirectional composite material under tensile and compressing loading, and shear.

3.2.1 Tensile test simulation

Progressive deformation of the laminated plate under tensile loading (applied velocity 33 mm/s) obtained from the simulation based on the implementation of Bi-Phase Model is shown in Fig. 3.22. The corresponding Force-Displacement diagram is presented in Fig. 3.23. As shown, the simulation yields a maximum force of $\approx 280\text{kN}$ at a displacement of $\approx 4.5\text{ mm}$.

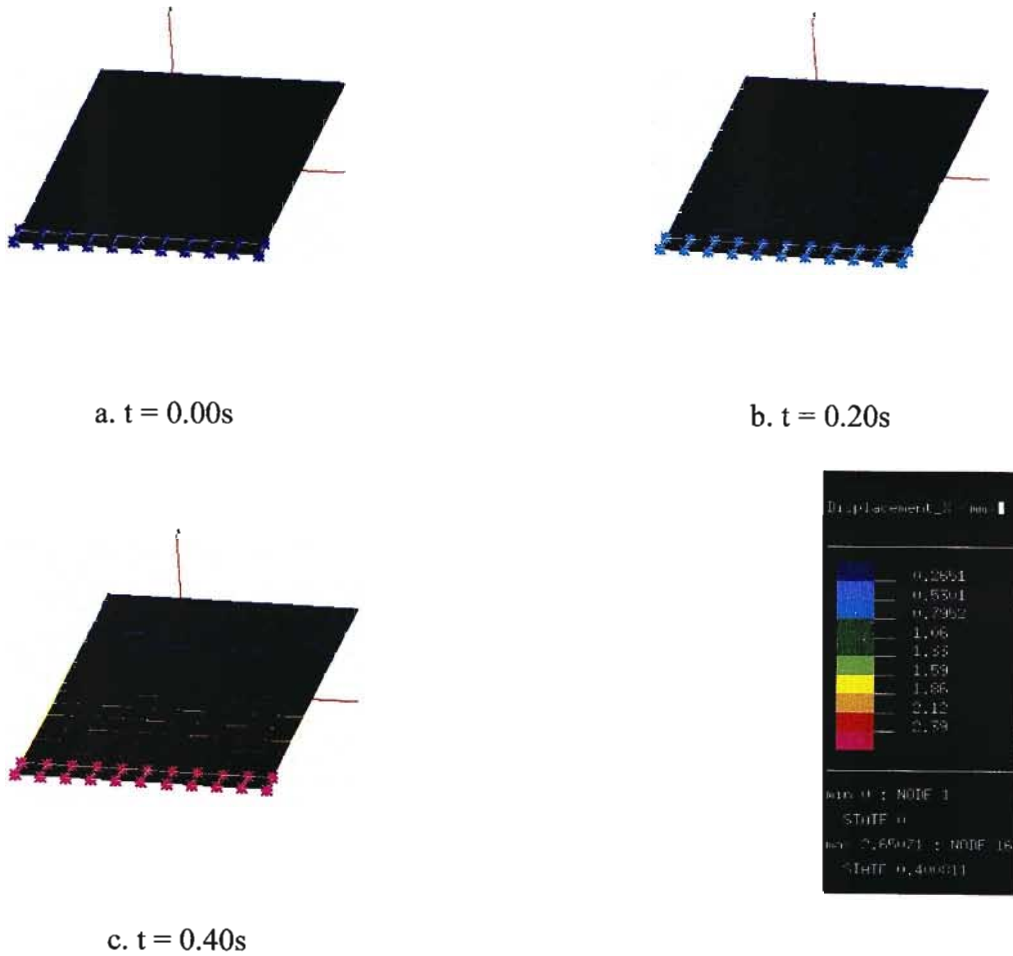


Fig. 3.22 Progressive deformation of laminated plate under tensile test at 33mm/s (PAM-CRASH, Bi-Phase Model).

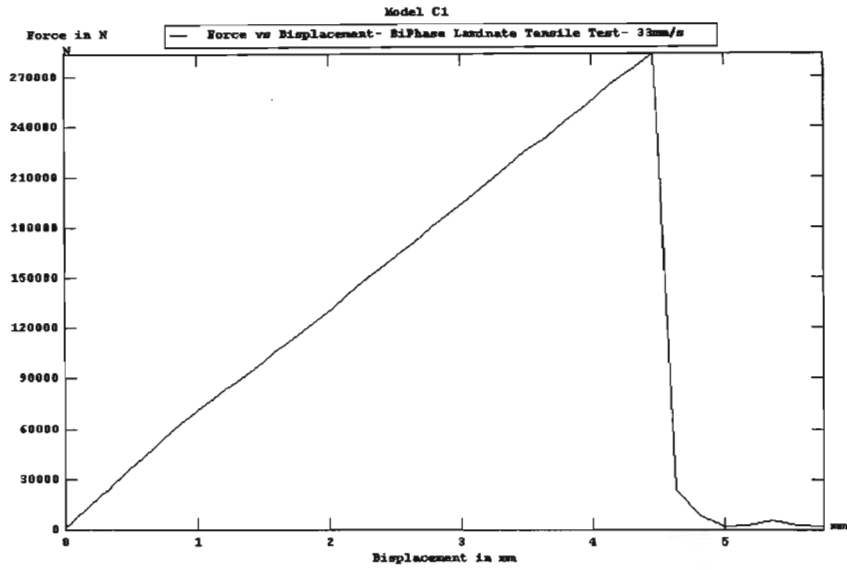


Fig. 3.23 Force-Displacement curve for tensile simulation using a constant velocity of 33mm/s (PAM-CRASH, Bi-Phase Model).

Progressive deformation of the laminated plate under velocity of 330 mm/s is shown in Fig. 3.24.

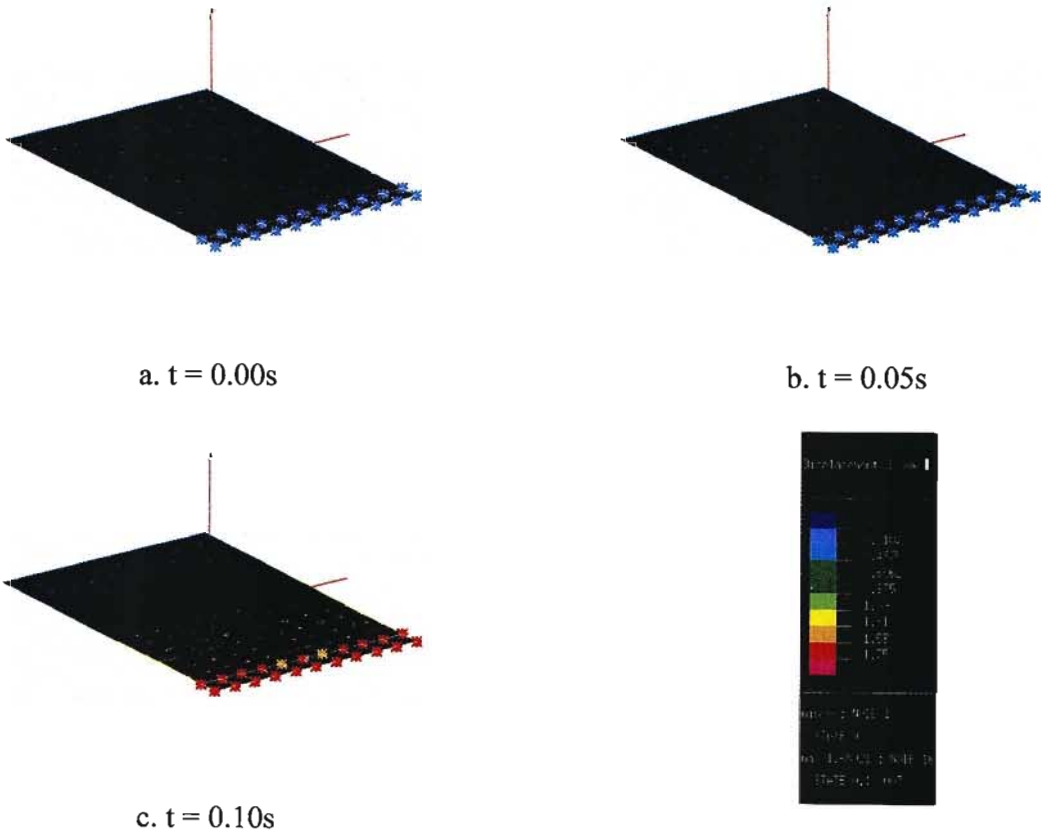


Fig. 3.24 Progressive deformation of laminated plate under tensile test at 330mm/s (PAM-CRASH, Bi-Phase Model).

Force-Displacement diagram obtained from the PAM-CRASH tensile simulation based on Global Ply Model is shown in Fig 3.25 (applied velocity is 33 mm/s). As shown the maximum force experienced for the Global Ply material tensile test at 33 mm/s is 15.5kN at a displacement of 0.45 mm.

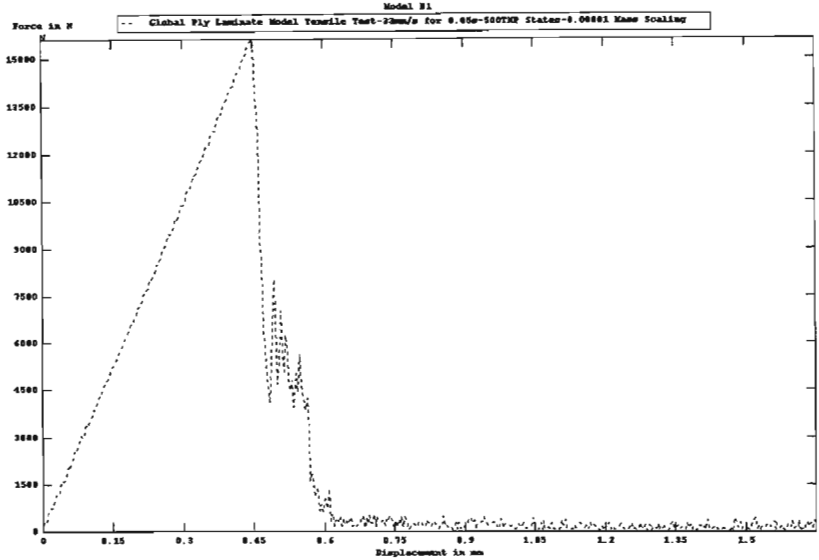


Fig. 3.25 Force-Displacement diagram for the tensile test simulation based on PAM-CRASH Global Ply Model (applied velocity is 33mm/s).

Results of LS-DYNA analysis are shown in the form of stress and displacements distributions at the different moments of time and Stress vs. Time, Displacement vs. Time curves. Simulations have been based on implementation of Chang-Chang Model and were performed for the two types of materials: Model material and the Glass-Epoxy laminated composite as discussed above.

Numerical results obtained from the tensile test simulations for the plate made from the Model material under velocity of 33 mm/s are shown in Figs 3.26-3.28.

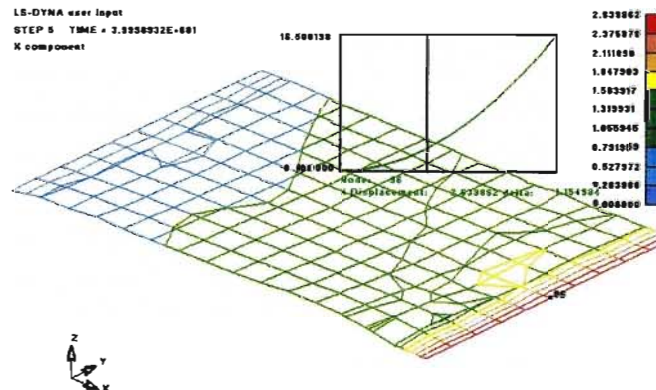


Fig. 3.26 Distribution of displacements in X direction corresponding to the maximum value of stress and Displacement vs. Time curve for node 96 (LS-DYNA simulation, Model material).

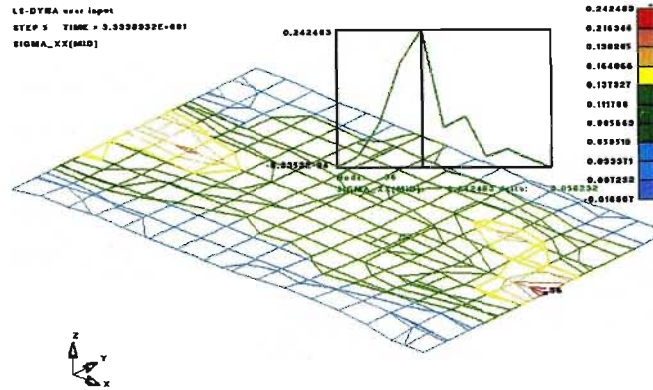


Fig. 3.27 Distribution of σ_x corresponding to the maximum value of stress and Stress vs. Time curve for node 96 (LS-DYNA simulation, Model material).

As shown in Fig. 3.27 the maximum value of stress 242 MPa is reached at the moment of 0.033 sec. The corresponding displacement is equal to 2.63 mm (see Fig. 3.26). The stress distribution in the plate at the moment of failure is shown in Fig. 3.28.

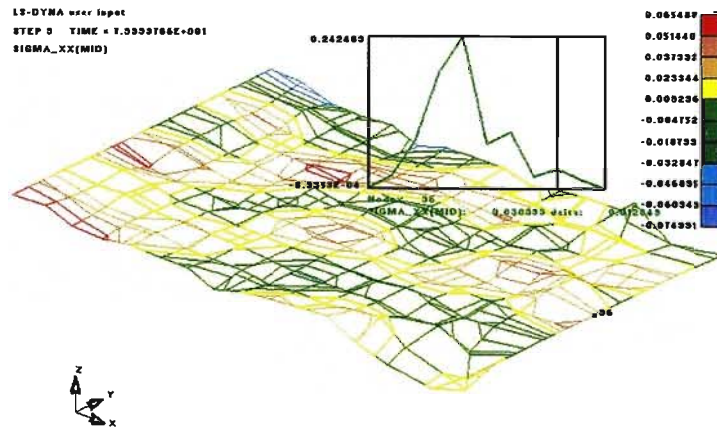


Fig. 3.28 Distribution of σ_x corresponding to the moment of material failure and Stress vs. Time curve for node 96 (LS-DYNA simulation, Model material).

Simulation results obtained for the tensile tests with the velocity of prescribed motion of 330 mm/s are shown in Figs 3.29-3.31.

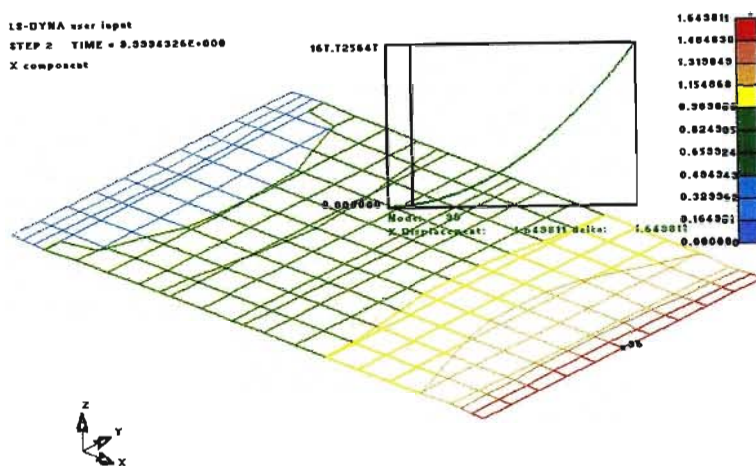


Fig. 3.29 Distribution of displacements in X direction corresponding to the maximum value of stress and Displacement vs. Time curve for node 96.
(LS-DYNA simulation, $v = 330$ m/s, Model material)

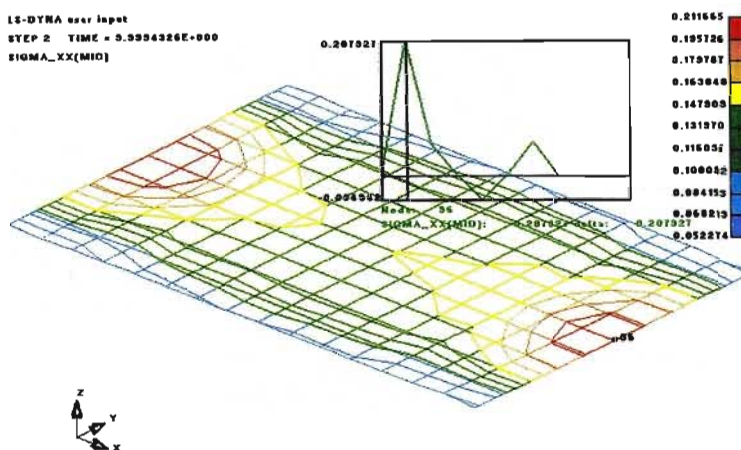


Fig. 3.30 Distribution of σ_x corresponding to the maximum value of stress and Stress vs. Time curve for node 96 (LS-DYNA simulation, $v = 330$ m/s, Model material).

As can be seen the maximum stress in this case takes place at 0.003999 sec. The value of this stress for node 96 (which is situated at the loaded edge) is equal to 207 MPa. Corresponding displacement at this moment is 1.64 mm. Stress distribution at the moment of material failure is shown in Fig. 3.31.

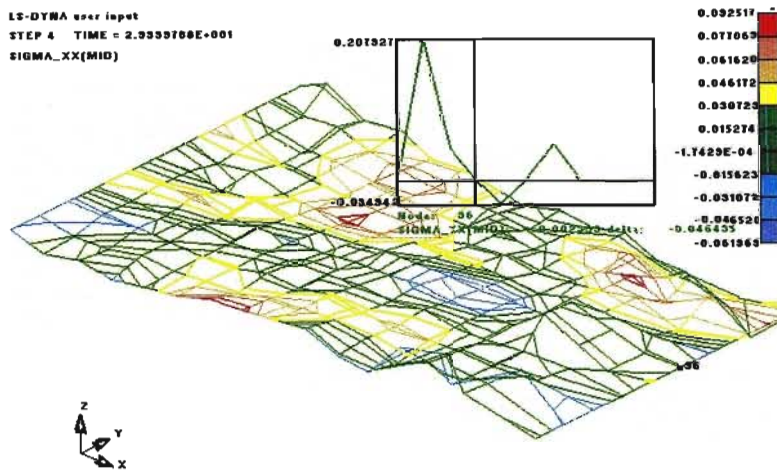


Fig. 3.31 Distribution of σ_x corresponding to the moment of material failure and Stress vs. Time curve for node 96 (LS-DYNA simulation, $v = 330$ m/s, Model material).

Numerical results obtained from the tensile test simulations for the plate made from the Glass-Epoxy laminated composite under prescribed velocity of 33 mm/s are shown in Figs 3.32-3.34.

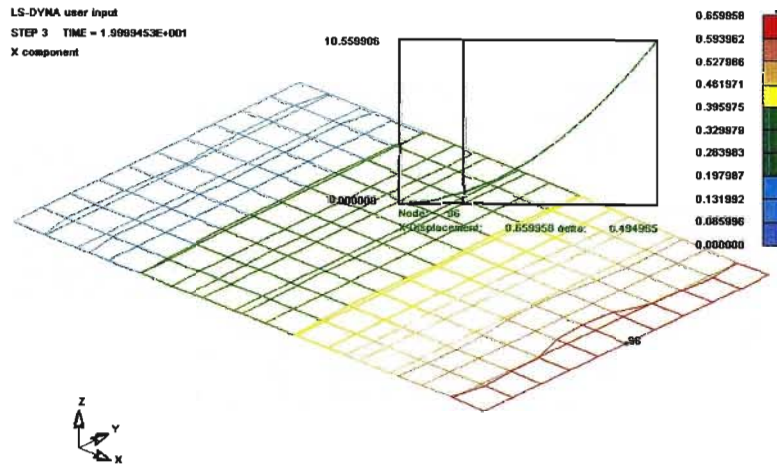


Fig. 3.32 Distribution of displacements in X direction corresponding to the maximum value of stress and Displacement vs. Time curve for node 96 (LS-DYNA simulation, $v = 33$ m/s, Glass-Epoxy composite).

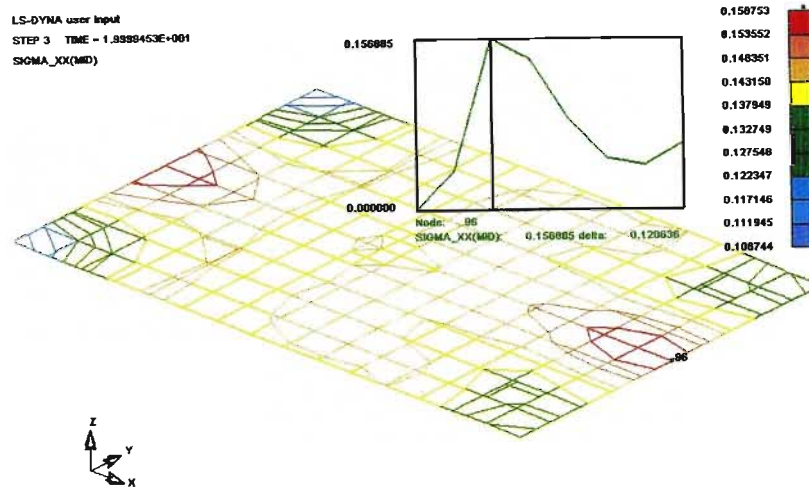


Fig. 3.33 Distribution of σ_x corresponding to the maximum value of stress and Stress vs. Time curve for node 96 (LS-DYNA simulation, $v = 33$ m/s, Glass-Epoxy composite)..

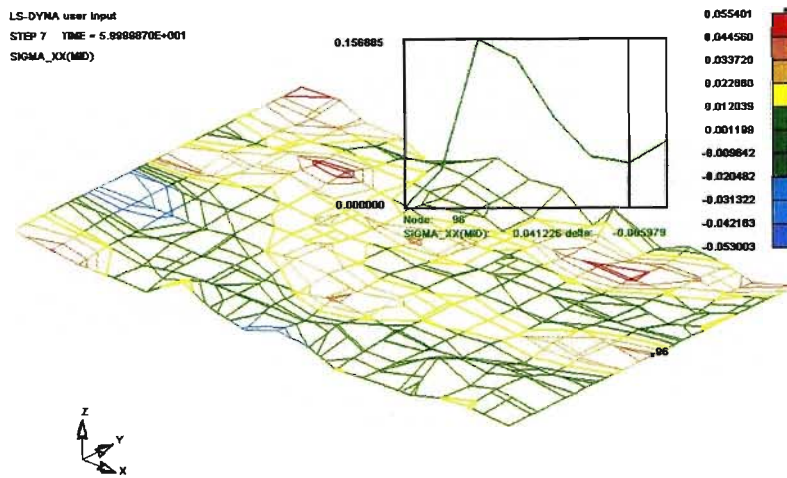


Fig. 3.34 Distribution of σ_x corresponding to the moment of material failure and Stress vs. Time curve for node 96 (LS-DYNA simulation, $v = 33$ m/s, Glass-Epoxy composite).

As shown (see Fig. 3.33) the stress reaches its maximum value of 156 MPa at the moment 0.019 sec and corresponding displacement is equal to 0.65 mm (see Displacement vs. Time curve, Fig. 3.32). The stress distribution in the plate at the moment of failure is shown in Fig. 3.34.

Simulation results for the same plate (Glass-Epoxy laminate) obtained for the prescribed velocity of 330 mm/s are presented in Figs 3.35 -3.37.

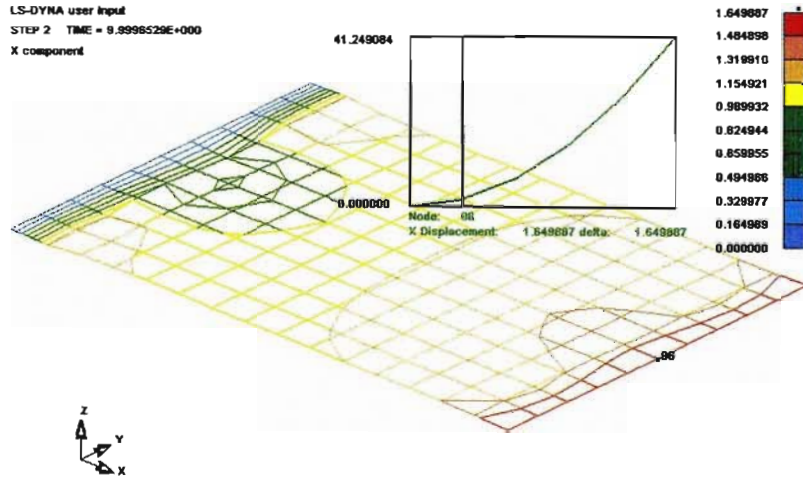


Fig. 3.35 Distribution of displacements in X direction corresponding to the maximum value of stress and Displacement vs. Time curve for node 96 (LS-DYNA simulation, $v = 330$ m/s, Glass-Epoxy composite).

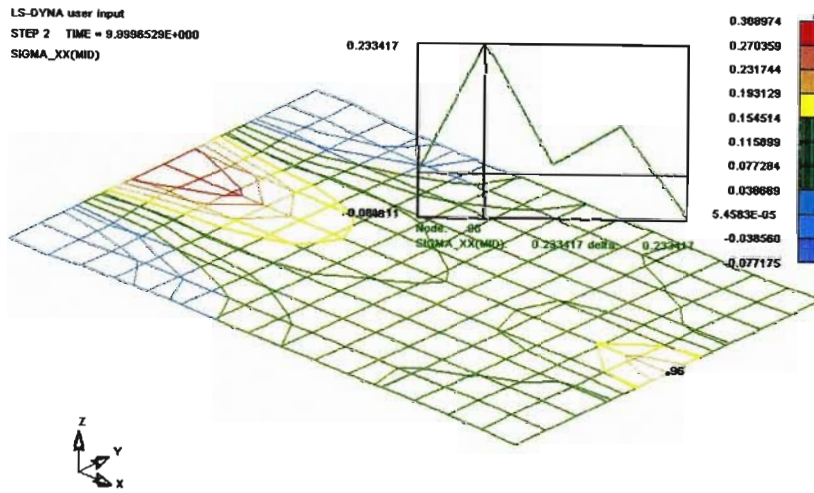


Fig. 3.36 Distribution of σ_x corresponding to the maximum value of stress and Stress vs. Time curve for node 96 (LS-DYNA simulation, $v = 330$ m/s, Glass-Epoxy composite).

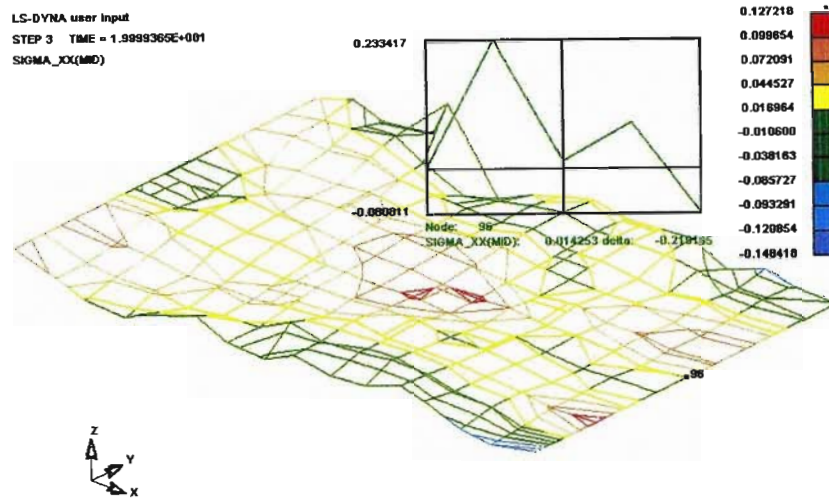


Fig. 3.37 Distribution of σ_x corresponding to the moment of material failure and Stress vs. Time curve for node 96 (LS-DYNA simulation, $v = 330$ m/s, Glass-Epoxy composite).

The displacement distribution for a tensile test with applied velocity of 330 mm/s at the moment of time 0.009 sec and the displacement vs. time curve are shown in Fig. 3.35. The stress distribution at the same moment of time and the stress vs. time curve for node 96 are presented in Fig. 3.36. As can be seen the stress reaches its maximum value of 233 MPa for node 96 at 0.009 sec of simulation. The corresponding displacement is 1.64 mm. The stress distribution in the plate at the moment of failure is shown in Fig. 3.37.

The Bi-Phase material comparison shows a discrepancy of approximately 2 times less for the LS-DYNA model (see Table 3.3). This discrepancy probably results from the formulation of the material parameters, which require some manipulation in the case of the PAM-CRASH definition. The damage parameters and stress-strain nature of the constituents in the Bi-Phase model could easily result in large errors, due to errors from parameter definition. The microscopic nature of the model, which requires estimates of the fibre and matrix behaviour as separate parameters, exposes the model to a large possibility of inaccuracy. The assumptions of damage taking on the behaviour of the fibres in the fibre direction and of the matrix in the direction transverse to the fibres, for example, might be less reasonable for the material considered than might be suggested.

Conversely the LS-DYNA model, which is much simpler, and more general, in formulation could possibly be disregarding these effects, and under predicting the strength of the material by failing either the matrix or fibre phase prematurely along with the other.

Table 3.3. Tensile test simulated results for Bi-Phase model of laminate material (33 mm/s prescribed velocity).

Simulation results	Elastic limit (MPa)	Displacement at elastic limit (mm)	Maximum Stress (MPa)	Displacement at maximum stress (mm)
PAM-CRASH	560	4.5	560	4.5
LS-DYNA	242	2.63	242	2.63
% Deviation	57	42	57	42

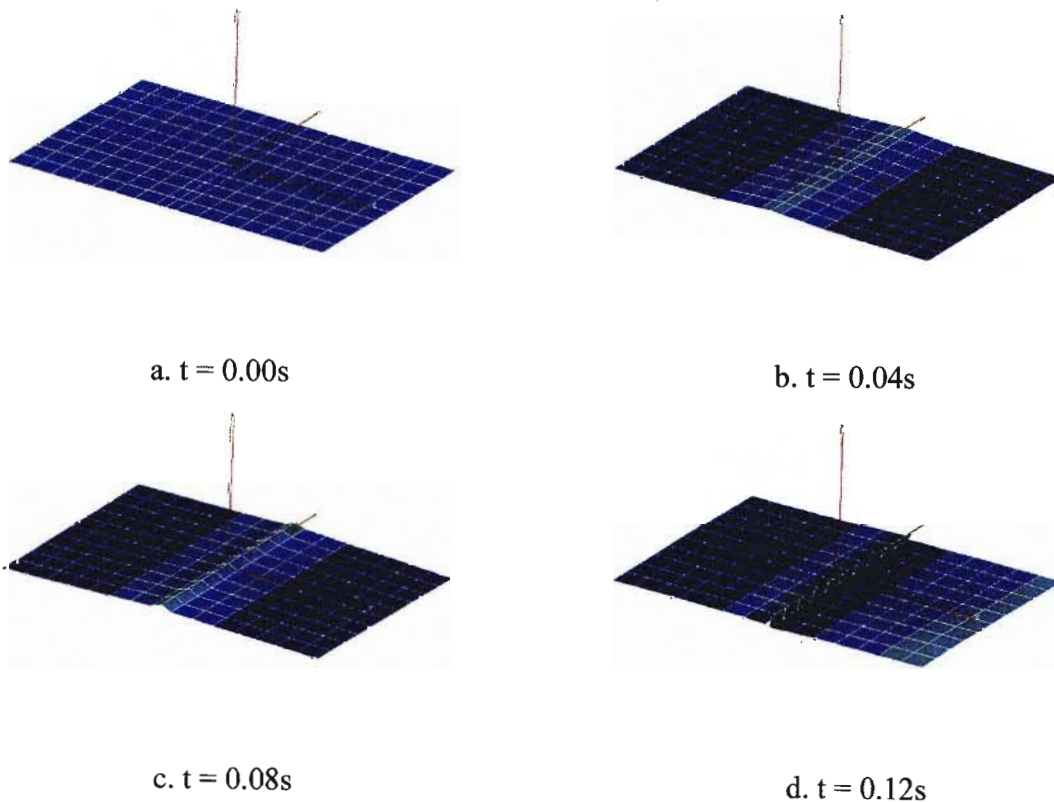
For the Global Ply Model, the tensile test simulations show a very large discrepancy, as much as 400% (see Table 3.4). This deviation may be attributable to the nature of the models in the two packages: the Global Ply Model relies on rather theoretically based damage parameters which may not be as robust as the purely physical parameters which govern the Chang-Chang model. Also, the actual derivation of these parameters may induce large errors in the final results. Conversely, the Chang-Chang model may not account for certain failures taking place at a lower stress threshold and may over predict the overall strength of the material because it does not take into account fibre, matrix and shear failure separately, from separate testing.

Table 3.4. Tensile test simulated results for Global Ply model of laminated composite. (33mm/s prescribed velocity)

Simulation results	Elastic limit (MPa)	Displacement at elastic limit (mm)	Maximum Stress (MPa)	Displacement at maximum stress (mm)
PAM-CRASH	31	0.45	31	0.45
LS-DYNA	156	0.65	156	0.65
% Deviation	403	44	403	44

3.2.2 Bending test simulation

Progressive deformation of the laminated plate under bending loading (applied velocity of 33 mm/s) obtained from the simulation based on the implementation of Bi-Phase model is shown in Fig. 3.38.





e. $t = 0.16s$

f. $t = 0.20s$

Fig. 3.38 Progressive deformation of laminated plate under bending test at 33mm/s (PAM-CRASH, Bi-Phase model).

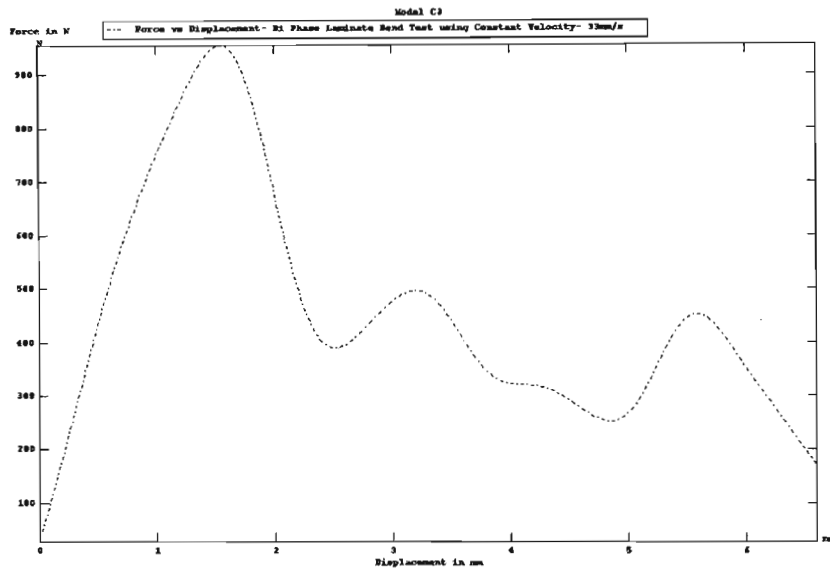
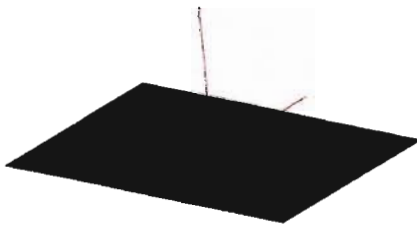


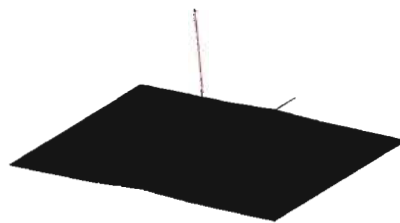
Fig. 3.39 Force-Displacement curve for bending simulation using a constant velocity of 33mm/s (PAM-CRASH, Bi-Phase model).

The bending test simulation at 33mm/s shows a maximum force of $\approx 0.95kN$ at a displacement 1.5mm (see Fig. 3.39).

Progressive deformation of the laminated plate (Bi-Phase model) under velocity of 330mm/s is shown in Figs 3.40-3.41.



a. $t = 0.00s$



b. $t = 0.004$

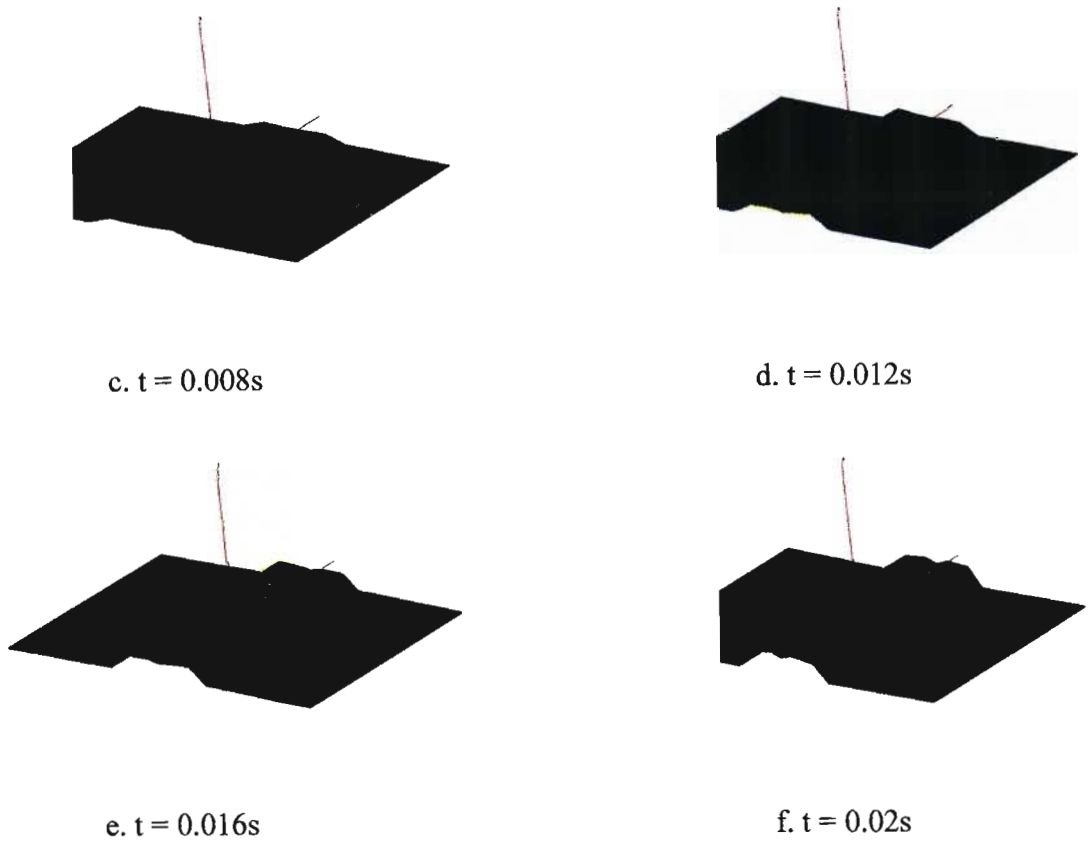


Fig. 3.40 Progressive deformation of laminated plate under bending test at 330 mm/s (PAM-CRASH, Bi-Phase model).

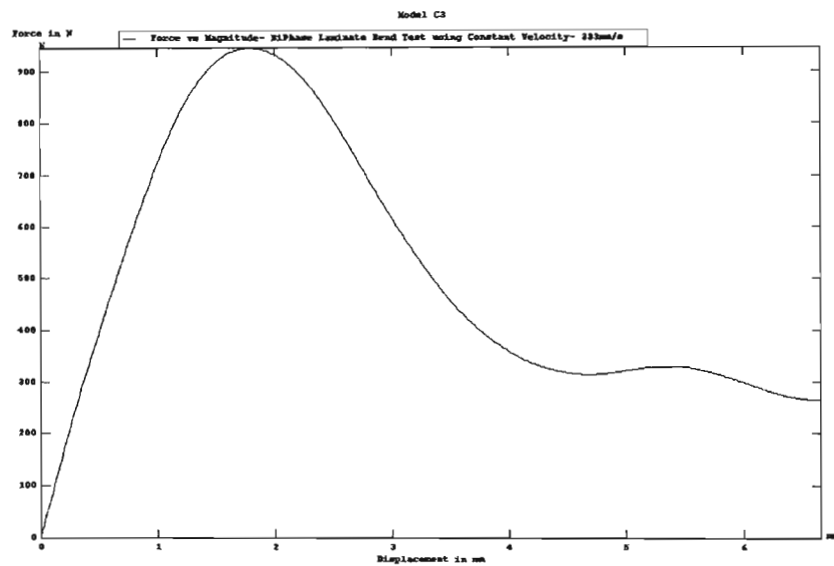


Fig. 3.41 Force-Displacement for simulation of bending test using a constant velocity of 333mm/s. (PAM-CRASH, Bi-Phase model).

The 330 mm/s plot shows similar values to the 33mm/s case, with a maximum force of $\approx 0.94\text{kN}$ at $\approx 1.8\text{ mm}$ (see Fig. 3.41).

Progressive deformation of laminated plate and Force-Displacement diagram obtained from the PAM-CRASH bending simulation based on Global Ply model are shown in Fig.3.42-3.43 (applied velocity is 33 mm/s).

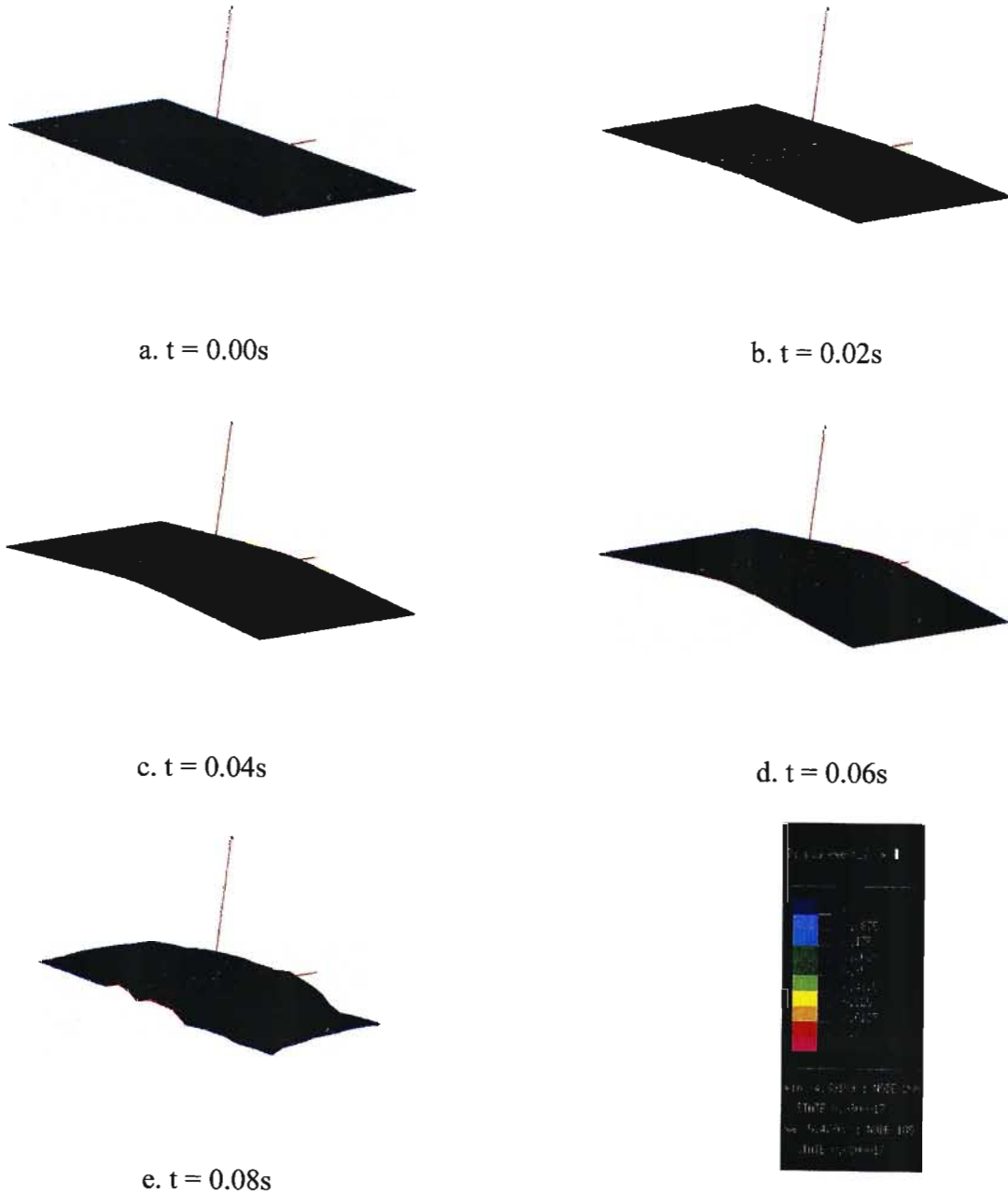


Fig. 3.42 Progressive deformation of laminated plate under bending test at 33mm/s (PAM-CRASH, Global Ply model).

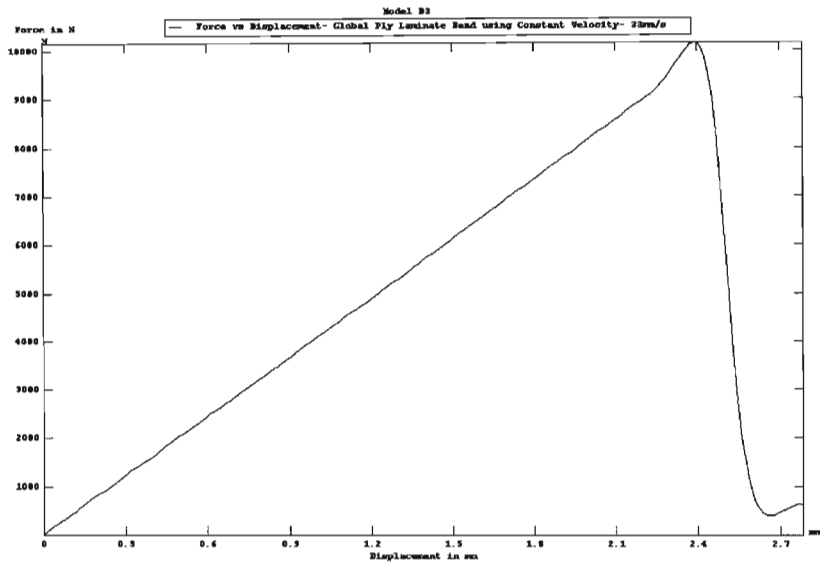


Fig. 3.43 Force-Displacement diagram for the bending test simulation based on PAM-CRASH Global Ply model (applied velocity is 33 mm/s).

The results presented in Fig. 3.43 for a Global Ply material bend test show a maximum force of $\approx 10.1\text{kN}$ at $\approx 2.4\text{mm}$.

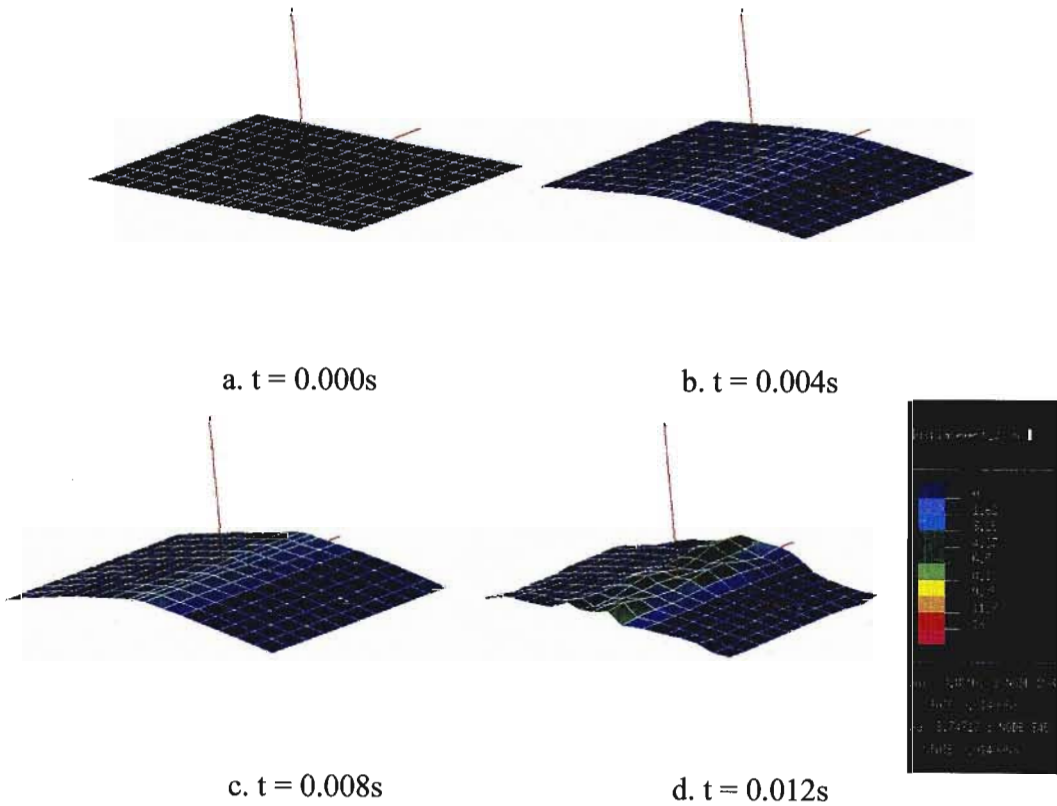


Fig. 3.44 Progressive deformation of laminated plate under bending test at 330mm/s. (PAM-CRASH, Global Ply model).

Progressive bending deformation of the laminated plate (applied velocity is 330 mm/s) is shown in Fig. 3.44.

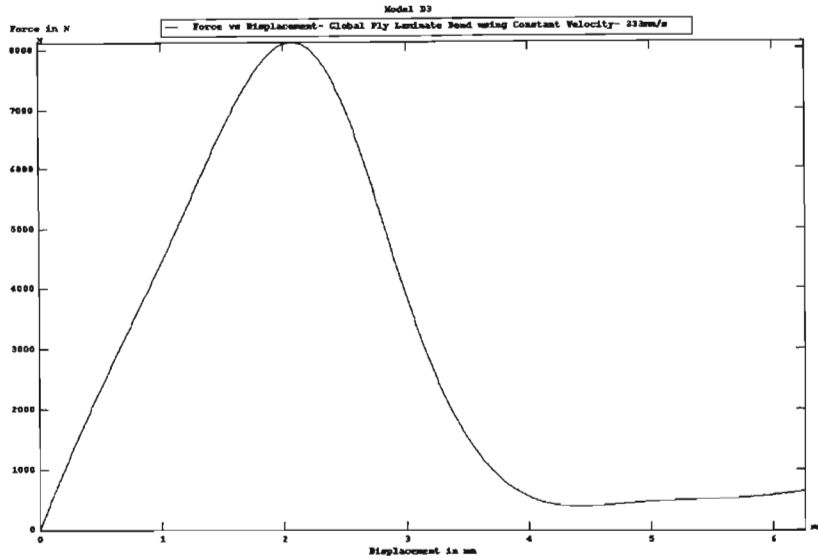


Fig. 3.45 Force-Displacement diagram for the bending test simulation based on PAM-CRASH Global Ply model (applied velocity is 330 mm/s).

For the 330mm/s bend test the maximum force is significantly reduced to $\approx 8.1\text{kN}$, as compared to the 33mm/s case, at a displacement of $\approx 2.1\text{mm}$ (see Fig. 3.45).

The results of LS-DYNA simulation (displacements and bending moment distributions and Displacement vs. Time, Moment vs. Time curves) are shown in Figs. 3.46-3.49. Simulations have been carried on using Chang-Chang Material model for the Model material with applied velocity of 33 mm/s.

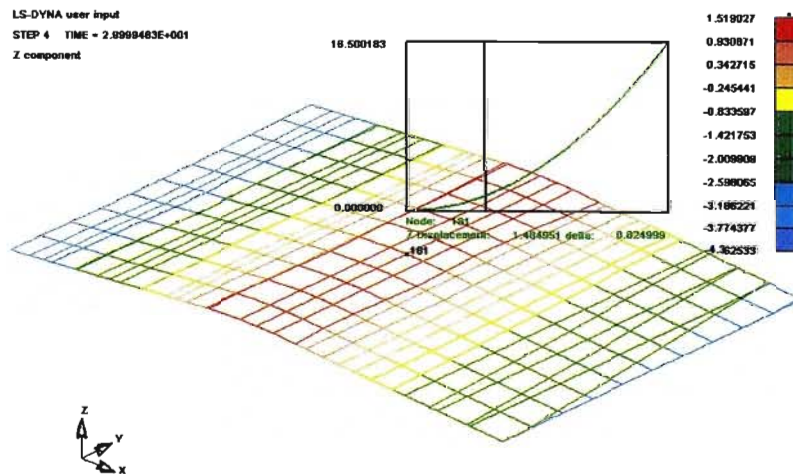


Fig. 3.46 Distribution of deflection corresponding to the maximum bending moment and Displacement vs. Time curve for node181 (LS-DYNA simulation, applied velocity 33 mm/s, Model material).

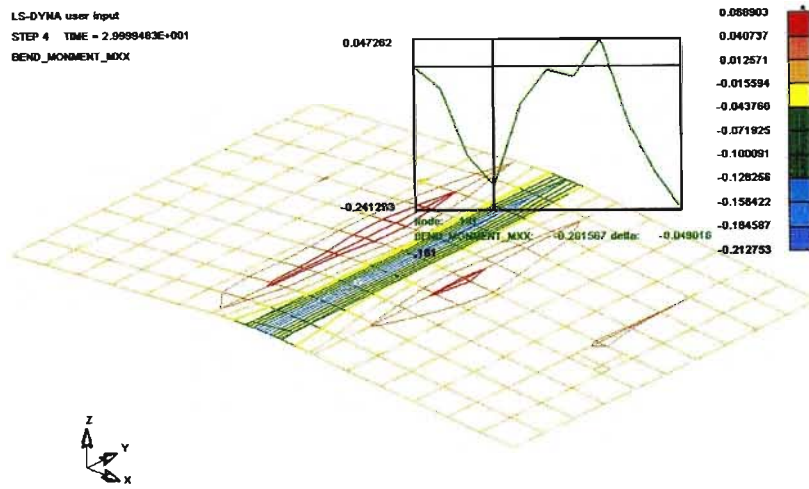


Fig. 3.47 Maximum bending moment (M_x) distribution and Moment vs. Time curves for node 181 (LS-DYNA simulation, applied velocity 33 mm/s, Model material).

As can be seen (Figs 3.46-3.47) the maximum bending moment is equal to 201 kNmm at 0.0299 s of simulation. The corresponding displacement is equal to 1.48 mm.

Figs. 3.48-3.49 illustrate results of simulation for applied velocity of 330 mm/s. Maximum bending moment of 198 kNmm and displacement of 1.64 mm take place at 0.009 sec of simulation (See Fig. 3.48 and Fig. 3.49)

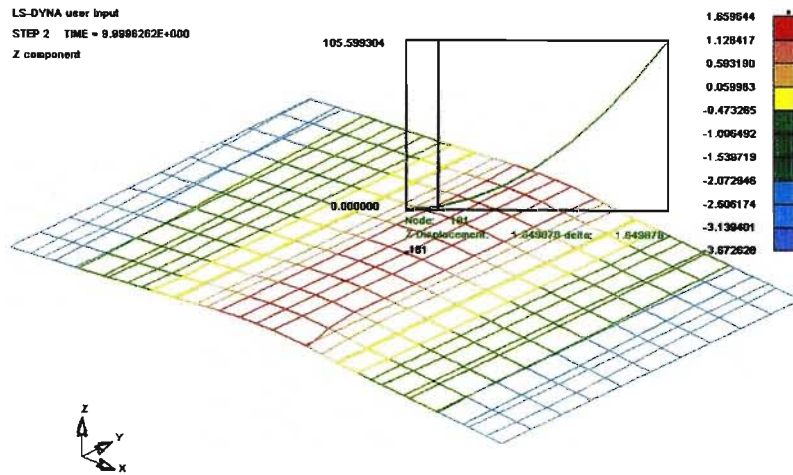


Fig. 3.48 Distribution of plate deflection corresponding to the maximum bending moment and Displacement vs. Time curve for node 181 (LS-DYNA simulation, applied velocity 330 mm/s, Model material).

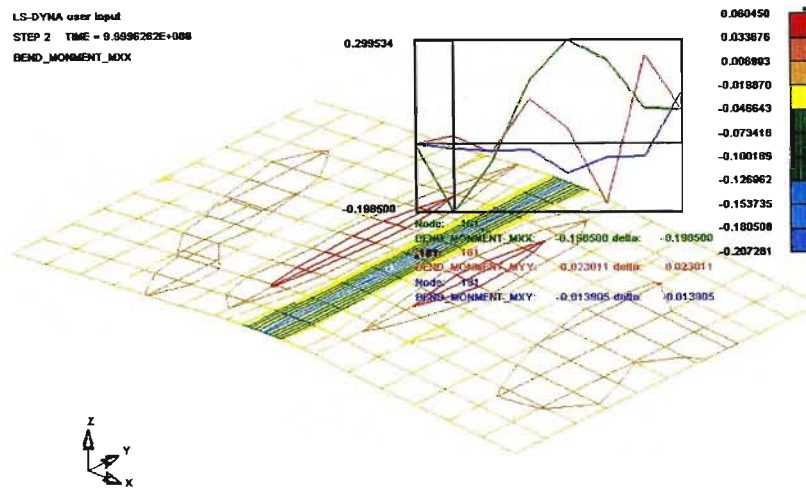


Fig. 3.49 Maximum bending moment (M_x) distribution and Moment vs. Time curves for node 181 (LS-DYNA simulation, applied velocity 330 mm/s, Model material).

Numerical results (distribution of deflection, and bending moment M_x , and Displacement vs. Time, Moment vs. Time curves) obtained from the bending test simulations for the plate made from the Glass-Epoxy laminate are shown in Figs 3.50-3.53.

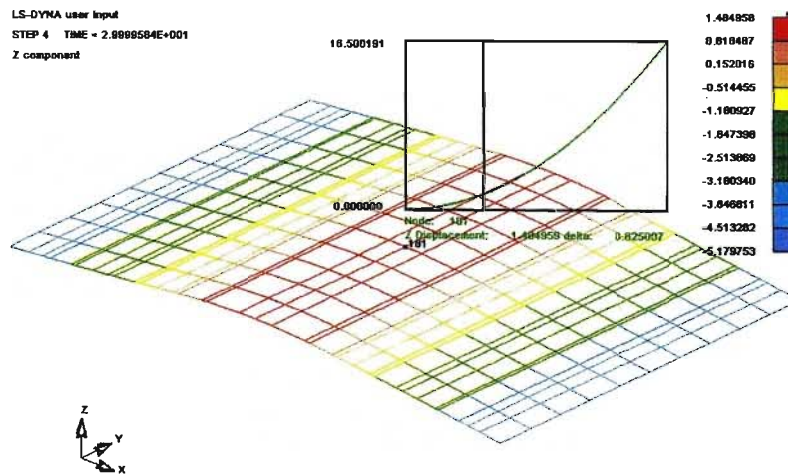


Fig. 3.50 Distribution of plate deflection corresponding to the maximum bending moment and Displacement vs. Time curve for node 181 (LS-DYNA simulation, applied velocity 33 mm/s, Glass-Epoxy composite).

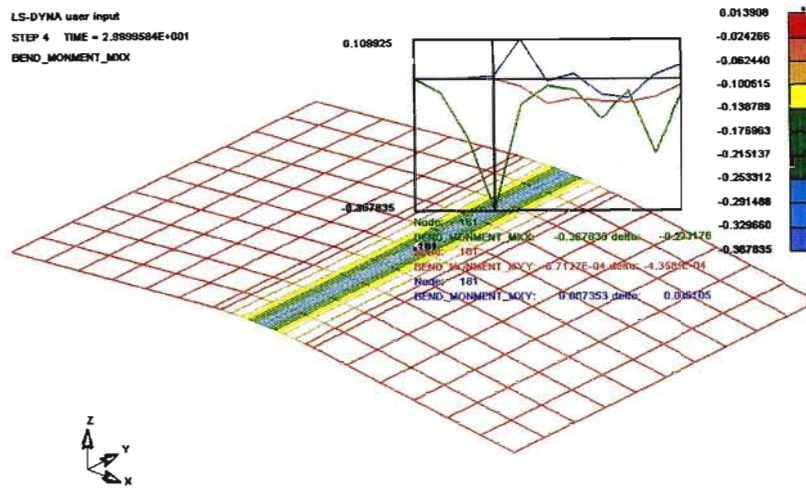


Fig. 3.51 Maximum bending moment (M_x) distribution and Moment vs. Time curves for node 181 (LS-DYNA simulation, applied velocity 33 mm/s, Glass-Epoxy composite).

In the case of bending simulation under applied velocity 33 mm/s maximum bending moment is equal to 367 kNmm and corresponding displacement is 1.48 mm (see Figs. 3.50 – 3.51).

As could be seen from the Moment vs. Time curve (Fig. 3.53) plotted for the velocity of 330 mm/s, maximum bending moment of 2.07 kNmm is reached at 0.0149 sec of simulation time and corresponding displacement is equal to 3.71 mm (see Displacement vs. Time curve in Fig. 3.52).

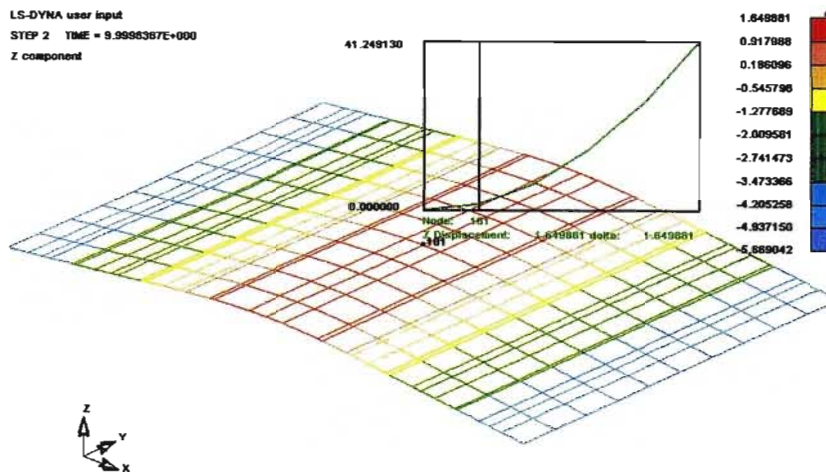


Fig. 3.52 Distribution of plate deflection corresponding to the maximum bending moment and Displacement vs. Time curve for node 181 (LS-DYNA simulation, applied velocity 330 mm/s, Glass-Epoxy composite).

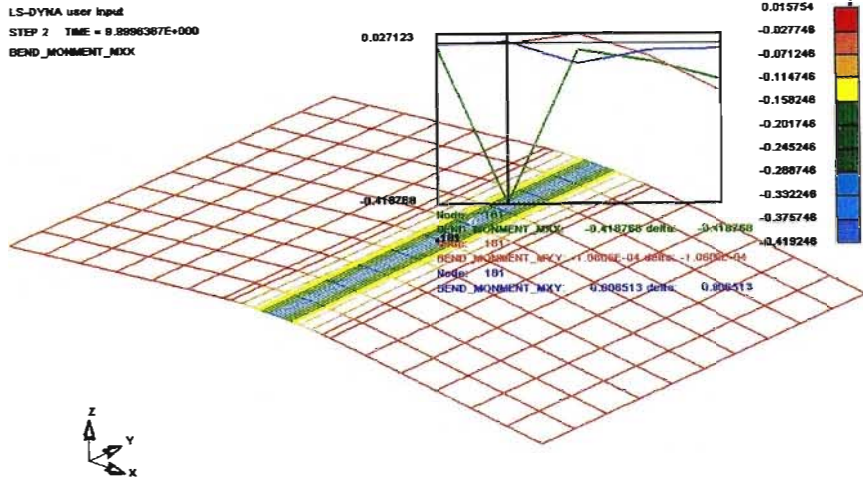


Fig. 3.53 Maximum bending moment (M_x) distribution and Moment vs. Time curves for node 181 (LS-DYNA simulation, applied velocity 330 mm/s, Glass-Epoxy composite).

Using the bending simulation results presented above the comparative analysis has been performed. For the bending test simulation, results in LS-DYNA are presented as Bending-moment vs. Time and Displacement vs. Time plots. The results from Pam-Crash are once again in the form of Force vs. Displacement plots. Additional calculations were implemented to convert numerical data and obtain to the comparable sets of parameters.

The progression of bending-moment in the material is shown to follow quite similar trends in Fig. 3.54. As can be seen the LS-DYNA model predicts a larger value for the maximum bending moment, but the maximum does occur at a similar point in both cases.

Laminated Composite (Bi-Phase Model) Bending Test Simulation (330mm/s)

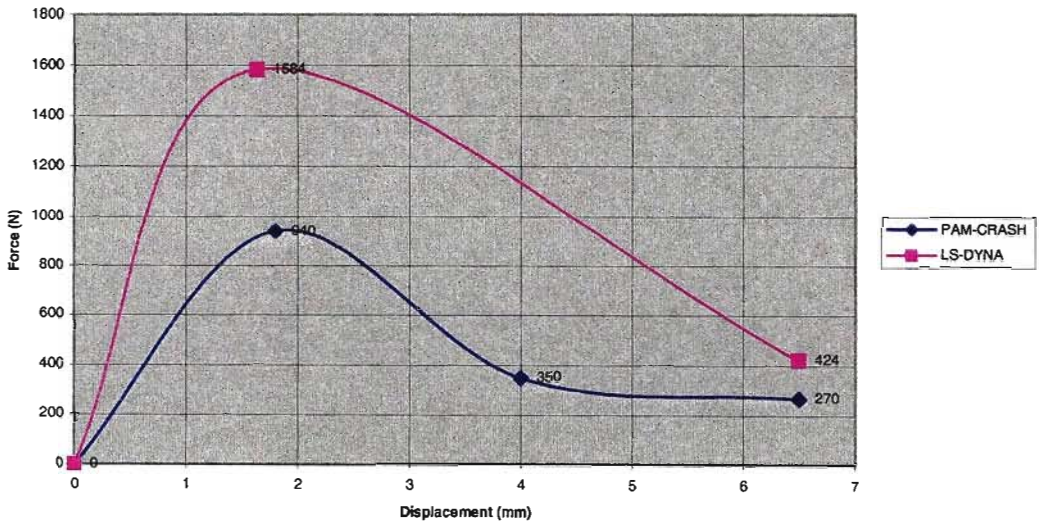


Fig. 3.54 Laminated composite (Bi-Phase Model) bending simulation comparison (330 mm/s).

Comparison of the maximum bending moments and corresponding displacements is given in Table 3.5.

Table 3.5 Bending test simulated results for Bi-Phase laminate material. (330 mm/s prescribed velocity).

Simulation results	Maximum Bending Moment (kN.mm)	Displacement at Maximum Bending Moment (mm)
PAM-CRASH	117	1.80
LS-DYNA	198	1.64
% Deviation	69	9

Table 3.6 Bending test simulated results for Bi-Phase laminate material. (33 mm/s prescribed velocity).

Simulation results	Maximum Bending Moment (kN.mm)	Displacement at Maximum Bending Moment (mm)
PAM-CRASH	143	1.50
LS-DYNA	201	1.48
% Deviation	40	2

Laminated Composite (Bi-Phase Model) Bending Test Simulation (33mm/s)

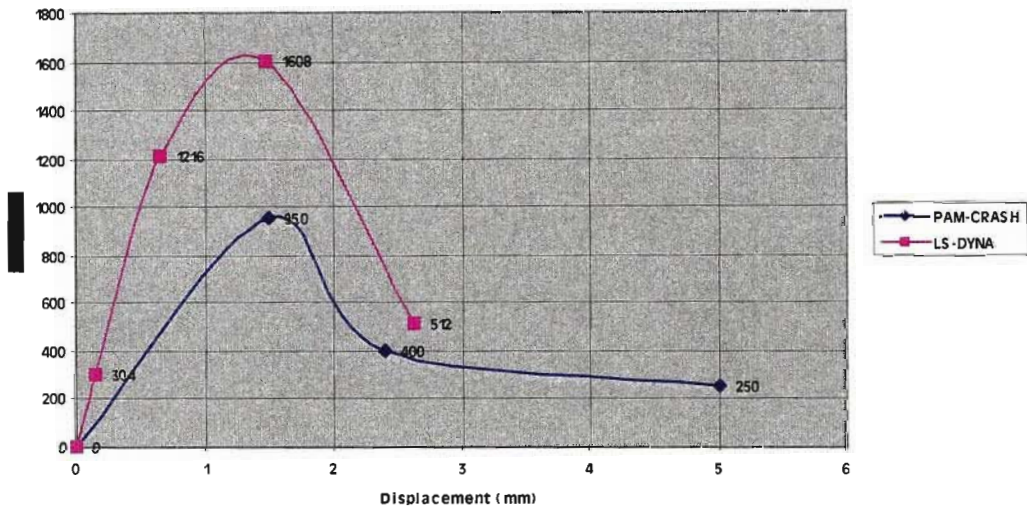


Fig. 3.55 Laminated composite (Bi-Phase Model) bending simulation comparison (33 mm/s).

The results presented in Table 3.6 and Fig. 3.55 show a similar trend in the progression of the bending moment, with the larger predicted values of LS-DYNA most likely resulting from modelling differences. The Bi-Phase model explicitly models damage in each phase whereas the

Chang-Chang Model of LS-DYNA applies damage at the macroscopic level. Introduction of damage in each case is also very differently handled. In PAM-CRASH the material properties are reduced on reaching specified strain points. In LS-DYNA the elements predicted to fail according to the specified failure criterion are removed altogether.

The similar comparative results have been obtained for the numerical data acquired from the simulations based on Global Ply model

Table 3.7 Bending test simulated results for Global Ply laminate material (330 mm/s prescribed velocity).

Simulation results	Maximum Bending Moment (kN.mm)	Displacement at Maximum Bending Moment (mm)
PAM-CRASH	1000	2.1
LS-DYNA	418	1.64
% Deviation	58	22

Laminated Composite (Global Ply Model) Bending Test Simulation (330mm/s)

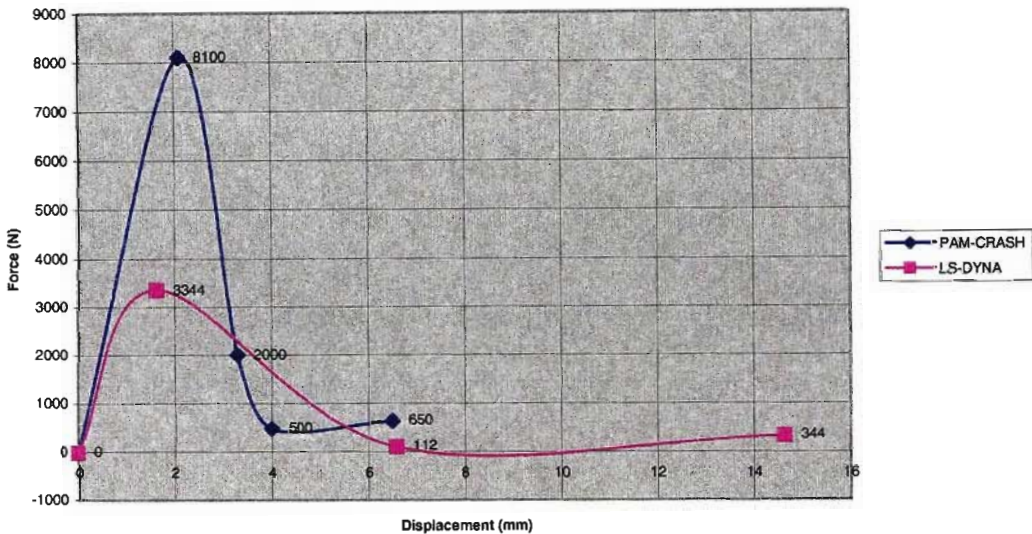


Fig. 3.56 Laminated composite (Global Ply Model) bending simulation comparison (330 mm/s).

Trend comparison (see Table 3.7 and Fig. 3.56) seems quite favourable, however the PAM-CRASH results are significantly larger. This may be attributable to the derivation of material characterisation, and the non-compatibility of the parameters available from the reference (Coutellier and Rozycki, 2000) and those required for input into LS-DYNA.

Table 3.8 Bending test simulated results for laminated plate (Global Ply Model) (33 mm/s prescribed velocity).

Simulation results	Maximum Bending Moment (kN.mm)	Displacement at Maximum Bending Moment (mm)
PAM-CRASH	1260	2.38
LS-DYNA	367	1.48
% Deviation	71	38

Laminated Composite (Global Ply Model) Bending Test Simulation (33mm/s)

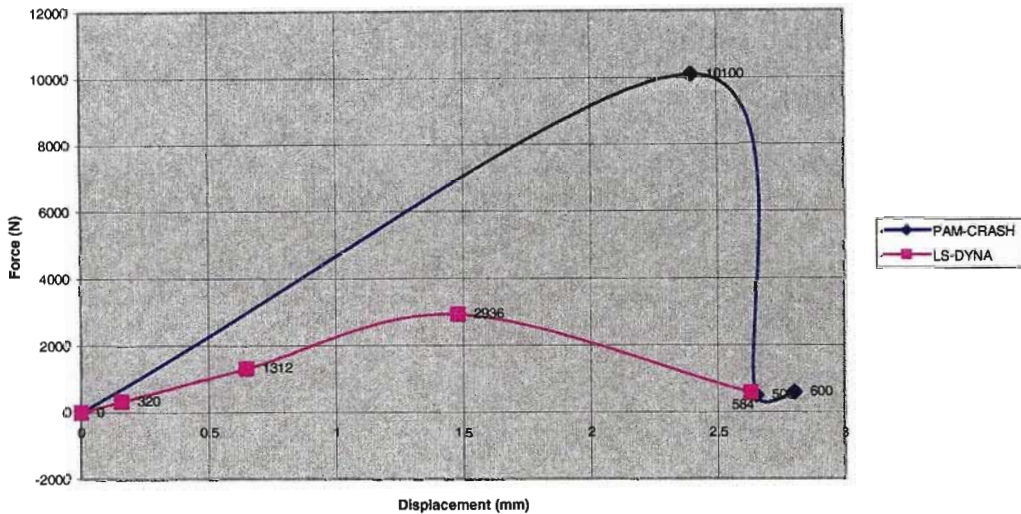


Fig. 3.57 Laminated composite (Global Ply Model) bending simulation comparison (33 mm/s).

In the case of bending test simulation for the velocity of 33 mm/s the deviation is even more significant (see Fig. 3.57). This may be attributable to the nature of PAM-CRASH Global Ply Model, which is strongly theoretically based, and dependent on the measurement of a series of parameters from experimentation to implement progressive damage. Compatibility with LS-DYNA Chang-Chang model was difficult to maintain, owing to very different material parameters being required for specification, and only the PAM-CRASH parameters being readily available from the reference (Coutellier and Rozycki, 2000). The parameters required for the Chang-Chang model were calculated from the damage relations specified, which would compound any experimental errors. It is also reiterated that the LS-DYNA plot is approximated by only a few time-step points due to simulation time constraints. A bending moment value between 2 and 2.5 seconds in Fig. 3.57, for example, would allow a more reasonable comparison.

Conclusions

SMC material

At this stage the choice of the appropriate model is limited to the two models already presented within software: Elastic-Plastic with Isotropic Damage Model (PAM-CRASH) and Elastic-Plastic with Kinematic Hardening Model (LS-DYNA). It appears obvious that the two models show little deviation up to failure, with similar maximum stress values. After failure though, it may be seen that the PAM-CRASH model introduces damage so that the material loses load carrying ability suddenly. The LS-DYNA equivalent shows a typical plastic degradation of the material, with a more gradual loss of load carrying ability. This would seem more appropriate for metallic modelling, and rather not representative of the progressive failure of composite materials. It is thus advised that, barring the implementation of the proposed models, the PAM-CRASH SMC material model should be adopted for analysis. However, accuracy of the model does depend a great deal on the experimentally obtained stress-strain curves as described in the previous sections. These curves must be accurately and completely drawn up to ensure the model retains its advantages.

Laminated material

The laminated material model choices are the following:

- (a) Bi-Phase Model (PAM-CRASH)
- (b) Global Ply Model (PAM-CRASH)
- (c) Chang-Chang Model (LS-DYNA)

The results obtained for the laminated models above show a substantial deviation in results. These may be attributable to the differences in modelling, but these differences do not immediately seem to warrant the extent of the deviation if this is the case. Another source of deviation may be the derivation of the material parameters themselves. The different models all make use of quite different parameters, especially in the way of introduction of damage criteria, and the definition of these parameters may not be completely accurate in some cases. The only way to make a valid selection on the basis of these results is to introduce experimental results as a reference. Unfortunately, all three models could not be set up in the comparable way for the same material due to limitations set by the need for different material characterisation procedure to be applied in each case (see Sections 2.3.2.1 – 2.3.2.3). For example, the set of input parameters required for the implementation of the Bi-Phase model is represented by the following characteristics: unidirectional properties, matrix phase data, fibre phase data and damage behaviour of both phases. The Global Ply model acts at the level of the unidirectional ply, with material parameters being defined for the ply in the respective directions. This modelling is achieved through homogenisation of the elementary layer. Damage is introduced in the form of matrix microcracking, fibre-matrix debonding and fibre failure. The Chang-Chang model represents a ply discount method based on the assumption of brittle failure. After failure, a ply is losing its load capacity in the dominant stress direction associated with the failure mode. The failure is assumed to be instantaneous and the elastic constants are reduced to zero in a predetermined number of time steps. Three failure criteria are used in the model. The constitutive constants can vary through the shell thickness by using the user defined integration rule. The corresponding testing techniques and material characterisation procedures required for these models are discussed in detail in Sections 2.3.2.1-2.3.2.3. As can be

seen, the sets of the input parameters are not consistent due to different nature of the material models under consideration. Thus, they would reflect the mechanical properties of one and the same material in different ways. It would appear at this stage that the results obtained in LS-DYNA are less susceptible to large inaccuracies, based on the model make-up that uses mostly macroscopic parameters measured on the material as a whole. This would imply that the deviation between the results could be attributed to problems in the implementation of the two PAM-CRASH models, as these both bring into account parameters that are not necessarily robust as they are theoretically defined and based on micromechanics at times (see Sections 2.3.2.1-2.3.2.3).

Thus, posed with the choice between models, and not allowing a choice of more than one model to complement each other, it is proposed that the LS-DYNA Chang-Chang Model would provide the most easily implementable, yet robust, option. However, taking into account the substantial variation in results obtained, experimental validation should be considered a priority.

Simulation software

PAM-CRASH offers the most options when it comes to composite modelling. There are more material models present for this purpose specifically, and the models are less general than in LS-DYNA. Also, support for the implementation of user-defined models has already been proven to exist.

Chapter 4

CRASHWORTHINESS MODELLING OF THIN-WALLED COMPONENTS MADE FROM SMC COMPOSITES

The development of an appropriate way of modelling and analysing progressive failure of thin-walled composite components with complex geometries is one of the main goals of the present research. As mentioned before (see e.g. Section 2.3) this approach requires an implementation of the specific dynamic analysis and design software tools, material models development and material characterisation.

A review of existing models and comparative numerical analysis of different software packages was presented in previous sections. As shown, the choice of the material model, determines the set of experimental data to be obtained from mechanical testing (material characterisation). In many instances the experimental programme of composite material characterisation is cumbersome and includes too many parameters to be defined. At present, many models have successfully been devised (see Sections 2.2-2.3) which are found to adequately simulate the response of composite materials. Some of these models are also found to be ready-implemented in commercially available analysis tools. However, an examination of the most commonly used software packages shows that although composite material models have indeed been implemented, these models are almost entirely limited to the family of continuously reinforced composite materials, with the modelling of discontinuous (short-fibre) composites almost completely lacking.

At present, those models that are integrated into finite element analysis software generally approach the modelling of short-fibre composites as isotropic materials, incorporating some form of damage law to take into account the progressive failure nature of the material. This approach to short-fibre reinforced composites modelling is investigated here, and a comparative analysis is made between simulated and experimental results, as a means of the model validation. According to this, the research programme from this point has been restricted by consideration of dynamic behaviour of thin-walled composite components made from SMC composites.

Manufacturing and testing of material specimens have been undertaken, thus providing the necessary experimental data for dynamic simulation. Progressive failure of composite plates and thin-walled automotive components has been performed using PAM-CRASH simulation software package. Whilst models for laminates composed of continuous fibre reinforced plies are readily available in the PAM-CRASH environment, no SMC specific model exist and an attempt has been made to adapt the existing "Elastic-Plastic Material Model with Isotropic Damage Behaviour" (Material Type 105, PAM-CRASH Solver Notes 2000) for modelling of SMC composites.

The model and simulation results were validated experimentally using mechanical testing of the prototypes.

4.1 Material characterisation

This section specifically deals with the design and implementation of a testing program to obtain experimental results, as required for input into the material models being explored.

The development of the testing schedule begins first with the selection of a suitable material, and progresses as first specimens and then the prototype demonstrator are designed and tested.

Coupled with component manufacture are the specific requirements of the material, geometric considerations, physical properties and finish all have to be taken into account when designing the complete manufacturing process. Care has been taken that the specimens mirror the properties of the prototype.

4.1.1 Specimens manufacture

The flat specimens, plates, and prototypes were manufactured using pre-mixed sheets of SMC material. This form of SMC negates the need for physical mixing of the constituents, is readily available in set fibre volume percentages, and is relatively easy to store and transport. Drawbacks do include the need for a pre-heat process, and less flexibility with regards to fibre volume percentage, however these were considered justifiable when weighed up against the time and labour saving, and the added benefit of a much better expected finish. The SMC sheets in question have been supplied by *ABB, Bloemfontein* in 20% and 35% fibre volume compositions.

To cure, the material requires both heating and pressure. The heating is achieved by pre-heat of the moulds being used, while pressures are applied using a suitable press. During the curing process the layers bond together and fill up the mould cavity, thus allowing for variable thickness to be achieved, depending on the actual volume of material placed in the mould. Curing time is approximately 40 seconds per millimetre of thickness, under temperatures ranging from 130 °C to 170 °C and pressures in the range of 7-15 MPa.

A suitable press is readily available for installation of the required moulds, and it has been decided to fulfill the heating requirements using electrical heating elements. Heating by means of electrical cartridge heaters (pictured in Fig. 4.1) embedded into the mould itself (as opposed to being placed into a separate platen) was adopted as the most viable method due to its flexibility and relative ease of implementation.

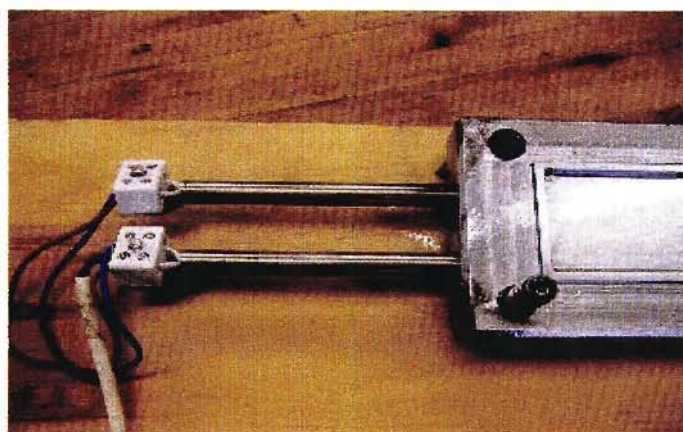


Fig. 4.1 Electrical cartridge heaters.

These cartridges are readily available (*Kaytherm, Pinetown*), and facilitate the option of using the same elements in both the sample and prototype moulds (by simply making them removable), require no complicated machining, are custom-made as dictated by the heating requirements (length, diameter, shape, power output), and are relatively durable.

Tensile specimens were designed with a dumb-bell shaped, straight-sided configuration, with a thickness of 4 mm. The length and width of these specimens were constrained by available fixturing and the test-rig dimensions. In the case of compression testing, the specimens are of a simple rectangular shape.

The length to thickness ratio of these specimens is relatively small, so as to avoid the introduction of buckling phenomena during testing.

The SMC material being used (as described previously) requires both pre-heating of the moulds being used, and the application of a suitable pressure. The pre-heat requirement dictates that the moulds be manufactured out of metal, and that a suitable heating process be incorporated into these moulds. Additionally, since specific temperatures are required, a heating control system has to be set in place.

A schematic of the complete mould, including fittings necessary to fix the mould to the hydraulic press being used to apply the required pressure is shown in Fig. 4.2.

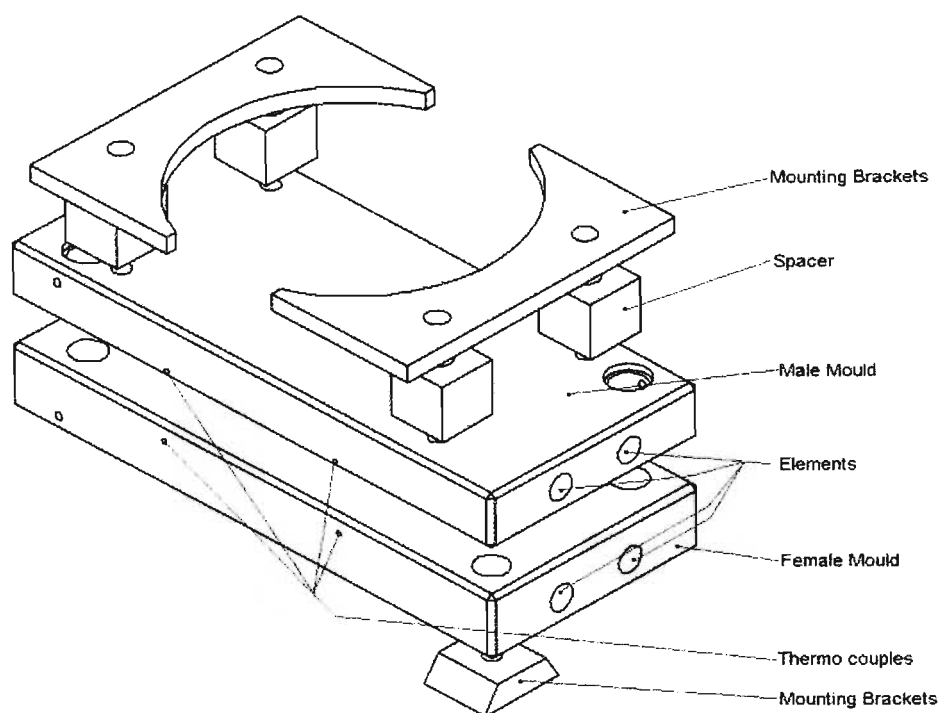


Fig. 4.2 Specimen mould design including required fixtures.

The mould decided upon is a semi-positive type matched mould, with each half designed to be bolted to the upper and lower platens of the press respectively.

The cylindrical heating elements have been designed to run length-ways through both the female and male sections of the mould.

The placement and number of the elements, as well as the actual diameter and power output required of the individual cartridges was determined from data sheets supplied by the manufacturer (*Kaytherm, Pinetown*) and a *FLUENT* analysis, and the elements were supplied as such. Typically, the spacing for 600-watt elements in steel is one per 100 mm.

Temperature control is to be achieved using a set of thermocouples embedded in the mould at identified key points, together with a pair of temperature controllers (see Figs. 4.3-4.4) which allow for the setting and maintaining of specific temperatures through feedback control (Fig. 4.5). Each element is connected to a contactor, which enables up to four elements to be connected/powerd at a time. Cartridge heaters were manufactured by *Kaytherm* (15 mm diameter, 300 mm length, 1000W output, 220V). J-type controllers (0-400 °C), 220V were supplied by *ATC*

South Africa. Contactors (40 A, up to 4 points of contact) were manufactured and supplied by *Lavato*.

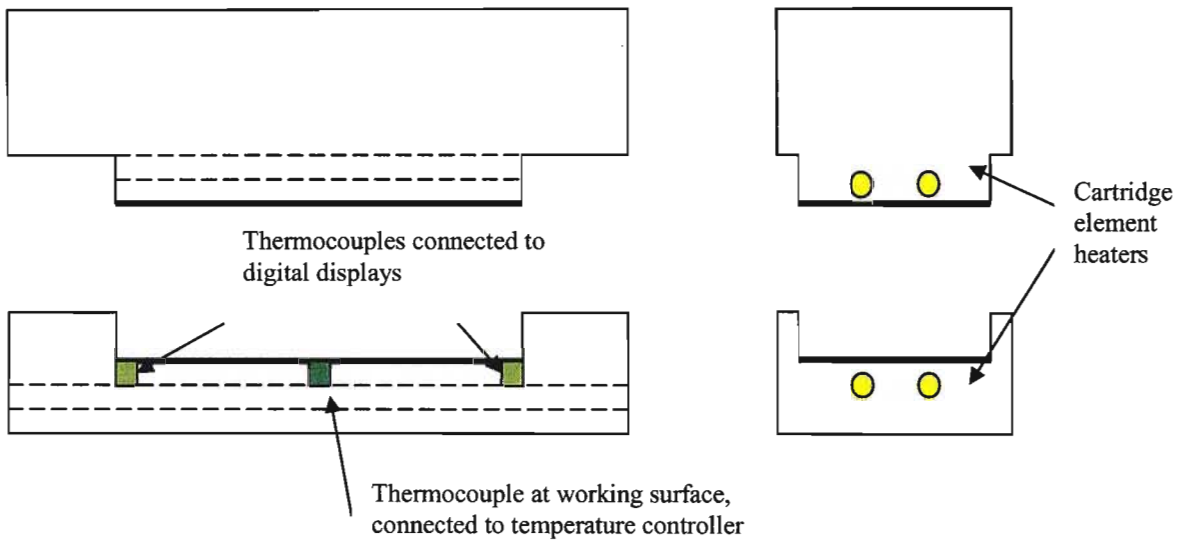


Fig. 4.3 Schematic of the heated moulds showing thermocouple and element positions.

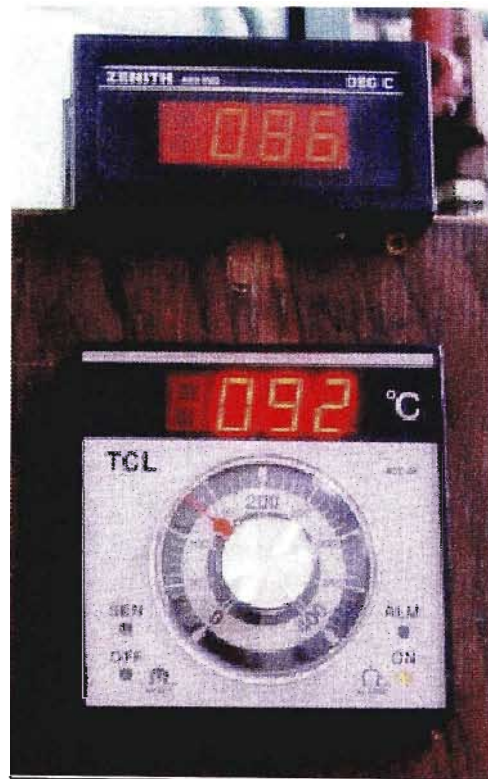


Fig. 4.4 Temperature controller (ATC, South Africa) and secondary temperature display (Zenith, South Africa).

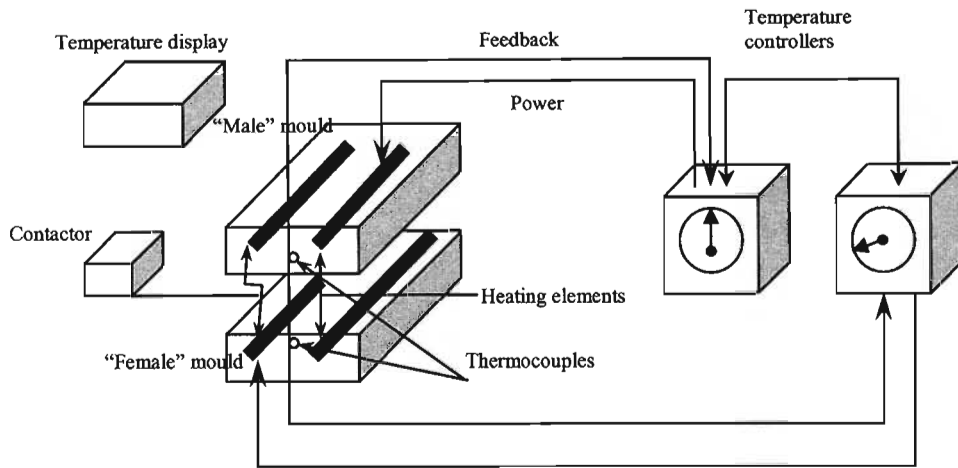
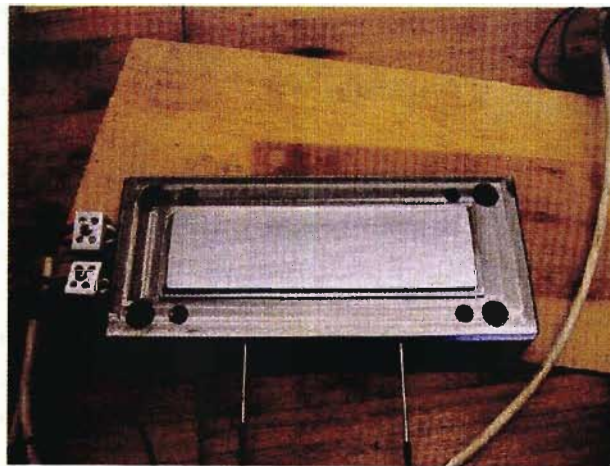


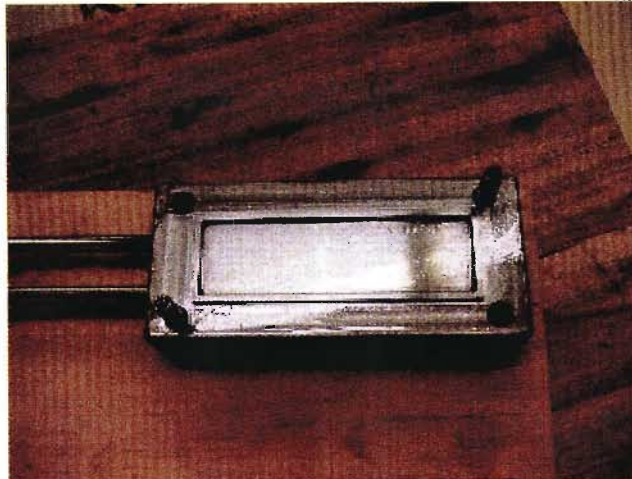
Fig. 4.5 Temperature control system.

The specimens were cut out of a cured plate of SMC, thus allowing for any dimensional changes to the specimens at a later stage, as well as preventing the possibility of damage to the specimen shape during the moulding and ejection processes. Allowance in the mould size for the heating elements, an ejection mechanism, guide pins, and alignment with the hydraulic press fittings, together with the primary strength requirements SMC volumetric requirements and shrinkage dictated the dimensions of the plate to be moulded at a time to be 230 mm by 60 mm, with variable thicknesses possible.

The actual product, manufactured at the university is shown in Fig. 4.6.



(a)



(b)

Fig. 4.6 Completed specimen mould (a) 'Male' section (b) 'Female' section.

Included in the design of the mould are two guide-pins, located diagonally opposite each other, which maintain the correct relative positioning of the mould halves. Also, to aid in removal of the specimen from the moulds after curing, a 1° draft angle is incorporated into the walls of the mould. The mould is also designed such that the thermocouples and heating elements may be easily removed as necessary, for possible maintenance or adjustment.

For the required size of SMC plate to be produced, the moulding process requires the following:

Temperature: 130 °C

Press load: 110 kN

Curing time: 90 s

(calculated according to supplier's data- *ABB, Bloemfontein*)

The two halves of the mould are first installed on the press to be used for manufacturing (Fig. 4.7), through the use of spacers and brackets (Fig. 4.8) as necessary.



Fig. 4.7 Hydraulic press used for specimen manufacture.

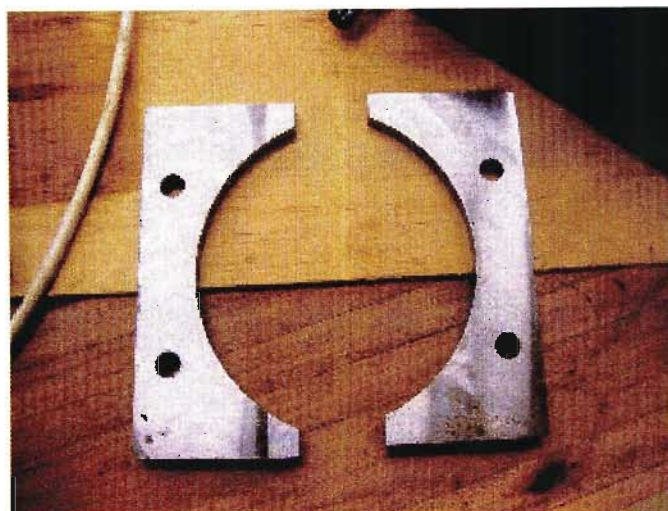


Fig. 4.8 Brackets used to fix mould to press.

Once the moulds are installed onto the press, the two halves are aligned using the guide pins (Figs. 4.9-4.10).

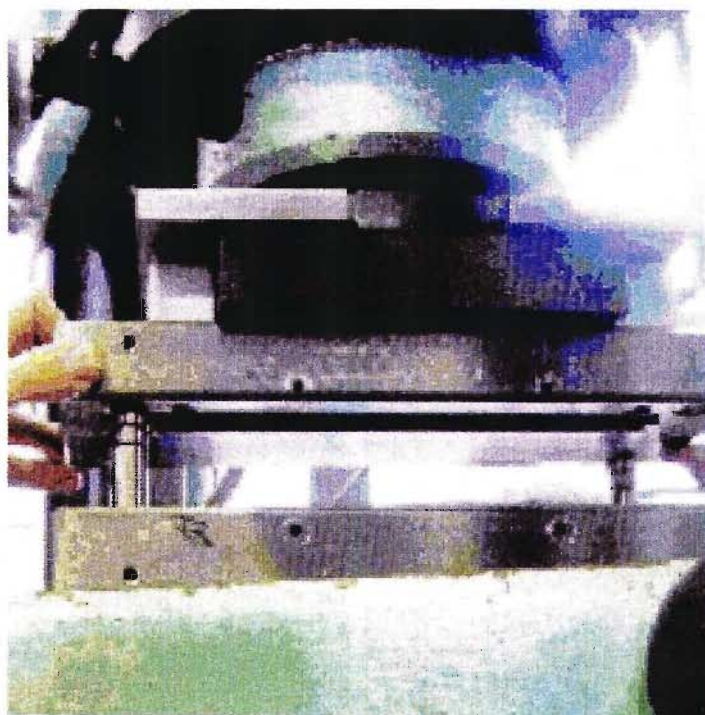


Fig. 4.9 Alignment of mould using guide pins.

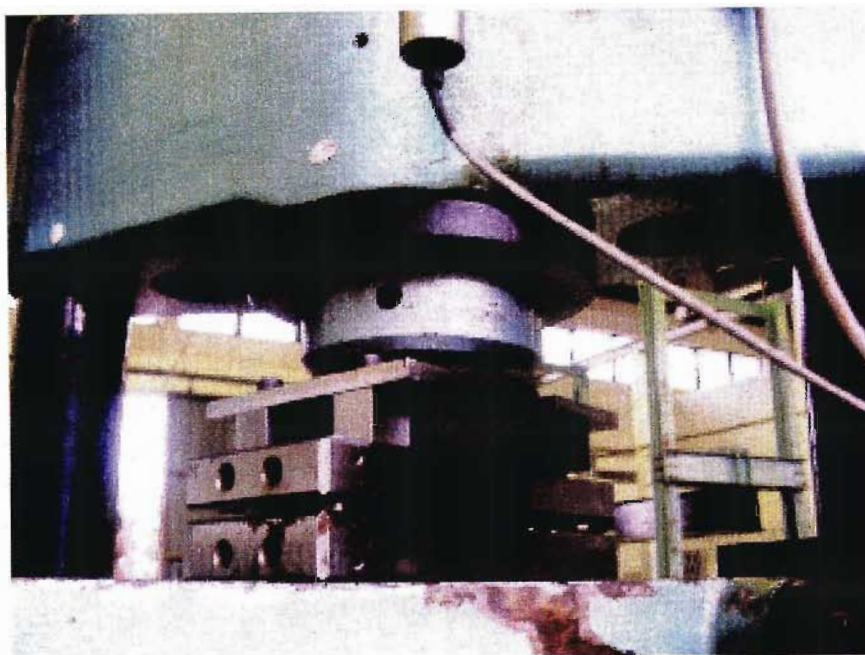


Fig 4.10 Mould fitted and aligned.

The thermocouples and heating elements are then installed in the mould (Fig. 4.11).

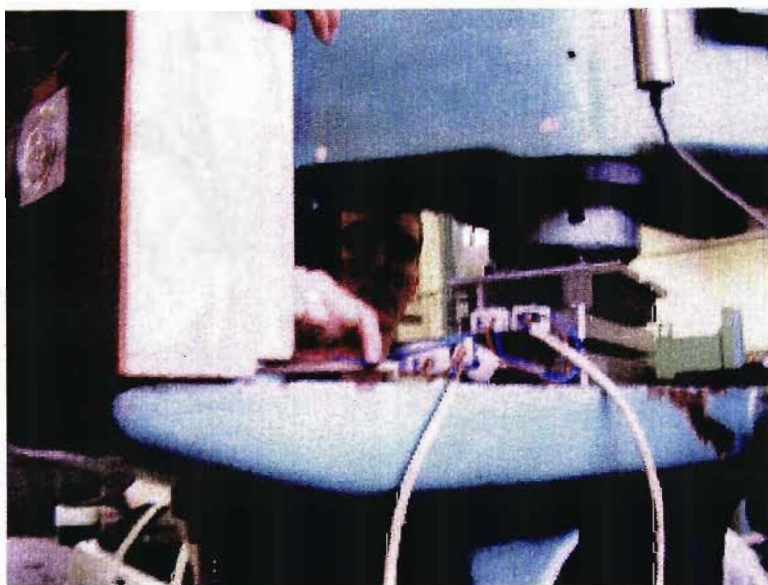


Fig. 4.11 Installation of thermocouples and heating elements.

The heating control system was set up next to the press (Fig. 4.12).

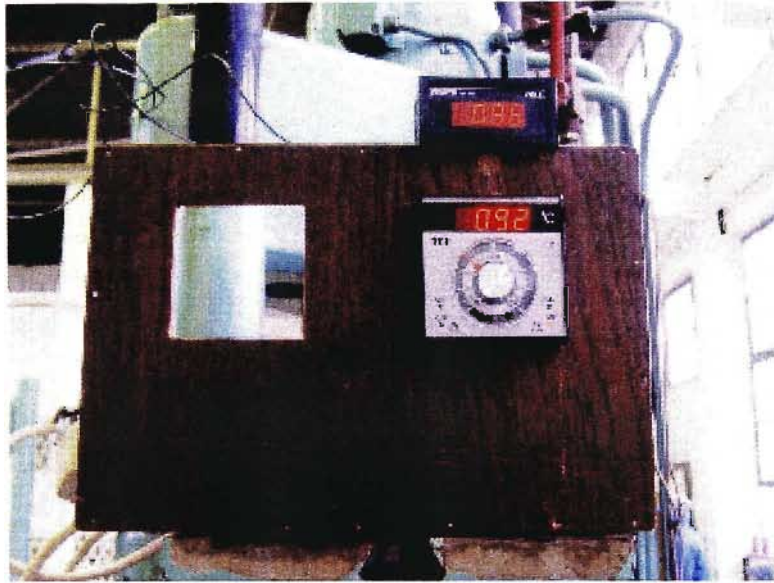


Fig. 4.12 Temperature controller and temperature display.

Once the set-up was complete, the temperature was set to the necessary level, and the mould was heated up. Once the required temperature was attained, the necessary volume of SMC material was placed in the mould cavity, and the mould closed under the required pressure so that the material may be cured (Fig. 4.13).

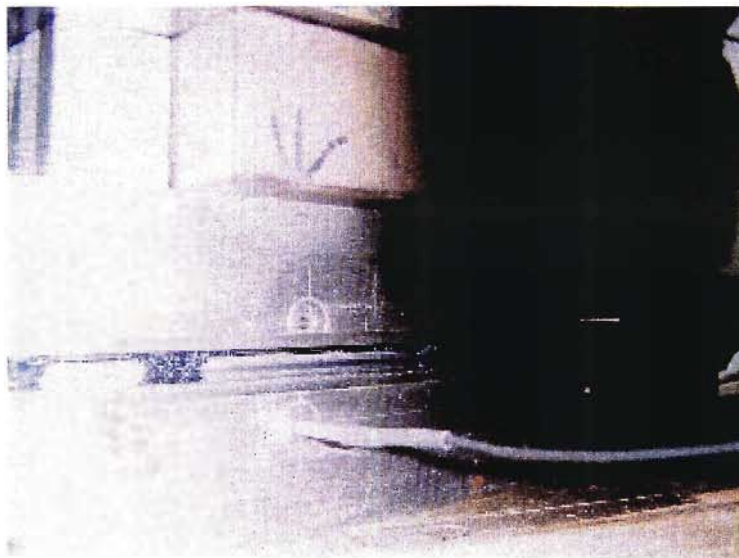


Fig. 4.13 The SMC material being cured under temperature and pressure

The curing process is completed after 90 seconds under temperature and pressure. After that the moulded plate (Fig.4.14) is allowed to cool and is then removed with the aid of a compressed air ejection system.

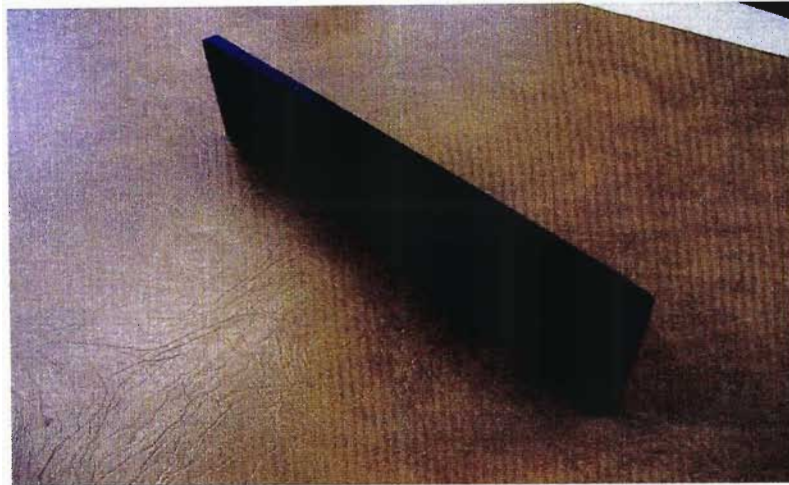


Fig. 4.14 Moulded SMC plate.

The required specimen geometry is then cut out of the plate (see Fig. 4.15).

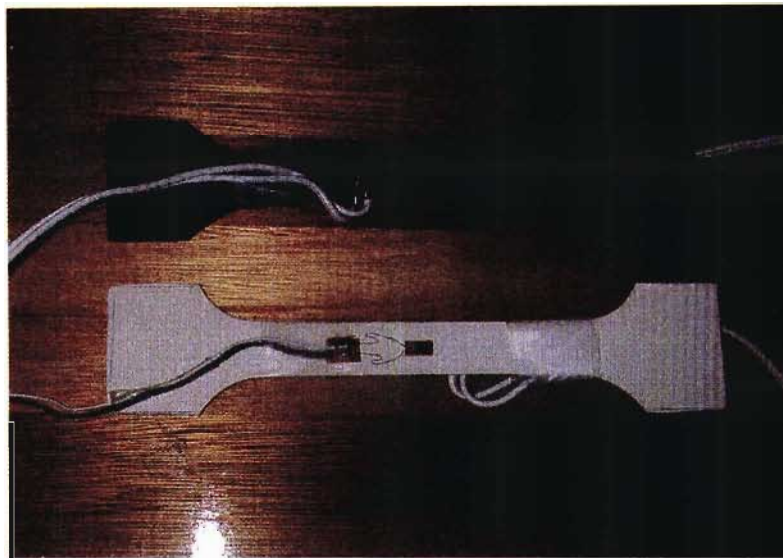


Fig. 4.15 Cut samples ready for testing.

4.1.2 Specimen testing

Tensile tests have been performed at the *Durban Institute of Technology* on a Lloyds test rig (Fig. 4.16) at a test velocity of 0.5mm/min, so that the parameters required for the material characterisation within the PAM-CRASH model for SMC composites could be obtained.

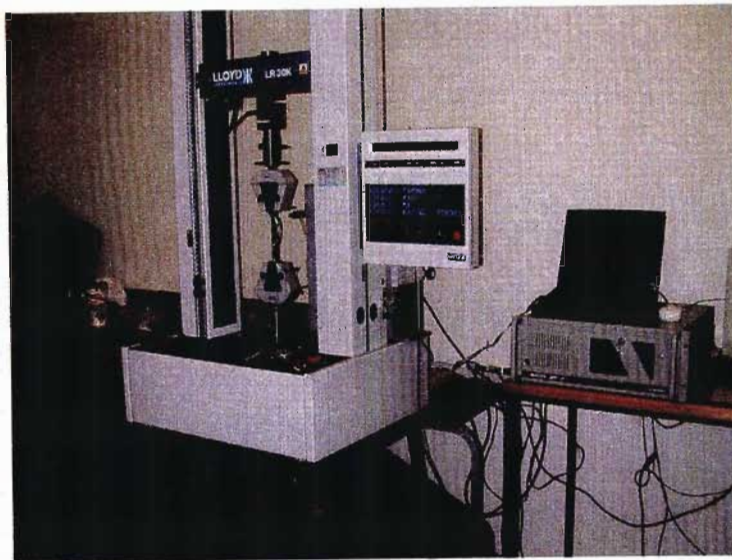


Fig. 4.16 Lloyds test setup.

Test results are shown in Fig. 4.17

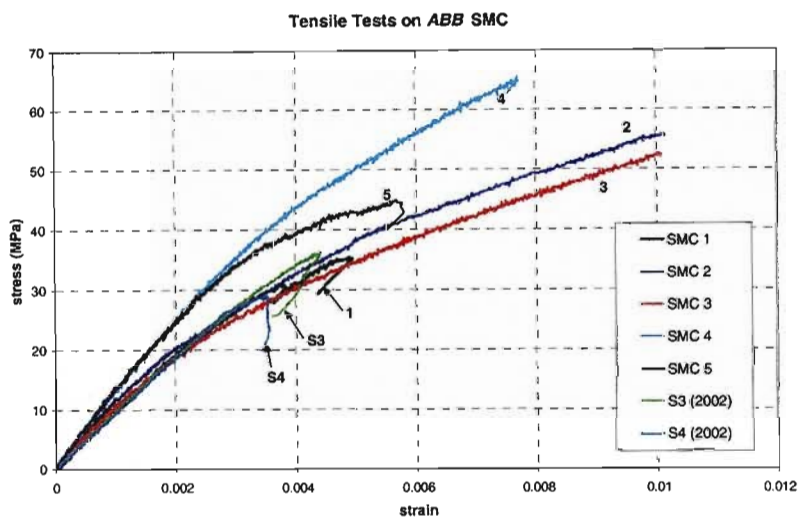


Fig. 4.17 Stress-strain curves for SMC material.

Modelling parameters then were extracted from the stress-strain curves in order to obtain a range of simulated responses. The variation in properties for the specimens in the sample set is partly attributed to random variations experienced during manufacture and material structure. The chosen tensile specimen and experimental methodology must also be examined so that better repeatability of test results can be obtained.

The scatter evident indicates room for relatively flexible definition of the material characterisation parameters. As a means to evaluate the effect of this scatter on the simulation results, the upper and lower limit curves for the data range (see Fig 4.17) were identified and used for the simulation of the crushing response. Figs 4.18-4.19 show the extraction of material characterisation parameters from the limit curves obtained from tensile testing. A further case of material characterisation included here (Fig. 4.20) is for a tensile curve lying in between the upper and lower limit curves (see Fig. 4.17).

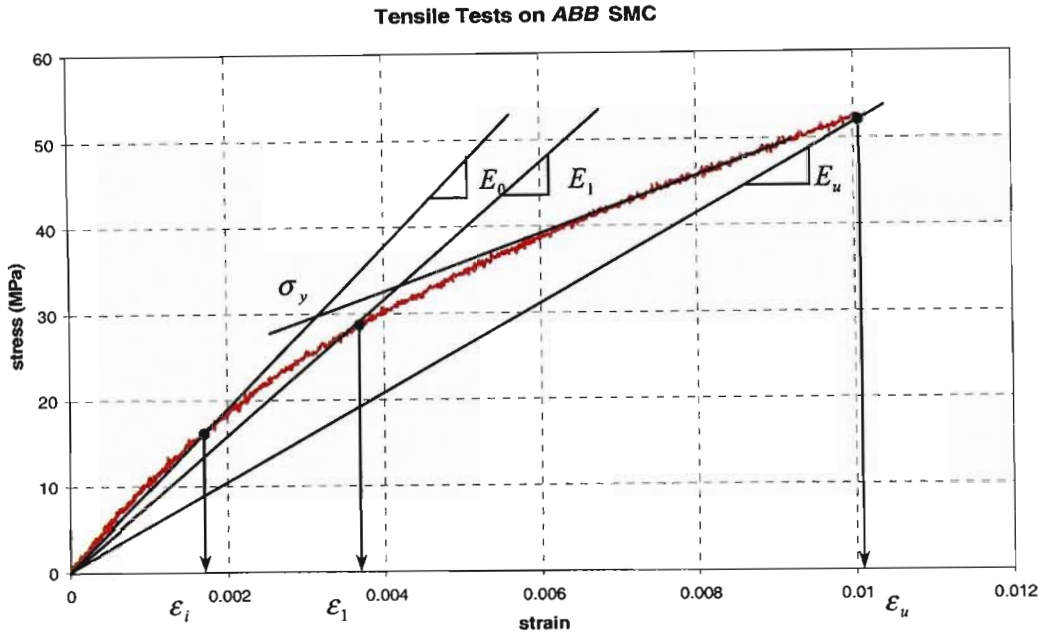


Fig. 4.18 Lower tensile curve.

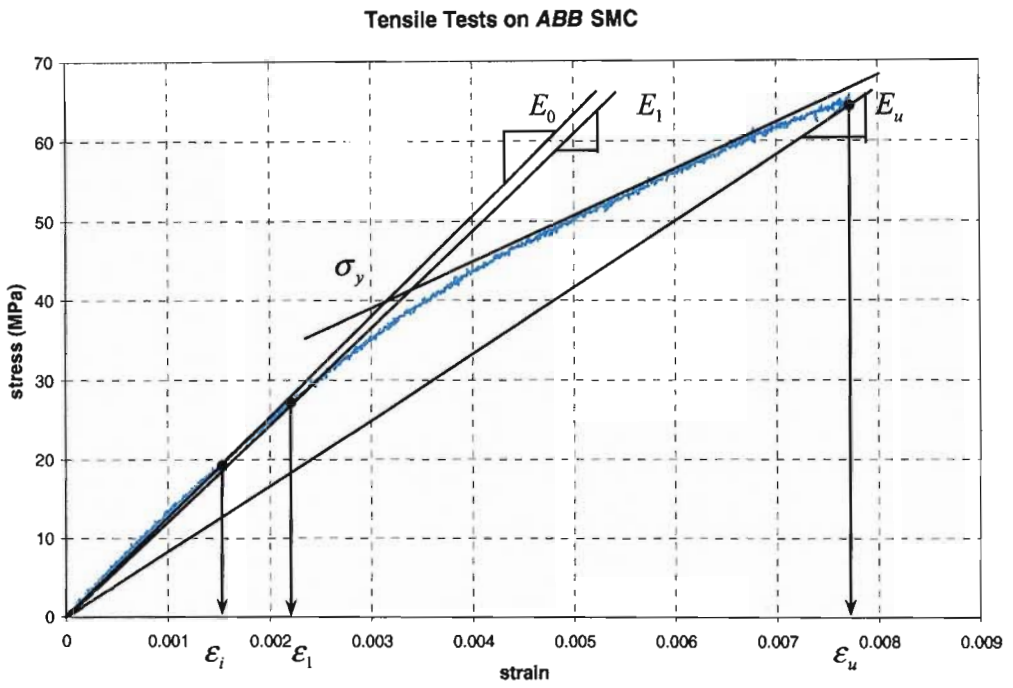


Fig. 4.19 Upper tensile curve.

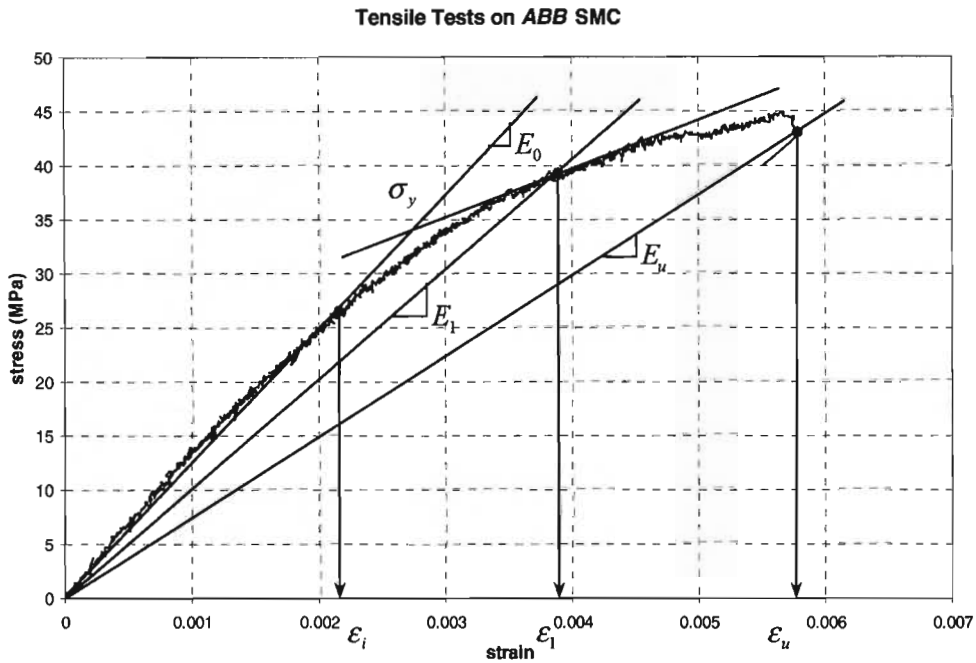


Fig. 4.20 Middle tensile curve.

Simulation of the structural components' response was also conducted using the materials characterisation obtained from compressive tests. It was reasonable to expect that characterisation of the material by way of compression test results would yield another 'limit' for the structural response.

Samples were tested in compression using an Instron test rig at a test velocity of 2.5 mm/min and the typical compressive stress-strain curve obtained is shown in Fig. 4.21. Two of the destroyed samples are shown in Fig. 4.22.

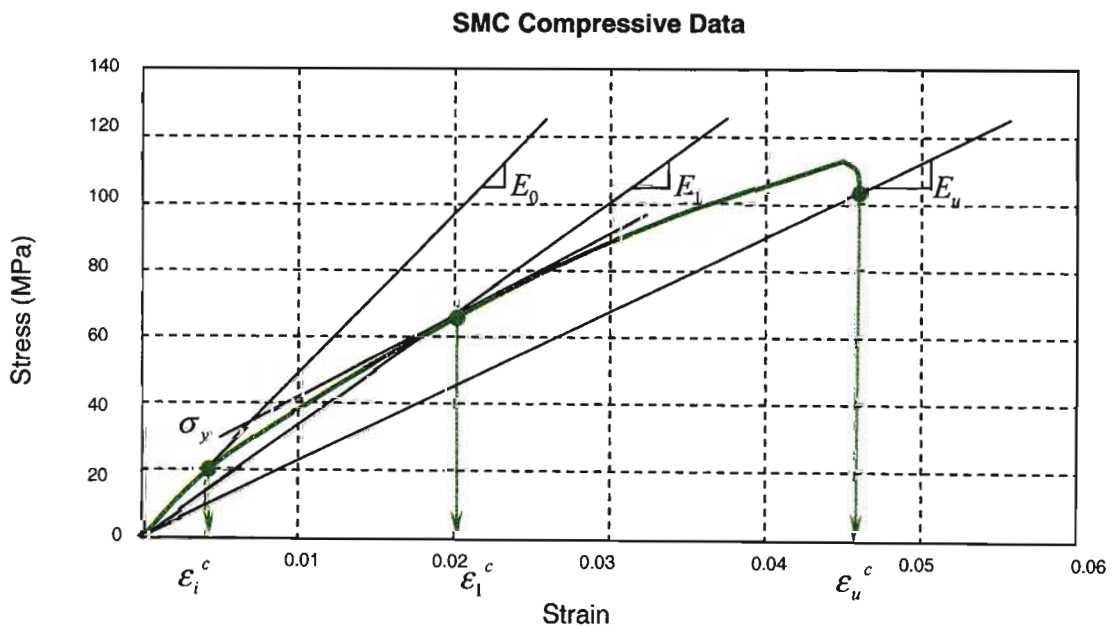


Fig. 4.21 Compressive curve.

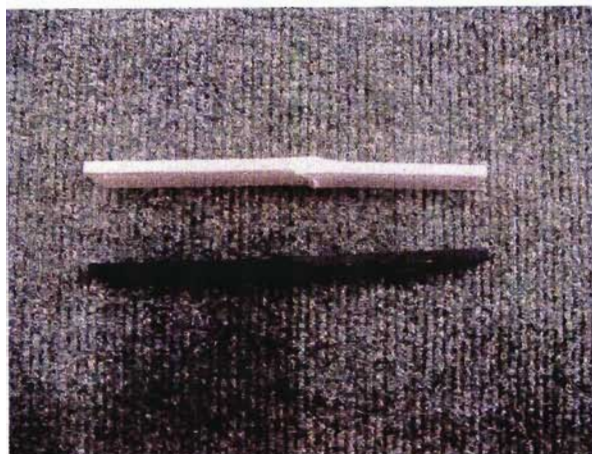


Fig. 4.22 Destroyed compressive test samples.

The material characterisation parameters so obtained from the tensile and compressive curves (for all four cases) are presented in Table 4.1.

Table 4.1. Material characterisation parameters.

Material parameters	Experimental curves			
	Tensile upper curve	Tensile middle curve	Tensile lower curve	Compression curve
Young modulus, E_0 MPa	13750	12500	10000	4800
Poisons ratio, ν	0.3	0.3	0.3	0.3
Initial strain, ϵ_i	0.0011	0.0023	0.0016	0.003
Intermediate strain, ϵ_1	0.0022	0.0039	0.0036	0.02
Ultimate strain, ϵ_u	0.0077	0.0058	0.0101	0.046
Intermediate damage, d_1	0.09	0.2	0.0225	0.305
Ultimate damage, d_u	0.333	0.25	0.354	0.324

4.2 Progressive failure of SMC composite plate under bending loading

The bending of the composite plate was chosen as a basis for a preliminary validation of the progressive failure model because this mode of loading was considered to be representative of the complex nature of loading in structural components subjected to crushing loads. The tensile loading case was chosen as the basis for the damage parameters definition in the material law. This choice would appear logical since failure would most probably be initiated in tension, so this would be the more conservative approach.

Fig. 4.23 is a schematic representation of the experimental setup used to investigate mechanical behaviour of the plate under bending conditions. Note that the load is applied midway between the supports (which are separated by a distance of 80mm) and that the overall dimensions of the samples used are shown in the figure. The actual experimental set-up is shown in Fig. 4.24. One of the samples made to fail under bending loading is shown in Figs 4.25-4.26.

Bending tests were performed independently using both an Instron machine (Fig. 4.27) and MTS test rig (Fig. 4.28). Testing on the MTS rig was conducted at velocities of 2mm/s and 100mm/s and the data was captured using the WaveBook / 516TM 16 bits 1 MHz Data Acquisition Systems. Testing on the Instron rig was conducted at the single velocity of 2mm/s and data was captured via a *built in data acquisition system* (this machine is not capable of testing at the higher velocities reached by the MTS rig). Experimental Force vs. Time curves are shown in Figs 4.29-4.30.

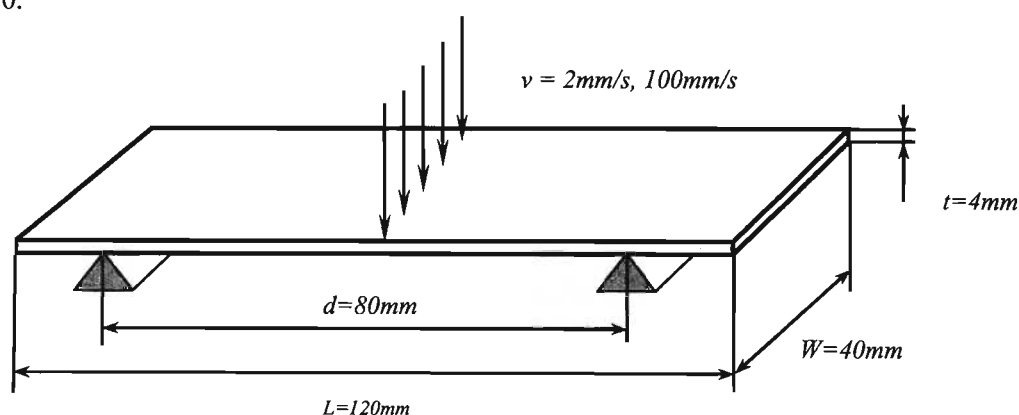


Fig. 4.23 Schematic of three point bend test.



Fig. 4.24 Three point bend test (actual set-up).

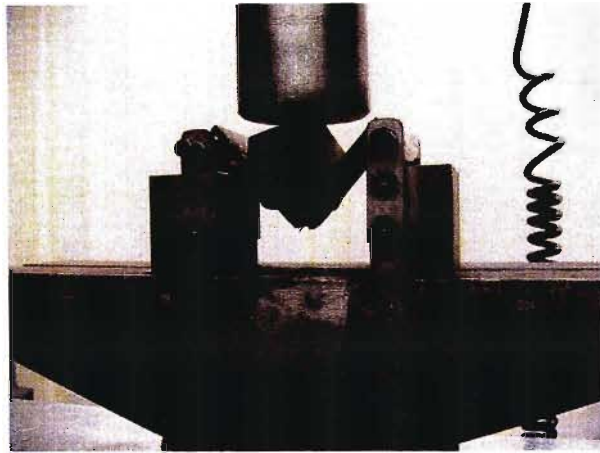


Fig. 4.25 Close up of failed sample (still mounted).



Fig. 4.26 Close up of failed sample, showing fracture.

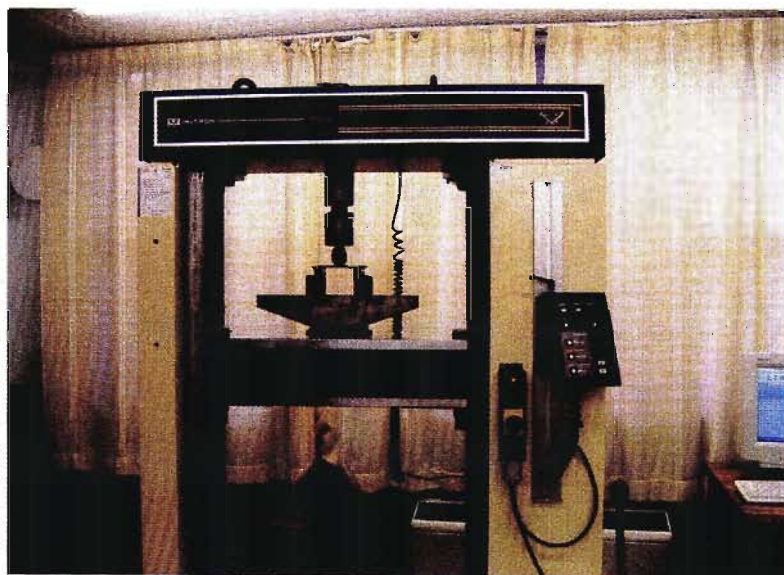


Fig. 4.27 Instron test rig ready for testing.

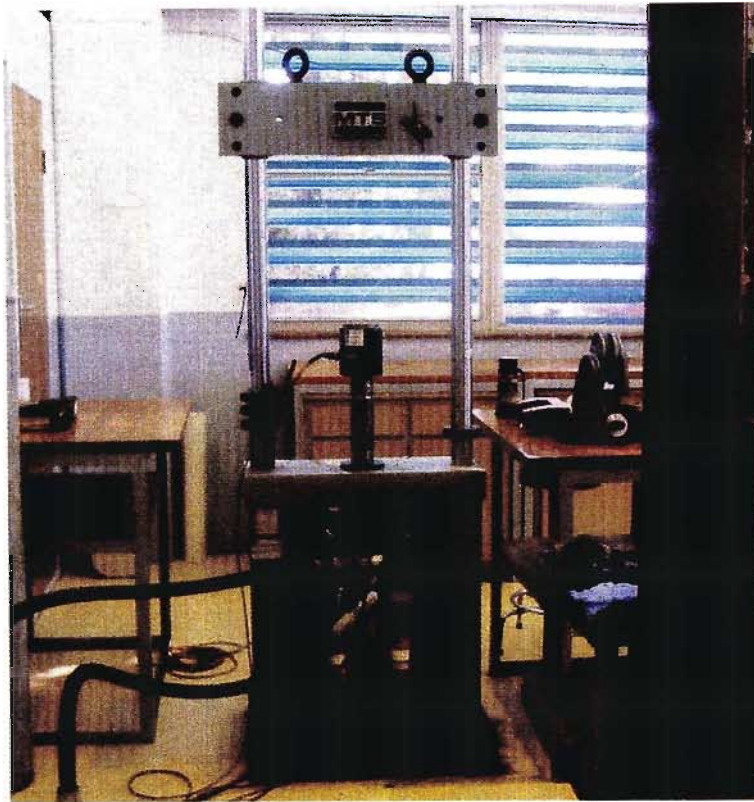


Fig. 4.28 MTS test rig with load cell.

Bending Test (2 mm/s)

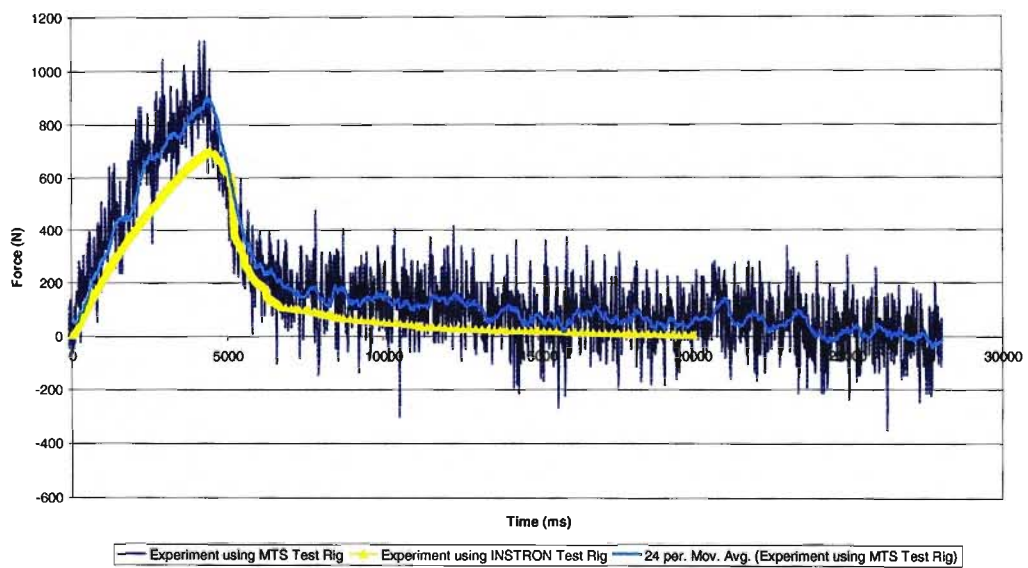


Fig. 4.29 Force vs. Time experimental curve under loading with prescribed velocity of 2 mm/s.

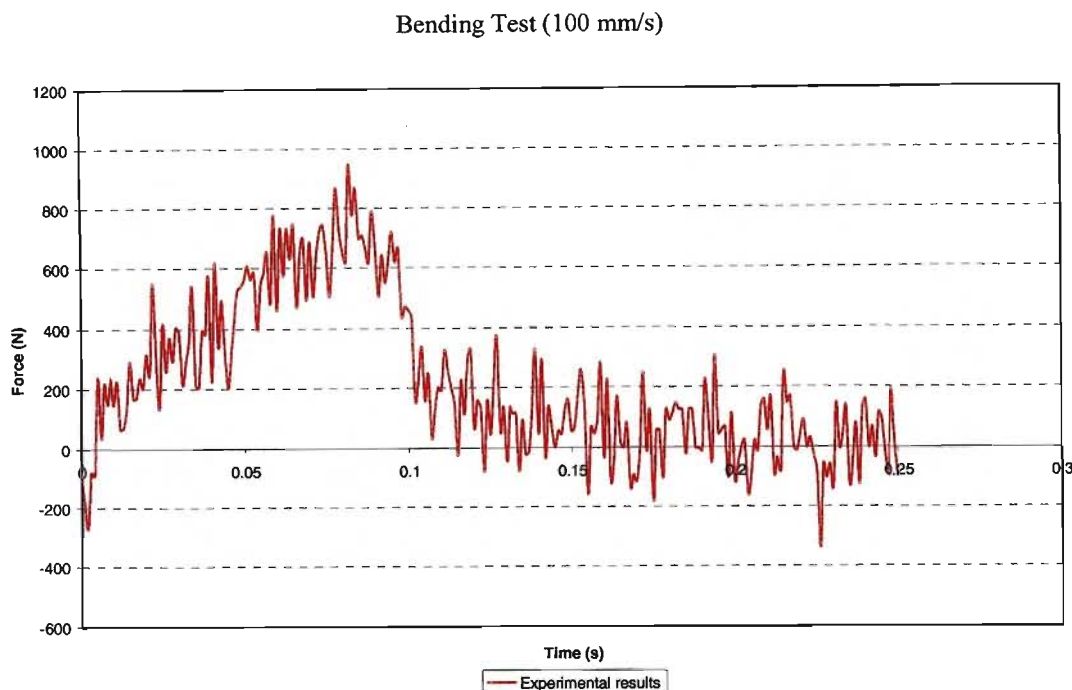


Fig. 4.30 Experimental Force vs. Time curve for the bending loading with prescribed velocity of 100 mm/s.

The separately acquired results for the testing velocity of 2mm/s are shown together in Fig. 4.29. The graph (Fig. 4.29) shows favourable comparison between the independent tests, with the displacement at peak load being equal for both cases. There is a difference between the separately recorded peak loads which can be expected, since the two independent tests cannot be exact replicas of each other (variations in sample, apparatus and data acquisition system exist).

The bending test has been simulated using the PAM-CRASH model for SMC composites. The model makes use of an isotropic material that includes a damage law to model the progressive failure of the SMC composite, the details of which have previously been fully discussed (see Section 3.1.2). The material characterisation parameters used to define PAM-CRASH material type 105 are shown in Table 4.1. The mesh representing the plate model was created using MSC.NASTRAN (Fig. 4.31) and comprises 48 plate elements, each with dimensions 10x10mm. This mesh is then exported to PAM-CRASH and loading is applied using the software's constant velocity boundary condition, whilst the simple supports are modelled using a displacement boundary condition.

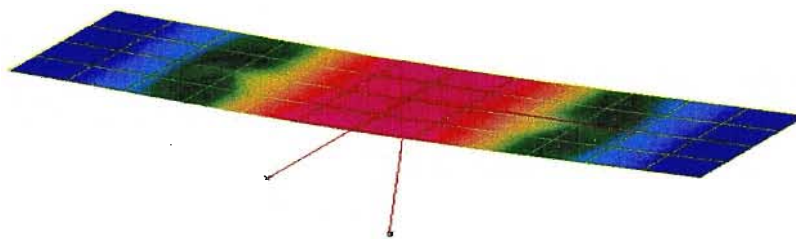


Fig. 4.31 Meshed plate.

Firstly, a refinement of the plate element mesh was performed, increasing the 48 plate elements originally employed to 128 square plate elements with side length of 5 mm (Fig. 4.32). It was found that a finer mesh visibly improved the accuracy of results until too fine a mesh introduced numerical problems (Morozov et al., 2003).

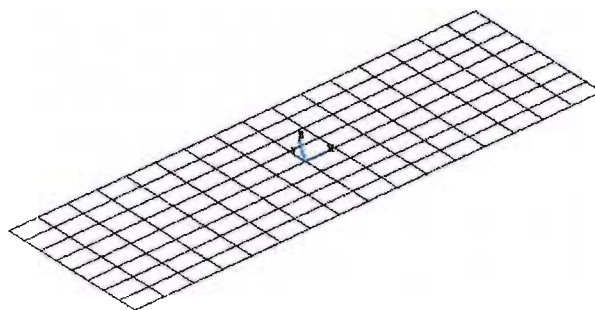


Fig. 4.32 Plate meshed with 128 plate elements (element size 5 x 5mm).

As a second avenue for refinement, a solid element mesh was explored as an alternative to the previously adopted plate elements. PAM-CRASH Material Type 16, the solid element equivalent of plate Material Type 105, which employs identical characterisation and damage behaviour, was selected (Morozov et al., 2003). At first the mesh utilised consisted of only one element across the thickness of the plate (Fig. 4.33), and produced poor results. The solid element size was then reduced so that two elements (with size 2 x 2 x 2 mm) now made up the thickness of the plate (Fig. 4.34). The results obtained from this simulation, employing 2 x 2 x 2 mm solid elements, proved to be the closest yet to those obtained from the bending experiment.

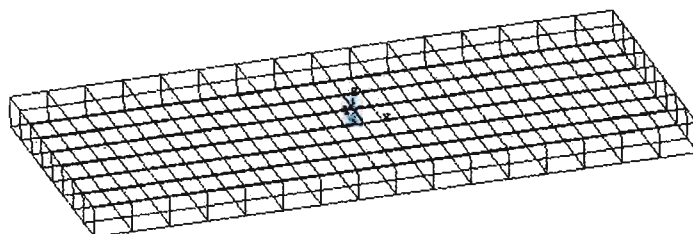


Fig. 4.33 Plate meshed with 128 solid elements (element size 5 x 5 x 4mm).

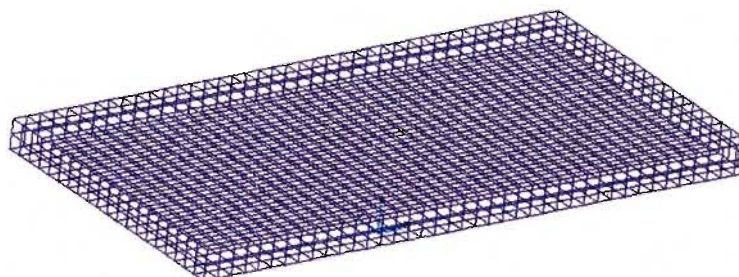


Fig. 4.34 Plate meshed with 1600 solid elements (element size 2 x 2 x 2mm).

Results, obtained from simulation using an even finer mesh, 1 x 1 x 1 mm elements with 4 elements across the thickness, are virtually the same as results for the 2 x 2 x 2 mm elements, thus exhibiting convergence, so that further refinement of the solid element mesh is deemed unnecessary. The output demonstrates realistic deformations as experienced by the plate under bending loading.

At this juncture, with a fair level of confidence that the mesh selection and refinement process had revealed the optimum available options in these areas, the numerical simulations were performed using the refined mesh and adopting corresponding sets of the material parameters presented in Table 4.1, as input data.

The respective results for the velocity of $v = 100$ mm/s are included in Fig. 4.35. The resultant Load vs. Time curves for two limit cases (upper tensile and lower tensile) show the scatter effect the material characterisation data (see Fig. 4.17) has on the final structural response for the bending simulation. As can be seen (Fig. 4.35), the maximum load for the experimental curve is clearly lies between these two “extreme” cases as would be expected. In general, the simulation results follow the experimental curve fairly closely. Thus choice of a representative set of experimental data to characterise the material in question is shown to be of foremost significance; as is the need for a series of experiments in order to obtain representative results.

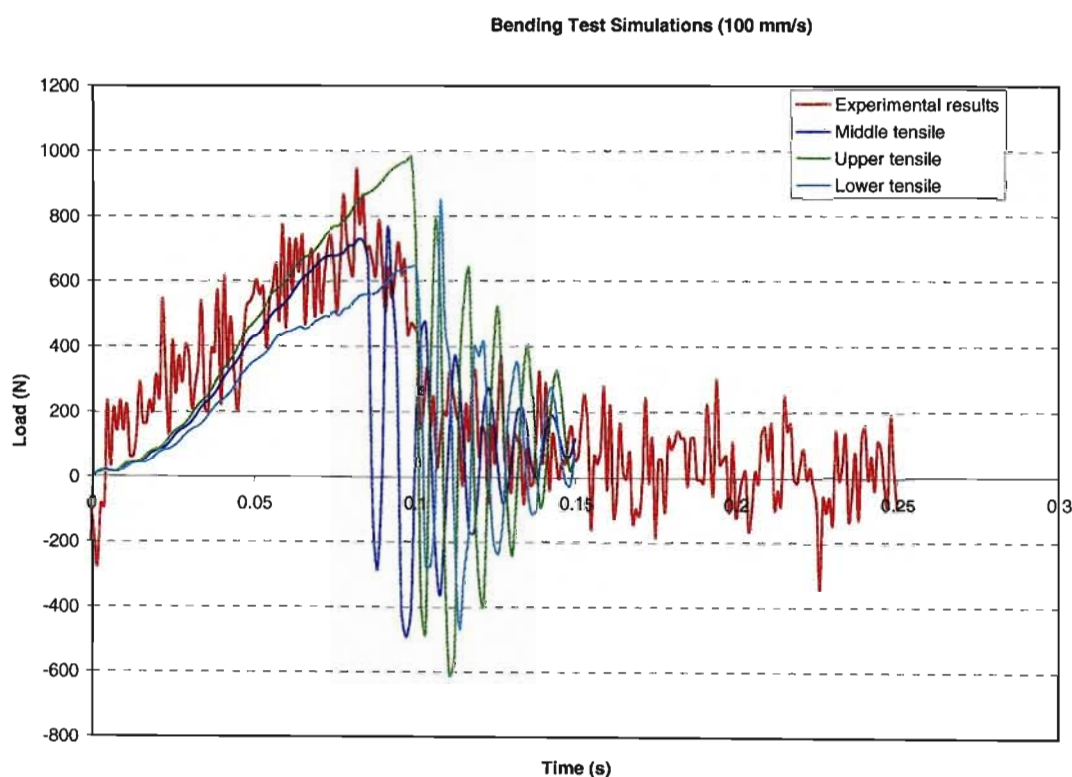


Fig. 4.35 Complete comparative results incorporating the tensile characterisation.

4.3 Crashworthiness modelling and simulation of the thin-walled composite automotive component

Another attempt in the development of a working simulation model for the crash behaviour of a thin-walled composite component with complex geometry involves manufacturing, testing and simulation of the selected prototype (demonstrator). The adopted geometry of the prototype was

selected to be similar to the spare wheel compartment of the Renault Clio. In order to simplify testing and analysis, the prototype shape was modified to a flat rectangular section combined with the cylindrical spare wheel compartment area as shown in Fig. 4.36.

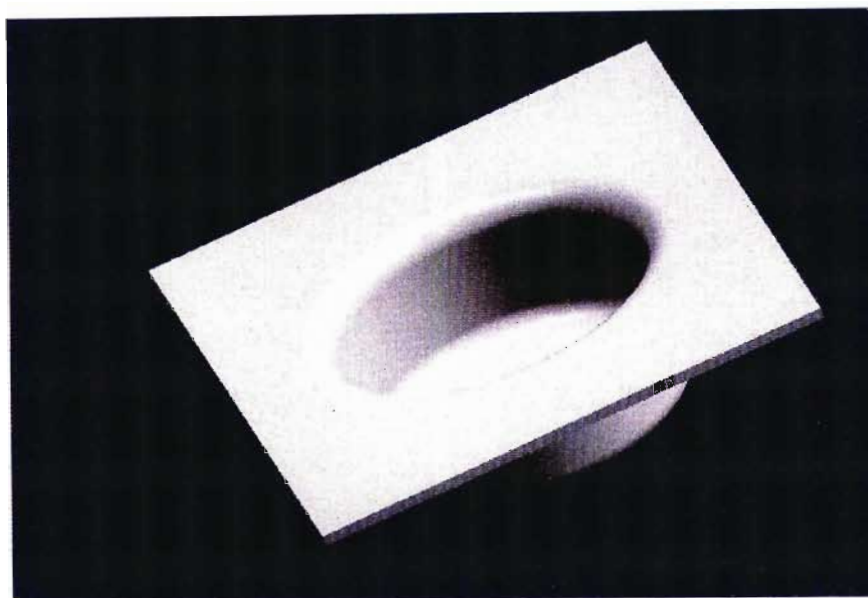


Fig. 4.36 Prototype geometry.

Scaling of the prototype was predetermined by the power and size of working area of the available testing equipment.

The design model dimensions were 1000 mm wide by 1120 mm in length with hole diameter of 640 mm and depth of 100 mm. The test prototype was scaled down to 230 x 190 mm, with a hole diameter of 120 mm and depth of 50 mm. A uniform thickness of 4 mm was selected for moulding of the prototype.

4.3.1 Prototype manufacture

The material and manufacturing process for the prototype fabrication were the same as for flat specimens and plates (see Section 4.1.1). A thermosetting material such as SMC requires a moulding process that is suitable for its sheet form. In this regard it is usually recommended that compression moulding using matched dies of steel or aluminium is used. In this case, pre-heating of the material is not required, but pre-heating of the dies is. The temperature is dependent on the resin chemistry and filler content, and ranges from 140-160 °C. The mechanical pressure applied on the male die depends on the flow characteristics of the feed material, and ranges from 10-50 MPa.

The relatively complicated geometry of the prototype meant much consideration had to be given to how the heating of the moulds would be performed. After all options were weighed up, it was decided that the most practical option would be to use the same cartridge heaters used in the specimen moulds. This would substantially save on outlay, as the very same elements could be re-used during prototype manufacture, along with the controllers, thermocouples and digital output displays. Arrangement of the cartridges was carefully considered, until the design shown in Figs 4.37-4.39 was decided upon. This arrangement ensures relatively even heat distribution and ease of access.

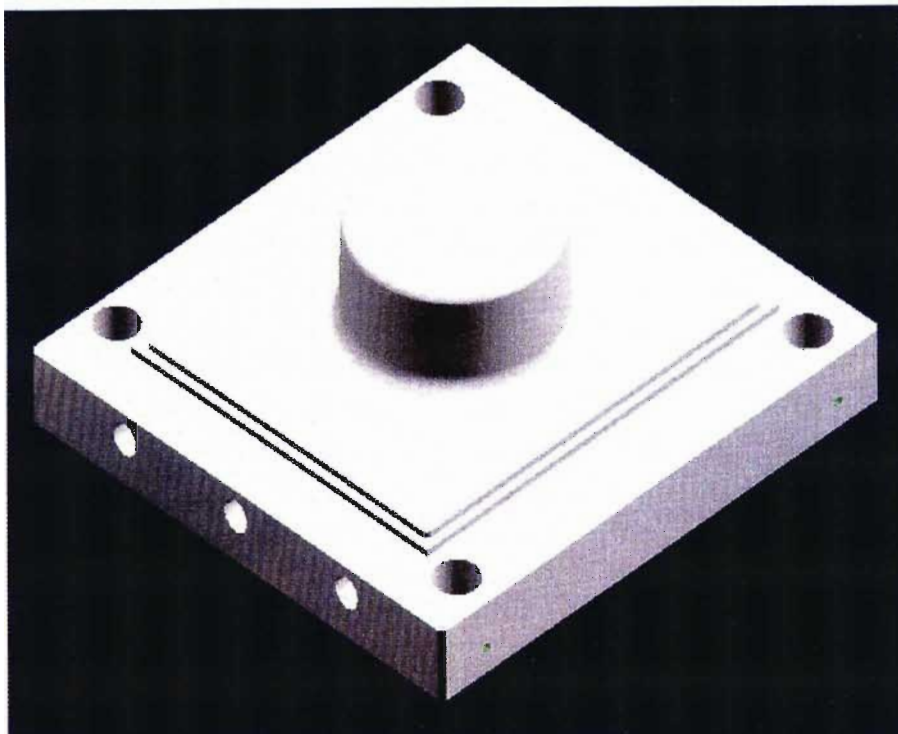


Fig. 4.37 Prototype mould 'male' section.

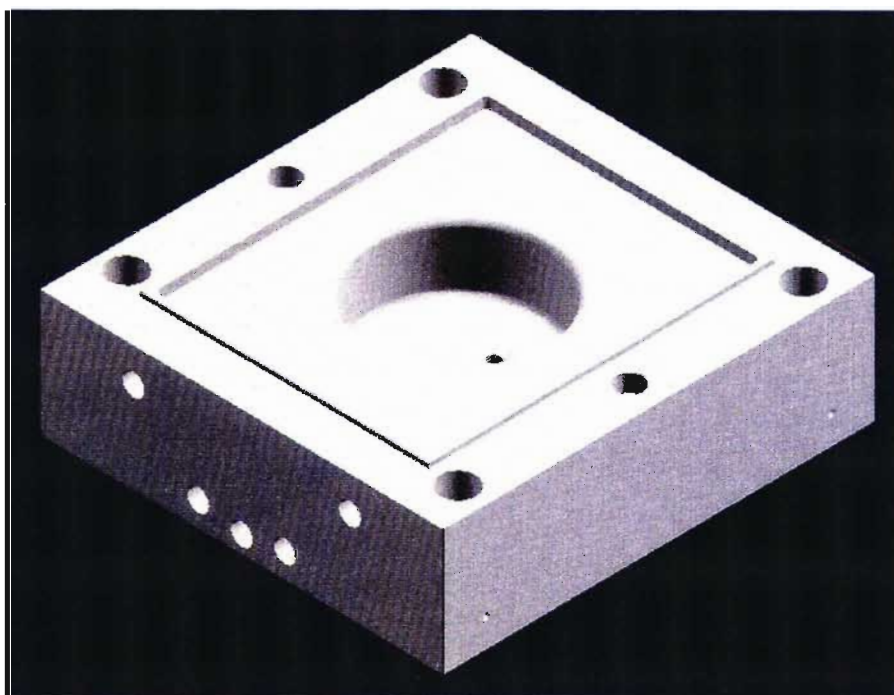


Fig. 4.38 Prototype mould 'female' section.

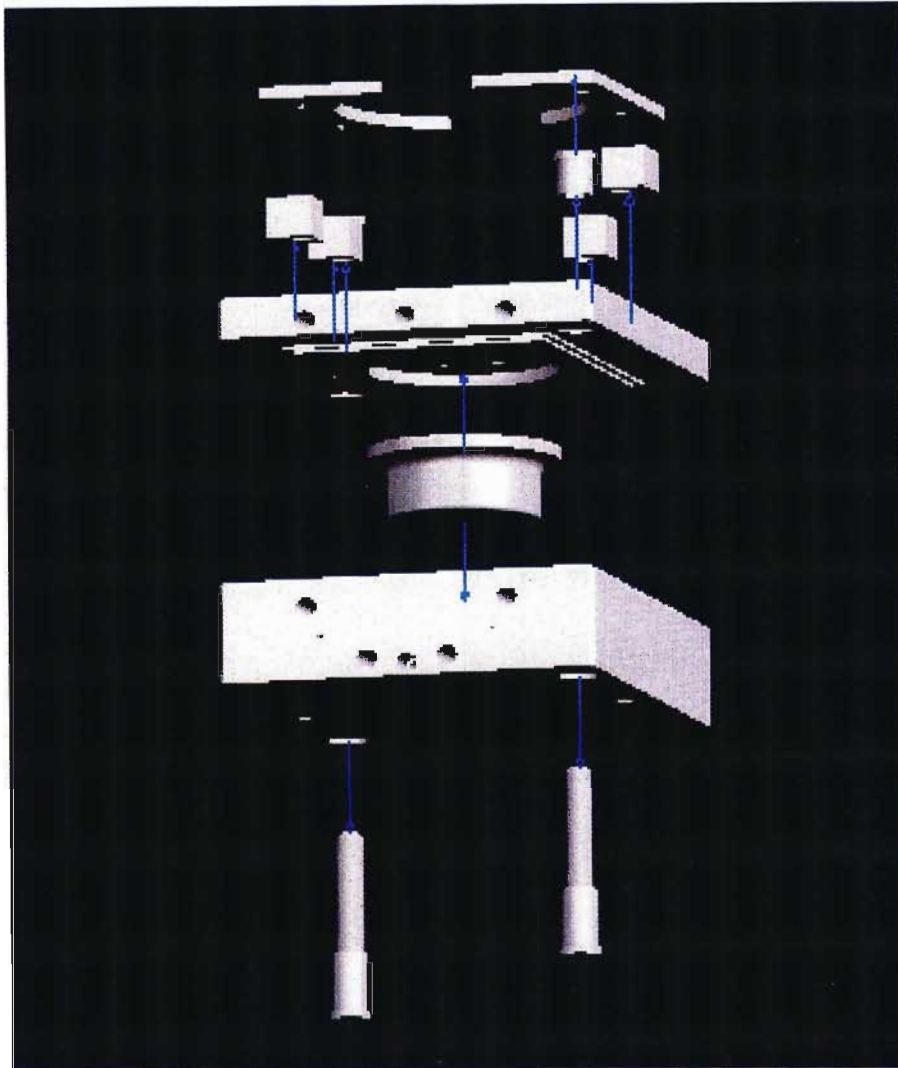


Fig. 4.39 Schematic of the prototype mould including mounting brackets, spacers, and guide pins.

The material had a shrinkage value of 0.05% and due to the size of the component this effect was neglected. The moulded part was designed for removal from the bottom mould. This was achieved by designing the female mould with a draft angle of 1° . A mild steel has been used for the mould fabrication. An ejection mechanism has been incorporated for easy and clean removal of the component.

Manufacturing process included the following set of operations:

- (1) Mould and ejector pin cleaned and polished.
- (2) Setting of upper and lower mould temperature with power supplied to heating elements.
- (3) Once upper and lower mould reach required temperature the correct amount of material is inserted into the mould.

- (4) Press is activated and ram closes until the required pressure is reached. This pressure is kept constant for the required curing time.
- (5) Press opened and component ejected by compressed air operated ejection pin.
- (6) Cooled component is finished by grinding.

Process specifications are: temperature -150°C , press load -330kN , curing time -120 sec .

The schematic of hardware setup is shown in Fig. 4.40. Fig. 4.41 shows the temperature controller which is connected to the cartridge heating elements that are inserted into horizontally bored holes in the mould halves. The placement of the elements is shown in Fig. 4.42, where the end-connectors and attached electric cables can be seen on the female mould half. As per design, the female mould is heated by four elements and the male mould is heated by three elements (these are on the reverse side of the male mould in Fig. 4.42). Each of the two separate temperature controllers shown in Fig. 4.41 controls the temperature of one half of the the mould. The production cycle of the component is shown in Figs 4.42-4.47.

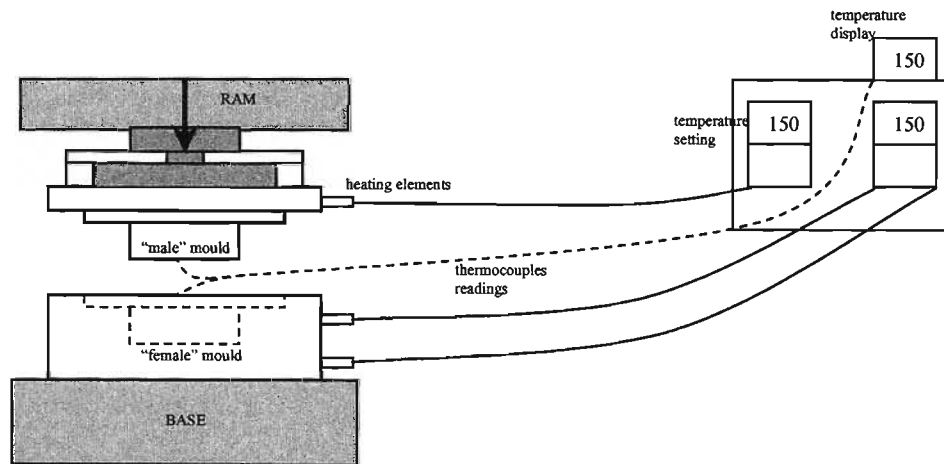


Fig. 4.40 Prototype manufacturing process.

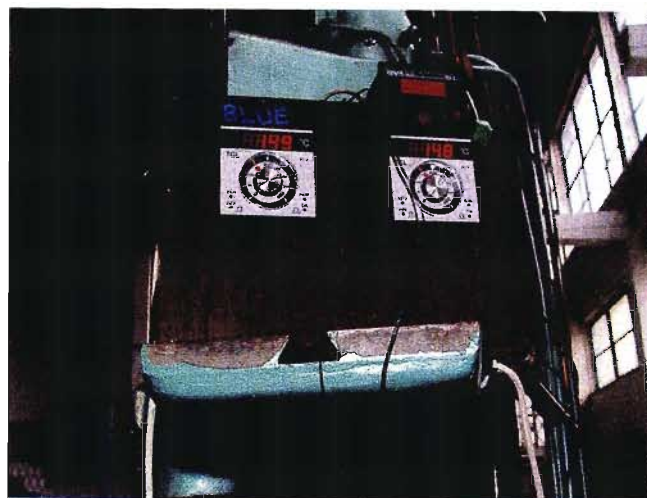


Fig. 4.41 Temperature controllers

The two halves of the mould assembled on the press are shown in Fig. 4.42. The heater elements are shown inserted into the moulds. The two guide pins are used to align the two halves of the mould.

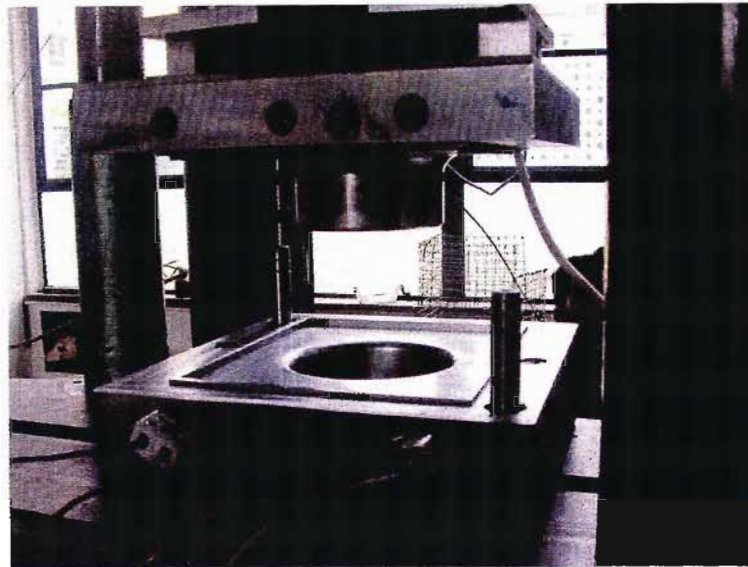


Fig. 4.42 Mould assembled on press.

The moulds are then heated to the appropriate temperature, and the required volume of raw SMC composite material is placed in the mould cavity, as shown in Fig. 4.43.

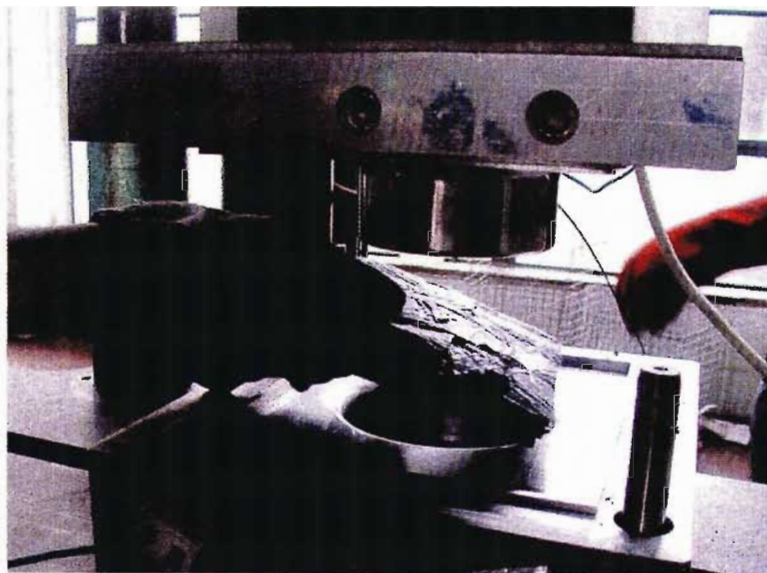


Fig. 4.43 Raw SMC material being placed in mould.

Pressure is then applied and the mould closed, as shown in Fig. 4.44.

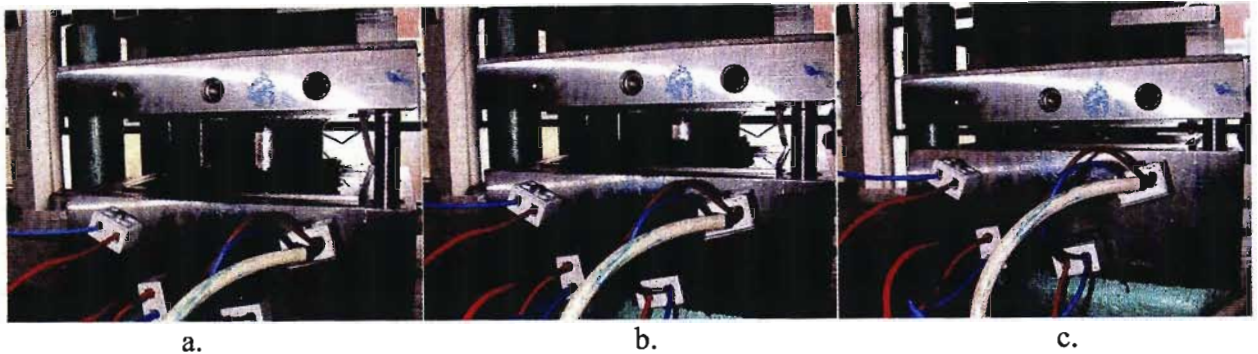


Fig. 4.44 Closing the moulds.

Once the mould is closed, a force of 33 tons is applied for a curing time of 120 seconds.



Fig. 4.45 Prototype attached to male section after curing.

The moulded prototype, of uniform 4mm thickness, is then ejected using an ejection system built into the female mould, and removed. The moulded component is shown in Fig. 4.46, immediately after removal from the mould.

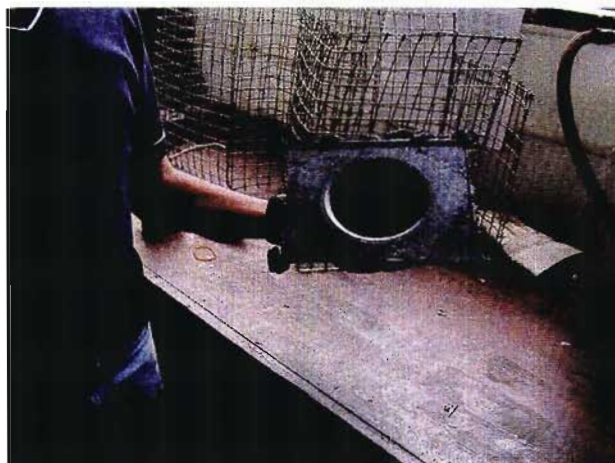


Fig. 4.46 Moulded prototype.

The moulded prototype was then finished, by grinding off any excess material (see Fig. 4.47).

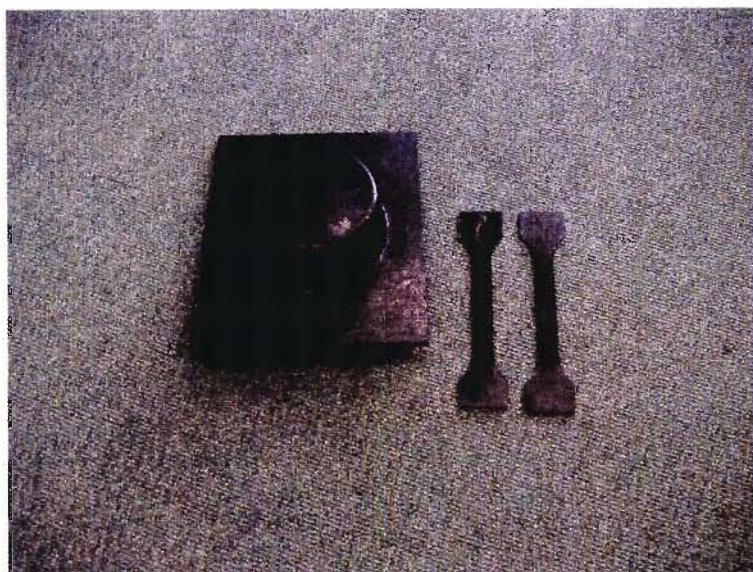


Fig. 4.47 The completed specimens and prototype.

The short moulding time, coupled with an efficient temperature control and ejection system allows components to be produced relatively quickly. A number of prototypes have been produced, to allow for multiple crash runs, and subsequent refinement of the crash testing process (see Fig. 4.48).

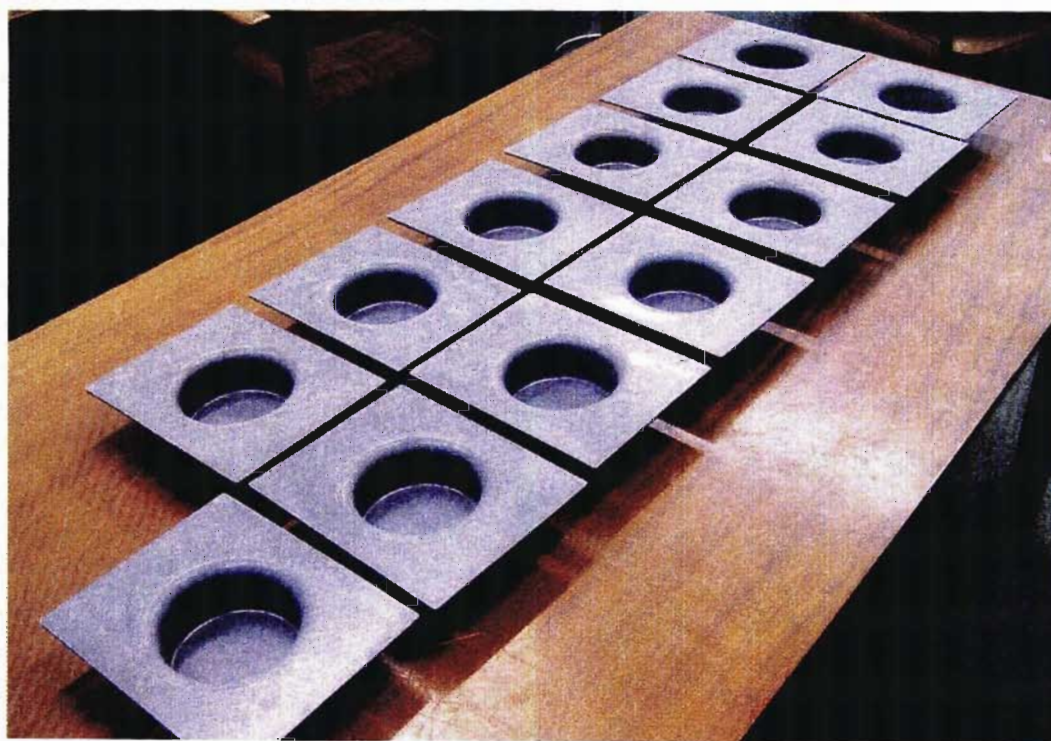


Fig. 4.48 Prototype production run.

4.3.2 Prototype testing

Prototype testing has been used for further evaluation of the performance of the instituted model. Direct comparison between the simulated data and that obtained during physical testing served as the basis for model validation.

The part has been tested under crushing in order to demonstrate a typical failure of the spare wheel holder due to a rear impact to the vehicle. The data obtained from the test is presented as a force displacement curve which shows the maximum load the component can withstand before failure and demonstrates the components ability to sustain load during the impact/crushing process. Further calculations that may be made from this curve include calculation of the total energy absorbed and the energy absorbed per unit mass of the material. A similar concept used to evaluate the crash performance of impact absorbing composite members is the specific sustained crushing stress (SSCS), which is a measure of the energy absorbed in crushing each kilogram of the composite.

Testing was conducted on an MTS test rig and the experiment setup is shown in Fig. 4.49. Possible methods of supporting the prototype during testing included incorporation of adhesive tabs, use of grip wedges or special design of end fixtures. Design of two piece end fixtures was the route followed, as this allows for easy fitting to the test rig and facilitates mounting and removal of the test-piece during testing.

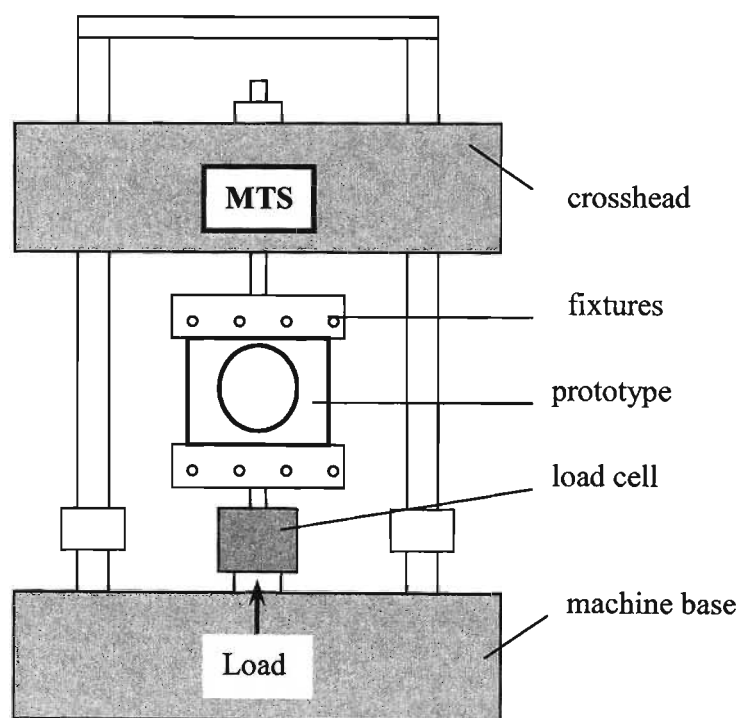


Fig. 4.49 Prototype test setup.

Loading of the part in compression is accomplished through the rig's hydraulically activated piston and the applied load is read via the load cell. Time readings allow for conversion of the data in order to produce force displacement plots. This was done for the three velocities of 2, 50, and 100 mm/s and the results are shown in Fig. 4.50. Examples of the destroyed part are provided in Fig. 4.51.

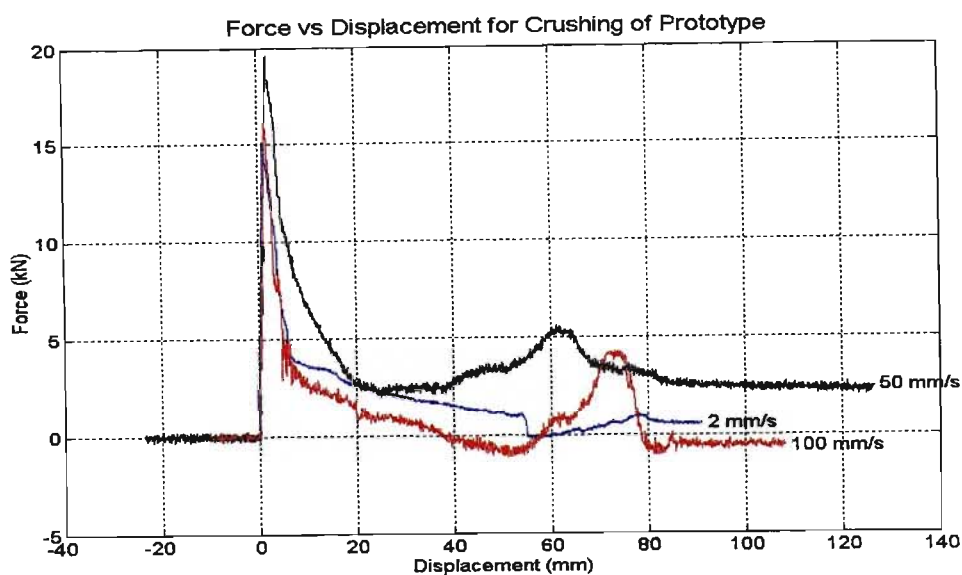


Fig. 4.50 Results for crash of prototype demonstrator.

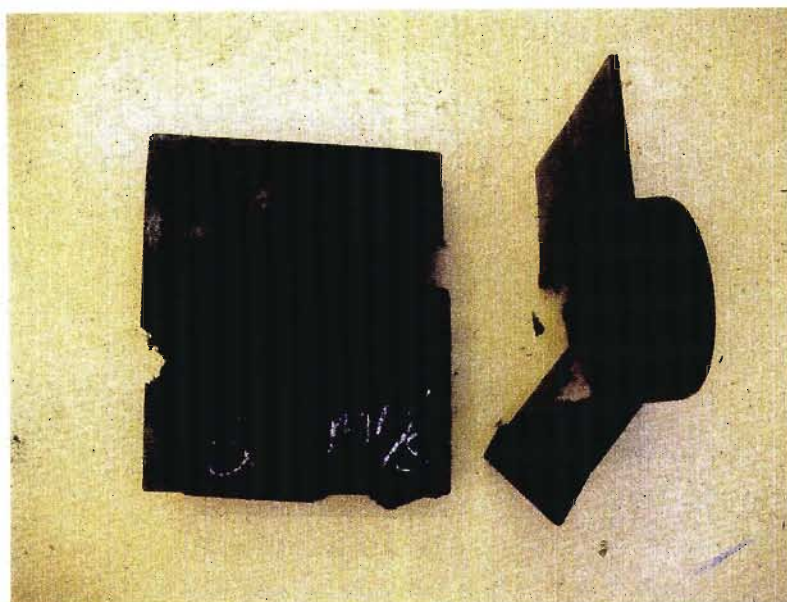


Fig. 4.51 Destroyed prototype demonstrator.

4.3.3 Prototype simulation

The next stage in the development of a working model for the crash behaviour of a thin-walled composite component, involves the simulation of the crushing of the selected prototype. As has been previously detailed, the prototype component is a scale model of the spare wheel compartment. A batch of these prototypes has been manufactured and physical crushing of the prototype was conducted on an MTS test rig (see Sections 4.3.1-4.3.2). The material from which the prototype is manufactured has also already been characterised and the material characteristics

entered into the model to describe PAM-CRASH Material Type 105 (which is the selected material model for SMC composites) (see Section 4.1.2).

With the material already described in the PAM-CRASH environment, the mesh representing the prototype was constructed using MSC.NASTRAN and comprises 673 nodes (Fig. 4.52). Further simulation parameters are shown below.

PAM-CRASH simulation parameters:

Number of nodes:	673
Element type:	shell
Termination time:	3 sec
Number of states for time history:	50
Number of states for mesh plot:	10
Type of time step:	small
Material type:	105

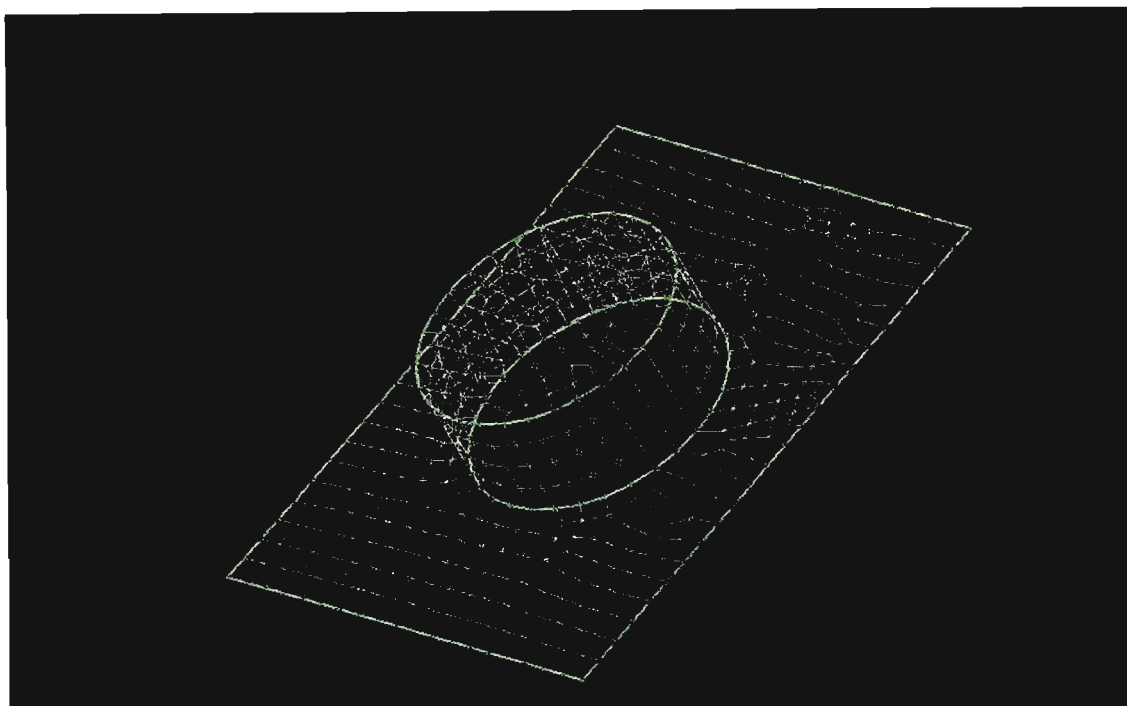


Fig 4.52 Meshed prototype.

Boundary conditions were applied to the nodes along the two shorter edges of the prototype, as they are applied during testing. This means that no rotation or translation is allowed on one edge (the 'clamped' end) and the opposite edge is free only to translate in the direction of the applied velocity. The velocity applied to the moving edge forces it to translate at 100mm/s. Fig. 4.53 shows

the force plots obtained from the simulations, together with the results obtained from physical testing. The numerical simulations were performed using the four sets of experimental data (see Table 4.1.). The corresponding Force-Displacement curves are presented in Fig. 4.53. As can be seen, all four simulated responses follow the experimental curves and are in reasonable correlation with the test results.

The differences in the peak loads could be explained by the mixed buckling – progressive bending mode of failure of the component (see Fig. 4.54). As shown, buckling of the flat portion of the prototype occurs at the initial stage of loading. This provides a justification for the existing difference (typical for buckling analysis) between the experimental results and simulation. Further deformation process involves combined post-buckling bending and progressive folding of the component, which is concluded by the fracture (see Fig. 4.51).

Force Displacement Plots for Crushing of Prototype

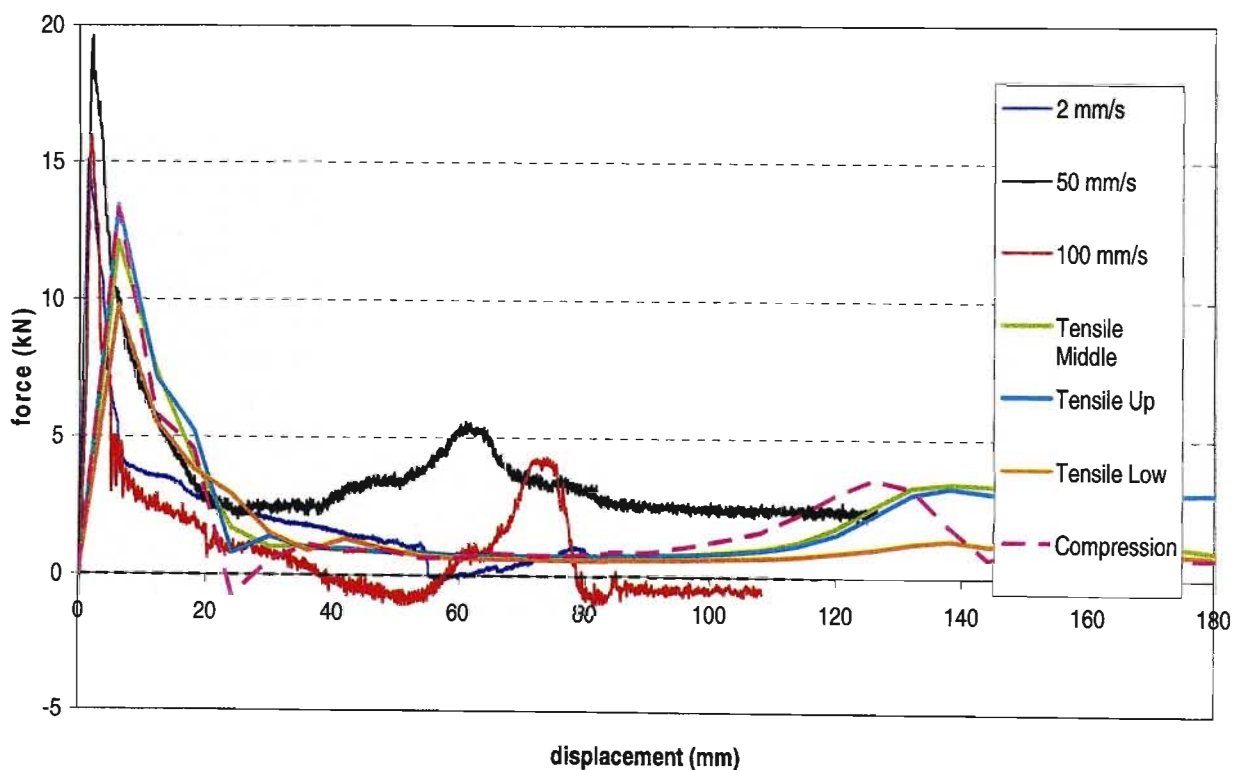


Fig. 4.53 Force-Displacement curves for crushing of prototype (comparison of simulation and experiment).

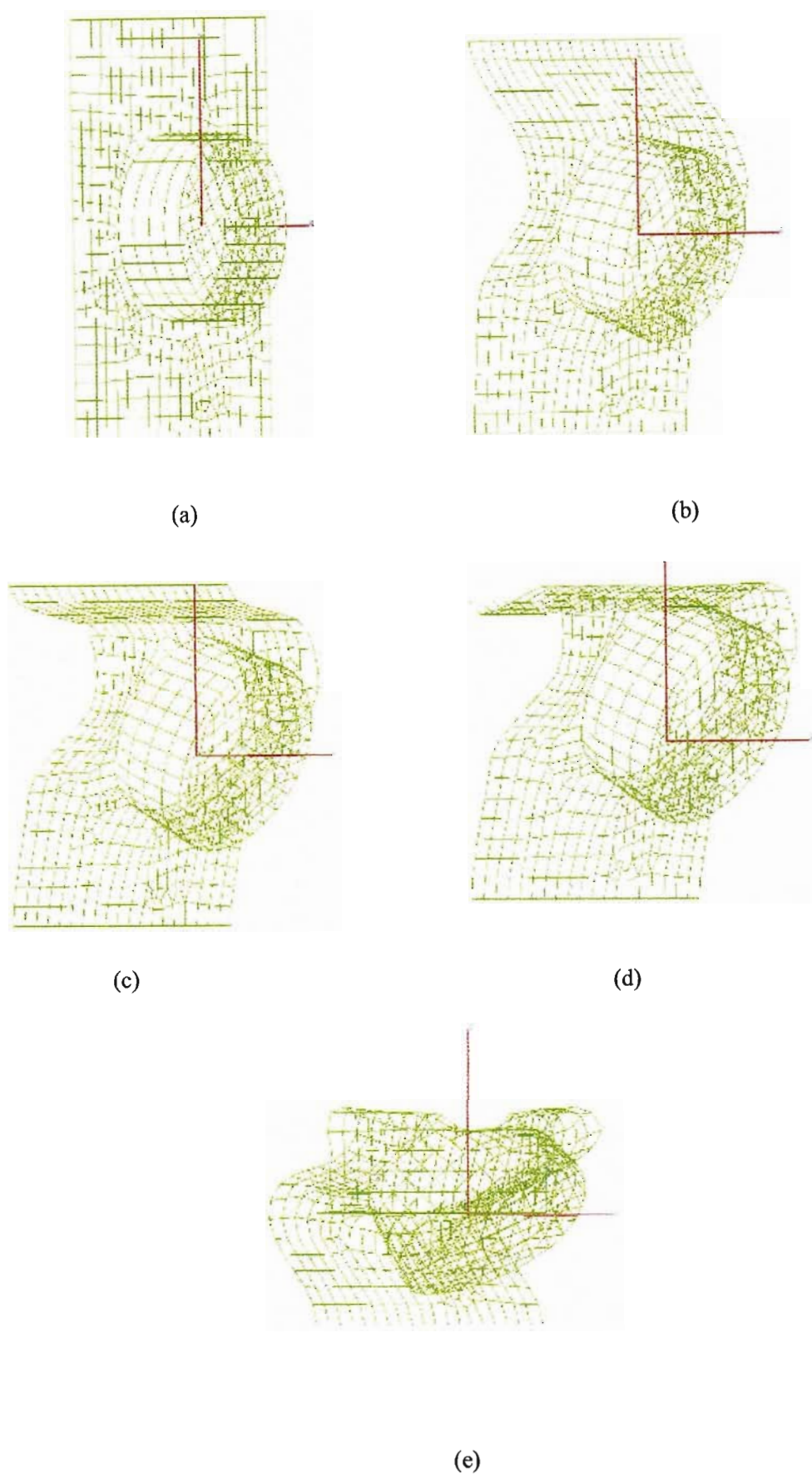
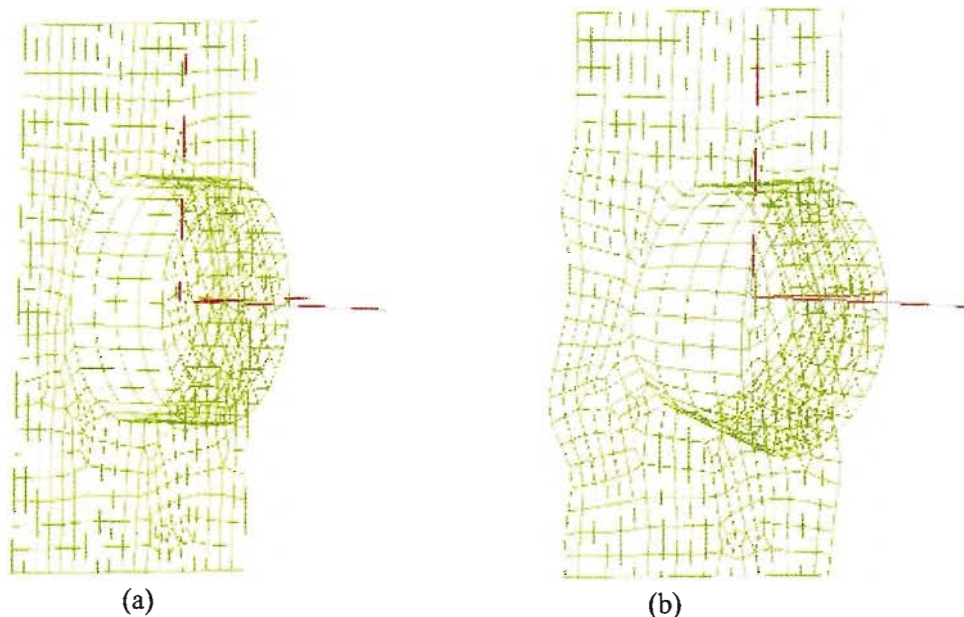


Fig. 4.54 Progressive deformation of the prototype.

As follows from the comparative results displayed (see Fig. 4.53), the modelling of SMC composite structures using the selected material model provides results, which whilst certainly showing a similar trend and failure profile, yields some discrepancy when compared to the experimental results. This might point to a need for experimentation with regard to primary material characterisation to be more closely investigated and refined, so that a fair level of confidence in the exact evaluation and definition of the model parameters is justified. The nature of randomly reinforced materials ensures that this task is both necessary and complex, since scatter in the exhibited properties of the material is usually apparent, due to its inherent inhomogeneity. Experimentation should also be repeated as often as it feasible, to create a set of data that is reflective of the average nature of the material being analysed. In general, the progressive failure simulation model (including material characterisation procedure and numerical analysis) considered in the present work could be adopted as a tool for the virtual crash-simulations of a thin-walled SMC-composite structures with complex shape and geometry.

Simulations of the prototype crushing have been also performed for impact loading conditions. The prototype has been subjected to the impact of added mass with prescribed initial velocity. The load has been applied to the edge of the prototype that could only translate in the direction of loading (as for the compression test simulation). No rotations or translations were allowed at the opposite clamped edge. Simulations have been conducted for the added mass of 1000 kg and initial velocities of 1 m/s and 5 m/s. Simulation results obtained for the initial velocity of 1 m/s are presented in Figs 4.55-4.56. The corresponding plots obtained for the initial velocity of 5 m/s are shown in Figs 4.7-4.58. As could be seen (Figs 4.55-4.58), the modes of progressive failure of the prototype under this type of loading differ from the mode obtained for the crushing under constant velocity (compressive test conditions) (see Fig. 4.54). The failure modes shown in Fig. 4.55 and Fig. 4.57 demonstrate distinctive influence of the dynamic character of loading.



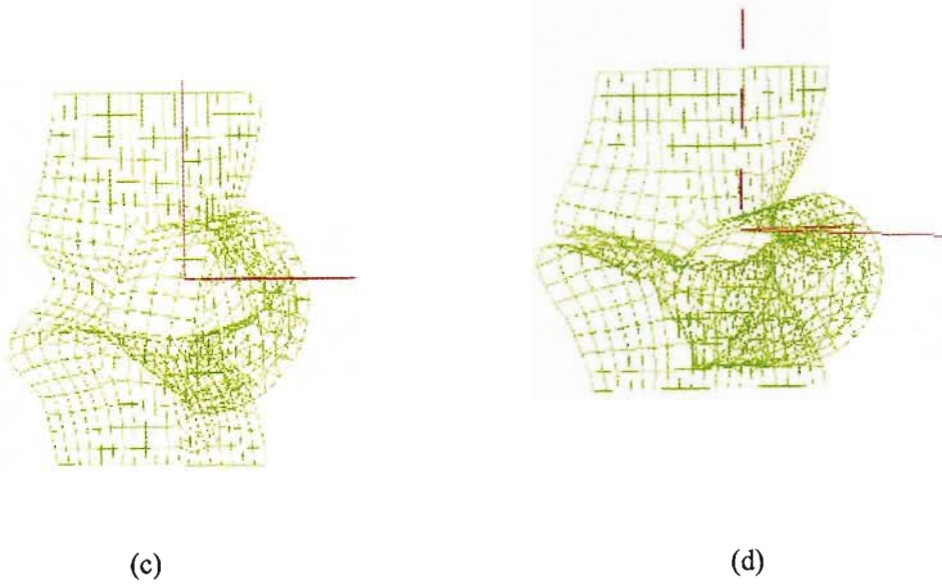


Fig. 4.55 Progressive prototype deformation (Initial velocity 1 m/s).

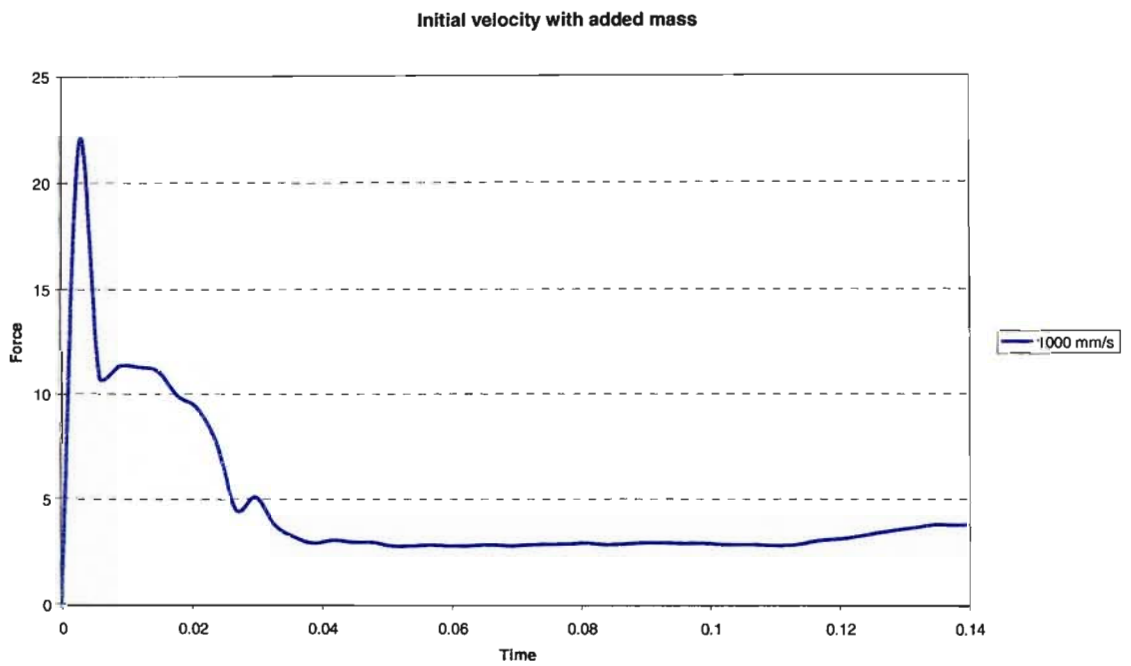


Fig. 4.56 Force-Time curve for simulation with initial velocity 1 m/s.

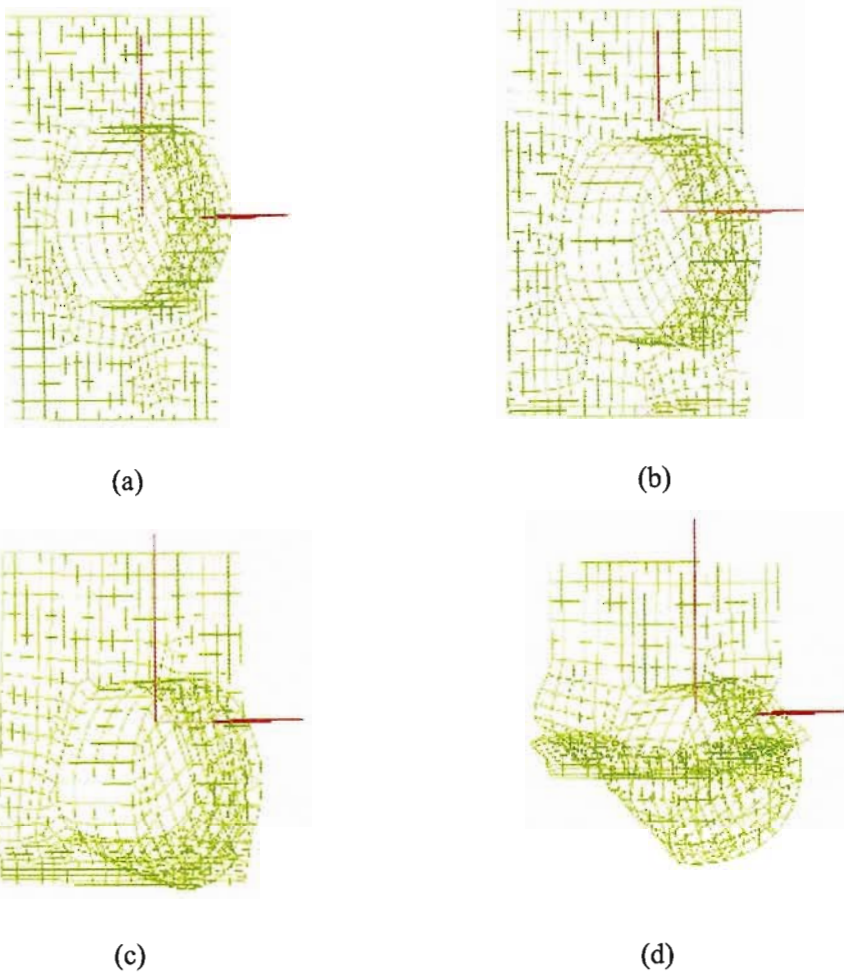


Fig. 4.57 Progressive prototype deformation (Initial velocity 5 m/s).

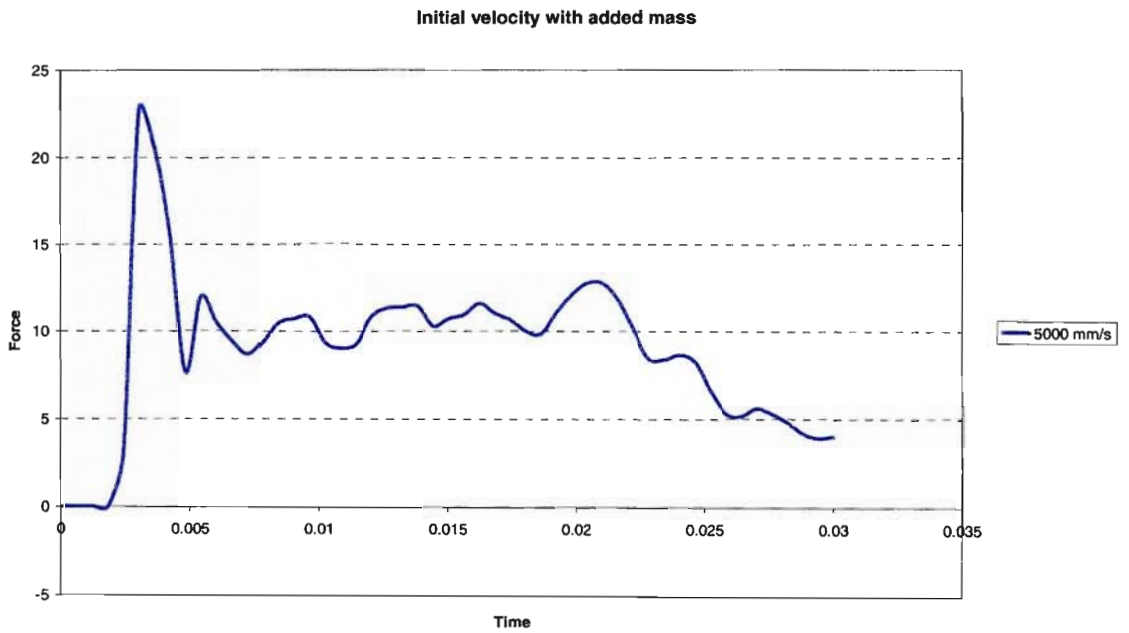


Fig. 4.58 Force-Time curve for simulation with initial velocity 5 m/s.

It should be noted that the SMC material utilized in this work did not exhibit substantial susceptibility to the strain rate effect. Correspondingly, the crushing simulations of the prototype were performed under assumption that the material properties were not affected by the rate of loading. At the same time the model and software considered here have all the necessary capabilities to incorporate the strain rate dependence into analysis, subject to the availability of the appropriate experimental data (see strain rate model description presented in Section 2.3.1.1).

In conclusion, the simulation results of the prototype progressive failure obtained for the impact loading conditions in this work demonstrate the capability of the model and the approach as a whole to provide reliable prediction of the structural crashworthiness of the thin-walled components made from SMC composites.

Chapter 5

PROGRESSIVE FAILURE MODEL DEVELOPMENT

This chapter deals with the development of an SMC composite material model (Morozov et al., 2003), incorporating a homogenisation model and statistical damage criteria. The model theory and the basis for implementation of the model into a commercial finite element analysis package are both presented here. Coarse model validation is performed by evaluating the model parameters for a set of sample data, and applying these to the modelling of the progressive fracture of an SMC plate under tensile loading.

An overview of the progressive damage models (see Sections 2.2.1-2.2.2) that have been developed for the analysis of SMC composite materials reveals two distinct methods of modelling. Firstly, the material may be modelled on the basis of micromechanics using the material constituents, viz. the fibres and matrix and their volumetric fractions as main structural components of the material. The homogenisation procedure is normally applied in order to obtain the overall properties of the composite. Secondly, the SMC material may be characterised using a macroscopic approach, which is based on the testing of a sample of the actual material itself. The model developed here is an example of the former, with the material constitution adopted from work carried by Chen et al. (1992), and a newly proposed damaging model based on the work of Desrumaux et al. (1995).

5.1 Progressive failure criterion

The model makes use of the Mori-Tanaka homogenization scheme (see Chen et al., 1992) to express the overall properties of a randomly reinforced short fibre composite in terms of the properties of its constituents.

5.1.1 Material constitution

The constitution of a transversely isotropic solid (in this case the fibre phase in local coordinates) may be expressed as follows:

$$\begin{bmatrix} s \\ \sigma \end{bmatrix} = \begin{bmatrix} k & l \\ l & n \end{bmatrix} \begin{bmatrix} e \\ \varepsilon \end{bmatrix} \quad (5.1)$$

$$\tau_{12} = 2p\varepsilon_{12}, \quad \tau_{13} = 2p\varepsilon_{13}, \quad \tau_{23} = 2m\varepsilon_{23},$$

where

$$s = \frac{1}{2}(\sigma_{22} + \sigma_{33}), \quad \sigma = \sigma_{11}, \quad e = \varepsilon_{22} + \varepsilon_{33}, \quad \varepsilon = \varepsilon_{11} \quad (5.2)$$

Here σ_{11} is the stress, in the local co-ordinate frame of the fibre, experienced along the longitudinal axis of the fibre, σ_{22} is the stress transverse to the fibre, and σ_{33} is the stress along the orthogonal axis in the transverse plane. The strains ε_{11} , ε_{22} and ε_{33} are similarly assigned to these respective axes. Stresses τ_{12} and τ_{13} are the shear stresses acting in the plane of the fibre, along the transverse and orthogonal axes respectively, and τ_{23} is the shear stress in the transverse plane, acting along the orthogonal axis.

The parameters k , l , m , n and p are Hill's elastic moduli (Hill, 1964). Specifically, k is the plane-strain bulk modulus for lateral dilation without longitudinal extension, n is the modulus for longitudinal uniaxial straining, l is the associated cross modulus, m is the shear modulus in any transverse direction and p is the shear modulus for longitudinal shearing.

For composites reinforced with randomly oriented fibres, with the matrix (denoted by subscript $r = 1$) and fibre phases (denoted by subscripts $r = 2, 3, \dots, N$) being isotropic and transversely isotropic in the local frame respectively, the overall moduli may be given by the following relations (Chen et al., 1992):

$$\begin{aligned} K &= K_1 + \frac{1}{3} \sum_{r=2}^N c_r \frac{(\delta_r - 3K_1\alpha_r)}{\left[c_1 + \sum_{r=2}^N c_r \alpha_r \right]} \\ G &= G_1 + \frac{1}{2} \sum_{r=2}^N c_r \frac{(\eta_r - 2G_1\beta_r)}{\left[c_1 + \sum_{r=2}^N c_r \beta_r \right]} \end{aligned} \quad (5.3)$$

where

K , G are the overall bulk and shear moduli, respectively, of the composite material, c_r are the volumetric fractions of each phase r , with the matrix phase assigned $r = 1$ and the inclusion (fibre) phases following as $r = 2, 3, \dots, N$. Since usually only one fibre material or geometry is used for reinforcement, $r = 2$ usually pertains to that single material.

Thus

$$\begin{aligned} K &= K_1 + \frac{1}{3} c_2 \frac{(\delta_2 - 3K_1\alpha_2)}{[c_1 + c_2\alpha_2]} \\ G &= G_1 + \frac{1}{2} c_2 \frac{(\eta_2 - 2G_1\beta_2)}{[c_1 + c_2\beta_2]} \end{aligned} \quad (5.4)$$

Parameters $\alpha_r, \beta_r, \delta_r, \eta_r$ depend on the moduli and geometry of the phases, and for cylindrical fibres are given as follows:

$$\begin{aligned} \alpha_r &= \frac{3K_1 + 3G_1 + k_r - l_r}{3G_1 + 3k_r} \\ \beta_r &= \frac{1}{5} \left[\frac{4G_1 + (2k_r + l_r)}{3G_1 + 3k_r} + \frac{4G_1}{p_r + G_1} + \frac{2(\gamma_1 + G_1)}{\gamma_1 + m_r} \right] \\ \delta_r &= \frac{1}{3} \left[n_r + 2l_r + \frac{(2k_r + l_r)(3K_1 + 2G_1 - l_r)}{k_r + G_1} \right] \\ \eta_r &= \frac{1}{5} \left[\frac{2}{3} (n_r - l_r) + \frac{8m_r G_1 (3K_1 + 4G_1)}{m_r (3K_1 + 4G_1) + G_1 (3K_1 + 3m_r + G_1)} + \right. \\ &\quad \left. + \frac{8p_r G_1}{p_r + G_1} + \frac{4k_r G_1 - 4l_r G_1 - 2l_r^2 + 2k_r l_r}{3k_r + 3G_1} \right] \end{aligned} \quad (5.5)$$

where, for an isotropic matrix,

$$\gamma_1 = \frac{3G_1K_1 + G_1^2}{3K_1 + 7G_1} \quad (5.6)$$

Note that the elastic moduli of the fibre phases are defined in the local coordinate frame of that fibre.

It is also possible using this formulation to incorporate the possibility of the inclusion phases being so called 'composite fibres', made up of cylindrical unidirectional fibre composite material. The advantages of this modelling option are immediately evident. Typically, characterisation of the individual component phases of a composite is inconsistent and sometimes even unrealistic. The characteristics of the dry fibre are for example not necessarily reflective of the same fibre impregnated with matrix material, thus it makes sense to rather test samples that take this impregnated effect into account. To thus replace our fibre phase in the above formulation by a unidirectional composite, which is simpler to test and also takes into account the composite nature of the very inclusion itself, would appear justifiable.

5.1.2 Statistical damage law

It is proposed that damage is introduced in the material defined by the above formulation by introducing statistical theory based on that presented by Desrumaux et al. (1995), which makes use of the Weibull distribution. The application of this distribution to characterise the failure of brittle materials particularly is fairly well established (see Bury, 1975). The distribution may be imposed to statistically control the failure pattern of the composite material, by extrapolating the results of testing of standard samples to the analysis of structures under a variety of loading, through certain statistical relations. Statistical analysis also in some way accounts for the large scatter in experimental results that usually exists in the testing of randomly reinforced composites particularly, attributable to the material's inherent structural inhomogeneity, the random distribution of the inclusion phase, and difficulty in maintaining manufacturing precision and repeatability.

The general statement for probability of failure of the material in question may be expressed as

$$P = 1 - [1 - F(\sigma)] \quad (5.7)$$

where P is the distribution function for the probability of failure of the material under the action of stress σ , which is defined by the specific strength criteria in place.

For example, for the three dimensional case, when applying the shear strain energy (Von Mises) criterion

$$\sigma = \frac{1}{\sqrt{2}} \sqrt{(\sigma_1 - \sigma_2)^2 + (\sigma_2 - \sigma_3)^2 + (\sigma_3 - \sigma_1)^2} \quad (5.8)$$

where σ_1 , σ_2 and σ_3 are principal stresses. The function F in Eqn. (5.7) is the probability function, expressed in terms of the Weibull distribution.

$$F(\sigma) = 1 - \exp\left[-\frac{V}{V_0}\left(\frac{\sigma}{S}\right)^m\right] \quad (5.9)$$

where m is the Weibull shape parameter, S is the Weibull scale parameter, V_0 is the original volume of the samples used for testing to obtain the Weibull distribution parameters, and V is the volume of the structure to which the distribution is extrapolated.

Whichever strength criterion is adopted, once a pre-determined limit for the overall probability, P , is attained, the material in question is considered 'failed' and either holds no more load carrying capability or is gradually degraded by the lowering of its stiffness properties, until the material is rendered completely failed.

5.2 Model application

Implementation in a finite element analysis environment requires, as a first step, definitions of the inputs of the model. From the above description, the following inputs are revealed:

The bulk and shear moduli, K_I and G_I , of the matrix, where $K_I = \frac{E}{3(1-2\nu)}$ and $G_I = \frac{E}{2(1+\nu)}$ respectively, and where E is the elastic modulus, and ν the Poisson's ratio of the matrix material. These parameters may be obtained from standard specimen tensile testing, or, for commonly used materials such as polyester matrix, such data is readily available.

Parameters k, l, m, n, p for the fibre material can be found as follows. The model definition allows for the possibility that the reinforcement phase may be made up of different materials, but since usually only one fibre material is included, only one set of these constants is required. Once again, these material properties may be obtained from testing, however for traditionally used materials, such as glass fibres, such material constants are available from reference. The constants may be related to more commonly adopted stresses by manipulating Eqn. (5.1), which may be rewritten as

$$\begin{bmatrix} k & l \\ l & n \end{bmatrix} = \begin{bmatrix} s \\ \sigma \end{bmatrix} \begin{bmatrix} e \\ \varepsilon \end{bmatrix}^{-1} = \begin{bmatrix} \frac{1}{2}(\sigma_{22} + \sigma_{33}) \\ \sigma_{11} \end{bmatrix} \begin{bmatrix} \varepsilon_{22} + \varepsilon_{33} \\ \varepsilon_{11} \end{bmatrix}^{-1} = \begin{bmatrix} \frac{1}{2}\sigma_{22} \\ \sigma_{11} \end{bmatrix} \begin{bmatrix} \varepsilon_{22} \\ \varepsilon_{11} \end{bmatrix}^{-1} \quad (5.10)$$

(Assuming no stress and strain contributions along third axis (two-dimensional case))

Thus the strain response of the material under loading (stress), which allows us to find the moduli (k, l, n) is needed to be defined. This may be obtained, once again, from standard specimen testing.

The only shear term that applies for our two-dimensional case is τ_{12} , and since $\tau_{12} = 2p\varepsilon_{12}$ (Eqn. (6.1)), this implies that $2p$ corresponds with the material shear modulus G_{12} , which is also obtainable from testing or reference.

The outputs of the material model, which will in fact serve as inputs to a finite element analysis solver, are the overall bulk and shear moduli, K and G respectively, of the SMC composite material in question. These moduli are defined in a similar manner to which the Young's modulus, E , and the shear modulus, G , are defined for an isotropic material, within the solver. The proposed progressive failure model may then be applied.

Data derived from sample tensile testing is extrapolated to component analysis by applying the Weibull distribution function expressed in Eqns (5.7) and (5.9) above. The purpose of the sample testing is to statistically describe the distribution of the material strength, by evaluation of the Weibull shape and scale parameters. The shape parameter m , may be found by plotting a graph of $(\ln(-\ln(1-F)))$ vs. $\ln(\sigma)$, where F corresponds to the percentage of samples that fails at stress σ . The slope of the graph may be shown to be equal to m , and the scale parameter S , is then obtainable from functions relating the scale and shape parameters (see Eqn. (5.11) for example).

Depending on the number of samples tested, the range of failure for the samples should thus first be sub-divided into appropriate intervals. The cumulative number of failures at each interval is then noted and plotted (Fig. 5.1).

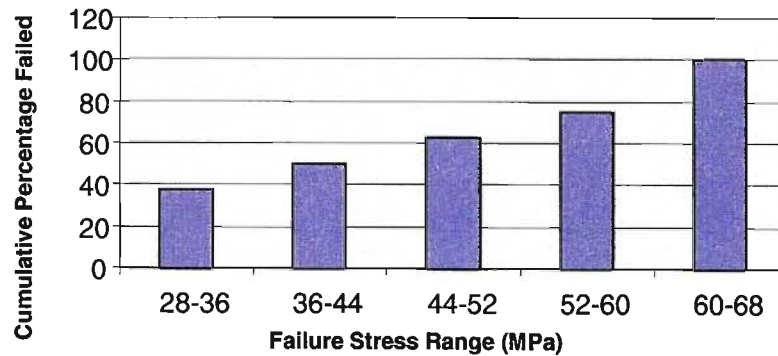


Fig. 5.1 Cumulative distribution for failure stress of samples.

Each interval may then be characterised by its median stress, σ_{fm} , and the cumulative percentage failures (which corresponds to F for the sample distribution) may be plotted against these in the form $(\ln(-\ln(1-F)))$ vs. $\ln(\sigma_{fm})$ (Fig. 5.2) so that the corresponding value of m , the shape parameter, may be found.

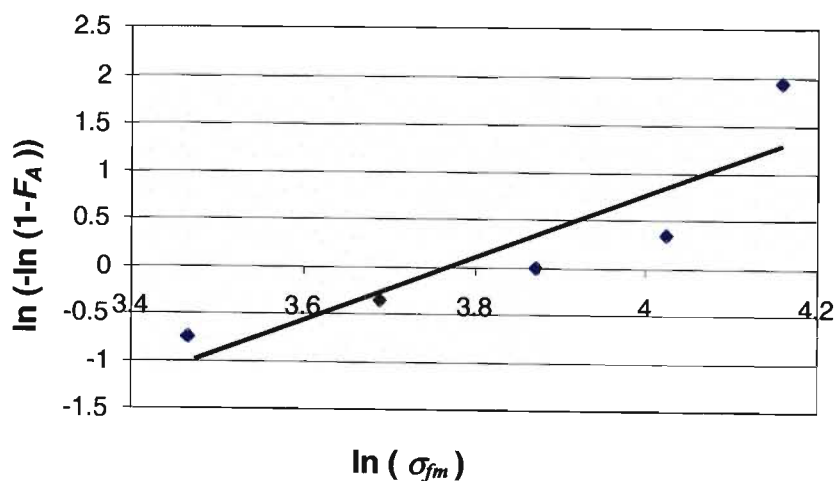


Fig. 5.2 Weibull Shape parameter identification.

The Weibull shape parameter is thus found to be 3.37 (by suitably approximating the slope of the graph). The scale parameter, S , may then be evaluated, since it may be shown (Bury, 1975), that when $\ln(\sigma_{fm}) = 0$,

$$(\ln(-\ln(1-F))) = -m \ln(S) \quad (5.11)$$

The scale parameter S is thus evaluated for our set of experimental data to be 43 MPa. Parameters m_B and $B_{\text{composite}}$ may be similarly found, but with experimental data for sample failure in shear being used.

Alternative methods are also applicable, one such method being an iterative process for finding suitable shape and scale pairs for a given set of experimental data. This involves selecting one of the two variables and then calculating the second, and repeating until convergence of the selected and calculated values occurs (Bury, 1975). Using this technique, values of m and S were found to be 3.5 and 51 MPa respectively for the set of data presented here.

It should also be noted that a so called small-sample 'unbiasing factor', a function of the number of samples taken, N , is usually applied to the shape parameter for relatively small values of N i.e. a low number of observations, typically less than 120. The unbiasing factor for $N=8$ samples here is given as 0.82 (Bury, 1975).

The suitably unbiased shape parameter and the calculated scale parameter may then be substituted into the expression for F (Eqn. (5.9)) to find the probability of failure of the analysed component. The Von Mises stresses (for the shear strain strength criterion) in the material are calculated by the finite element analysis solver, and we may then apply the probability of failure (P), as governed by the above derived formulae, to determine whether an element fails (and therefore either does not contribute any load-carrying capability in the next solver iteration, or is degraded), or not.

For the purposes of an illustrative example, a 150x100x5 mm SMC plate, loaded in tension has been considered. The associated volume of this specimen, 7500 mm³ represents the original volume value V_0 . For the present analysis the volume V is taken to be equal to the volume of each element of the finite element analysis. Thus, failure is attributable at the element level and the progressive degradation of the structure could be observed as elements are progressively degraded. Since the analysis uses an 8x8 mesh, the fraction V/V_0 is thus equal to 1/64 here.

The values for the shape and scale parameter yielded by the iterative technique described above have been used to draw up a table of Probability of Failure vs. Von Mises Stress, for any level of stress, and define that stress level (according to the corresponding probability) that denotes failure of the element. Setting 70 % as the probability limit here, it could be seen that a stress level of 230 MPa corresponds to this limit (Fig. 5.3).

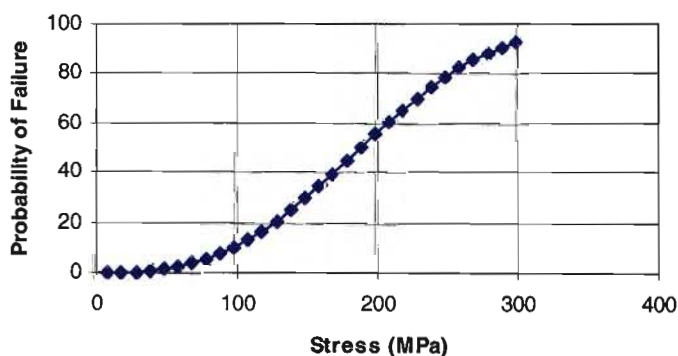


Fig. 5.3 Probability of Failure vs. Stress.

Thus, above a stressed level of 230 MPa, it could be defined that the element in question is rendered failed, and ‘removed’ (converted to so called ‘null’ elements which contribute to volume but not strength), or degraded for the next iteration. Once all the failed elements are ‘removed’ or degraded, the solver is to recalculate the stresses in the material at the next iteration step. It was chosen to merely degrade the stiffness properties of the failed elements by a factor of 50%, which might be more applicable to more ductile materials. The stress levels in the specimen are computed at each step by finite element analysis, as shown in Fig. 5.4.

For computational ease, the example shown here degrades the specimen by groups of 16 elements at a time (quarters of the model), but of course, a more refined degradation (which would require individual elements being assigned individual material properties) is simple to institute especially in a tailor-made analysis algorithm within a user-defined material in a suitable finite element analysis package. The darkest areas above correspond to the areas where stress has exceeded the limit stress of 230 MPa, and is thus degraded appropriately. For this coarse example, once more than 50% of the elements in any quarter exceeded the limit, the entire quarter was degraded by halving the material stiffness properties of that quarter.

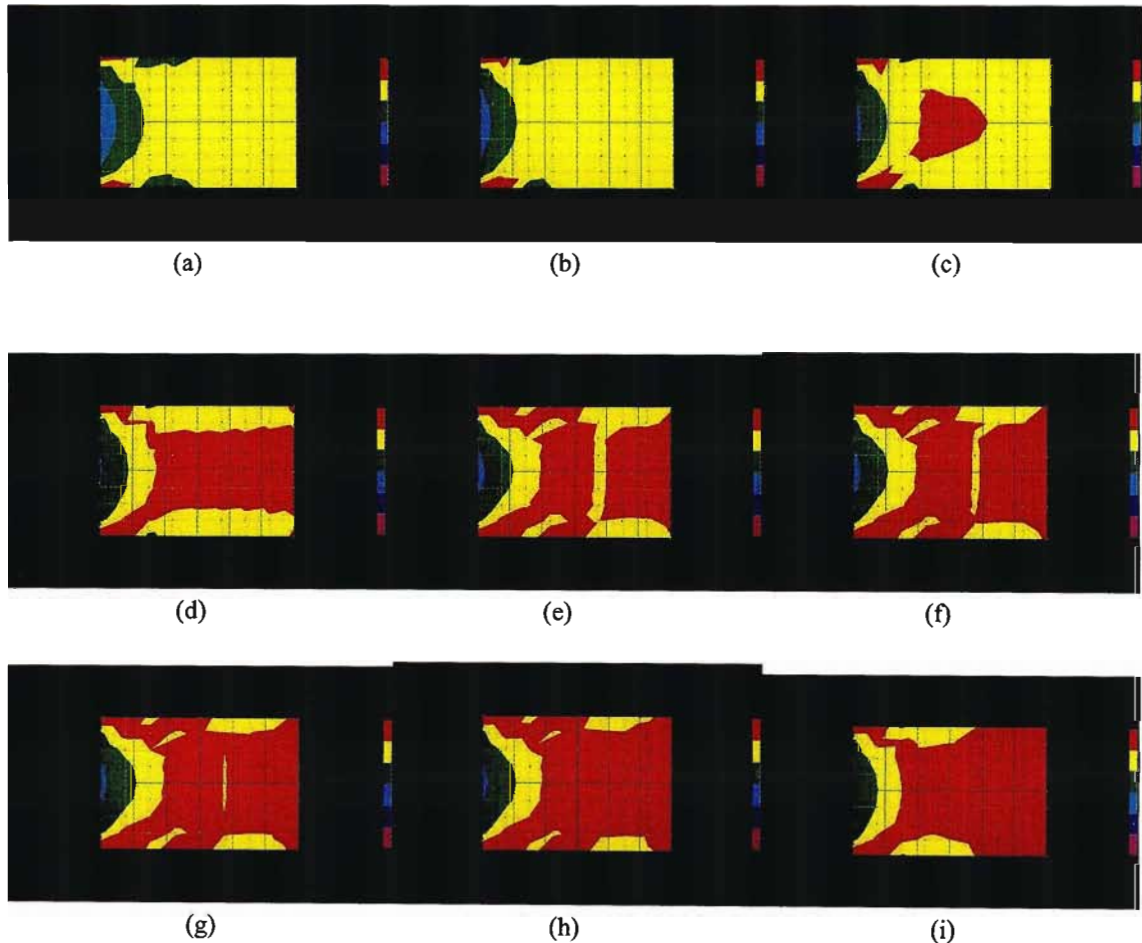


Fig. 5.4 Progression of stress damage in tensile specimen. (a) Loading of 55 kN. Damage initiated. Only 1 element fails. (b) Load increased to 56 kN. Damage progresses to incorporate second element. (c) Load increased to 57 kN. More elements fail. (d) Load increased to 57.5 kN. The two right quarters now almost completely meet the criteria and are both degraded by halving their stiffness properties. (e) The load in the new ‘damaged’ material is increased to 57.6 kN and the stresses redistribute accordingly. The right half

meets degradation criteria again and its stiffness is again degraded by half. The left half is degraded for the first time. (f)-(h) This pattern continues, with each 100N increment yielding successive degradation of the material. (i) At a load of 58kN the material is degraded fully to some limit level (10% stiffness chosen here) and then enters the accelerated fracture phase, characterised by catastrophic degradation of the material stiffness.

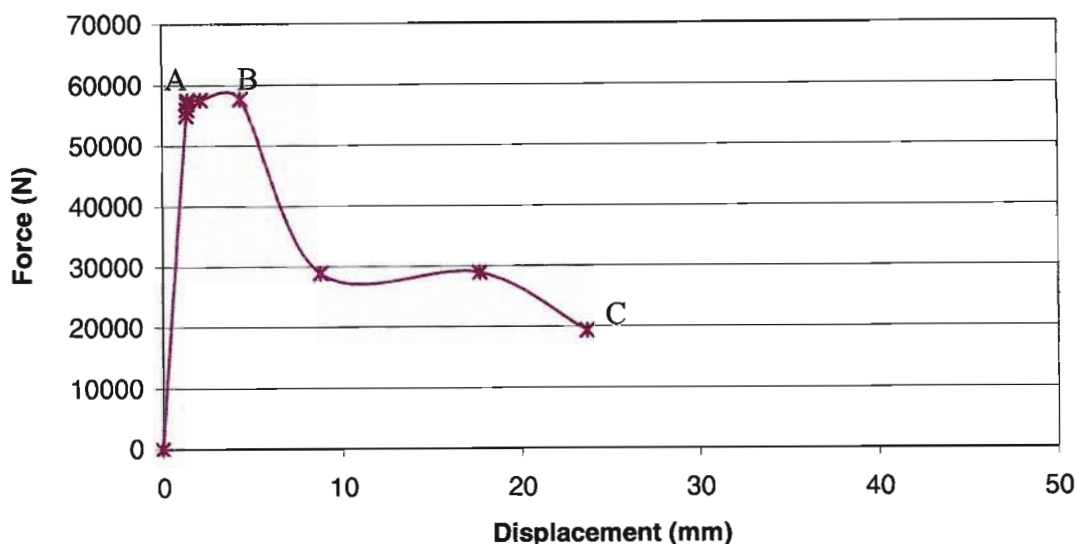


Fig. 5.5 Applied Force vs. Displacement curve for illustrative example

The Force vs. Displacement curve presented in Fig. 5.5 shows the nature of the material behaviour as it undergoes progressive degradation. Point A represents the initiation of damage (initial reduction in stiffness in a portion of the structure, as described in Fig. 4). Point B represents the initiation of catastrophic loss of load carrying ability. The region B-C is modelled by an inverse analysis, where the material stiffness is degraded by a factor of 50% at each increment, and the corresponding force calculated at regular displacement intervals.

At present those material models used for the analysis of SMC composite materials within commercially available finite element software packages take advantage of the overall isotropic nature of these materials. Though this approximation is indicative of the general response of SMC composite materials, it does not allow for any analysis in terms of the material constituents. A model developing a relation between the properties of the constituent phases allows for comparative analysis using various fibre materials, resin materials, and fibre volume percentages. As a further step, stresses within the material may also be associated with the orientation of the fibre phase, before the homogenisation, thus allowing for more representative failure of the reinforcement.

The rather coarse simulation program shown here represents only a first step in the implementation of the proposed model. Efficient and accurate refinement, only be possible once the material model is incorporated directly into a finite element analysis environment, has yet to be performed. Such refinement would include the accurate selection of the probability failure limit (the amount of 70% was arbitrarily chosen here), based on comparison with extended experimental data. Critically also, this sort of implementation will allow for individual material properties to be assignable and degradable at the element level, in real time as and when the element meets the failure criterion, as is the required by the proposed model. Here, limited by step-by-step analysis, only the degradation of large segments of the loaded component, comprised of multiple elements

have been dealt with, thus leading to degradation of these segments, rather than individual elements. Simulation within a dynamic analysis environment will also allow the assignment of a constant velocity loading case, which will eliminate the need to adopt two separate analysis phases (A-B and B-C in Fig. 5.5).

The progressive failure model proposed here has been adopted for integration into a commercial finite element analysis package (PAM-CRASH) as a user-defined option for analysis. This will allow numerous refinement iterations to be performed, so that the material failure limits may be accurately evaluated and validated by experimental comparison.

Chapter 6

CONCLUSIONS

The development of the crashworthiness simulation methodology applicable to thin-walled composite structural components with complex (mixed) shape and geometry has been presented in this work. The approach devised here is based on the integral implementation of finite element analysis combined with explicit dynamic simulation algorithm, progressive failure modelling, and composite material characterisation.

Existing models and methods of crashworthiness prediction for both conventional and composite thin-walled structural components were studied and reviewed in order to get a better understanding of the problem under consideration. The models and approaches have been assessed on the grounds of their feasibility for practical industrial implementation. The main criteria were the simplicity and reliability of the testing procedures included into the experimental material characterisation programmes.

The ability to model the geometrically non-linear dynamic structural response is determined by the performance of the finite element crash simulation software package adopted as a simulation tool. Comparative software and material model analysis has been conducted for both SMC and laminated composite structures. The two finite element analysis tools, PAM-CRASH and LS-DYNA, were evaluated using composite material models available within the software. A number of tensile and bending test simulations have been performed for composite plates made from SMC and laminated materials. As a result of this comparative analysis the PAM-CRASH software was adopted for further modelling and simulation. It was shown, that although composite material models have indeed been implemented, these models were almost entirely limited to the family of continuously reinforced composite materials, with the modelling of discontinuous (short-fibre) composites nearly completely lacking. At the same time more and more SMC based composites are used for the manufacturing of body panels in the automotive industry due to their operational and cost efficiency. The attempt has been made to develop the crash simulation methodology applicable to structural components made from SMC composites.

Manufacturing and testing of SMC GFRP specimens have been undertaken, thus providing the material characterisation, necessary for the material modelling. Progressive failure analysis of composite plates under bending loading has been conducted. Numerical results were compared with the experimental data in order to calibrate the model. The refinement of the model and numerical simulation procedure were completed. Further model validation has been performed for the scaled down thin-walled automotive component with complex (mixed) geometry.

The prototypes (demonstrators) have been manufactured using the same SMC material and tested under compressive loading. Simulation outcomes displayed that the modelling technique provided results, which showed a similar trend and failure profile compared to the experimental data.

In general, it has been concluded that the progressive failure simulation model, (including material characterisation procedure and numerical analysis) considered in the present work could be adopted as a tool for the virtual crash-simulations of thin-walled structures made from SMC composites. The proposed simulation methodology would provide the capability of analysing the design parameters without building and testing the actual prototypes.

The existent quantitative discrepancies between the simulation results and experimentation indicate the need for further refinement of material characterisation procedure. The nature of randomly reinforced materials ensures that this task is both necessary and complex, since scatter in the exhibited properties of the material is usually apparent, due to material's inherent inhomogeneity.

The progressive failure model incorporating a homogenisation model and statistical damage criteria has been developed and coarse model validation performed. The model has been adopted for integration into commercial finite element software package (PAM-CRASH) as a user-defined option for analysis. This will allow future refinement iterations to be performed.

Results obtained in this work were presented at two international conferences and published in the refereed conferences proceedings, and "Composite Structures" journal:

E.V. Morozov, K.E. Morozov and V. Selvarajalu. Damage model development for SMC composites. Proceedings of the Fourth International Conference on Composite Science and Technology (ICCST/4), Durban, South Africa, 2003, pp. 205-210.

E.V. Morozov, K.E. Morozov and V. Selvarajalu. Progressive damage modelling of SMC composite materials. Proceedings of the Fourth International Conference on Composite Science and Technology (ICCST/4), Durban, South Africa, 2003, pp. 531-537.

E.V. Morozov, S. Kaczmarczyk, K.E. Morozov and V. Selvarajalu. Numerical simulation of the progressive failure of SMC composite materials. Proceedings of the 14th International Conference on Composite Materials (ICCM-14), San Diego, USA, July 2003. 8pp. (CD-ROM). (The paper has been also selected and published as Technical Paper EM03-308 of the Society of Manufacturing Engineers (SME), Dearborn, MI, USA, 2003. 8pp.)

E.V. Morozov, K.E. Morozov and V. Selvarajalu. Damage model development for SMC composites. Composite structures, Elsevier, Vol. 62/3-4, 2003, pp. 373-378.

E.V. Morozov, K.E. Morozov and V. Selvarajalu. Progressive damage modelling of SMC composite materials. Composite structures, Elsevier, Vol. 62/3-4, 2003, pp. 361-366.

REFERENCES

- Abramowicz, W. (1983). The effective crushing distance in axially compressed thin-walled metal columns. *International Journal of Impact Engineering*, 1, pp. 309-317.
- Alexander, J.M. (1960). An approximate analysis of the collapse of thin cylindrical shells under axial loading. *Quarterly Journal of Mechanics and Applied Mathematics*, 13, pp.10-15.
- Anceau, J.H. (1994). *Models Cinematiques en Flexion*. These de Doctorat, Université de Valenciennes, France.
- Avalle, M., Belingardi, G. and Vadori, R. (1995). Numerical simulation of impact and damage in composite material structures. *Impact and Dynamic Fracture of Polymers and Composites* (a cura di J. G. Williams e A. Pavan), atti del convegno ESIS 19, Olbia, pp. 329-340.
- Avalle, M. and Belingardi, G. (1996). Experimental analysis of the collapse modes in the axial crushing of circular tubes, atti del XXV Convegno Nazionale AIAS, Gallipoli, Lecce, 4-7, pp. 867-874.
- Barenyi, B. (1952). Kraftfahrzeug, Insbesondere zur Beforderung von Personen. Patentschrift Nr 854147, Deutsches Patentamt.
- Belingardi, G. and Avalle, M. (1995). Investigation on the crushing of circular tubes: theoretical models and experimental validation, atti del Crashworthiness Symposium - ASME Int. Mechanical Engineering Congress, San Francisco (USA).
- Bury, K. V. (1975). *Statistical Models in Applied Science*. John Wiley & Sons.
- Chamis, C.C., Murthy, P.L.N. and Minnetyan, L. (1996). Progressive fracture of polymer matrix composite structures. *Theoret. Appl. Fracture Mech.*, vol. 25, no. 1, pp. 1-15.
- Chang, F.K. and Chang, K.Y. (1987a). Post-failure analysis of bolted composite joints in tension or shear-out mode failure. *Journal of Composite Materials*, Vol. 21, pp. 809-833.
- Chang, F.K. and Chang, K.Y. (1987b). A progressive damage model for laminated composites containing stress concentration. *Journal of Composite Materials*, 21, pp. 834-855.
- Cheikh Saad Bouh, A.B. (1992). *Evaluation des Performances de Divers Elements Finis et des Effets d'Anisotropie pour les Plaques Composites en Flexion*. Doctoral dissertation, Université Claude Bernard, Lyon.
- Chen, T., Dvorak, G. J. and Benveniste, Y. (1992). Mori-Tanaka estimates of the overall elastic moduli of certain composite materials. *Journal of Applied Mechanics*, Vol. 59, pp. 539-546.
- Cimpoeru, S.J. and Murray, N.W. (1993). The large deflection pure bending properties of a square thin-walled tube. *Int. J. Mech. Engng.* 35, pp. 247-256.

- Coutellier, D. and Rozycki, P. (2000). Multi-layered multi-material finite element for crashworthiness studies. *Composites: Part A*, 31, pp. 841-851.
- Desrumaux, F., Meraghni, F. and Benzeggagh, M.L. (1995). Micromechanical modelling of damage mechanisms in randomly orientated discontinuous fibre composite. *Proceedings of ICCM-10, Whistler, B.C., Canada, Volume I: Fracture and Fatigue*, pp. 487-494.
- Farley, G.L. and Jones, R.M. (1992a). Crushing characteristics of continuous fibre reinforced composite tubes. *Journal of Composite Materials*, Vol. 26, No. 1, pp. 37-50.
- Farley, G.L. and Jones, R.M. (1992b). Prediction of energy absorption capability of composite tubes. *Journal of Composite Materials*, Vol. 26, No. 3, pp. 388-404.
- Hahn, H.T. and Tsai, S.W. (1973). Nonlinear elastic behaviour of unidirectional composite laminates. *Journal of Composite Materials*, Vol. 7, pp. 102-118.
- Hashin, Z. (1979). Analysis of the properties of fibre composites with anisotropic constituents. *Journal of Applied Mechanics*, 46, p.543.
- Hashin, Z. (1980). Failure criteria for unidirectional fibre composites. *Journal of Applied Materials*, 47, pp. 329-334.
- Haug, E. and De Rouvray, A. (1993). Crash response of composite structures. Chapter 7. *Structural Crashworthiness and Failure* (N. Jones and T. Wierzbicki, eds.), Elsevier, pp. 237-294.
- Hill, R. (1964). Theory of mechanical properties of fibre-strengthened materials: I. Elastic behaviour. *J. Mech. Phys. Solids*, 13, pp. 189-198.
- Hoffmann, L., Kabelka, J. and Ehrenstein, G.W. (1995). Damage process modelling on SMC. *Proceedings of ICCM-10, Whistler, B.C., Canada, Volume I: Fatigue & Fracture*, pp. 335-342.
- Horton, W.H., Bailey, S.C. and Edwards, A.M. (1966). Nonsymmetric buckle patterns in progressive plastic buckling. *Experimental Mechanics*, Vol. 6, pp. 433-444.
- Hu, H.T. (1993). Buckling analysis of fibre composite laminate plates with material nonlinearity. *Proceedings of ICCM/9, Madrid, Volume V*, pp. 487-494.
- Huang, C., Cheikh Saad Bouh, A.B. and Verchery, G. (1993). Progressive failure analysis of laminated composites with transverse shear effects. *Proceedings of ICCM-9, Madrid, Volume V: Composites Behaviour*, pp. 97-104.
- Kabelka, J. and Ehrenstein, G.W. (1992). Structure and thermo-elastic properties of SMC. 47th Annual Conference, CI SPI, Cincinnati, Sess. 1-E.

- Kecman, D. (1983). Bending collapse of rectangular section tubes and square section tubes. *Int. J. Mech. Sci.*, 25, pp. 623-36.
- Kecman, D. (1989). Deep bending collapse of thin-walled beams and joints. *Manual of Crashworthiness Engineering*, Vol. 5, Center for Transportation Studies, MIT, Cambridge, MA.
- Kindervater C.M. and Georgi H. (1993). Composite strength and energy absorption as an aspect of structural crash resistance. Chapter 6. *Structural Crashworthiness and Failure* (N. Jones and T. Wierzbicki, eds.), Elsevier, pp. 189-234.
- Krieg, R.D. and Key, S.W. (1976). Implementation of a time dependant plasticity theory into structural computer programs. *Constitutive Equations in Viscoplasticity: Computational and Engineering Aspects* (American Society of Mechanical Engineers, New York, N.Y.), Vol. 20, pp. 125-137.
- Lardeur, P. (1990). *Developpement et Evaluation de Deux Nouveaux Elements Finis de Plaques et Coques Composites avec Influence du Cisaillement Transversal*. Doctoral dissertation, Universite de Technologie de Compiègne.
- LS-DYNA Key-Words Manual. (2001). Vol. 2, Livermore Software Technology Corporation.
- LS-DYNA Theory Manual. (1998). Livermore Software Technology Corporation.
- Matzenmiller, A. and Schweizerhof, K. (1990). Crashworthiness simulations of composite structures – a first step with explicit time integration. *Nonlinear Computational Mechanics- A State of the Art*, (P.W. Wriggers, et al., eds.), Springer-Verlag.
- Maltzenmiller, A., Lubliner, J. and Taylor, R.L. (1991). An Anisotropic Damage Model for Fibre Composites. Report UCB-SEMM-91/09, Dept. of Civil Eng., Univ. of California at Berkely, Berkely, CA.
- Mamalis, A.G., Manolakos, D.E., Demosthenous, G.A. and Ioannidis M.B. (1998). *Crashworthiness of Composite Thin-Walled Structural Components*, Technomic.
- McGregor, I.J., Meadows, D.J., Scott, C.E. and Seeds, A.D. (1993). Impact of aluminium structures. Chapter 10. *Structural Crashworthiness and Failure* (N. Jones and T. Wierzbicki, eds.), Elsevier, pp. 385-421.
- Meraghni, F. and Benzeggagh, M.L. (1995). Micromechanical modelling of damage mechanisms in randomly orientated discontinuous fibre composite. *Proceedings of ICCM-10*, Whistler, B.C., Canada, Volume I: Fracture and Fatigue, pp. 487-494.
- Minnetyan, L., Murthy, P.L.N., and Chamis, C.C. (1990). Composite structure global fracture toughness via computational simulation. *Computers and Structures*, Vol. 37, No. 2, pp. 175-180.

- Minnetyan, L. (1992). Progressive fracture in composites subjected to hygrothermal environment. *International Journal of Damage Mechanics*, Vol. 1, No. 1, pp. 60-79.
- Minnetyan, L. and Chamis, C.C. (1993). Effects of progressive fracture on the buckling resistance of composite structures. *Proceedings of ICCM-9, Madrid, Volume VI: Composite Properties and Applications*, pp.369-376.
- Mori, T., and Tanaka, K. (1973). Average stress in matrix and average elastic energy of materials with misfitting inclusions. *Acta Metal.*, 21, pp. 571-574.
- Morozov E.V., Morozov K.E., and Selvarajalu V. (2003a). Damage model development for SMC composites. *Composite structures*, Elsevier, Vol. 62/3-4, pp. 373-378.
- Morozov E.V., Morozov K.E., and Selvarajalu V. (2003b). Progressive damage modelling of SMC composite materials. *Composite structures*, Elsevier, Vol. 62/3-4, pp. 361-366.
- Murthy, P.L.N. and Chamis, C.C. (1986). *Integrated Composite Analyser (ICAN). Users and Programmers Manual*, NASA Technical Paper 2515.
- Narayanaswami, R. and Adelman, H.M. (1977). Evaluation of the tensor polynomial and Hoffman strength theories for composite materials. *Journal of Composite Materials*, Vol. 11, pp. 399-377.
- PAM-CRASH Solver Notes. (2000). ESI Group.
- Pugsley, Sir A. and Macaulay, M. (1960). The large scale crumpling of thin cylindrical columns. *Quarterly Journal of Mechanics and Applied Mathematics*, 13, pp. 1-9.
- Reddy, J.N. (1987). A Generalization of two-dimensional theories of laminated composite plates. *Communications in Applied Numerical Methods*, Vol. 3, pp.173-180.
- Reddy, J.N. and Reddy, Y.S.N. (1993). An accurate prediction of failure in composite laminates using a layerwise model. *Proceedings of ICCM-9, Madrid, Volume III: Composites Modelling and Processing Science*.
- Rozycki, P., Coutellier, D., Walrick, J.C. and Mascaro, J. (1998). *Caracterisation Experimentale des Parametres d'Endommagement d'un Modele Bi-Phase pour la Simulation du Comportement de Composites Fibres/Matrice*, 11^{emes} Journees Nationales des.
- Shahid, I. and Chang, F.K. (1993). Progressive failure analysis for laminated composites under multiple in-plane loads. *Proceedings of ICCM-9, Madrid, Volume V: Composites Behaviour*, pp.105-113.
- Shahid, I. and Chang, F.K. (1992). Modelling of progressive failure of cross-ply composites subjected to combined in-plane loads. *Seventh Technical Conference on Composite Materials*, American Society for Composites, Pennsylvania, USA.

- Timoshenko, S. P. and Gere, J. M. (1963). *Theory of Elastic Stability*, 2nd edition, Mc Graw-Hill Book Company.
- Tsai, S.W. and Wu, E.M. (1971). A General theory of strength for anisotropic materials. *J. of Composite Materials*, Vol. 5, pp. 58-80.
- Vasiliev, V.V. and Morozov, E.V. (2001). *Mechanics and Analysis of Composites Materials*, Elsevier Science.
- Wierzbicki, T. (1983a). Crushing behaviour of plate intersections. *Structural Crashworthiness*, (N. Jones and T. Wierzbicki, eds.), Elsevier, pp. 66-95.
- Wierzbicki, T. (1983b). Crushing analysis of metal honeycombs. *International Journal of Impact Engineering*, 1 (2), pp. 157-174.
- Wierzbicki, T. and Bhat, S.U. (1986). A moving hinge solution for axisymmetric crushing of tubes. *International Journal of Science*, 28 (3), pp. 135-51.
- Wierzbicki, T., Bhat, S. U., Abramowicz, W. and Brodtkin, D. (1992). A two folding elements model of progressive crushing of tubes. *International Journal of Solids and Structures*, Vol. 29, n. 4, pp. 3269–3288.
- Wierzbicki, T., Recke, L., Abramowicz, W., Gholami, T. and Huang, J. (1994). Stress profiles in thin-walled prismatic columns subjected to crush loading- II Bending. *Computers and Structures*, 51, pp. 625-641.
- Williams, K. and Vaziri, R. (1995). Finite element analysis of the impact response of CFRP composite plates. *Proceedings of ICCM-10*, Whistler, B.C., Canada, Volume V: Structures, pp. 647-654.